Use of Positron Emission Particle Tracking (PEPT) for Studying Laminar Mixing in Static Mixers

By

Marjan Rafiee

A thesis submitted to
The University of Birmingham
for the degree of
DOCTOR OF PHILOSOPHY

School of Chemical Engineering
College of Engineering and Physical Sciences
The University of Birmingham
September 2013

Dedicated to my parents, for their unconditional support and love.

Abstract

Over the last few decades, static mixers have been used commonly in different industries mainly for mixing of high viscosity fluids. The performance of this group of mixers has been investigated by many groups via numerically based studies. Experimental studies, however, are limited, particularly for measurement of the flow fields with fluids of complex rheology; there is also a lack of fundamental understanding of laminar flow and mixing performance for such duties. This is essential in order to gain improved design procedures for the selection and operation of the mixers in blending applications.

PEPT is a flow visualisation technique, which has been developed at The University of Birmingham and has been used in a wide range of applications. The main objective of the work presented in this thesis is to use PEPT to study laminar flow and mixing in one of the most common types of static mixer, the Kenics (KM) mixer, as well as a recently developed SMX-plus design. The Lagrangian and Eulerian analyses presented are the first attempt in demonstrating the application of PEPT as a tool to characterise the flow and mixing performance in static mixers.

PEPT has enabled experimental determination of full three-dimensional flow fields within Kenics and SMX-plus mixers when blending both Newtonian and non-Newtonian fluids. The Eulerian velocity distribution maps are studied along the mixer geometry, as well as the shear rate and residence time distribution. The velocity maps help in visualizing the flow split at the transition regions between consecutive elements, and the re-blending of this along each element. The results from axial, tangential and cross-sectional velocity maps of the Newtonian fluid were in agreement with the literature.

The experimental RTD was fitted to the convection and dispersion models, which demonstrated the distributive and dispersive mixing mechanisms along the mixers. It was shown that dispersive mixing happens mainly in the transition regions. The shapes of the striations have been determined by visualising the changes of striations along the mixers. The mixing performance along the mixers was also characterised by means of a segregation index. The effect of changing the twist angle of the blade on the motion of the Newtonian fluids and the mixing performance along the Kenics mixer was studied. It was shown that the Kenics mixer with 150° twist in blade has the best performance.

The data from the PEPT experiment on SMX-plus mixers showed improved mixing performance compared with the Kenics mixers. It was shown that each element of SMX-plus is equivalent to three mixing element of Kenics mixer.

ACKNOWLEDGMENTS

First and foremost, I would like to express my gratitude towards my supervisors Dr. Andy Ingram and Prof. Mark Simmons, not only for their valuable guidance and input during this research, but also for their friendship. I am also thankful to the financial support of Johnson & Matthey Company, and Prof. Hugh Stitt.

I would like to thank Prof. David Parker, Dr. Thomas Leadbeater, and Dr. Joseph Gargiuli from the Positron Imaging Centre of University of Birmingham, and also Mr. David Boylin for their assistance with the PEPT experiment. I am also grateful to Dr. Serafim Bakalis for his suggestions during the early stages of this work.

A special thank to Dr. Andrea Gabriele for the advice and assistance during my research, and also for his invaluable presence. Sam, for all the conversations and laughs that we had during the last eight years in university, which will always stays in my memory. Nima, for his precious encouragement and friendship during the last few years. Parihan and Siavash, for being there as good friends whenever I needed them. Negar, Ashkan, Amir, and Benny for all the fun and happy memories in Birmingham. Dr. Fabio Chiti, for his friendship and guidance. All the people from the General office, especially Lynn, for their continuous support.

Most of all, I would like to thank my parents for their incredible support and encouragement during my education, and also my sister, Mina, for always being there for me.

Table of Contents

Table of Figures

Chapter 1 . INTRODUCTION

1.1 Background

Mixing plays an important role in the quality of the final product in nearly all industrial chemical processes. Inadequate mixing could end up increasing the production cost and lowering product quality. Increasing energy input has been used usually as a solution to mixing problems in practice, which results in higher costs and often leads to diminishing returns. Consequently, the research on mixing and its relation to the flow behaviour is required to get a better understanding about any possible improvement on the mixing efficiency, which could reduce also the energy consumption.

Static mixers have been used for many years in different industries with a wide range of applications such as blending of multicomponent drugs in the pharmaceutical industry, mixing additives into polymers in the polymer industry, ice cream production in the food industry, etc. They are often used for mixing of high viscosity fluids in continuous processes for different reasons such as low cost of installation, easy maintenance, small spaced required for operation, and low pressure drop. The basic design of static mixer contains a number of stationary mixing elements installed within an empty pipe. The main mixing mechanisms are due to the division and re-orientation of the fluid elements (dispersive mixing), and the stretching and elongation of them (distributive mixing).

During the last fifty years different designs of static mixers have been developed, and currently there are more than ten different types that are being used in different industries. This work is focused on one of the most common static mixers, the Kenics static mixer, and also SMX-plus, which is one of the most recent static mixers developed by Sulzer Company.

In the last twenty years, the use of static mixers in different industries has increased significantly. Knowledge of flow behaviour and mixing performance of this group of

mixers has become beneficial in order to optimise the production process. Consequently, a high number of numerical works focussed on simulating the flow in the Kenics mixer using Lagrangian techniques (Hobbs and Muzzio (1997a), Hobbs, Swanson et al. (1998), Rauline, Tanguy et al. (1998), Jaffer and Wood (2009), Galaktionov, Meijer et al. (2002)), to get a better understanding about the flow behaviour within this type of mixer. Experimental study, however, is limited, particularly measurement of the instantaneous flow field. Most of the experimental Lagrangian techniques available for analysing the flow field in different mixers, including static mixers, require transparent fluids and mixers (see §2.2.1). Positron emission particle tracking (PEPT) however is the most promising technique to study opaque systems, which works based on detecting a radioactive particle within the system. PEPT has been used widely in both dry and liquid systems (Wong (2006), Marigo, Cairns et al. (2010), Marigo, Davies et al. (2013), Guida, Nienow et al. (2010), Guida, Nienow et al. (2011) Chiti, Bakalis et al. (2011), Gabriele (2011)). This technique generates a three dimensional data contains the movement of the tracer in *x*, *y,* and *z* direction at different time intervals, which can be used to study the flow fields at any location within the mixer. PEPT has been applied previously to different batch mixing devices such as stirred vessels (Guida, Fan et al. (2009),Guida, Nienow et al. (2010), Chiti, Bakalis et al. (2011)). In this work, we applied PEPT to continuous flow in the Kenics and SMX-plus static mixers to generate three-dimensional Lagrangian data, in order to study the flow behaviour and mixing performance within these mixers.

1.2 Objectives

The objectives of this work are:

- *Develop a methodology to study laminar flow behaviour in different static mixers.* The main objective of this work is to use PEPT experimental data to develop a

general methodology to characterise the Laminar flow of Newtonian and non-Newtonian fluids in static mixers. In the course of the methodology development, both the procedure used and the MATLAB® scripts developed for the analysis of the PEPT data obtained from static mixers will be described in detail enabling the reuse for other systems by simply re-defining the key parameters. Different flow characteristics such as Eulerian velocity distribution maps and residence time distribution will be studied in this work to get a better understanding about the operation of static mixers.

- *Characterise the mixing performance of static mixers using PEPT.* The use of the PEPT Lagrangian data allows construction of experimental maps of the distribution of the particle movements in the various Kenics and SMX-plus mixers. This information generated is used to quantify the local segregation index, which in turn defines the overall performance of the mixers.

- *Study the effect on mixing of changing the twist of the blade in the Kenics mixer to identify an optimum design of this type of mixer.* The original design of the Kenics mixer with 180° blade twist angle has been modified into 150° and 120° twist. The effect of changing the twist angle of the blade on the mixing performance and flow behaviour of the mixer will be studied experimentally for the first time in this work by means of segregation index, and an optimum twist angle will be suggested at the end.

- *Characterise the flow and mixing performance of the SMX-plus mixer.* The flow behaviour of SMX-plus mixer will be studied to get a better understanding about the

mixing mechanisms and flow motion within this complex geometry. The mixing performance and RTD of SMX-plus will be compared with the Kenics mixer to get a better understanding about the effect of using the complex geometry of SMX-plus on the flow.

1.3 Thesis Layout

The layout of this thesis is as follows:

- Chapter two gives an overview of the current literature on laminar mixing fundamentals, mixing quantification methods, common experimental techniques which have been used to obtain flow fields, and work carried out on static mixers, focusing on the existing literature on Kenics, SMX, and SMX-plus mixers.
- Chapter three reviews the experimental procedure, the equipment, and the geometry specifications of the mixers used during the experiments. The in-depth analysis of the parameters and the routines used to process the raw data from the PEPT measurement is discussed in this chapter. The Lagrangian and Eulerian methods used during the data analysis are also described.

Chapters four to seven contain the results, analysis and discussion of the PEPT experiments:

- Chapter four describes the investigation of the flow behaviour of a Newtonian model fluid (glycerol) in Kenics mixer. The Eulerian velocity maps and the residence time distribution are studied in this chapter. The mixing performance of the mixer is characterised using two different parameters: coefficient of variance (CoV) and the segregation index.

- Chapter five describes studies the flow behaviour of non-Newtonian fluids in Kenics static mixer. Two different concentrations of aqueous Carbopol solution are used as non-Newtonian model fluids in this work. The flow behaviour and mixing performance of these two fluids are compared to each other and also to the Newtonian fluid.
- Chapter six is concerned with the effect of changing the twist angle of the blade in Kenics mixer on the performance of this mixer. An optimum twist angle is suggested by the end of this chapter.
- Chapter seven explains the measurements made on the SMX-plus mixer. The motion of the fluid within the mixer is studied by investigating the Eulerian velocity distribution maps and residence time distribution. The mixing performance of SMX-plus mixer is characterised using the segregation index, and compared with that of the Kenics mixer.
- Finally, in Chapter eight, are given the conclusions and recommendations for the future work.
- The Attached DVD contains four animations about the distribution of the particles along both Kenics and SMX-plus mixer, using PEPT experimental data.

For clarity purposes a separate notation section presenting the symbols used within a chapter has been added to the end of each chapter. Please note some of the symbols might represent different quantities in different chapters.

Chapter 2 . LITERATURE REVIEW

This chapter contains a review of the current literature on the fundamentals of laminar mixing and research work carried out on Kenics mixer, SMX and SMX-plus static mixers. The first part of this chapter presents the classification of the fluids according to their rheological properties, and describes the main mixing mechanisms in laminar mixing, focusing on the mechanisms used in static mixers. Different experimental techniques which have been used in the literature to quantify mixing in both dynamic and static mixers are also described, as well as the positron emission particle tracking technique which is the experimental technique used in the current work. The development of static mixers during the last forty years is discussed, focusing on Kenics and SMX-plus mixers.

2.1 Fluid dynamics

2.1.1 Rheology

Fluids can be described with rheological models, which relate the deformation of the fluid when subjected to applied stresses. These models provide information about the relationship between the dynamic state of deformation (shear stress) and kinematic state of deformation (shear rate). For a Newtonian fluid, the relationship between the shear stress and shear rate is linear:

$$\tau = \mu\dot{\gamma} \qquad \textbf{(Equation 2.1)}$$

where τ is the shear stress (Pa), $\dot{\gamma}$ is the shear rate (s^{-1}), and μ is the dynamic viscosity of the fluid ($kg.m^{-1}.s^{-1}$). The viscosity of the Newtonian fluid is constant at a given temperature and pressure. The flow condition of the Newtonian fluids can be

classified by the ratio of the inertial forces to the viscous forces: the Reynolds number:

$$N_{\mathrm{Re}} = \frac{\rho u D}{\mu} \qquad \textbf{(Equation 2.2)}$$

where ρ is the density of the fluid ($kg.m^{-3}$), u is the average velocity in the system ($m.s^{-1}$), and D is the characteristic length, which usually is considered as the diameter of the tube. If N_{Re} is less than 2100, the flow is considered to be in the laminar regime. In laminar regime the viscosity plays an important role in the relative motion of the fluid. The transition regime is defined when $2100 < N_{Re} < 10000$, and the turbulent regime is defined when $N_{Re} > 10000$.

Fluids which have a non-linear relationship between shear rate and shear stress, are classified as non-Newtonian. The apparent viscosity of non-Newtonian fluids is thus not constant for a given temperature and pressure, and depends on the shear rate. Non-Newtonian fluids can be classified according to their flow curve (Figure 2.1).

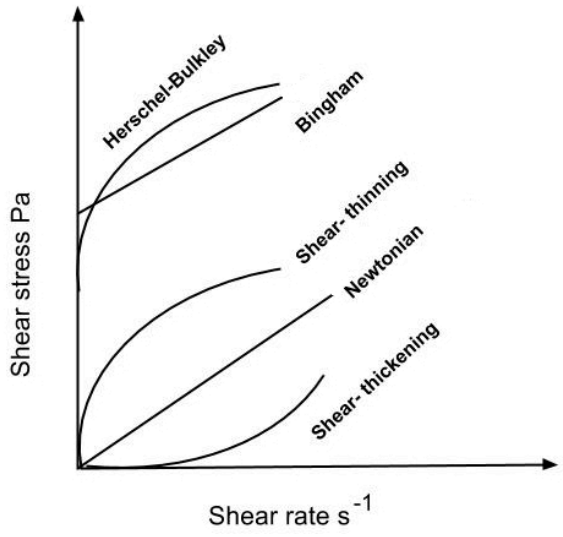

Figure 2.1. Flow behaviour curve for typical non-Newtonian fluids (adopted from Steffe (1996)).

There are different ways of classifying the non-Newtonian fluids according to their rheological properties. The most common classification is dividing them into three groups, shear thinning, shear thickening, and viscoplastic.

The first group, shear-thinning fluids, are the ones for which the shear stress increases less than in proportion with the shear rate, hence viscosity decreases with increased shear rate. These fluids are generally composed of long molecules, which are randomly oriented within a structure. By applying increasing shear stress, the molecules align and thus slip over each other more easily, resulting in a decrease in viscosity. There are different mathematical models which are used to describe shear thinning fluids. The simplest model is the *power-law* model:

$$\tau = k\dot{\gamma}^n \qquad \textbf{(Equation 2.3)}$$

where k is the consistency index and n is the power law exponent. The smaller the value of n is, the fluid is more shear-thinning. Cream, polymer melts, and paper pulp are examples of shear-thinning fluids.

The fluids with $n > 1$ in Equation 2.3 are considered as shear-thickening fluids. The apparent viscosity of shear-thickening fluids increases with increasing the shear rate. Some of the unlinked polymers are considered as shear-thickening fluid due to the existence of mechanical entanglements between the molecules of their rigid chains. The higher the shear stress is, the more molecule chains may prevent the relative motion between themselves and therefore the fluid viscosity increases. These fluids are usually suspensions with high solid contact. Corn flour in water and china clay are examples of shear-thickening fluids.

The third group, Viscoplastic fluids, do not deform until the shear stress exceeds a certain value called yield stress. For viscoplastic fluids, the material starts to flow if the external forces acting on it become larger than the internal structural forces. Fluids such as grease, toothpaste, and cement are considered as viscoplastic fluids. The viscous properties of the fluids with a yield stress can be defined in this type of non-Newtonian fluids. There are different mathematical models, which are used to describe the rheological behaviour of viscoplastic fluids, and two of them will be described in this section: Bingham, and Herschel-Bulkley fluids.

Bingham model describes the behaviour of a viscoplastic fluid with a linear flow curve above the yield stress (Figure 2.1):

$$\tau = \tau_0 + \mu\dot{\gamma} \qquad \textbf{(Equation 2.4)}$$

where τ_0 is yield stress. Tomato paste, grease, and vegetable fats are some of the examples of this type of fluids.

On the other hand, Herschel-Bulkley model represents the fluids, which have a non-linear flow curve:

$$\tau = \tau_0 + k\dot{\gamma}^n \qquad \textbf{(Equation 2.5)}$$

The value of k and n can be found by curve-fitting techniques. Herschel-Bulkley fluids are also considered as generalised power law model, since the equation representing their model is same as the power law one with the addition of yield stress term. Typical example of Herschel-Bulkley fluids includes yogurt, kaolin slurries, and soft cheese. The non-Newtonian fluids used in this work are considered as Herschel-

Bulkley fluids. The related rheological properties of these fluids will be described later in Chapter 5.

2.1.2 Laminar Mixing

Mixing is a process, which increases the homogeneity (or decreases the heterogeneity) of a mixture containing two or more components. Convection is the main movement, which causes mixing in liquid and gas systems. This movement occurs in different ways by:

1. Advection
2. Eddy motion
3. Molecular diffusion

Molecular diffusion is the main mechanism of mixing in gases and low viscosity fluids, and driven by the concentration gradient in the mixture. For highly viscose fluids, molecular diffusion is happening extremely slowly and in a much larger time scale than the required mixing time, and therefore does not play an important role in the mixing process of this type of fluids. Eddy motion can cause molecular diffusion in turbulent mixing. For highly viscose fluids, the flow is laminar, and consequently eddy motion and molecular diffusion do not contribute in the mixing process. Hence, for highly viscose fluids the main mechanism of mixing is due to the convective forces. Advection involves the movement of the fluid elements through the mixture due to the applied physical forces. Advection causes two main phenomena, the increase in the interfacial area between different component of the mixture (Spencer et al., 1951), and distribution of one component among the other one without increasing the interfacial area (Bergen et al., 1958).

In general, mixing of highly viscous fluids requires two main mixing mechanisms: distributive mixing, and dispersive mixing (Tanguy et al., 2005). For highly viscous fluids, distributive mixing is achieved by imposing a deformation to the fluid elements by means of shear, stretching, and squeezing the mixture. Figure 2.2 demonstrates the distributive and dispersive mixing using blue and red particles. As is shown in Figure 2.2, distributive mixing includes rearrangement of the fluid elements as a result of flow division and random or ordered re-orientation. On the other hand, dispersive mixing involves breaking down the lumps or the fluid elements by applying mechanical forces on the mixture.

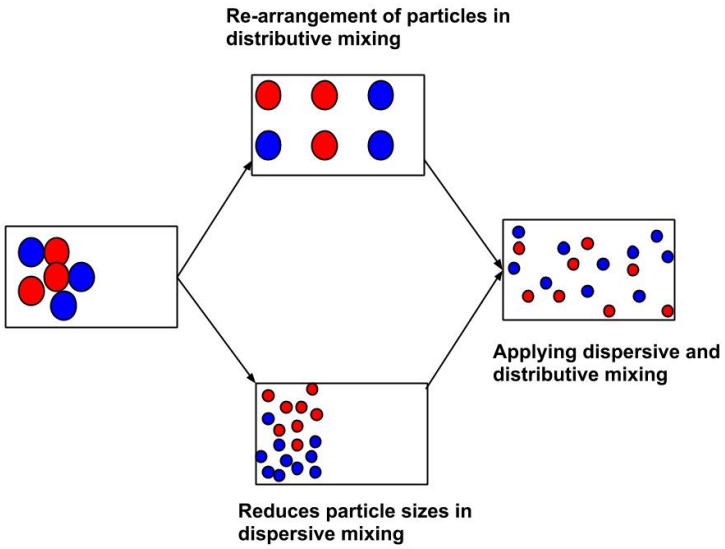

Figure 2.2. Distributive and dispersive mixing mechanisms.

Most of the convective mixers, such as motionless (static) mixers operate under both distributive and dispersive mixing. The mixing process in static mixers will be discussed in more detail in Section 2.2.

2.1.2.1 Mixing quantification

The study of mixing quantification dates back many years by defining a well-mixed mixture using both quantitative and qualitative measurements. Different quantitative measurements have been used in literature to measure the mixedness within a mixture. In this section, some of the most common mixing quantification methods will be described.

2.1.2.2 Intensity and scale of segregation

Danckwerts (1952) did one of the earliest studies on quantifying mixing in molecular scale by introducing two important properties: intensity and scale of segregation. With reference to Figure 2.3, the scale of segregation is defined as a measurement of the break-up process without the action of molecular diffusion. The intensity of segregation is a measure of the concentration difference between each species in the fluid.

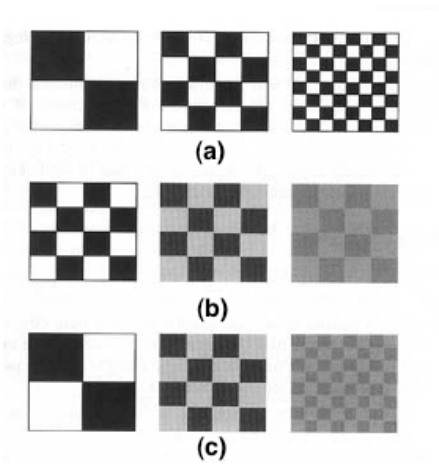

Figure 2.3. (a) Decrease in scale of segregation; (b) Decrease in intensity of segregation; (c) Decrease in both scale and intensity of segregation (adopted from Tanguy et al. (2005)).

According to Danckwerts definition, the intensity of segregation can be calculated as the ratio of the variance in the concentration of random samples taken from a mixture compared with the maximum value of variance present in the mixture at the start of the mixing process. The variance is calculated as:

$$\sigma^2 = \frac{\sum_{i=1}^{n}\left(C_i - \bar{C}\right)^2}{n-1} \qquad \textbf{(Equation 2.6)}$$

where C_i is the concentration of the i^{th} sample, $\bar{C}$ is the average concentration through the mixture, and n is the number of samples taken from the mixture.

The intensity of segregation is then defined as (Aubin et al. (2003)):

$$I = \frac{\sigma^2}{\sigma^2_{\max}} \qquad \textbf{(Equation 2.7)}$$

At the start of the mixing process, the value of intensity of segregation (I) is equal to one. For a homogenous mixture, the molecules are distributed down to the molecular scale, and the value of I is equal to zero as $\sigma^2 \rightarrow 0$. Danckwerts' work became the basis of many studies, which focused on the concentration distributions and also the parameters that could affect this distribution.

Another groups of works presumed that the concentration distributions are known and examine how it is modified by the various factors such as shear and initial striation thickness. The work by Mohr et al. (1957) calculated the striation thickness based on the initial thickness of the fluid elements, and the rate of decrease in the striation thickness was related to the mixture quality. It was shown mathematically that in laminar flow systems the final striation thickness is equal to the initial striation thickness divided by the product of the amount of the shear supplied. The result of

their work caused future research to relate the changes of striation thickness to the quality of the mixture.

Cooper Jr (1966) showed the effect of shear, elongation, and rotation of the fluid elements on the striations. It was shown the re-arrangement, folding, and division of the fluid elements are extremely important to improve the mixture homogeneity.

A similar statistical method to Danckwerts work involves calculation of the coefficient of variance (CoV), which is the standard deviation of the concentration at different locations in the mixture normalised by mean concentration (Kukukova et al., 2009):

$$CoV = \frac{1}{N_t}\sum_{i=1}^{N_t}\left(\frac{C_i - C_{mean}}{C_{mean}}\right) \qquad \textbf{(Equation 2.8)}$$

where N_t is the total number of measurement locations, C_i is the concentration at location i, and C_{mean} is the mean concentration.

Following the concept of Danckwerts intensity of segregation, Hobbs et al. (1997a) used a number based standard deviation for a system which uses tracer particles to measure the mixing performance in Kenics static mixer. In this numerical work, N_t numbers of tracer particles were injected into the system, and the geometry was divided in n number of cells. By finding the number of particles in each cell, the average number of particles per cell was then calculated as the ratio of the total number of particles (N_t) to the number of cells (n). By substituting C_i and $\overline{C}$ in Equation 2.6 with N_i and $\overline{N}$, the number based variation coefficient was calculated. As a measurement for characterising mixing, the reduction of variation coefficient was then calculated by the following relation:

$$\frac{\sigma}{\overline{N}} = B \ \exp(\ -G \ \ \frac{L}{D}\ ) \qquad \textbf{(Equation 2.9)}$$

where $\sigma/\overline{N}$ is called the relative standard deviation (RSD), $\overline{N}$ is the average number of particles per cell, B is the CoV of the unmixed inlet stream, and G is the rate of decrease of the coefficient of variance per unit length of the mixer (mixing rate), and L and D are the length and the diameter of the mixer. The statistical analysis of the concentration in samples from the mixture based on Danckwerts intensity of segregation, and also the quantitative measurement of the reduction of variation coefficient, became the basis of the mixing characterisation in static mixers in a number of later works (Mickaily-Huber et al. (1996) , Hobbs et al. (1997a), Hobbs et al. (1998a), Bakker et al. (1998), Zalc et al. (2002b), Rauline et al. (2000), Galaktionov et al. (2003), Szalai et al. (2003)).

Kukukova et al. (2009) suggested a new model to characterise the mixing performance based on three key concepts: intensity of segregation, scale of segregation, and exposure. It has been discussed that according the Danckwerts work on intensity and scale of segregation, the measurement of one variable (i.e. intensity of segregation) does not provide enough information about how well mixed is the system since it is inferring information about the other variable. This issue is illustrated in Figure 2.4.

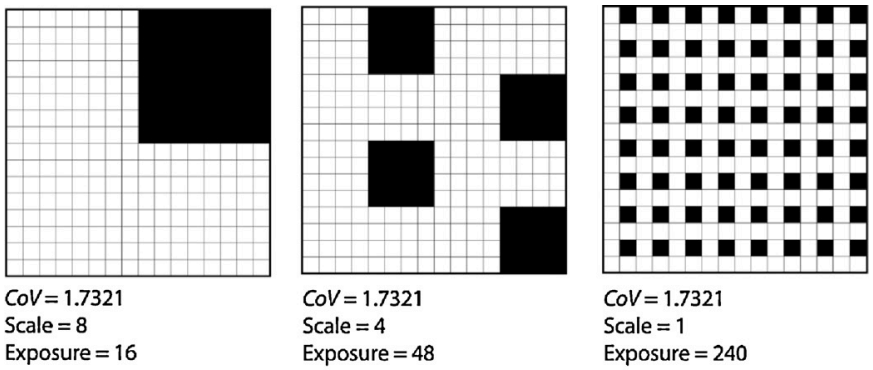

Figure 2.4. Three dimension of mixing: intensity of segregation, scale of segregation, and exposure (Kukukova et al. (2009)).

Figure 2.4 shows checkerboard patterns, which are organised from left to right by size of the pattern. The scale of segregation on this graph is equal to the number of the neighbouring cells on one side of each black square. They also defined a new parameter, called exposure, which is the rate of reduction in segregation:

$$E \cong \sum_{i=1}^{N_t} \sum_{j=1}^{N_b} \frac{1}{2} \; k' \quad a_{ij} \quad (C_i - C_j) \qquad \textbf{(Equation 2.10)}$$

where N_t is the number of squares in check board, N_b is the number of the neighbouring squares, $k' = 1$ is the strength of the interaction, $a_{ij} = 1$ is the contact area per side, and $(C_i - C_j)$ is the concentration difference between two consecutive neighbours. The concentration of the black squares is defined as $C_i = 1$, and for white squares as $C_i = 0$.

By the first look at this graph, an observer might say the mixing is improved from left to right since the black squares are more distributed among the white ones. However, it is shown the value of CoV is constant for all these graphs. This indicates the intensity of segregation alone contains no information about the arrangement of the black and white squares. They discussed that CoV (intensity of segregation) is not

enough to completely define mixing, since the scale of segregation also plays an important role as it is shown in Figure 2.4. It has been shown in this work that the exposure decreases when CoV reduces but when the scale of segregation becomes smaller the effect of concentration variance becomes less important. In summary, by showing some experimental and numerical examples they demonstrated that CoV contains no information about the scale of segregation and the arrangement of the fluid elements in the mixture. It was suggested that all three discussed parameters in this work (intensity of segregation, scale of segregation, and exposure) play important roles in industrial mixing problems, and therefore they should be considered all to characterise the mixing performance.

2.1.2.3 Stretching histories

Another criterion, which can be used to quantify mixing, is the stretching of the fluid elements. The first group of works on this subject focused on determining the evolution of mixing by studying the stretching of the fluid elements in two-dimensional time-periodic flows (Rom-Kedar et al. (1990), Muzzio et al. (1991), Muzzio et al. (1992a), Muzzio et al. (1992b), Liu et al. (1994)). The inter-material surface generated in different regions of the mixture is proportional to the stretching of the fluid elements, and therefore the rate of mixing can be determined by the stretching area (Hobbs et al. (1997a)). This method of quantification is widely used in numerical works and in chaotic systems, including static mixers. For such a system, the fluid particles are located close to each other before starting the mixing process, and diverge exponentially in time by passing through the mixer. The exponential divergence of the fluid elements is desirable in a mixing process, since it shows the dispersion of the clusters of material. The stretching of fluid elements in a mixture can

be characterised by studying the Lyapunov exponent (Tanguy et al. (2005)). |The initial distance between two particles is represented as l_0, which can be changed due to the reorientation and elongation of the velocity field passing through different regions of the fluid. The length of this vector after time t_n is represented by l_n (Figure 2.5).

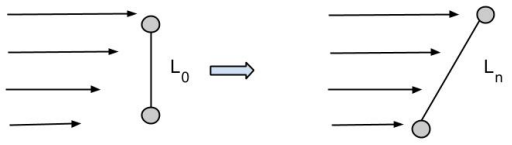

Figure 2.5. Calculating the Lyapunov exponent from the fluid elements stretching. A small material filament, represented by a vector l_0, is convected by the flow and consequently the length increases to l_n (adopted from Tanguy et al. (2005)).

The ratio of l_n / l_0 is called stretching of the fluid element:

$$\lambda = \frac{l_n}{l_0} = e^{\Lambda t} \qquad \textbf{(Equation 2.11)}$$

λ represents the intensity of the mixing experienced by material element. The exponential rate of average growth of vector (Λ) is called the Lyapunov exponent (Oseledets (1968)).

Hobbs et al. (1997a) represented the first application of this technique in a complex three-dimensional industrial mixer. 20000 tracer particles were placed on the entrance of the mixer, and their position along the mixer was calculated using tracking software. The stretching histories of the fluid elements were calculated by assigning an initial stretch vector to each particle at time zero. At the end of each mixing element, the position and components of stretch vector (l) was recorded, and the total accumulated stretching (λ) was calculated after sometime using Equation 2.11. The

geometric mean of the stretching values for all the *N* particles was calculated at the end of each mixing element using the following equation:

$$\langle \lambda_g \rangle = \left(\prod_{i=1}^{N} \lambda_i \right)^{1/N} \qquad \textbf{(Equation 2.12)}$$

The logarithm of $<\lambda_g>$ was then plotted vs. number of mixing element (Figure 2.6).

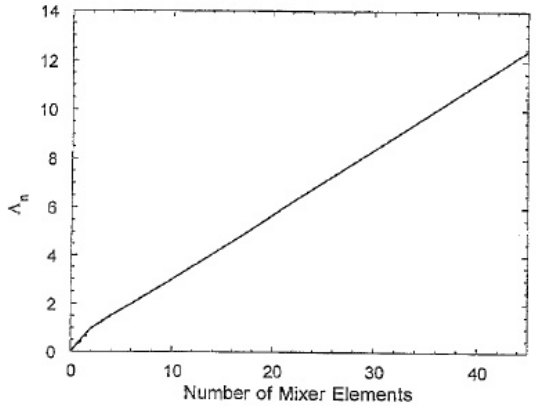

Figure 2.6. Logarithm of mean stretching vs. number of mixer elements, where $\Lambda_n = \log_{10} < \lambda_g >$ (Hobbs et al. (1997a)).

It was shown that along the first two elements, the initial orientation of the stretch vectors are realigned to correspond to the principal stretching of the flow. After the realignment, the mean stretch grows at a steady exponential rate vs. number of mixer element, which is a signature of chaotic flow.

Hobbs et al. (1998a) used this technique to study the effect of changing the twist angle of the blade in Kenics static mixer on the mixing performance. They characterised mixing for a Newtonian fluid with Reynolds number of 0.15 based on two techniques that were described above: using the rate of decrease in variation coefficient (Equation 2.9), and studying the stretching histories of the fluid elements. They showed that the results calculated from both techniques are similar, and therefore the stretching computation provides a measurement of mixing performance. They also

defined a new variable to study the mixer efficiency, β, which was defined as the mean stretching rate normalised by the pressure drop. This work will be described in much more detail in Section 2.2.1.

After the two above key works, measuring the stretching rate was used as one of the most common methods to characterise the mixing performance in static mixers. The effect of Reynolds number on mixing performance of Kenics static mixer (Hobbs et al. (1998b), comparing the performance of Kenics with SMX static mixer (Rauline et al. (2000)), and the effect of flow rate on the performance of static mixers (Szalai et al. (2003)) are some of the examples of this group of studies. These works will be described in more detail in Section 2.2.

2.1.3 Measurement techniques

The study of flow patterns is a common way to understand the fluid behaviour and more importantly to determine the mixing performance in a system. Different experimental techniques (including both optical and non-optical) have been used to get information about different characteristics such as fluid behaviour, velocity distribution, and mixing performance in both dynamic and static mixer under laminar regime. The use of optical techniques however is limited to the transparent fluids and non-opaque systems. In this section, some of the most common optical and non-optical techniques in understanding the flow patterns and mixing performance will be reviewed.

2.1.3.1 Planar Laser Induced Fluorescence (PLIF)

Planar Laser Induced Fluorescence (PLIF) is an optical technique which tracks the spatial distribution of a passive scalar added to the flow field as a function of time. This technique involves a fluorescent tracer injected into a fluid with a laser sheet passing through the mixer. The tracer interacts with the laser sheet and absorbs the fluorescing light, which is captured by a camera angled to the laser sheet. It is possible to observe the concentration maps before the dye is fully mixed, which can be used to show the flow patterns and dead zones in the system. This technique has been used widely in stirred tanks under laminar regime to study the flow, visualizing the mixing patterns, studying the stretching of the fluid elements, and also characterising mixing by means of the gradient of concentration and segregation (Alvarez et al. (2002a), Szalai et al. (2004), Zalc et al. (2002a), Ottino (2000), Arratia et al. (2006), Alvarez et al. (2002b), Zalc et al. (2001), Arratia et al. (2004)). PLIF has also been demonstrated as a valuable method to quantify mixing times in agitated vessels both in the laminar and turbulent regime, by determination of the time required for the concentration of the dye scale to become uniform within a given confidence interval (Chung et al. (2007), Simmons et al. (2007), Hall et al. (2004))

Static mixers have been more recently characterised using PLIF to determine the concentration field and its variance to quantify mixing. Pust et al. (2006) presented the concentration field in the cross-section area at the outlet of the SMX static mixer for laminar flow, and used CoV to measure the mixture homogeneity. Jaffer et al. (2009) quantified mixing in Kenics static mixer with 90° twist per element by measuring the striation thickness and variance of striation using this experimental technique. They identified the areas with vortices from the flow visualisation maps, and showed operating the mixer at lower Reynolds number produces striations equal

in thickness and distribution to those produces in higher Reynolds number. The work by Lehwald et al. (2010) studied the mixing behaviour of SMX static mixer by using the velocity and concentration fields and measured the micro and macro mixing in a Newtonian fluid with Reynolds of 562. Alberini et al. (2012) used PLIF to determine the mixing performance in a standard Kenics static mixer with 180° twist per element. They studied the effect of number of mixing elements, fluid rheology and apparent viscosity ratio of the fluids on the mixing performance of this mixer, as well as determining the striation thicknesses. They proposed a method, which considers both intensity and scale of segregation to characterise the mixing performance based on the PLIF experimental data.

All the above-mentioned works showed the ability of PLIF to study the flow pattern and concentration maps and quantifying the mixing performance in both dynamic and static mixers. However, the use of this technique is limited to the transparent fluid.

2.1.3.2 Laser Doppler Velocimetry (LDV) or Laser Doppler Anemometry (LDA)

LDV/LDA is used to measure the velocity field and flow patterns at a single point in a flow field. This technique used two laser beams pointed on a location in the mixer, creating a small control volume. Small reflective neutral buoyancy particles are injected into the fluid, and their velocity causes a frequency shift according to the Doppler effect. This shift is detected and allows calculation of the velocity component within the control volume in plane of the crossed laser beams, normal to their source. The laser light is detected and used to calculate the velocity at each location, and determined the overall flow field. LDV has been used widely in stirred vessels to determine the flow field and the velocity components for a large number of applications (Van der Molen et al. (1978), Wu et al. (1989), Rutherford et al. (1996),

Jaworski et al. (1996), Ng et al. (1998), Mishra et al. (1998), Li et al. (2004), Jaworski et al. (2001)).

There are a limited number of studies on static mixer, which used this technique to investigate the local instantaneous velocity components of velocity. Adamiak I. (2001) performed LDV on a non-Newtonian fluid in Kenics static mixer, and investigated the velocity field for the Reynolds number of 160 to 640. They showed the velocity fields corresponding to different Reynolds numbers, and observed strong increase of fluctuation of the axial velocity for Reynolds of 640. Van Wageningen et al. (2004) investigated the flow in Kenics static mixer using both numerical and experimental techniques. LDV was used to validate the flow field and dynamic behaviour in Kenics static mixer, as well as obtaining the tangential and axial velocity components. LDV provided information about the transition of the flow from steady state to the transient flow. A good agreement was found between the results obtained from Fluent and LDV. However, the use of this technique same as the other optical techniques is limited to the transparent fluids.

2.1.3.3 Particle Image Velocimetry (PIV)

PIV uses a laser sheet projected into the mixer and a fast CCD camera at 90° to the laser sheet to obtain flow fields within the plane of the laser sheet. The velocity components measured are generally only those in the plane of the sheet i.e. 2-D, but novel methods have been developed enabling 3-D measurements (Coupland et al. (1992), Lawson et al. (1997), Gharib et al. (1995)).

In this technique, tracer particles which emit fluorescent light are injected into the system, then a laser light sheet illuminates a plane in the flow, and the position of the

particles in that plane are recorded using digital cameras. After a known fraction of time, another laser pulse illuminates the same plane, and creates the second image of particles. Every image is subdivided into a grid cell, and by analysing them by image software the particle displacement for the entire flow region can be determined. Knowing the particle displacements and the fraction of times, the velocity maps can be obtained. The principle of this technique in more details can be found in many publications (Adrian (1991), Willert et al. (1991)). PIV is one of the most common techniques used in stirred vessels (La Fontaine et al. (1996) ,Sheng et al. (1998), Lamberto et al. (1999), Zalc et al. (2001), Alvarez et al. (2002b), Aubin et al. (2004), Pianko-Oprych et al. (2009a)).

The work by Lamberto et al. (1999) studied the effect of changing the impeller speed and Reynolds number on the flow field obtained by PIV. In this work, a tank was equipped with a single 6-blade radial flow impeller and was shown by increasing the Reynolds number within the range of 8 to 70, the position of the segregated regions moves outwards in the radial direction. Szalai et al. (2004) used this technique to measure the flow patterns and mixing performance of a Rushton turbine. The number of the works on static mixer using this technique is limited. The work by Jaffer (1998) is one of the few works on static mixers which compared the velocity fields obtained by PIV with the ones from LDV. They showed the results from PIV are in agreement with the ones obtained from LDV. The development of the velocity profile along each element was found in a close agreement with the previous numerical works by Hobbs et al. (1997a) and Hobbs et al. (1998a). They showed the main concern of using PIV in static mixers is the fact that the flow is highly three dimensional, and therefore there is an error associated with the two dimensional PIV technique.

2.1.3.4 Computer automated radioactive particle tracking

Computer automated radioactive particle tracking (CARPT) is a Lagrangian technique which uses a radioactive particle to study the flow behaviour. The positron emitted from the radioactive particle labelled with Scandium (^{46}Sc) annihilates with a local electron, producing back-to-back gamma rays. The gamma rays are detected by the 16 scintillation detectors located around the geometry. The system is calibrated by positioning the tracer at various known locations, and the final location of the tracer during the experiment can be determined by this calibration (Larachi et al. (1995), Doucet et al. (2008), Guida et al. (2011)).

The main development of this technique was done by Rammohan et al. (2001) which used CARPT for the first time to study the flow behaviour in stirred tank. The full three-dimensional Lagrangian measurements obtained by this technique provides better flow visualisation, and made it possible to observe the dead zones at the bottom of the tank. However, due to the big size of the tracer (2.3 *mm*) and the slow rate of data sampling (50 Hz), it is not possible to capture the some of the true behaviours of the fluid such as velocity, especially close to the solid boundaries. The use of this technique is not limited to the transparent fluids like PLIF, PIV, and LDV.

2.1.3.5 Positron Emission Particle Tracking

Over the last 30 years, positron emission tomography (PET) has been applied to industrial applications as well as the medical ones (Hawkesworth et al. (1986), Bemrose et al. (1988), Parker et al. (1995), Barigou (2004)). PET works based on detecting back-to-back gamma rays produced by the emission and annihilation of a positron from an emitting source. The positron camera uses two positron sensitive

detectors located around the system under study. For two-dimensional imaging, the stationary detectors measure a single two-dimensional projection of the distribution of positron emitting tracer. By rotating the detectors around the system it is possible to obtain three-dimensional images. The special resolution of PET is around 5 *mm* in the latest generation of clinical PET (Parker et al., 2008). PET suffers from the long time required to generate enough data statistics to produce a good quality 3D image. PET images are mainly time averaged (up to hours) from a steady state system and therefore there are some complications on applying PET for the flowing systems, considering the slow rate of data recording. For industrial imaging a modified version of PET, which is called Positron Emission Particle Tracking (PEPT) has been developed by Prof. David Parker and Colleagues in the School of Physics and Astronomy at the University of Birmingham (Parker et al. (1993).

PEPT is Lagrangian technique, which locates the position of a labelled radioactive particle via triangulation of the back-to-back gamma rays produced. It can be applied to any system provided the boundaries do not attenuate the gamma rays, which are typically penetrate through a few centimetre of steel without issue. PEPT has been used for both dry (Parker et al. (1997), Cox et al. (2003), Wong (2006), Marigo et al. (2010), Marigo et al. (2013)) and liquid (Guida et al. (2009), Guida et al. (2010), Guida et al. (2011), Chiti et al. (2011), Gabriele (2011)) systems.

The tracer particles can either be produced by direct irradiation or adsorption of irradiated water into their surface (Fan et al. (2006), Leadbeater et al. (2012)). For both cases, a beam of ^{3}He is used to convert oxygen to the radionuclide of ^{18}F. In ^{18}F isotope a proton is converted into a neutron, a positron, and a neutrino. The positron emitted from the particle annihilates with a local electron in the surrounding environment, producing a pair of back-to-back gamma rays:

P (Proton) → Neutron (n) + Positron (β^+) + Neutrino (υ)

Positron (β^+) + e^- → 2 gamma rays

The gamma rays are then detected by a positron camera located in the department of Physics and Astronomy of University of Birmingham. The camera consists of two opposed detector heads, which can be rotated about the horizontal axis. Each detector has an active area of 500 × 400 mm^2. The position of the tracer is determined by applying a triangulation process (Parker et al. (1993)) from a small number of detected gamma-ray pairs. In practice, many of the detected events are corrupted due to the photon scattering and incorrect pairing (Figure 2.7). As shown in Figure 2.7, the back-to-back gamma rays (which are also called as line of response or LORs) have to meet at a single point in order to have a valid location (true pairing). Since the camera also detects the corrupted events, it is necessary to have sufficient number of LORs so that the algorithm could distinguish between the valid and non-valid ones. The algorithm then eliminates the corrupted LORs, and calculates the final location of the tracer as a point, which has a minimum mean perpendicular distance from the remaining LORs.

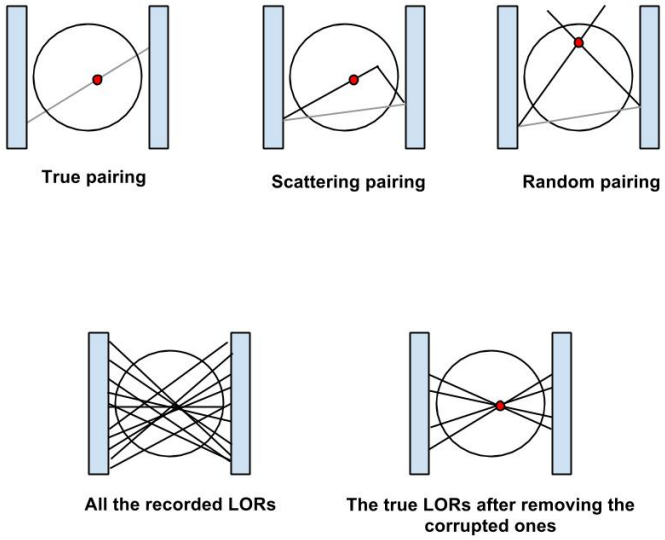

Figure 2.7. LORs classifications according to the algorithm.

After finding the location of the tracer, the algorithm converts the data to an ASCII file, which contains the location of the tracer in *x, y,* and *z* coordinates at different time steps. Different analyses can then be performed to obtain information about the flow behaviour within the system.

For PEPT to be used to obtain fluid velocities, the assumption of ergodicity must be made, so that the tracer motion is representative of all the liquid or solid phase within a system, (Wittmer et al. (1998)). The assumption of ergodicity means the information contained in a single particle trajectory is same as the information provided by a group of particle trajectories that are obtained simultaneously. It can be shown mathematically that if the probability of the tracer visiting everywhere is high, ergodicity can be assumed. In this case, it is necessary to record the tracer trajectories over sufficiently long time, to achieve satisfactory data resolution in every region (Wittmer et al. (1998)). It is also important to show the tracer particle suspended in a fluid is actually following the fluid streamline closely. In this case, Stokes number can

be used as dimensionless parameter to govern the behaviour of the tracer particle in the fluid. Stokes number can be calculated as the ratio of the particle response time to the fluid response time. Large stokes number (St >> 1) indicates the particle responds slowly to changes in fluid velocity, while small Stokes number (St << 1) shows short particle response time, and therefore good tracking of the fluid streamlines.

Stewart et al. (2001) used PEPT to study the motion of glass beads in a vertical axis mixer with slowly rotating flat blades. The motion of the material through the entire bed was investigated using this experimental technique and the results were compared to the ones simulated with DEM modelling. The instantaneous velocities along the tracer path were calculated using the "six-point" method (described in Chapter 3, § 3.3.3). The results on the velocity fields were in agreement with the ones calculated with DEM modelling method.

A new cyclotron, which was more flexible and powerful than the previous one, was purchased in 2002 and made it possible to use of smaller tracers (100 - 200 μm). The cameras were also upgraded to increase the resolution. Consequently, the resolution and the accuracy of the data were improved. Bakalis et al. (2004) used PEPT to study the flow of a sucrose and CMC solution in an aluminium pipe as a continues system. The flow patterns were presented using the experimental data, and the Lagrangian particle velocities of the tracer were calculated by finding the displacement of the tracer between each two consecutive points over the time. This technique was a rough estimation of velocities in comparison with the methods used in the future works (Chiti (2008), Guida et al. (2009), Gabriele (2011)), which will be described later. However, the experimental and theoretical velocities agreed within the 10% range (Figure 2.8).

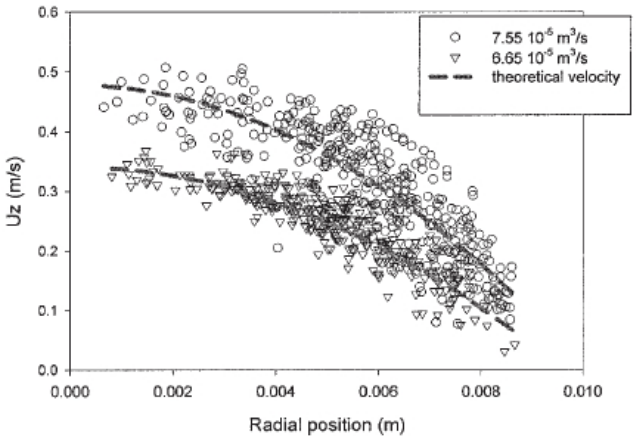

Figure 2.8. Comparison between the theoretical and experimental velocities of sucrose solution in an aluminium pipe using two different averaged velocities (Bakalis et al. (2004)).

The use of PEPT is not just limited to the liquid systems. Solid-liquid suspensions in non-Newtonian liquids have been investigated using PEPT in a number of works (Fairhurst et al. (2001), Barigou et al. (2003)), as well as the agitation of non-Newtonian liquids with or without particles in stirred vessels (Fangary et al. (2000), Fangary et al. (2002)). The work by Barigou (2004) studied solid-liquid systems in stirred vessel with axial hydrofoil impeller, using spherical Acetal particles in CMC solution. The tracer was embedded into one of the particles by drilling a hole in it. By considering the assumption of ergodicity in the system, the velocity of the tracer was assumed to be same as the other particles. The calculated Stokes number of the tracer in a single-phase system showed the tracer is naturally buoyant. The velocity maps were calculated using the same methodology used in the work by Bakalis et al. (2004). The fluid circulation was calculated using the ratio of the average velocity of the particles and the impeller speed. It was observed that by increasing the impeller speed, the particle circulation increases, as expected. It was also shown an increased in solid concentration causes the reduction in the frequency of particle circulation. The use of

a numerical technique was suggested to investigate whether the results from PEPT experiment could be used to validate the numerical ones.

The work by Chiti (2008) was a turning point in using a new methodology of PEPT analysis in different systems. He introduced a new methodology to calculate the Lagrangian and Eulerian velocities with more accuracy in comparison with the ones used in the previous works. In his work, PEPT was used to study the flow behaviour in a standard baffled vessel stirred by Rushton turbine in a turbulent system. The system was also studied using another experimental technique (PIV) and a numerical one (CFD). It was shown the choice of basic parameters, which are used to process the raw PEPT data, could affect the accuracy of the flow and velocity fields, and therefore the optimum value of these parameters should be obtained for each different experiment separately. In this work, it was proposed for the first time to calculate the Lagrangian velocities by finding the equation of the straight line of the "best-fit". The least square method was used to find the equation of the "best-fit" line which passes through each five consecutive data point. The slope of the best-fit line was representing the velocity of that group of points. The velocities were then calculated in Eulerian reference system, by defining a three dimensional grid, and finding the value of average velocity in each cell. It was shown in this work that PEPT might underestimate the velocity in areas with a rapid change of direction, i.e. the areas close to the impeller (up to 50% lower than the measured value using PIV). This is due to the fact that by considering the same rate of data recording in all the regions, by passing through a high-speed area the number of the recorded points decreases consequently. The slope of the best-fit line passing through five points which are far from each other could deviates more from the actual velocity in that region than the slope of the line calculated over five points that are located close to each other. In this

case, he suggested using interpolation of the data for these regions, and showed the interpolation could partially solve this problem.

PEPT has been also used to study the flow fields and velocity profiles in multiphase systems. Guida et al. (2009) studied a mechanically agitated solid-liquid suspension, of coarse glass particles in water with pitch blade turbine impellers (PBTU and PBTD). He showed the location of the tracer could affect the probability of the detection (Figure 2.9). In Figure 2.9, the two back-to-back γ - rays must travel within the grey area in order to calculate the final location of the tracer. The probability that the LORs successfully hit both detectors is higher for the tracer located near the centre of the field of view. Hence, by getting closer to the centre of the field of view, the quality of the recorded data improves.

Figure 2.9. Effect of the location of the tracer on the probability of true LOR detection by the cameras.

Pianko-Oprych et al. (2009b) studied the flow generated by pitch blade turbine in single and multiphase systems using both PIV and PEPT techniques. An excellent agreement was found between the velocity profiles calculated with each technique, except the area around the impeller. This might be due to the rapid change of direction close to this area, which was discussed before by Chiti (2008). Guida et al. (2010) used PEPT to determine two-phase flow field and spatial phase distribution in a stirred vessel containing coarse glass particles suspended in water. The local solid

concentration was studied using the PEPT data. The vessel was divided into a number of surfaces (*s*) at different heights (*h*), and the number of the particles going in and out of each surface was found (Figure 2.10).

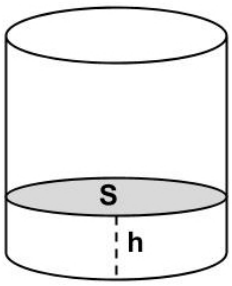

Figure 2.10. Calculating the solid concentration in the vessel (Guida et al. (2009)).

The solid mass balance throughout the vessel and the mass continuity of the two phases were accurately verified so that:

$$\frac{1}{N_H}\sum_{j-1}^{N_H} C_h^{(j)} = \langle C_s \rangle \qquad \textbf{(Equation 2.13)}$$

and

$$\sum_s u * \Delta s \cong 0 \qquad \textbf{(Equation 2.14)}$$

where *s* is a close surface (shown in Figure 2.10), C_s is the volume concentration of solid, C_h is the volume concentration at level *h*, N_h is the number of the horizontal levels, and *u* is the 3D velocity vector ($m.s^{-1}$). After defining a grid and dividing the vessel into a number of cells, a global uniformity index, ξ, was used to study the degree of uniformity of the distribution using the variation of the local solid concentration:

$$\xi = \frac{1}{\sigma^2 + 1} = \frac{1}{\frac{1}{N_C}\sum_{i=1}^{N_C}\left(\frac{C_i - \langle C_s \rangle}{\langle C_s \rangle}\right)^2 + 1} = \frac{\langle C_s \rangle^2}{\langle C_s^2 \rangle} \qquad \textbf{(Equation 2.15)}$$

where σ is the standard deviation of the normalised concentration, N_C is the number of the grid cell, and C_i is the concentration in cell i (equivalent to the number of particles in cell i). By calculating the uniformity index throughout the vessel, it was shown a down-pumping PBT achieves significantly better homogeneity than up-pumping PBT.

Marigo et al. (2012) compared and validated the PEPT experimental data and DEM simulations for turbulent mixing in a rotating drum containing glass bead solid particles. In this work, the dispersion in axial and radial direction was investigated by calculating the coefficient of axial and radial direction D_x and D_r for the data from both DEM simulation and PEPT experiment:

$$D_x = \frac{1}{N-1}\sum_{k=1}^{N-1}\frac{\left(x^{k+1}-x^{k}\right)^2}{\left(t^{k+1}-t^{k}\right)}$$

$$D_r = \frac{1}{N-1}\sum_{k=1}^{N-1}\frac{\left(r^{k+1}-r^{k}\right)^2}{\left(t^{k+1}-t^{k}\right)} \qquad \textbf{(Equation 2.16)}$$

where x^{k+1} and x^{k} are the axial positions of the particle at time t^{k+1} and t^{k} ,and N is the total shaft rotation. Similar general trend in particle displacement between PEPT and DEM simulations were observed, however the difference in absolute value was seen. The values obtained from DEM were about 50% higher than the ones from PEPT. The difference was related to the choice of DEM input parameters or some statistical errors. It was suggested to investigate the effect of the choice of the DEM input parameters on the results.

Among the characterisation techniques that have been described in this chapter, PEPT has been applied widely in literature to both transparent and non-transparent fluids, as well as single and multiphase systems. The validation of PEPT results using other experimental techniques and numerical works in some of the above mentioned works shows PEPT can be used as a powerful Lagrangian technique.

2.2 Static mixers

Static mixers or motionless mixers are in-line mixing devices, which consist of a number of mixing elements placed inside an empty pipe. Static mixers have been available commercially for several decades, since the 1970's, however, the patent is older. Nobel (1962) described a mixing element which divides the tube into two annuli. In this design, the mixing occurred due to the spilt and relative rotation of the fluid elements between the two annuli. A low pressure mixing device was described by Armeniades (1966), which consists of a series of helical elements with the length to diameter ratio of 1.5. Each element had a 180° twist and was aligned orthogonally to the following element. This was the first description of the Kenics static mixer, which was later developed for commercial use. Tauscher et al. (1973) from Sulzer Bros developed low pressure mixing elements that split the fluid into separated streams, which meet each other as they flow transversely through the element (Godfrey (1997)). In this design, each two consecutive elements are also normal to each other. This mixer was called SMX, and its geometry has been developed during the last thirty years. Different companies have introduced several types of static mixers since then. A summary of these mixers is available in Table 2.1.

The basic design of static mixer is a series of elements, which are motionless and installed within an empty pipe. The design of the elements makes it possible for the fluid elements to redistribute in radial or tangential directions. Due to the wide range of static mixer's types, and by considering the use of Kenics static mixer and SMX-plus in this work, this section will be focused on the available information about these two types of mixers.

Table 2.1. Summary of different types of static mixers (adopted from Etchells et al. (2004)).

Company and mixer name	Description
Chemineer (Kenics)	
• **KMS**	Twisted ribbon with left and right hand side twist, with the aspect ratio of 1.5. Adjacent elements are rotated 90° relative to each other.
• **KMX**	Series of inclined retreated curve rods forming an X lattice.
• **HEV**	A series of four tabs spread around the pipe.
Koch-Glistch	
• **SMV**	Several stacked sheets of corrugated metal with the angle of 30 or 45° to the pipe axis, and the aspect ratio of 0.5 or 1. Adjacent elements are rotated 90° relative to each other.
• **SMX**	Guide vanes are intersecting bars at 45° to the pipe axis, with aspect ratio of 1, and 90° rotation between each two consecutive elements.
• **SMXL**	Similar to SMX, but with bars located at 30° to the pipe axis, and with fewer bars per element in comparison with SMX.
• **SMR**	Guide vanes are hollow tubes.
• **SMF**	Three guide vanes projected from the tube wall with no contact between them.
Komax system	
• **Komax mixer**	Crossed elliptical plates with a flat at the centre line.
Sulzer Chemtech	
• **SMV, SMX, SMXL, SMF, SMR**	As described above. Joint development by Koch and Sulzer.
• **SMX-plus**	Similar to SMX, with reduced number of bars from eight to six to improve the performance.

2.2.1 Kenics Static mixer (KM)

A typical Kenics static mixer consists of a number of helical elements with 180° twist. The leading edge of each element is normal to the following one, which has an opposite twist direction (Figure 2.11).

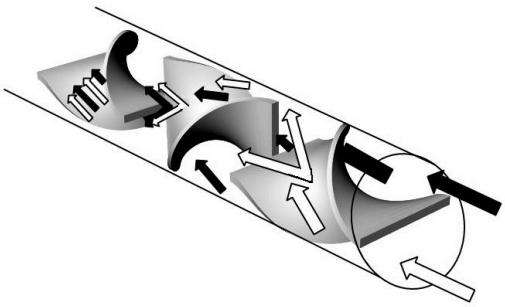

Figure 2.11. Mechanism of flow division in Kenics static mixer.

In the Kenics static mixer the main mechanisms of mixing the streams with each other are the flow division and radial mixing. The fluid rotates relative to the blade, and moves from the wall towards the blade and vice versa. Hence, by reaching to the next element the fluid would have moved radially. Consequently, the radial mixing is happening as a result of the shifting the velocity components of the fluid by the helical elements. Flow division is accomplished by having the elements edges about 90° to one another. By passing through each transition region between two consecutive elements, the fluid splits into two parts, and follows the path created by the twisted element until it splits into two parts on the next transition region again. The striations are created as a result of stretching the fluid layers due to the velocity gradient in the cross-section. The theoretical number of striations after *n* number of elements can be calculated by the following equation (Devellian, 1972):

$$N_t = 2^n \qquad \textbf{(Equation 2.17)}$$

Avalosse et al. (1997) showed the creation of striations experimentally in Kenics static mixers by using coloured clay as a power law fluid with N_{Re} = 0.01, and a disassemblable Kenics mixer. The dismountable Kenics mixer made it possible to remove and separate each section of the mixer containing both the blade and the pipe around it. They used a thin blade normal to the mixer's blade at the entrance of the mixer, and injected clay with two different colours. After passing the clay through six elements, the flow was stopped, and the mixer was put inside a freezer. Each section was dismounted and slices of clay were cut perpendicular to the axis, cleaned and photographed. The arrangement of striations was compared to the results from the numerical work (Figure 2.12).

The stretching of the fluid elements by progressing along a single element can be observed from Figure 2.12(a). The 90° rotation of the consecutive elements can also be observed on the transition from Figure 2.12(a) to (b) by looking at the position of the blade. They showed the mixing progress from the entrance of the mixer up to the end of the fourth element, where the striations became too thin to be observed.

The number of the striations was changing according to Equation 1.17, and the numerical results found to be in a good agreement with the experimental results.

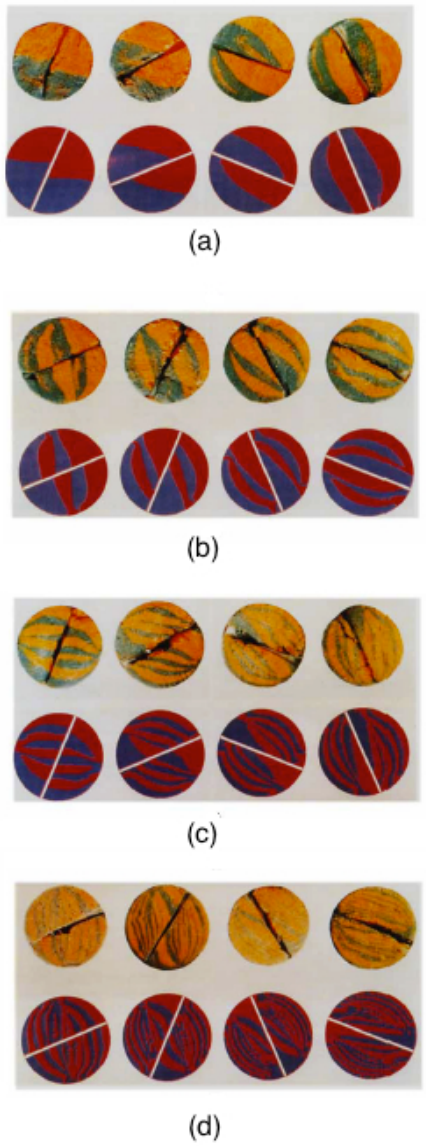

Figure 2.12. Comparison between the numerical and experimental results on arrangement of the striations along :(a) first element; (b) second element; (c) third element; (d) fourth element (Avalosse et al. (1997)).

The mechanism of flow division and re-orientation of the fluid elements in the Kenics static mixer can be illustrated by the Baker's transformation map, which shows the stretching of the fluid elements to double length and folding them in each unit (Figure 2.13). During the fluid passage through each single element of the Kenics static mixer, the fluid elements stretches following the same mechanism that is shown in Figure

2.13(b) and by passing through the area between each two consecutive element (transition region), they re-oriented and folded on top of each other (Figure 2.13(c)).

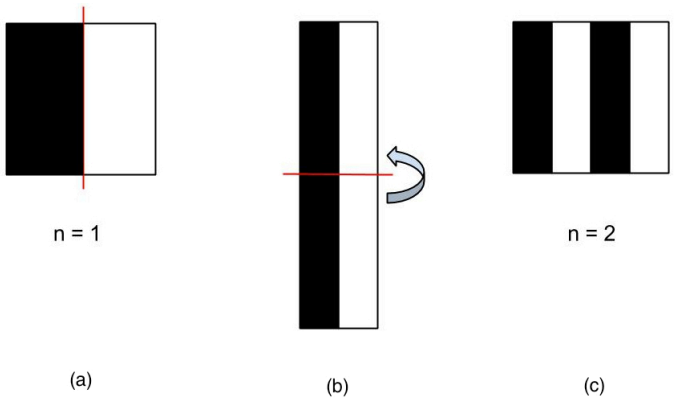

Figure 2.13. Baker's map illustration, *n* is the number of elements (adopted from Tanguy et al. (2005)).

Distributive and dispersive mixing, are the two main mixing mechanisms happening in Kenics mixer. It was discussed before that the distributive and dispersive mixing mechanisms are caused by the stretching of the fluid elements and the reduction in their sizes. As it was demonstrated on Figure 2.12 and Figure 2.13, the distributive mixing is happening while the fluid is passing through each element and as a result of stretching of the fluid elements. On the other hand, the dispersive mixing is happening between each two consecutive elements, where the arrangement of the blades makes the fluid elements to be cut and therefore reduces their sizes.

The previous works on Kenics mixer can be classified into a number of groups. The first group of works focused on determination of some correlations for online parameters required for the mixers operation. These parameters, such as pressure drop and residence time distribution have been correlated to the number of elements, the

aspect ratio of an element (the ratio of the length of the element to the diameter), and the Reynolds number.

Most of the works on estimating the pressure drop in Kenics mixer designed some experimental and numerical measurements to develop empirical correlation on pressure drop as a function of Reynolds number (Grace (1971), Wilkinson et al. (1977), Pahl et al. (1982), Allocca (1982), Boss et al. (1982), Heywood et al. (1984) , Shah et al. (1991), Gokul Chandra et al. (1992), Joshi et al. (1995)). The majority of these works used the z-factor approach. The z-factor is a non-dimensional pressure drop, with z being as the ratio of the pressure drop through the Kenics mixer to the pressure drops of an empty pipe. Grace (1971) proposed a correlation between the Reynolds number and the pressure drop ratio as:

$$z = 4.86 + 0.68 N_{\mathrm{Re}}^{0.5} \qquad \textbf{(Equation 2.18)}$$

while Wilkinson et al. (1977) suggested:

$$z = 7.19 + 0.03125 N_{\mathrm{Re}} \qquad \textbf{(Equation 2.19)}$$

and Heywood et al. (1984) recommended $z = 6.88$.

The Reynolds number in these works was calculated as $\rho u d / \mu$, using the diameter of the mixer for the value of d. All of the Reynolds numbers were below 10, which shows the flow was in laminar regime. Each of the mentioned works suggested a different correlation. The inconsistency between various published results might be due to the fact that some of the geometrical aspects such as the ratio of the element length to the diameter of the pipe (the aspect ratio) have been considered differently among these works. A summary of different works and their suggested correlations is available in the work by Rauline et al. (1998).

There are few works in literature, which studied residence time distribution in Kenics static mixer using both numerical and experimental techniques (Tung (1976), Nigam et al. (1980), Nauman (1982), Kemblowski et al. (1988), Nauman (1991) Olmiccia et al. (2011)). The common issue between most of the numerical works were creating a structure, which has a close shape to the actual mixing elements of Kenics mixer. The first theoretical model of RTD in Kenics mixer was presented by Tung (1976).The model was derived based on the basis of the velocity profile of a Newtonian fluid in Kenics mixer, however, the effect of number of elements on the residence time distribution was not considered (cited in Pustelnik (1986)).

Nauman (1982) replaced the elements by a complete plane, and proposed an RTD model for this system, and showed the number of the mixing elements has a significant effect on residence time distribution. Nevertheless, the relation between the number of the actual Kenics mixer elements and the considered complete plane in this work was not explained (cited in Kemblowski et al. (1988)). Pustelnik (1986) did an experimental work on Kenics mixer to study residence time distribution, using CMC and glycerol solutions as the modelling Newtonian and non-Newtonian fluids. The RTD was obtained using a pulse input of Sodium Chloride solution as the tracer fluid. The log normal distribution of residence time was plotted for different number of elements and for the Reynolds numbers between the range of 0.72 to 442 (Figure 2.14). It was shown that by increasing the number of the mixing elements, the shape of the residence time distribution curve becomes closer to the one for the plug flow.

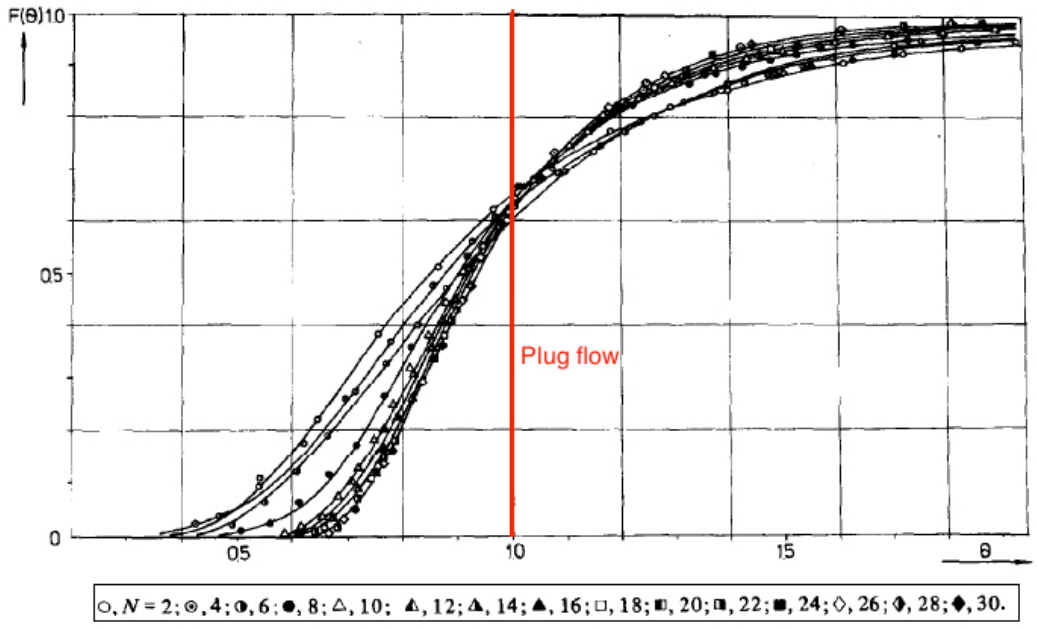

Figure 2.14. Experimental RTD curves for constant Reynolds of 8.14 (Pustelnik (1986))

Hobbs et al. (1997a) used Lagrangian methods to investigate numerically the RTD in Kenics static mixer, using a Newtonian fluid with Reynolds of 0.15. The residence time distribution was calculated by tracking around 20000 tracer particles that were initially placed at the entrance of the mixer to cover the whole cross-section. The particle trajectories were tracked along the mixer by using a tracking software, and the residence time of particles were recorded each time that they were passing through a periodic plane (i.e. after the second element, forth element, sixth element, and etc.). The fraction of the total flow volume that had a residence time between τ and $\tau+d\tau$ was calculated as the total number of particles weighted by the inlet flow that it represented. The final weighting for each particle was then computed as the cross-sectional area represented by the particle multiplied by the inlet axial velocity of the particle, $v_{x,in}$. The cumulative residence time distribution, $F(\tau)$, for a given value of τ was estimated as:

$$F(\tau) = \frac{\sum_{t=0}^{\tau} v_{x,in} dA}{Q_{in}} \qquad \textbf{(Equation 2.20)}$$

where Q_{in} is the total inlet volumetric flow rate. By normalising τ by the residence time of a particle travelling at the average volumetric flow rate, the normalised residence time, θ, was obtained. Figure 2.15 shows the comparison between their simulated results and the previous experimental and numerical works in the literature (Tung (1976), Pustelnik (1986)).

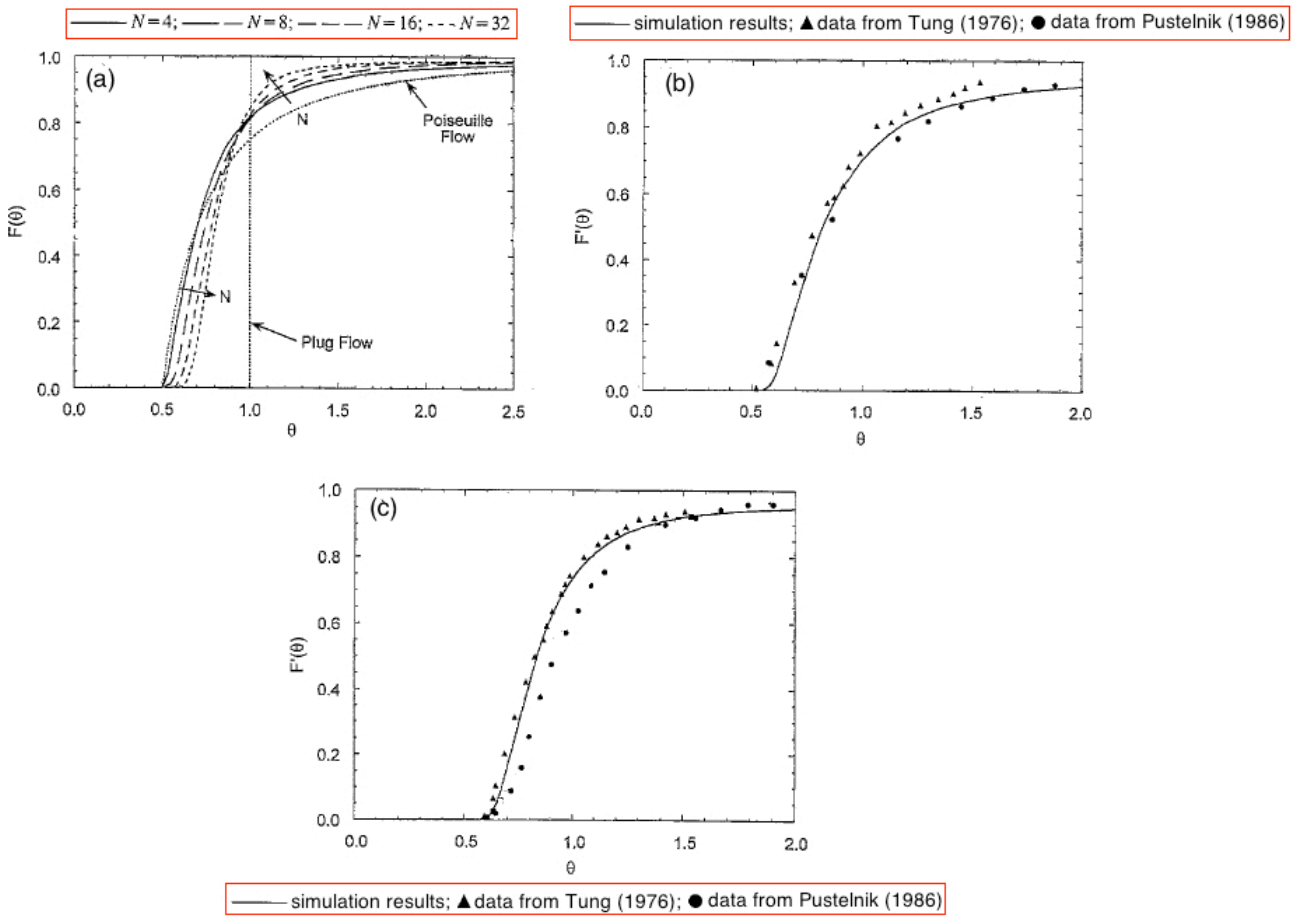

Figure 2.15. (a) Residence time distribution vs. number of mixing elements from simulations done by Hobbs et al. (1997a). The arrows show the direction that the curves shift by increasing the number of elements; (b) simulated area-weighted RTD by Hobbs et al. (1997a) vs. experimental data by Tung (1976), and Pustelnik (1986) after eight mixing elements and (c) sixteen mixing elements (adopted from Hobbs et al. (1997a)).

The examination of the previous mentioned numerical and experimental works done by Hobbs et al. (1997a) showed the reported results do not represent the true RTD, but an alternative one which is weighted based on the cross-sectional area of the inlet fluid rather than the volumetric flow rate. Therefore, they used an area weighted *F(θ)* from their particle tracking simulations to be able to compare their results with the previous work on literature (Figure 2.15(b),(c)).

As it is shown in Figure 2.15(a), the simulation results showed by increasing the number of mixing elements, the RTD curve is shifting towards the one for plug flow profile. This means ideally after going through a high number of mixing element in Kenics mixer, the particles would become so distributed and well-mixed that they could represent a plug flow. They also showed the data from the literature and the simulated RTD from their work exhibit sigmoid shaped curves. A good agreement was found between the previous mentioned works and their simulated RTD results.

One of the main common issues between all the experimental works on RTD of Kenics mixer is that these techniques were unable to show the RTD for each single element, and therefore determining the changes of RTD by going through each single element along the whole length of Kenics mixer.

The next group of works that will be discussed here is the ones that simulated the velocity field in Kenics static mixer. Most of these works used computational fluid mixing (CFM), which uses a high number of particle trajectories (10^4 -10^6) in a simulated flow to model the lamellar structure created by the flow field. By studying the simulated flow structure, different flow characteristics such as velocity distribution and mixing performance could be investigated (Tung (1976) , Byrde et al. (1999), Hobbs et al. (1997a), Hobbs et al. (1997b), Hobbs et al. (1998b), Hobbs et al.

(1998c), Bakker et al. (1998), Rauline et al. (1998), Byrde et al. (1999), Rauline et al. (2000), Galaktionov et al. (2003), Szalai et al. (2003), Van Wageningen et al. (2004), Kumar et al. (2008), Jaffer et al. (2009), Saatdjian et al. (2012)).

Hobbs et al. (1997a) investigated the flow field and mixing performance of a Newtonian fluid with N_{Re} = 0.15 using computational fluid dynamics (CFD) software. The flow was simulated and characterised by tracking the motion of a large number of fluid tracer particles. The velocity fields, striation evolution, variation coefficient, and stretching histories of the fluid elements were calculated as a function of mixing elements in Kenics mixer. The average stretching of the fluid elements was calculated by Equation 2.11 and it was shown it increases exponentially with the number of the mixing elements. Equation 2.9 was used to calculate the variation coefficient in order to characterise the mixing performance. The methodology of calculating the stretching rates and variation coefficient from particle trajectories in this work introduced a new way to characterise mixing performance in Kenics mixer, and was used in a number of works later (Hobbs et al. (1997b), Hobbs et al. (1998c),Hobbs et al. (1998a), Hobbs et al. (1998b), Rauline et al. (1998), Szalai et al. (2003)).

Similar methodology of mixing characterisation was used in a numerical work by Hobbs et al. (1997b), which studied the effect of tracer injection location on mixing performance in Kenics mixer, using a Newtonian fluid with Reynolds number of 0.15. Nine injection locations were chosen near the inlet of the mixer, with each location positioned axially 0.1 *cm* upstream from the leading edge of the first mixing element. 10000 tracers were placed in the flow at the injection points. By finding the spread of the tracer the variation coefficient was calculated. It was shown in this work that after sufficient mixing elements the tracer injection location has little effect on the final

quality of mixture. The effect of injection location is more significant for the first few elements.

The effect of Reynolds number on mixing performance and flow behaviour in Kenics mixer was investigated in the work by Hobbs et al. (1998b). Stretching histories and variation coefficient were also used in this work to characterise the mixing performance at different Reynolds numbers. The velocity fields and Poincare sections were presented for the Reynolds number between the ranges of 0.15 to 1000. For each Reynolds number, the mixing performance was characterised by calculating the rate of reduction in variation coefficient (using Equation 2.9), and the stretching histories (Equation 2.11). The Poincare maps were obtained by tracking fifteen tracers through the flow for 500 mixing elements, and recorded their cross-sectional position after passing through the 2^{nd} element, 4^{th} element, 6^{th} element, and etc. All the cross-sections were then super imposed to form a two-dimensional Poincare section. On the Poincare map, the chaotic flow regions appear as random cloud of particles, while the regular regions (islands) contains no particles. Although no actual mixer contains 500 elements, it was assumed the exchange material between the chaotic and regular regions can only occurs via slow diffusion process. Therefore, it is possible to relate the existence of the islands in different flow conditions to see how well-mixed the system is. It was shown for $N_{Re} < 10$, the mixing performance is independent of Reynolds number; however, by increasing the Reynolds number, i.e. $N_{Re} = 100$, significant island produced (Figure 2.16), indicating the mixing performance becomes poorer. The calculations from the reduction of the variation coefficient obtained for different Reynolds numbers showed the similar results, indicating the independency of mixing performance for $N_{Re} < 10$, and the decrease in the performance by increasing the Reynolds number (Figure 2.17).

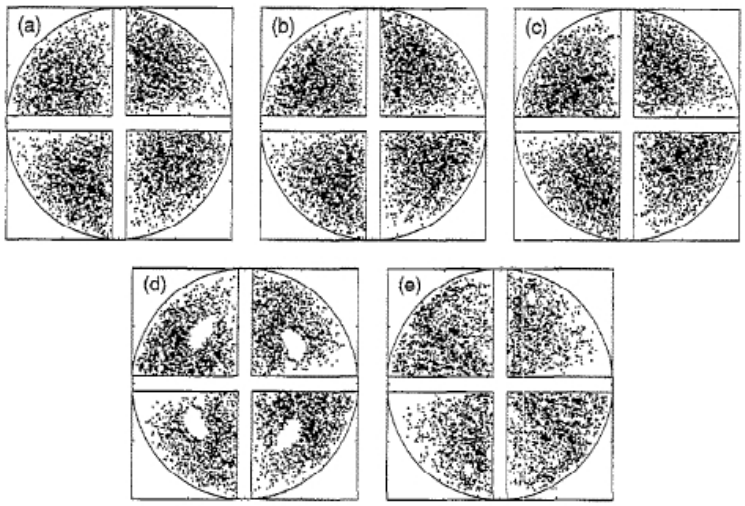

Figure 2.16. Poincare section for (a) N_{Re} = 0.15; (b) N_{Re} = 1; (c) N_{Re} = 10; (d) N_{Re} = 100; (e) N_{Re} = 1000 (Hobbs et al. (1998b)).

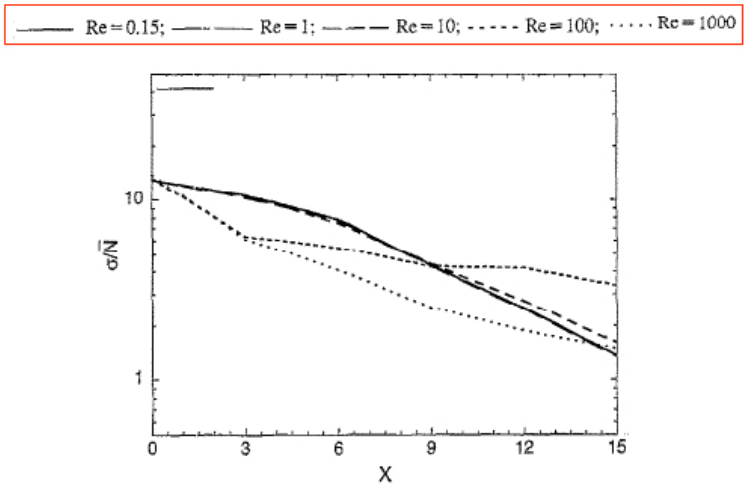

Figure 2.17. Variation coefficient normalised by average number of particles per cell ($\bar{N}$) Vs. normalised axial location for different Reynolds number (Hobbs et al. (1998b))

The work by Jaffer et al. (2009) performed some experiments to determine the effect of Reynolds number on mixing performance of Kenics mixer using PLIF. The mixing performance was characterised by measuring the number of striations and their thicknesses, variance of striation width and interfacial area for a Kenics mixer with

90° twist per element. It was shown in this work that operating the mixer at lower Reynolds numbers (N_{Re} = 43) produces striations equal in thickness and distribution to those produced at higher Reynolds number (N_{Re} = 125). This result is not completely in agreement with the work from Hobbs et al. (1998b), since in that work it was shown that the flow with a Reynolds number of 100 had poorer mixing than for a flow with a Reynolds number of 10. However, in the work by Jaffer et al. (2009) it was concluded that the mixing performance of the flow with N_{Re} = 43 is similar to the one with N_{Re} = 125. This disagreement might be due to two reasons. First, it might be nessesry to compare the flow with exactly the same Reynolds numbers, which is not possible since Jaffer et al. (2009) did not provide information about what would have happened if the Reynolds number were same as the ones used in the work by Hobbs et al. (1998b). Second, this could be due to the use of Kenics mixer with different twist angles in these works, since it was shown in some other works in literature, which will be discussed later, that the twist angle of the elements could affect the mixing performance of the mixer.

The variation coefficient and stretching histories were also used in some more recent works to compare the performance of different static mixers. Rauline et al. (2000) studied the performance of Kenics static mixer and SMX mixer based on different criteria such as pressure drop, Lyapunov exponent, and intensity of segregation for a Newtonian fluid with Reynolds number of $5*10^{-4}$. According to their work and by using the concept of stretching histories, the higher the Lyapunov exponent is, the more efficient the mixer is in principle. The results found from both intensity of segregation and stretching histories showed SMX is more efficient than Kenics mixer, by means of one mixing element of SMX is equivalent to two or three mixing element of Kenics mixer.

Another group of works on Kenics static mixer focused on studying the effect of changing some geometrical parameters in Kenics mixer on its performance in order to find the optimum design for Kenics static mixer. All of these works used numerical simulations to find the optimise twist angle per element for Kenics mixer, with no experimental work investigating this matter. One of the first few works which studied the mixing performance of different designs of Kenics mixer was the one by Hobbs et al. (1998a). The effects of three geometrical parameters on the performance of Kenics mixer were investigated in this work: the twist direction, the aspect ratio, and the twist angle per element. Mixing was quantified by calculating the stretching histories, variation coefficient, and Poincare sections map for a Newtonian fluid with Reynolds number of 0.15. It was shown mixing per element and energy efficiency are independent of the ratio of the element length to the diameter. Hence, it was suggested to use shorter mixer elements to obtained equivalent mixing in case of having smaller spaces or if a shorter residence time is required. The procedure of obtaining the Poincare map was same as the one that was described in detail before on the work by Hobbs et al. (1998b). After plotting the velocity distributions and also the Poincare maps, it was shown a mixer with same direction of twist (right-right or R-R configuration) has significant segregated regions, and therefore poor mixing performance (Figure 2.18). It was also shown if at the entrance of the mixer a tracer is injected into one of the chaotic regions shown in the Poincare map, it would stay in the chaotic region until the end. This suggested that there is no exchange of material between the segregated regions (islands) and the chaotic ones. It was suggested at the end to use the R-L configuration. A later work by Byrde et al. (1999) found the similar result about the poor mixing performance of R-R configuration.

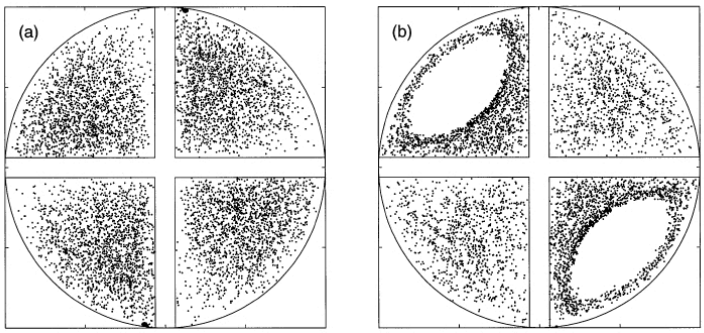

Figure 2.18. The Poincare section created by 15 tracer particles on the cross-sectional plain after each two elements for (a) R-L (right-left) configuration;(b) R-R (right-right) configuration (Hobbs et al. (1998a)).

Mixing efficiency was defined as stretching rate per pressure drop (shown as β on Figure 2.19(b)), and it was found although Kenics mixer with 150° twist per element has a better performance according to the stretching rates, the mixing efficiency of KM with 120° twist per element by considering the pressure drop is better by 44%.

On the other hand, Byrde et al. (1999) suggested the operating conditions might have a significant effect in the comparison between the mixing performance of Kenics mixer for different twist angle. They used CFD to find the optimise twist angle of Kenics mixer for a fluid with Reynolds number of 100. The mixer efficiency was defined as:

$$E_{eff.} = \left(-\Delta p * r_s\right)^{-1} \qquad \textbf{(Equation 2.21)}$$

where Δp is the pressure drop along the mixer after six mixing elements, and r_s is the striation thickness at the end of the sixth element (Figure 2.20).

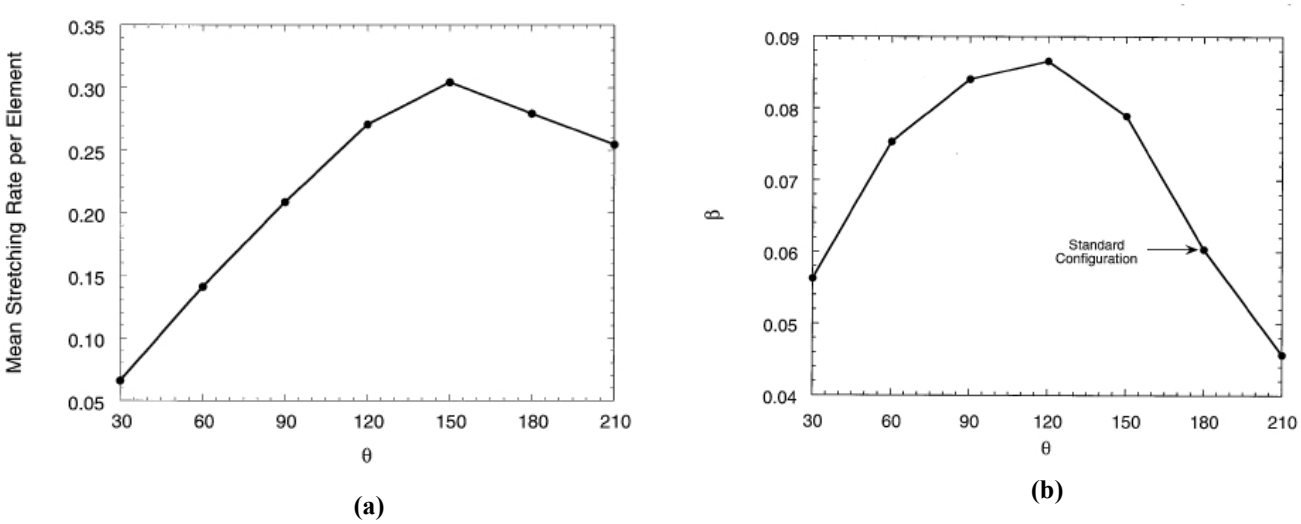

Figure 2.19. (a) Mean stretching rate per element for different twist angels; (b) Mixing efficiency (β) for different twist angles (Hobbs et al. (1998a)).

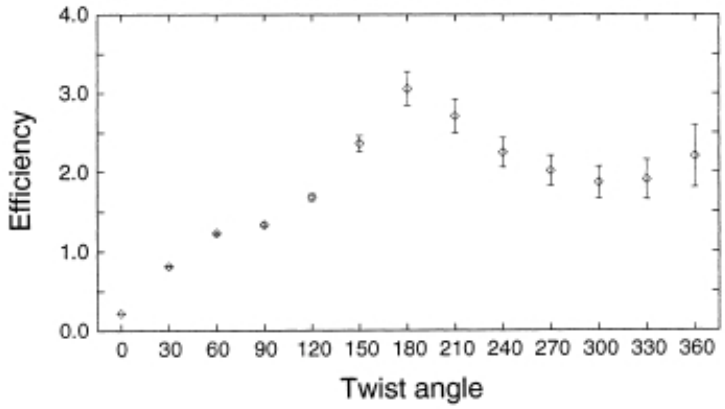

Figure 2.20. The effect of changing the twist angle on the mixing efficiency of Kenics mixer (Byrde et al. (1999)).

The optimise twist angle was found as 180°, and they suggested a more complete parametric study is required to find the optimum twist angle within a wider range of operating conditions. This result is different than the one from Hobbs et al. (1998a), which showed the optimum twist angle for a fluid with Reynolds of 0.1 is 120°. By considering the results of the work by Hobbs et al. (1998b), which showed the mixing

performance of the fluid with N_{Re} = 100 is poorer than the one with N_{Re} < 10, the difference in the optimum twist angles of the work by Hobbs et al. (1998a) and Byrde et al. (1999) could be due to the major difference in the Reynolds number that they were working with. It was also suggested by Byrde et al. (1999) that some caution should be taken for generalising this result to all the operating conditions.

The work by Galaktionov et al. (2003) considers the effect of shear thinning behaviour of the fluids in studying the mixing performance of Kenics mixer with different twist angle using a mapping method. The mapping method worked based on tracking of small flow domains, and following the domains from an initial grid at the start of the mixer to an end grid, with results stored in a mapping matrix. The velocity profile was calculated using a grid containing $1.6*10^5$ elements, and consequently the evolution of mixing can be studied by computing the concentration distribution of a side-by-side fed black and white fluid (Figure 2.21) with concentration of C = 1 for black and C = 0 for white fluid.

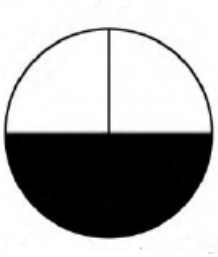

Figure 2.21. Black and white fluid feeding position at the start of the mixer (Galaktionov et al. (2003)).

Mixing was characterised by using the concept of intensity of segregation, and mixing efficiency was studied by plotting the changes of intensity of segregation versus pressure drop. It was shown by just considering the changes of intensity of segregation, Kenics mixer with 150° twist angle has the best performance (Figure

2.22(a)). This was in agreement with the results from Hobbs et al. (1998a). However, by considering the pressure drop, Kenics mixer with 140° twist has a better performance (Figure 2.22(b)).

Szalai et al. (2003) also studied the effect of aspect ratio and twist angle on mixing performance of Kenics mixer for Reynolds numbers between 19 to 1000 by calculating the velocity field, Lyapunov exponent, and variation coefficient for different Reynolds numbers using numerical simulations. It was shown that the element aspect ratio does not have a significant effect for $N_{Re} < 100$. The twist angle found to affect the mixing performance more than the aspect ratio, and the designs with lower twists angle (in window of 120° to 150°) per mixer element was suggested to be used.

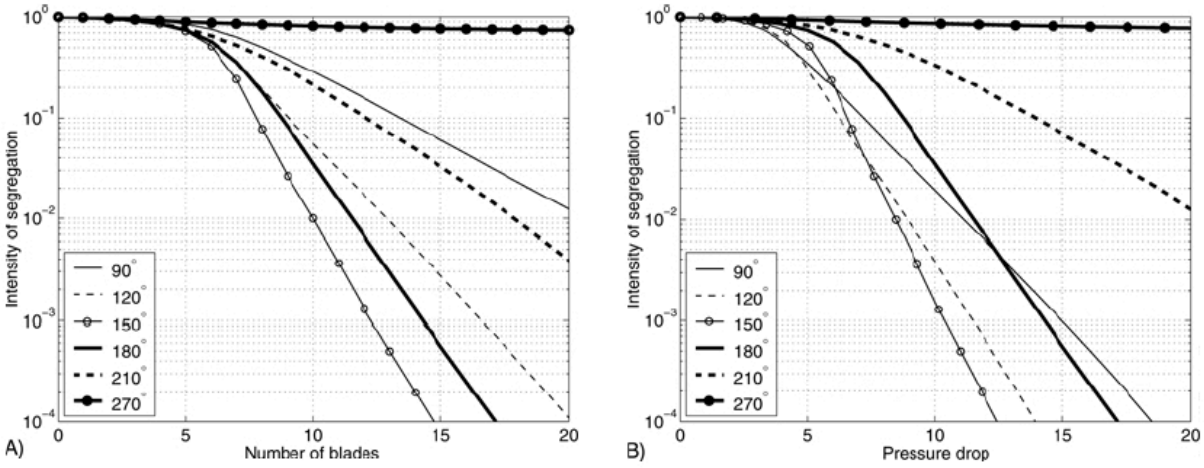

Figure 2.22. (a) The effect of twist angle per element on the intensity of segregation along twenty mixing elements; (b) The intensity of segregation vs. pressure drop as a function of twist angle per element (Galaktionov et al. (2002)).

Table 2.2 shows a summary on all the previous mentioned works on the optimise geometry of Kenics mixer. The result from Hobbs et al. (1998a) and Galaktionov et al. (2002) are the closest result to each other, using similar Reynolds number.

Table 2.2. Summery of the previous works on the optimise twist angle of Kenics mixer.

Previous work	Description
Hobbs et al. (1998a)	• N_{Re} = 0.15 • Using stretching rate→ 150 ° twist was the optimised one. • Using the stretching rate/pressure drop → 120 ° twist was the optimised one. • Poincare maps showed a better performance of R-L configuration.
Byrde et al. (1999)	• N_{Re} = 100 • Using mixer efficiency (pressure drop* striation thickness)→ 180° twist was the optimised one. • Suggested to take extra caution about generalising this result for other operating conditions.
Galaktionov et al. (2002)	• N_{Re} = close to zero • Using the intensity of segregation → 150° twist was the optimised one. • Using the intensity of segregation vs. pressure drop → 140° twist was the optimised one.
Szalai et al. (2003)	• $19 < N_{Re} < 1000$ • Using the Lyapunov exponent → twist angle between 120° to 150° was suggested.

2.2.2 SMX-plus

The Sulzer SMX mixer was introduced in 1980s, and since then it has been applied to a number of applications. This type of static mixer is quite common for mixing two fluids with significantly different viscosity. The geometry of SMX consists of an

array of crossed-bars, arranged at the angle of 45° against the pipe axis. Each element consists of eight bars, and consecutive elements are rotated by 90°. The radial mixing in this mixer is better than Kenics static mixer with lower pressure drop according to the Sulzer company due to the special arrangement of the bars within the element (Figure 2.23(a)). Most of the works on SMX have studied mixing performance and velocity fields using numerical techniques. Zalc et al. (2002b) studied the velocity fields and mixing performance of SMX by calculating the coefficient of variance for a Newtonian fluid with N_{Re} = 100. The Reynolds number was calculated as $\rho ud/\mu$, by using the diameter of the tube. Two streams with similar physical properties and flow rate were entered to the mixer. The evaluation of mixing structure showed the exponential decrease in CoV. It was also shown that the mixing is independent of Reynolds for $N_{Re} < 1$.

There are a number of works which studied SMX to improve its mixing performance by modifying its geometry (Visser et al. (1999), Zalc et al. (2002b), Liu et al. (2006), Singh et al. (2009)). The work by Singh et al. (2009) used the mapping method on SMX to study the effect of changing the number of bars, their angle and width on the mixing performance of SMX. It was shown that the mixing performance of SMX can be changed significantly by changing these geometrical parameters, and opened a new discussion about designing a new mixer based on the structure of SMX but with a better performance.

Sulzer introduced SMX-plus in 2009 (Hirschberg et al. (2009)), which according to them has a significant lower pressure drop by keeping the advantages of SMX. The number of bars in SMX-plus is reduced to six, and it features gaps between bars, which implies more available volume for the fluid. Same as SMX, the angle against the pipe axis is 45°. For stability reasons, the bars of SMX-plus are connected

together with pins. The comparison between a single element of SMX and SMX-plus is shown in Figure 2.23.

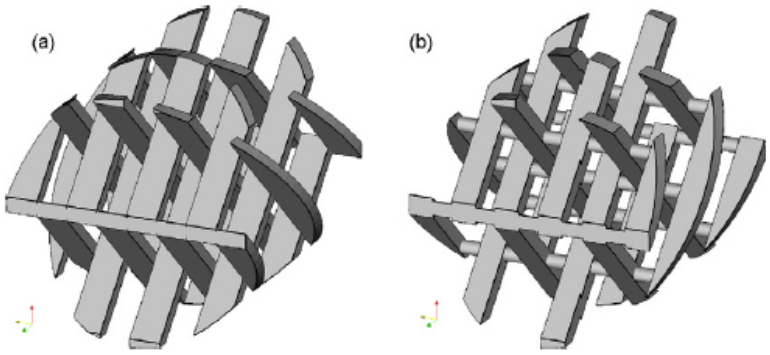

Figure 2.23. Arrangement of bars in a single element of (a) SMX; (b) SMX-plus (Hirschberg et al. (2009)).

Considering it has been just three to four years since Sulzer introduced SMX-plus, there are only two published works available on this mixer. Besides, the complex three-dimensional geometry of both SMX and SMX-plus causes it to receive significantly less attention in terms of numerical works in comparison with Kenics static mixer. The work by Hirschberg et al. (2009) from Sulzer company showed SMX-plus has 50% lower pressure drop than SMX. The concentration distribution maps for both mixers were calculated by CFD, and showed the striation thicknesses in SMX is slightly thinner than SMX-plus during the first four mixing elements (Figure 2.24).

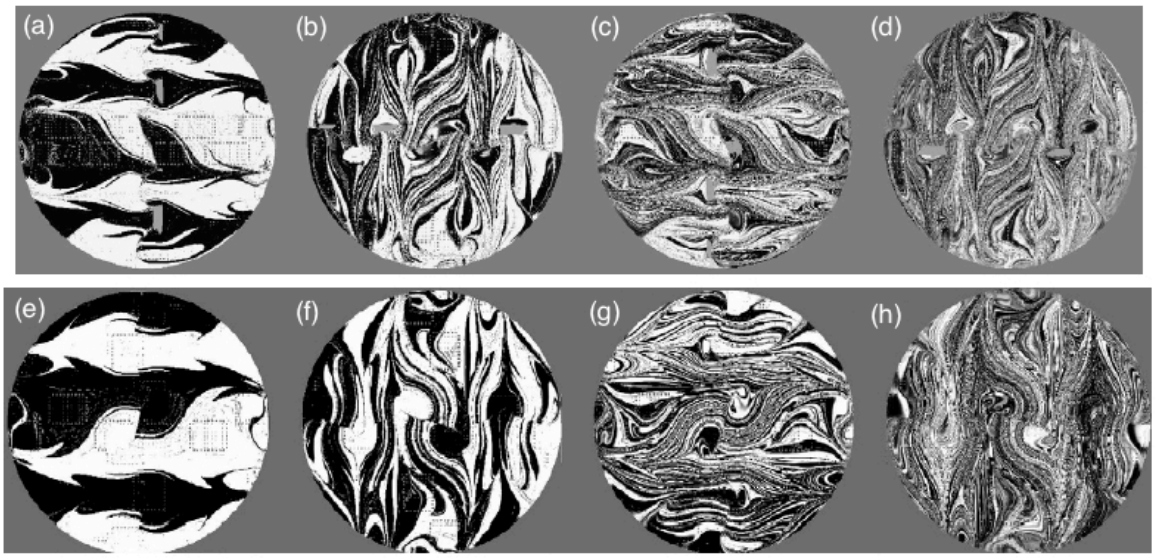

Figure 2.24. CFD prediction of concentration distribution for SMX (a to d) and SMX-plus (e to h) after :(a,e) first element; (b,f) second element; (c,g) third element; (d,h) fourth element (Hirschberg et al. (2009)).

The mixing performance was characterised using the concept of CoV, and it was found out the mixing quality of SMX-plus is poorer than SMX at the start, but it catches up with SMX after roughly seven elements and generates lower CoV after ten elements (Figure 2.25). Numerical results were also validated experimentally using laser induced florescence (LIF) technique.

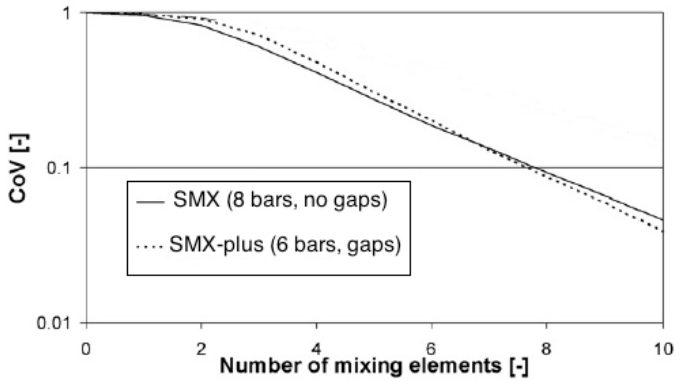

Figure 2.25. Comparison between the CoV of SMX and SMX-plus along ten mixing elements (Hirschberg et al. (2009)).

Meijer et al. (2011) studied the performance of several static mixers including SMX and SMX-plus. They calculated the performance of SMX-plus using the mapping method, and confirm the results from Hirschberg et al. (2009), showing SMX-plus is indeed performing better than SMX after going through around ten mixing elements.

2.2.3 Application of static mixers

While mechanical agitators are usually used in batch processes, static mixers are often used in continuous mixing processes because of different reasons such as the required size and space by them, flexibility on installation and low pressure drop. There is a wide range of industrial applications for different types of static mixers. For example, Kenics static mixers are used in process industries such as polymer dilution, pH control, mixing miscible or immiscible fluids, and etc. They also used to increase the rate of heat transfer in heat exchangers. The use of SMX is more specific, mainly in the processes, which include mixing of two fluids with different viscosities. A summary of the static mixers application in industry can be found in Table 2.3.

Table 2.3. Application of static mixers in different industries.

Name of the industry	Application
Food processing	• Ice-cream industry. • Fruit juices making process. • Flavoured yogurt. • Starch slurry cooking. • Liquid blending and emulsification process.
Chemicals and agricultural	• Mixing miscible and immiscible fluids. • Dissolving gasses (i.e. Chlorination process). • Dispersing liquids in washing processes • Fertilizer and pesticide preparation • Acid-based neutralization.
Polymer	• Mixing additives and catalysts into polymers. • Rapid uniform heating of polymers. • Preheating polymers. • Production of Polystyrene.
Pharmaceutical and cosmetics	• Mixing components of toothpaste, shampoo, lotions, and soaps. • Blending of multicomponent drugs • Sterilization.
Waste water treatment	• Waste water neutralization. • pH control. • Sludge de-watering process.
Pulp and paper	• Pulp blending. • Mixing bleaching chemicals with pulp. • Sludge conditioning. • pH control by mixing acid or base.
Petrochemical and refinery	• Blending grades of oil or gasoline. • Dispersing of kerosene in water. • Sweetening kerosene and gasoline. • Blending different hydrocarbon streams into gasoline. • Lub oil blending.

2.3 Conclusion

This chapter introduced and described some concepts of laminar mixing and previous work on Kenics static mixer and SMX in order to provide a background and better understanding about the current work. The first part of this chapter focused on some of the main mechanisms of laminar mixing, which are also the main mixing mechanisms used in Kenics and SMX static mixers. The methods, which are previously used to quantify the mixing performance in laminar regime, were described, with focusing on the use of these methods in the previous works on static mixers. In general, three main characterisation methods were discussed:

1. Using the concept of intensity of segregation to measure the level of homogeneity in a mixture. A similar statistical method (CoV) was also described.
2. Characterising the mixing performance by measuring the striation thicknesses and also qualitative measurements based on visualizing the striations.
3. Measuring the stretching histories of the fluid element based on Lyapunov exponent.

Different optical techniques, which are usually used to study the flow structure in both dynamic and static mixers, were also discussed. Most of these techniques required the used of transparent fluids, which is limiting their applications. Positron emission particle tracking was introduced as a technique, which record the movement of the tracer in three dimensions as a function of time. This technique does not have the limitations that that the other optical techniques suffers from, and it found to be a suitable technique to study the flow in Kenics and SMX static mixers in this work.

In terms of finding the optimise design of Kenics mixer, a number of numerical works previously showed using other twisting angle than the standard 180° one could increase the mixing performance of Kenics mixer; however, no experimental work has been validated this result.

PEPT has been used in this work for the first time as a unique Lagrangian technique, which makes it possible to study and compare experimentally different flow characteristics such as velocity distribution maps, residence time distribution within each single element of Kenics mixer, and also the shear rate maps in Kenics mixer, as well as the mixing performance. Although other experimental techniques such as PIV and PLIF could also be used in Kenics mixer to study the velocity distribution maps and mixing performance, using of them is limited to the transparent fluids. Besides, having the location of the tracer particle in three-dimensions through the whole geometry from the PEPT data, makes it possible to access all the mentioned flow characteristics at any point through the mixer, even within each single element of the mixer.

Notation

Roman letters

A	Cross-sectional area represented by the tracer particle.	m^2
B	CoV of the unmixed inlet	-
G	Rate of decrease of CoV per unit length of The mixer	-
C_{AA}	Contact number between particles of specie A	-
C_{BB}	Contact number between particles of specie B	-
C_{AB}	Contact number between particles of species A and B	-
C_h	Volume concentration of solid at level *h* (Guida et al., 2010)	-
C_i	Concentration at point *i*	-
C_{mean}	Mean concentration	-
C_s	volume concentration of solid (Guida et al., 2010)	-
D	Pipe diameter	m
D_x	Coefficient of dispersion in axial direction	-
D_r	Coefficient of dispersion in radial direction	-
E	Exposure	-
$F(t)$	Cumulative RTD	-
I	Intensity of segregation	-
k	Flow consistency index	Pa. s^{n-1}
k'	Strength of interaction	-
l_0	Initial distance between particles	m
l_n	Distance between particles after time t_n	m
n	Flow behaviour index	-
N_c	Number of grid cells	-

N_h	Number of horizontal levels (Guida et al., 2010)	-
N_{Re}	Reynolds number	-
N_t	Total number of measurements locations	-
Δp	Pressure drop	bar
Q_{in}	Total inlet volumetric flow rate (Hobbs et al., 1997a)	$m^3.s^{-1}$
r_s	Striation thickness	*m*
S	Segregation	-
St	Stokes number	-
s	Surface (Guida et al., 2010)	m^2
u	velocity	$m.s^{-1}$
$v_{x,in}$	Inlet axial velocity of the tracer particle (Hobbs et al., 1997a)	$m.s^{-1}$
X_A	Fraction of component A in a binary mixture	-
$\bar{X}_A$	Average fraction of component A in a binary mixture	-

Greek letters

β	Mean stretching rate normalised by pressure drop	-
ρ	Density of the fluid	$kg.m^{-3}$
μ	Dynamic viscosity of the fluid	$kg.\ m^{-1}s^{-1}$
τ	Shear stress	Pa
τ_0	Yield stress	Pa
θ	Normalised residence time	-
$\dot{\gamma}$	Shear rate	s^{-1}
σ	Standard deviation of concentration	-

λ	intensity of mixing experimented by material element	-
Λ	Lyapunov exponent	-

Chapter 3 . MATERIALS AND METHODS

3.1. Introduction

This chapter divides into two main sections. The 'Materials' section includes a description of the mixer geometries, fluids, and all the other materials and equipment used during the experiments. The second section describes the methodologies which are used to analyse the positron emission particle tracking (PEPT) data in this thesis.

3.2 Materials

3.2.1 The geometry

The experiments were carried out predominantly in one mixer geometry, the Kenics static mixer (KM). The geometry of the standard Kenics static mixer was modified to give two further geometries with respect to the twist angle of each element. The SMX-plus static mixer was also used during the experiments.

3.2.1.1 Kenics static mixer

A six-element 50 *mm* diameter Kenics static mixer, or KM, which is manufactured by Chemineer, with a 180° twist was selected as the base configuration. The geometry consists of six elements housed inside a pipe. According to the factory manual, the length of the each element should be 76 *mm*, however, in the mixers we purchased there were elements of different length, ranging from 74-76 *mm* (Figure 3.1). This difference between the lengths of the elements is taken into account in the data analysis.

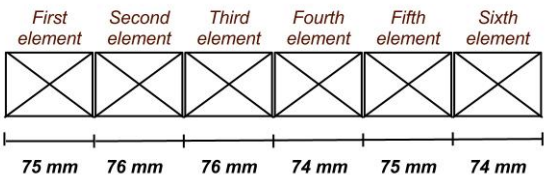

Figure 3.1. Length of each element for the KM at the 180° twist.

The details of the KM 180° twist geometry are given in Table 3.1.

Table 3.1. Mixer geometry.

Mixer geometry	
Diameter	5.08 *cm*
Number of elements	6
Length of the element	7.4-7.6 *cm*
Plate thickness	0.317 *cm*

The mixing elements are arranged in pairs, and each pair includes a right-handed and a left-handed 180° twist. The following edge of each element is normal to the leading edge of the following one. A sketch of the KM with the 180° twist in the blades is shown in Figure 3.2. Due to the manufacturing tolerances of the commercially obtained KM, the alignment of the two consecutive elements are not always exactly perpendicular and aligned (Table 3.2). This issue was observed in some part of the analysis, and will be discussed later.

Table 3.2. Angle between the blades of the two consecutive elements along the mixer.

Transitional area	**Angle between the leading edge of two consecutive elements**
1st and 2nd element	90°
2nd and 3rd element	90°
3rd and 4th element	90°
4th and 5th element	85°
5th and 6th element	92°

By changing the twist angle of the basic configuration (180° twist), the geometry was modified into two other geometries with a twisting angle of 150° and of 120°.

The first modification was done by changing the twisting angle of all the blades from 180° to 150°. Each element was cut and separated from the neighbouring elements in order to create the new twisting angle. The new length of the element with the 150° twist was calculated by using the following formula:

$$L_{150} = \frac{L_{180} * 150}{180} \qquad \textbf{(Equation 3.1)}$$

where L_{150} is the length of the element with the 150° twist, and L_{180} is the length of the element with the 180° twist, which is equivalent with 76 *mm*. Hence, the length of the element with the 150° twist was calculated as 63.3 *mm,* meaning 14 *mm* needed to be cut from each element. Subsequently, all the elements were attached together in the same order as before, keeping the edge of each element normal to the neighbouring element.

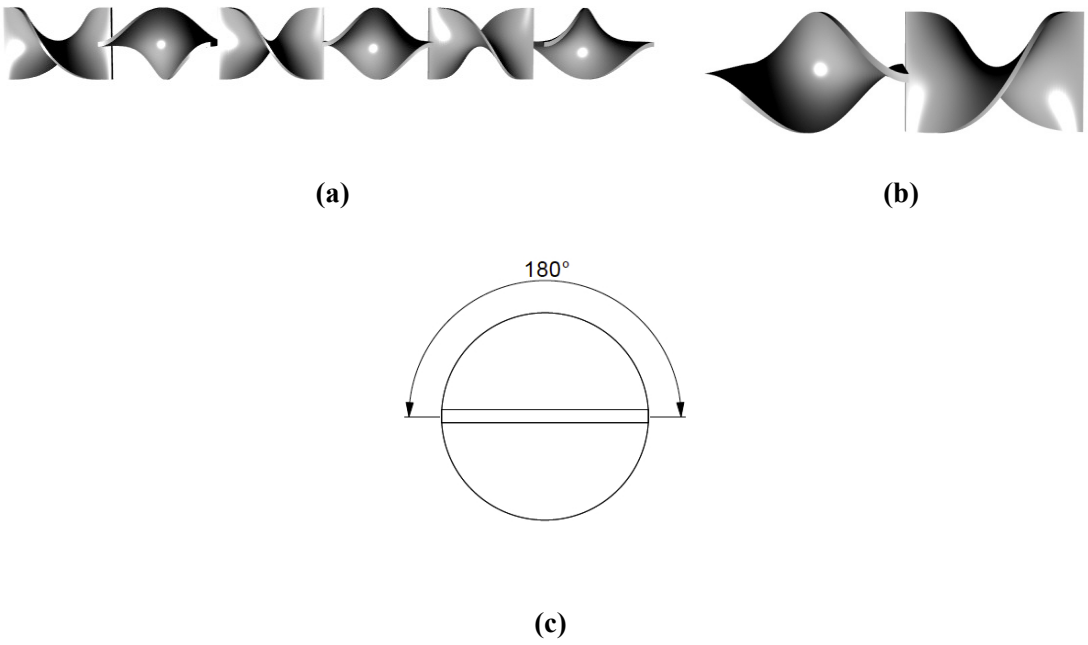

Figure 3.2. Mechanical drawing for the KM at the 180 ° twist: (a) whole length of the mixer; (b) two subsequent elements; (c) plan view of one element showing the twist angle.

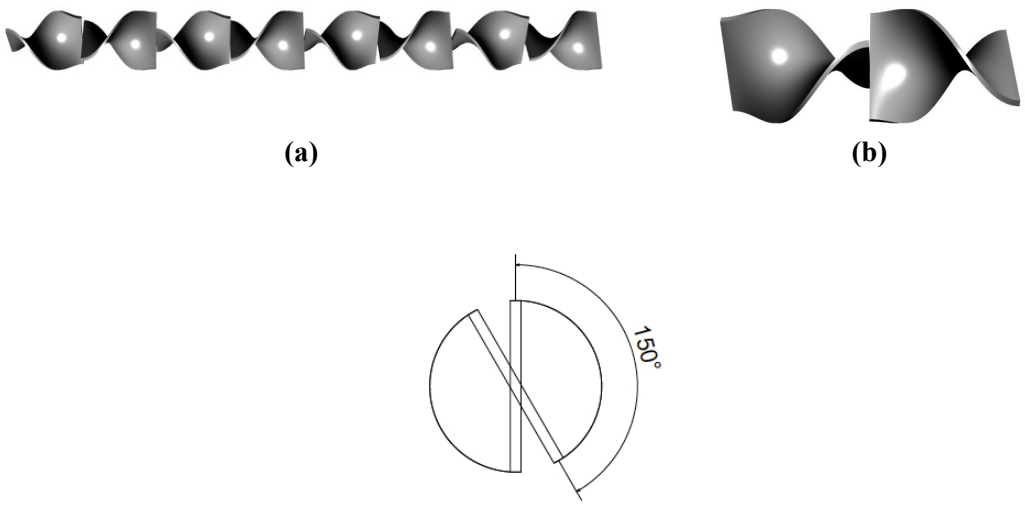

Figure 3.3. Mechanical drawing for the KM at the 150° twist: (a) whole length of the mixer; (b) two subsequent elements; (c) plan view of one element showing the twist angle.

The KM after the modification included eight elements. Figure 3.3 shows the mechanical drawing of the KM with the 150° twist in the blades.

The next modification was done by separating the mixer elements of the KM with the 150° twist in blades. Equation 3.1 was used to estimate the new length of the element with a 120° twist, which was calculated as 51 *mm*. By cutting 12 *mm* from each element, the length of each one was reduced to 51 *mm*. All the elements were re-attached together and created a new design of the KM, which contained ten elements with a 120° twist in the blades. A mechanical drawing of the KM with the 120° twist angle is shown in Figure 3.4.

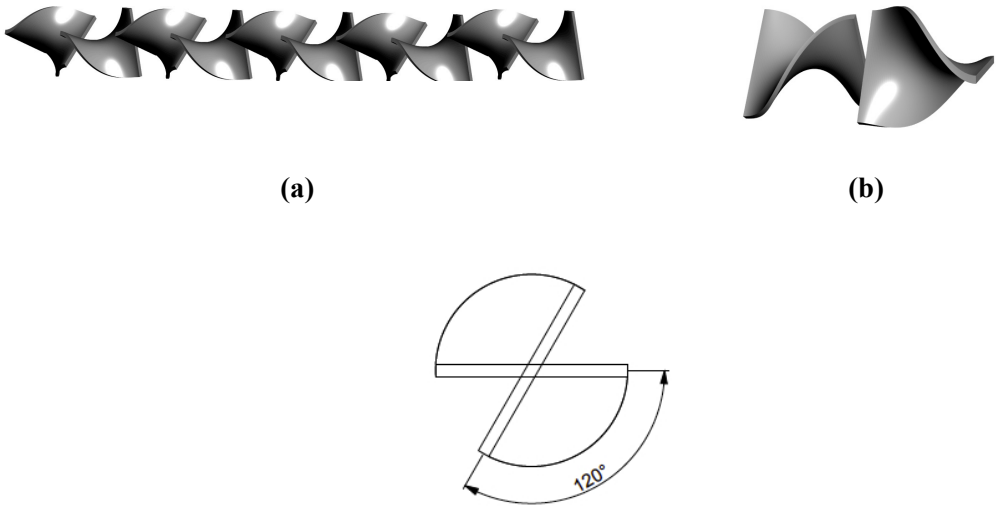

Figure 3.4. Mechanical drawing for the KM at the 120° twist: (a) whole length of the mixer; (b) two subsequent elements; (c) plan view of one element showing the twist angle.

3.2.1.2 SMX-Plus

A six-element 50 *mm* SMX-plus mixer (manufactured by Sulzer) was used for this static mixer configuration. The SMX-plus mixer consists of an array of crossed bars, which are located at the angle of 45° against the inner wall of the pipe. Each element contains six bars, which are connected at the crossing parts by pins. The leading edge of each element is perpendicular to the leading edge of the following element. The length of each element was measured around 50 *mm,* which is equal to the diameter of the mixer. Figure 3.5 shows the arrangement of the elements in the SMX-plus mixer.

(a) **(b)**

Figure 3.5. SMX plus mixer: (a) six elements; (b) two consecutive elements.

3.2.2 The fluids

3.2.2.1 Newtonian

The glycerol was purchased from Sigma Aldritch (UK), with a purity of > 98%, and used without any further purification process.

The rheological measurements for all the fluids were carried out in a TA AR 1000 (TA instruments) cone and plate, equipped with a 40 *mm* diameter 2° steel cone. The rheological measurements of glycerol will be presented in Chapter 4.

3.2.2.2 Non-Newtonian

Carbopol 940 was purchased from Sigma Aldritch (UK), and used to make two different concentrations of Carbopol solution, which are representative of the non-Newtonian fluids used by Johnson & Matthey.

A 0.1 wt% Carbopol solution with pH 4.50-4.70 was used as the first non-Newtonian fluid, which was prepared by mixing 20 *gr* of Carbopol with 20 *litres* of water to get a clear homogenous solution. The original pH of the solution was measured as 3.30-3.50. In order to reach the desired pH value (4.50-4.70), a solution of NaOH was prepared as a strong base and added to the mixture until the pH was in the desired range.

A 0.2 wt% Carbopol solution with pH of 4.80-5.00 was used as the second non-Newtonian fluid. This solution was prepared using the same methodology of preparation of 0.1 wt% Carbopol solution, as described before. The final pH value of this solution was measured as 4.80-5.00.

The rheological properties of both concentrations of Carbopol solutions were measured using the same rheometer as described in §3.2.2.1. The rheological measurement of both non-Newtonian fluids will be presented in Chapter 5. The table of the dependency of the rheological properties of both solutions on their pH can be found in Appendix A.

3.2.3 The Positron Emission Particle Tracking Tracer

The tracer used for this work was made by the School of Physics and Astronomy at the University of Birmingham. The technique used to produce the radioactive tracer consists of several different stages. The tracer is labelled with a positron-emitting nuclide by using ^{18}F, ^{61}Cu, or ^{66}Ga. ^{18}F was used in this work, considering its production of high gamma rays annihilation photons, and therefore providing a higher accuracy in detecting locations, in comparison with the other isotopes. ^{18}F can be produced either from purified water or solid materials under direct bombardment with ^{3}He beams:

$^{16}O(^{3}He, p)^{18}F$ or $^{16}O(^{3}He,n)^{18}Ne \rightarrow {}^{18}F$

In this work, 3 *mL* of ultrapure water is directly activated using the cyclotron at the School of Physics and Astronomy, and a ^{3}He beam (Fan et al. (2006)), producing a radioactive solution of ^{18}F. 1 *mL* of the radio-activated water is then added to a number of ion exchange resin beads, provided by Dow chemicals (Dowex SBR strong

base anion exchange). The resin is made of polystyrene with a micro-porous structure. The hydroxide ions (OH^-) of this compound exchange in solution with ^{18}F ions until equilibrium is reached. The micro-porous structure and the chemical compounds of the resin make it a good candidate to be the base material of the tracer.

The mixture is then placed under a flow of nitrogen gas and an infrared lamp, until all the water evaporates. Once fully dried, each resin bead is coated with a thin layer of fast-setting epoxy resin to encapsulate the activity and prevent leaching in aqueous systems. The diameter of the final tracer is 250-500 μm. The combination of the water-based nature of the solutions in this work, and the design of the geometry and the pump, provide a harsh environment for the tracer, where minor cracks on the paint surface can result in a leak of the radioactive label in the system. This risk is higher for the Carbopol solutions, which are higher in water content (up to 99%). Due to this technical difficulty, in some experiments using an extra layer of coating was found to be necessary in order to prevent the leakage of ^{18}F.

On finishing the process of making the radioactive particle, the tracer is injected into the system. The process of the radioactive tracer detection by the camera was described before in detail in Chapter 2, §2.1.3.5.

The tendency of the tracer to follow the fluid is estimated by using the Stokes number:

$$St = \frac{\tau_p}{\tau_f} \qquad \textbf{(Equation 3.2)}$$

where τ_p is particle response time and τ_f is the fluid response time. τ_p can be calculated by the following equation: $(\tau_p = (\rho_p + 0.5\ \rho_f) d_p^2 / 18\mu)$, where ρ_p is the density of the particle, ρ_f is the density of the fluid, d_p is the diameter of the particle,

and μ is the viscosity of the fluid. The fluid response time or τ_f can be calculated from $\tau_f = D/u$, where D is the diameter of the pipe, and u is the velocity of the fluid. A small value of a Stokes number indicates the particle responds fast to the changes of fluid velocity, meaning the particle follows the fluid streamline well. The values of the Stokes number for glycerol, Carbopol 0.1 wt%, and Carbopol 0.2 wt% are calculated as $3.0*10^{-5}$, $7.5*10^{-5}$, and $5.0*10^{-5}$, corresponding to the superficial velocity of 0.1, 0.08, and 0.15 $m.s^{-1}$. These values of Stokes number show the tracer follows the fluid streamline closely.

3.2.4 The PEPT experimental set up

Each experiment consisted of positioning the mixer between the PEPT cameras, levelling the mixer to be as vertical as possible, and placing it at the centre of the distance between the two detectors. The rig was filled up with the fluid by using a gear pump to pump the fluid from the tank and through the mixer. A schematic of the rig is given in Figure 3.6(a).

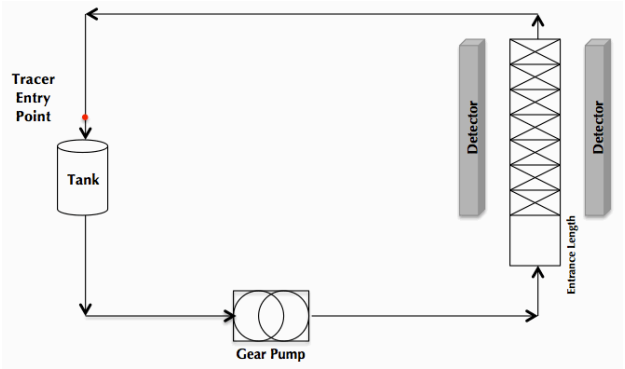

(a) **(b)**

Figure 3.6: (a) schematic diagram of the rig; (b) the KM within the PEPT camera.

The tracer was injected before the tank and the fluid was pumped around the closed circuit, passing repeatedly through the mixer. As shown in Figure 3.6(b), the mixer was located between the positron cameras; each time the tracer passed through the mixer, its path was recorded temporally and spatially. Each passage of the tracer through the mixer is defined as one pass. *z* is in the direction of the vertical axis across the length of the mixer, while *y* is across the geometry between the detectors.

The corresponding data for each condition was taken over five days of experiments. The radioactivity of a typical tracer used in these experiments was high enough (between 600 to 1000 μCi) for collecting good quality data for five to six hours of experiments per day. As mentioned before, although the tracer was coated with an extra layer of paint for the experiments with the non-Newtonian fluids, it was observed the radioactivity of the tracer was decreasing faster than in the experiments with the Newtonian fluid. With considering the water-based nature of the non-Newtonian fluids, ^{18}F was leaking into the fluid after two or three hours, which reduced the number of passes achievable per day. For the Newtonian fluid, the average number of passes for each experiment was around 2000, while this number was between 800 - 900 using the non-Newtonian fluids.

The Carbopol solution was made each morning, and used in the rig for five to six hours. At the end of each day, the rig was emptied, and the next batch of the solution was prepared the day after in the same way as described above.

The superficial velocity used for each experiment was calculated by measuring the volumetric flow rate of the fluid and dividing it by the cross-sectional area of the pipe.

Due to some mechanical problem with the gear pump used in this work, the value of the superficial velocity for the Carbopol 0.1 wt% solution had to be chosen as half of

the one for the Carbopol 0.2 wt% solution in the KM 180 mixer. The superficial velocity of glycerol, the Carbopol 0.1 wt%, and the Carbopol 0.2 wt% solutions were reported as 0.09, 0.08, and 0.15 *m/s* in the KM mixers and 0.15 *m/s* for Carbopol 0.1wt% in the SMX-plus mixer.

3.3 Methods

3.3.1 Introduction to PEPT data analysis

The method to find the actual location of the tracer was first developed by Parker et al. (1993) through a program called *Track.exe*. Figure 3.7 shows an example of the output of this program. The first four columns of the data file correspond to the time and three Cartesian coordinates. The fifth column gives an error, which will be described in detail later. The sixth and seventh columns are not required in the data processing, while the last column shows the number of the LORs (Line of response), which are used to find the final location.

Separation= 250

f(opt) : 0.1 Displacement parameters : 300, 400, 1500

Fixed slices: 200 events/slice, 1 locations/slice

Time (ms)	x (mm)	z (mm)	y (mm)	error			
132931.1	193.3	357.5	97.9	9.1	0.0	0.00	10
160785.1	281.2	161.2	126.9	9.8	0.0	0.00	11
163646.9	279.9	140.5	123.2	9.4	0.0	0.00	9
163961.9	323.1	148.2	119.0	8.7	0.0	0.00	10
164139.5	278.7	85.9	182.7	6.9	0.0	0.00	8
164214.5	292.2	87.5	114.5	7.7	0.0	0.00	8
164285.5	317.1	118.2	132.9	8.4	0.0	0.00	8
164359.8	263.4	123.8	139.8	8.5	0.0	0.00	9
164412.7	290.3	117.3	118.2	9.2	0.0	0.00	9
164463.1	275.6	109.2	150.2	6.9	0.0	0.00	9
164513.6	289.1	125.3	139.2	8.2	0.0	0.00	9
164571.9	277.4	122.2	134.7	9.3	0.0	0.00	9
164624.3	293.4	80.9	134.3	9.3	0.0	0.00	9
164654.5	292.5	111.8	137.4	6.3	0.0	0.00	8

Figure 3.7. An example of the output of *Track.exe*

The recorded data from the PEPT experiment contains a list of consecutive events, which divide into a number of subsections (*No. of events/slice*). For each subsection, the program finds the location of a point (*x, y, z*), which has a minimum distance from all the recorded paths of the events. By identifying all the paths, which are the furthest from this location, and considering them as corrupted paths, they are removed from the list of the events. Subsequently, a new location (*x, y, z)* is calculated based on the events that are left, and the process is repeated until only a specific fraction of the events (f_{opt}) is left. Then, the last calculated location (*x, y, z*) is recorded by the program as the final position of the tracer for that specific subsection, and it moves to the next one repeating the same process. This means the final location of the tracer is calculated over (f_{opt} * *No. of events*). At the end, each data file contains all the calculated locations, which together create the overall *No. of locations*.

Considering the process of calculating the one final location from a set of events that are measured experimentally, an error is produced. The error value measures the spread of the lines around the tracer position, by calculating the standard deviation of the perpendicular distances from each line used in finding the final location, to the point calculated as the location. By dividing this value by the square root of the number of the lines used to calculate the final location (the square root of the eighth column of the data file), a normalised standard error could be produced.

The magnitude of the error scales with the value of f_{opt}. The smaller the value of f_{opt}, the higher the number of lines rejected from the total number of events, causing to cut off all the corrupted events and resulting in having only the good data and a smaller error. Nevertheless, if the value of *No. of events* is small, e.g., 100, then a small value of f_{opt} such as 0.05 would lead to the use of only five events to calculate the final location. It should be mentioned that the reduction of error is complementary, but it is

important to have the statistically significant value of actual trajectories over which to reconstruct the location. Hence, a solution is suggested to find the best *No. of events* and f_{opt}, which considers having both the minimum standard error and a high *No. of locations*. A data file was processed with different values of f_{opt} and *No. of events*, and the standard error and the total *No. of LORs* were calculated separately for each condition. A new parameter was defined as the ratio of the standard error over the *No. of LORs* for each condition. Figure 3.8 shows the result of changing f_{opt} and *No. of events* on the normalised standard error by the number of locations. It is desirable to find the values of f_{opt} and *No. of events* at which the standard error over *No. of LORs* has its minimum value, meaning having a small value of standard error and a high *No. of LORs*. According to Figure 3.8, the value of standard error over *No. of LORs* is minimum for the f_{opt} between 0.1 and 0.2, and *No. of events* between 150 and 200. Therefore the entire data set was processed with the value of f_{opt} = 0.1 and *No. of events* of 200.

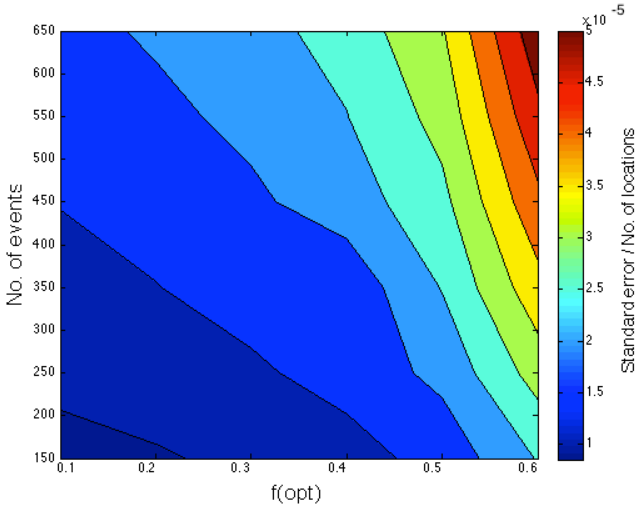

Figure 3.8. Normalised standard error by the *No. of locations* as a function of the changes in f_{opt} and *No. of events*.

3.3.1.1 Rotation of the data

After finding the f_{opt} and *No. of events/slice*, the data was pre-processed in order to be ready for the analysis. All the data files were unified into one file. First, it was necessary to make sure the mixer and the recorded data are positioned to be the most vertical possible. By plotting all the recorded particle paths, it was possible to observe the overall shape of the mixer, and compare it to the vertical axes.

The routine *rotaz.m* was written in order to rotate the recorded data in a way that the geometry becomes vertical. Considering the geometry as a complete cylinder, two small sections of this cylinder, located at the top and at the bottom were selected (Figure 3.9). For each section (which are indicated by red lines in Figure 3.9), the average of all recorded x and y of the points, which are located within that section was calculated, showing as p_1 (x_1, y_1, z_1) and p_2 (x_2, y_2, z_2) in Figure 3.9. If the mixer is completely vertical, the slope of the line, which is connecting p_1 to p_2 has to be 1, otherwise the slope would be bigger or smaller than 1. Consequently, the angles between the line connecting p_1 and p_2 with the positive x-axis (α), and with the positive y-axis (β) were calculated. The rotation matrix, which is a matrix that rotates a point in Euclidean space, was used to find the new rotated locations by using the below relations:

$$\begin{bmatrix} x' \\ z' \end{bmatrix} = \begin{bmatrix} \cos(\alpha) & -\sin(\alpha) \\ \sin(\alpha) & \cos(\alpha) \end{bmatrix} \begin{bmatrix} x \\ z \end{bmatrix} \quad \textbf{(Equation 3.3)}$$

$$\begin{bmatrix} y' \\ z' \end{bmatrix} = \begin{bmatrix} \cos(\beta) & -\sin(\beta) \\ \sin(\beta) & \cos(\beta) \end{bmatrix} \begin{bmatrix} y \\ z \end{bmatrix} \quad \textbf{(Equation 3.4)}$$

where x', y', and z' are the new positions after the rotation.

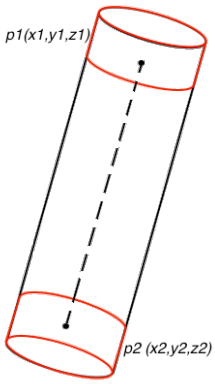

Figure 3.9. The view of the non-vertical geometry and how to rotate it. The red lines indicate the sections.

3.3.1.2 Data centring and filtering

The origin of the PEPT coordinate system is located at the corner of the left detector, therefore, as the first step the coordinates need to be centred. By subtracting the radius of the mixer from all the y and x values of the recorded points, the recorded data was centred at $(0,0)$ (Figure 3.10).

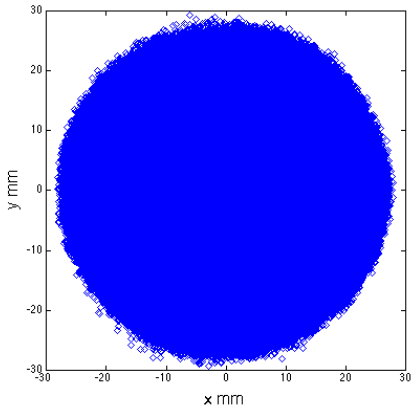

Figure 3.10. Recorded data point on the cross-section of the mixer.

Due to the water-based nature of the non-Newtonian fluids, ^{18}F would leach into the solution over a period of time, resulting in both decreasing the activity of the tracer and the creation of some corrupted data points, which are recognised as noise. Figure

3.11 presents nine random particle trajectories while they are passing through the length of the mixer, showing as blue, and the red points between them, which are recognised as the noise. These noises are visible within the time interval that the tracer is actually outside the mixer, meaning the fluid contains a small level of radiation.

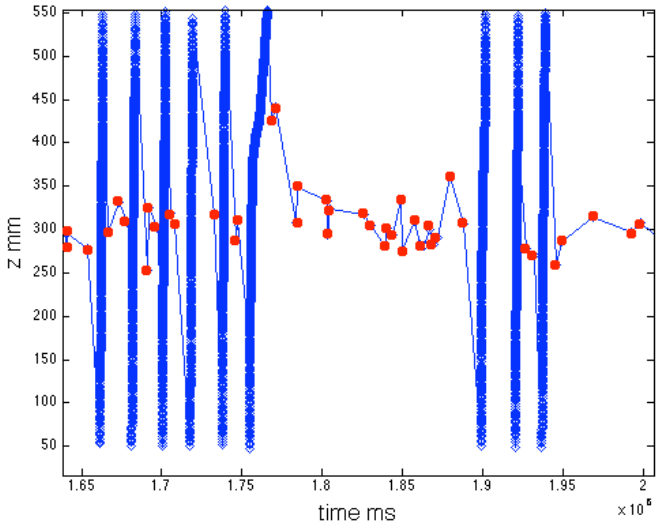

Figure 3.11. Axial movement of nine random particles vs. time along the mixer. The red points indicate the noise.

To overcome this problem and remove the corrupted data, the routine *Filtering_man.m* was written in order to filter the noise manually. This routine presents the data in the same graphical form as Figure 3.11, showing the noise as well as the actual data. A complete pass, containing a tracer entering and leaving the mixer, could be selected by clicking directly on the start and the end point, and the data between these two points is recorded automatically in a separate file. By selecting all the complete passes, the final file contains just the passes without the noise. Figure 3.12 shows the axial particle movement vs. time after removing the corrupted data.

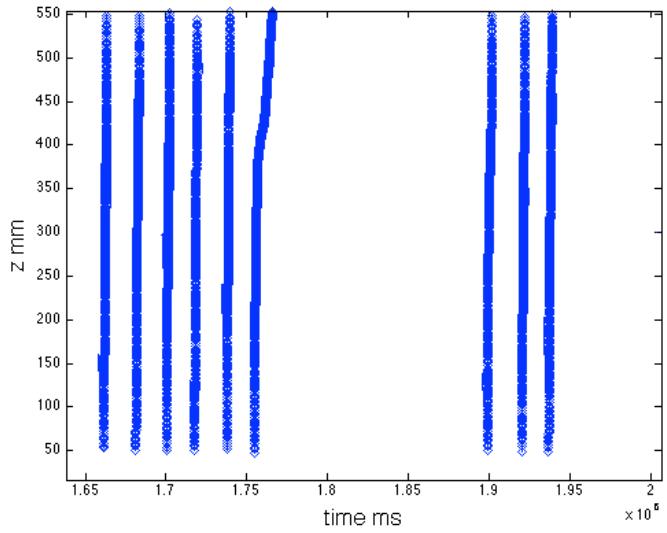

Figure 3.12. Axial movement of random particles vs. time along the mixer after applying the filter.

As shown in Figure 3.12, all the "noises" were removed, and each pass is separated by a time interval corresponding to the time spent by the tracer outside the field of view in the flow loop.

3.3.2 Particle trajectories and identifying the location of the elements

After the initial preparation of the data file, it is possible to plot the particle trajectories to gain a better understanding of the fluid behaviour inside the system. Figure 3.13 shows the axial movement of three random passes vs. x. As expected the particle paths do not follow a straight line by going along the mixer, and they are following the geometry.

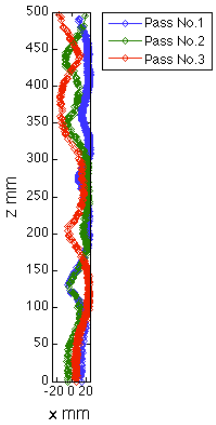

Figure 3.13. Axial movement of three random passes vs. *x*.

As mentioned in §3.2.1.1, the commercial version of the KM that was used in this work does not follow the exact design characteristics of the factory manual, i.e., the length of the elements are not exactly equal. By measuring the length of each element, the transitional areas between each two consecutive elements were located along the recorded data. Figure 3.14 shows the cross-section of the mixer, which includes all the particle trajectories, for each 10 *mm* along the first element.

The white empty space in the middle of the mixer represents the blade. The blade is rotating anti-clockwise along the first element, until it reaches the transitional area between the first and the second element, which becomes normal to the leading edge of the blade in the second element. Figure 3.15 shows the particle trajectories at different cross-sections along the mixer located on the transitional areas between the elements. As shown in Figure 3.15, on the transitional area between each two consecutive elements, the blades are (approximately) perpendicular to each other.

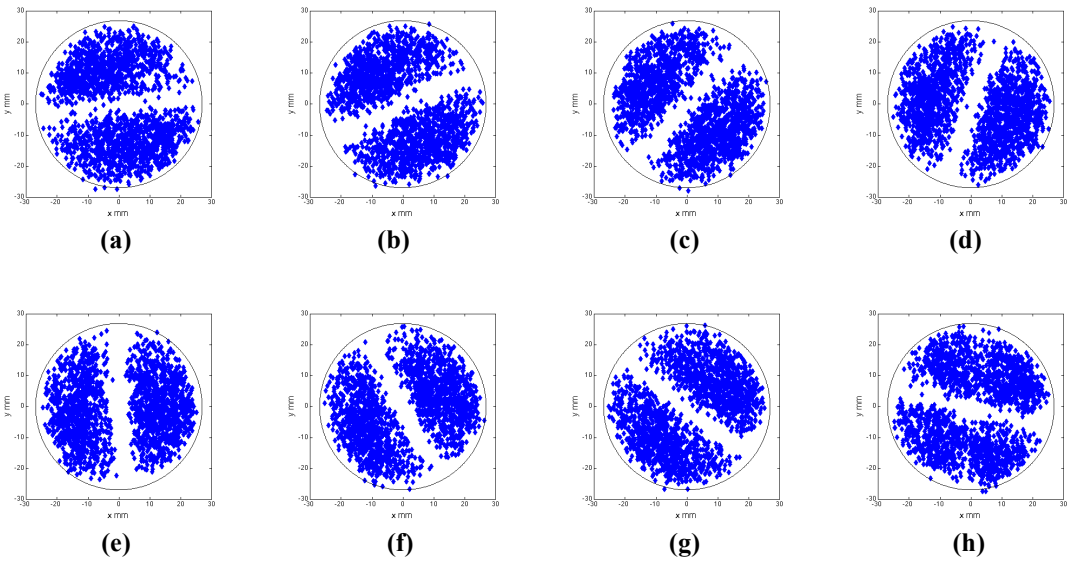

Figure 3.14. Particle trajectories for the cross-section of the mixer along the first element, with the length of *L = 76 mm,* at: (a) *z* = 0 *mm*; (b) *z* = 10 *mm*; (c) *z* = 20 *mm*; (d) *z* = 30 *mm*; (e) *z* = 40 *mm*; (f) *z* = 50 *mm*; (g) *z* = 60 *mm*; (h) *z* = 70 *mm*.

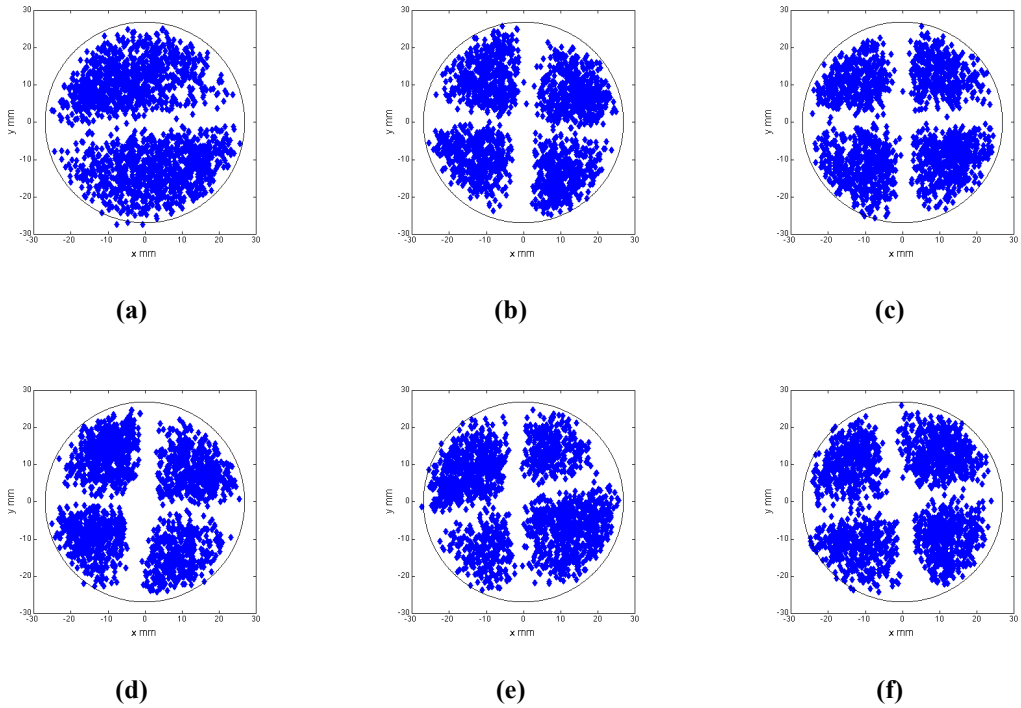

Figure 3.15. Particle trajectories for the cross-section of the mixer at: (a) entrance of the mixer; (b) start of the 2nd element; (c) start of the 3rd element; (d) start of the 4th element; (e) start of the 5th element; (f) start of the 6th element.

Figure 3.15 shows that the blades of two consecutive elements in the transitional areas are not always normal to each other and aligned on a perpendicular line. As mentioned before, this is due to the differences between the commercial KM provided by the manufacturer and the theoretical definition of the geometry of the KM.

3.3.3 Velocity calculations

There are different methods which can be used to estimate the Lagrangian velocities by using the PEPT data. The simplest way to calculate the local velocity is a two-point differentiation, using the equation below (Bakalis et al. (2004)):

$$v(i) = \frac{(x(i) - x(i-1))}{(t(i) - t(i-1))} \qquad \textbf{(Equation 3.5)}$$

where *v(i)* is the velocity for point *i* located at *x(i)* at the time *t(i)*. Another way of calculation commonly used in the School of Physics and Astronomy of the University of Birmingham is the 'six point' method, using 11 points rather than two points to reduce the effect of the PEPT error on the velocity calculation by using Equation 3.6 (Stewart et al. (2001)):

$$\begin{aligned} v_i = {} & 0.1\left[\frac{p_{i+5} - p_i}{t_{i+5} - t_i}\right] + 0.15\left[\frac{p_{i+4} - p_{i-1}}{t_{i+4} - t_{i-1}}\right] + 0.25\left[\frac{p_{i+3} - p_{i-2}}{t_{i+3} - t_{i-1}}\right] + 0.25\left[\frac{p_{i+2} - p_{i-3}}{t_{i+2} - t_{i-3}}\right] \\ & + 0.15\left[\frac{p_{i+1} - p_{i-4}}{t_{i+1} - t_{i-4}}\right] + 0.1\left[\frac{p_i - p_{i-5}}{t_i - t_{i-5}}\right] \end{aligned} \qquad \textbf{(Equation 3.6)}$$

where v_i is the velocity at point p_i with time t_i (Figure 3.16(a)) .

The method used in this work is based on the one that Chiti (2008) proposed, which was developed further by Gabriele (2011). This method finds the equation of the straight line of the 'best fit', which passes through the data set at different locations in time, using the least square method. Considering a degree of uncertainty about the

location of the tracer, the number of points which are chosen to find the 'best fit' line may affect the final calculated value of velocity. Chiti (2008) and Gabriele (2011) created a set of artificial data to compare the velocity calculated by different number of points. Guida et al. (2010) used the same method to calculate the velocity by choosing three to five points.

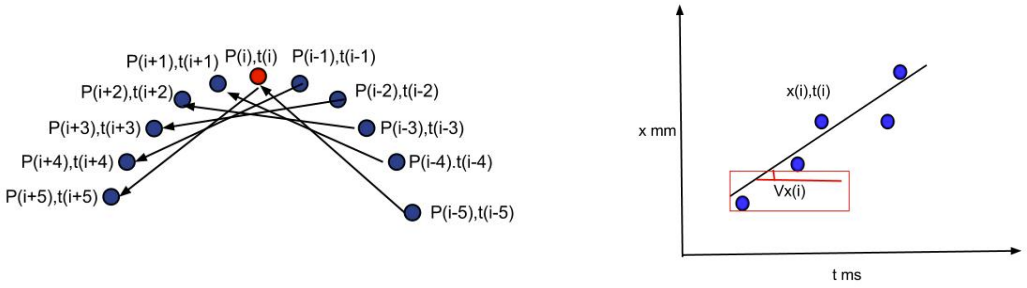

(a) **(b)**

Figure 3.16. (a) schematic of the six points method to find the velocity at point P(i),t(i); (b) 'best fit' method using five points at point x(i),t(i). The slope of the line represents the velocity (Vx(i)).

Table 3.3 shows a summary of the previous work, which used the least square method to find the 'best fit' line, the average velocity in each system, and the final chosen number of the points for each one.

Table 3.3. Chosen number of points to find the 'best fit' line with the least square method in previous related works.

Previous work	Average axial velocity in the system $m.s^{-1}$	No. of points to find the 'best fit' line
(Chiti,2008)	0.08	5 points
(Guida et al., 2010)	0.1	3-5 points
(Gabriele, 2011)	0.01	5 points

It was found that the average velocity of all the experiments reported here, which is around 0.09 *m/s*, is close enough to the velocity range presented in Table 3.3,

therefore the velocity was calculated by using five points through the routine *Kenics.m* (Figure 3.16(b)).

Due to the asymmetrical shape of the geometry, velocities are calculated in the Cartesian reference system. The routine *Eulerian_c.m* subdivides the volume of the pipe into iso-volumetric cells. The grid used in this work consists of 33 cells in *y* and *x* directions, and the number of cells in axial direction varies depending on the data density for each experiment. (Figure 3.17). Once the grid is built, a mean value velocity is defined for each cell using the following approach.

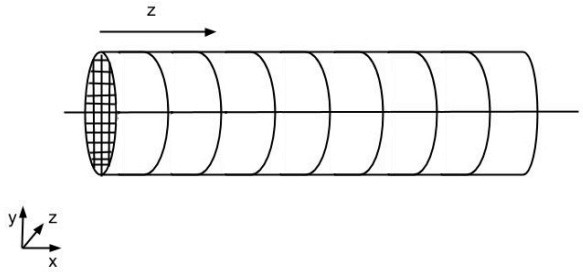

Figure 3.17. Dividing the geometry into a number of cells.

The routine *Eulerian_c.m* goes through all the recorded data points, and assigns them to different cells according to their location. The value of the velocity of a passing tracer is assigned to the right cell. A single averaged velocity assigned to each cell is defined by getting an average from the velocity of all the recorded locations within that cell. Equation 3.7 summarises the related calculations:

$$\bar{v} = \frac{\sum_{j=1}^{N} v_j}{N} \qquad \textbf{(Equation 3.7)}$$

where v_j is the velocity at the j^{th} location in a cell, N is the total number of the recorded locations within a cell, and $\bar{v}$ is the final average velocity of the cell (Figure 3.18).

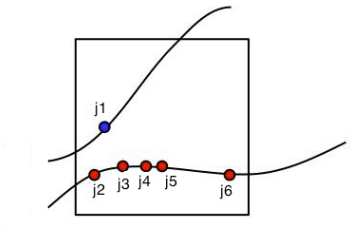

Figure 3.18. Recorded locations within two different passes . *j* represents the recorded location number.

The velocity maps that are presented in this work are plotted according to the calculated velocities though this method. The data was also interpolated in the axial direction.

3.3.4 Shear rate

In two-dimensional flows, shear rate is equal to the gradient of the velocity in a direction perpendicular to the velocity at that point. In three-dimensional flow, shear rate is defined using a tensor with six components. The rate of strain is calculated using the i^{th} component of velocity in the j^{th} direction (Ilievski et al. (2001)):

$$\Delta_{ij} = \frac{\partial v_i}{\partial x_j} + \frac{\partial v_j}{\partial x_i} \qquad \textbf{(Equation 3.8)}$$

The specific rate of strain in Cartesian coordinates is given by:

$$\Delta_{ij} = \begin{vmatrix} 2\frac{\partial v_x}{\partial x} & \frac{\partial v_y}{\partial x} + \frac{\partial v_x}{\partial y} & \frac{\partial v_z}{\partial x} + \frac{\partial v_x}{\partial z} \\ \frac{\partial v_x}{\partial y} + \frac{\partial v_y}{\partial x} & 2\frac{\partial v_y}{\partial y} & \frac{\partial v_z}{\partial y} + \frac{\partial v_y}{\partial z} \\ \frac{\partial v_x}{\partial z} + \frac{\partial v_z}{\partial x} & \frac{\partial v_y}{\partial z} + \frac{\partial v_z}{\partial y} & 2\frac{\partial v_z}{\partial z} \end{vmatrix} \qquad \textbf{(Equation 3.9)}$$

and the shear rate can be calculated by (R.Derby (1976)):

$$\dot{\gamma} = \sqrt{-\Pi} \qquad \textbf{(Equation 3.10)}$$

where

$$-\Pi = \left\{ 2\left[\left(\frac{\partial v_x}{\partial x}\right)^2 + \left(\frac{\partial v_y}{\partial y}\right)^2 + \left(\frac{\partial v_z}{\partial z}\right)^2 \right] + \left[\frac{\partial v_y}{\partial x} + \frac{\partial v_x}{\partial y}\right]^2 + \left[\frac{\partial v_z}{\partial y} + \frac{\partial v_y}{\partial z}\right]^2 + \left[\frac{\partial v_x}{\partial z} + \frac{\partial v_z}{\partial x}\right]^2 \right\} \qquad \textbf{(Equation 3.11)}$$

where for example the value of $\partial v_x / \partial x$ for cell *i* is calculated as:

$$\frac{\partial v_{x,(i)}}{\partial x} = \frac{v_{x,(i+1)} - v_{x,(i-1)}}{x_{(i+1)} - x_{(i-1)}} \qquad \textbf{(Equation 3.12)}$$

3.3.5 Visualising the striations

In order to get a better understanding of how the movement of the particles affects the creation of the striations along the mixer, the routine *Blue and Red.m* was applied to the PEPT data to visualise the striations.

According to the position of the blade at the entrance of the mixer, the cross-section of the geometry was divided into two semi-circles. The particles located on each semi-circle were found and labelled with different colours (blue and red) with respect to their position. Figure 3.19(a) shows the initial classification of the particles located at the start of the first element. Figure 3.19(b) shows three random particles belonging to each group located on the cross-section at the middle of the first element. As shown in Figure 3.19(b-c), after passing through the transitional area between the first and second elements, one of the red particles ended up on the opposite side of the blade,

while all the blue particles remained on the same side. This is just a simple example to show how the position of each particle changes along one element.

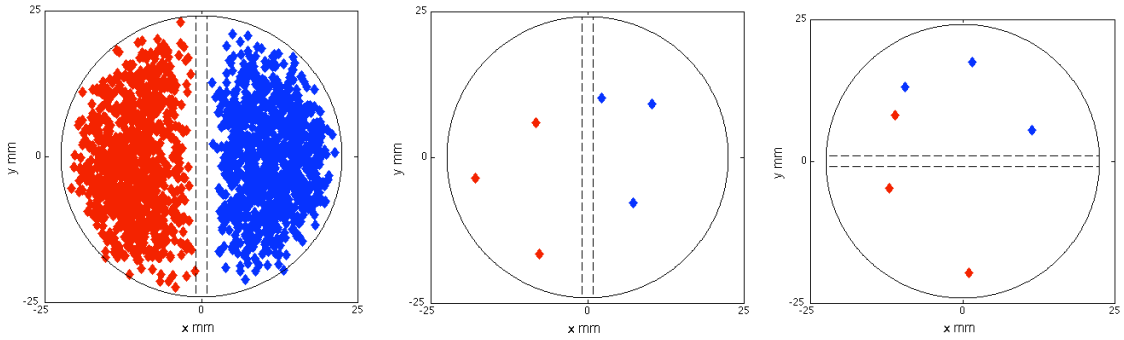

Figure 3.19.Classifying the particles into two groups according to their entrance position. The dash lines indicate the position of the blade. (a) Blue and red particles on the cross-section of the 1st element; (b) three sample of blue and red particles located on the of the 1st element; (c) the same three sample passes located on the cross-section at the start 2nd element.

3.3.6 Estimation of the coefficient of variance

The coefficient of variance (CoV) of the tracer concentration is used in order to characterise the radial mixing in the system, which is defined as the standard deviation of the concentration normalised by the mean concentration. There are different ways to estimate the standard deviation, depending on whether the samples represent the whole population or if they are randomly selected as a part of a bigger population. In this work, all the particles were used to calculate the coefficient of variance, which means the samples represent the whole population. Hence, the standard deviation of the samples could be calculated as:

$$S_N = \sqrt{\frac{1}{N}\sum_{i=1}^{i=N}(a_i - \bar{a})^2} \qquad \textbf{(Equation 3.13)}$$

where N is the total number of the samples, a_i is the observed value of the sample, and $\bar{a}$ is the mean value of the observations.

Considering the Lagrangian nature of PEPT experimental data, a MATLAB code is developed to calculate the *CoV*. First, the particles are classified into two groups by using the methodology, which was described in §3.3.5, labelled as Groups 1 and 2. The geometry is divided into a number of slices perpendicular to the mixer tube, and each slice is divided into '*N*' number of sectors. The *CoV* is defined across each slice by using the following formula:

$$CoV = \frac{1}{\bar{c}}\sqrt{\frac{1}{N}\sum_{i=1}^{N}(c_i - \bar{c})^2} \qquad \textbf{(Equation 3.14)}$$

$$c_i = \frac{n_{1,i}}{n_{1,i} + n_{2,i}}$$

where N is the total number of sectors per each slice, i indicates the sector number, c_i is the concentration of particles belong to Group 1 in sector i, n_{1i} and $n_{2,i}$ represent the number of particles belonging to Groups 1 and 2 located on sector i, and $\bar{c}$ is the average of c_i in each slice. A graphical expression of these parameters is shown in Figure 3.20.

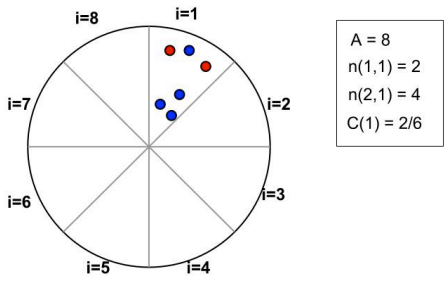

Figure 3.20. Graphical expression of the parameters used in calculation of the *CoV*. The circle represents a slice perpendicular to the mixer tube. *i* is the sector number, red particles represent Group 1, and blue particles represent Group 2.

The routine *Cov.m* acts over a few stages in order to find the changes of the *CoV* along the mixer. First, a 3D grid is created in order to have cells of equal volume; hence, the length of the mixer is divided into a number of segments, which are 2 *mm* long, and each cross-section is divided into twelve sectors with the size of $\pi/6$ (Figure 3.21(a),(b)). An alternative mesh configuration was also defined for the cross-section to study the effect of using different meshing configuration on the value of the *CoV* (Figure 3.21(c)). For this configuration, the cells in each cross-section are defined as the circles with the same centre but a different radius. The radius of each cell was calculated by considering the same area for each cell. The change in *CoV* was calculated along the axial length of the mixer.

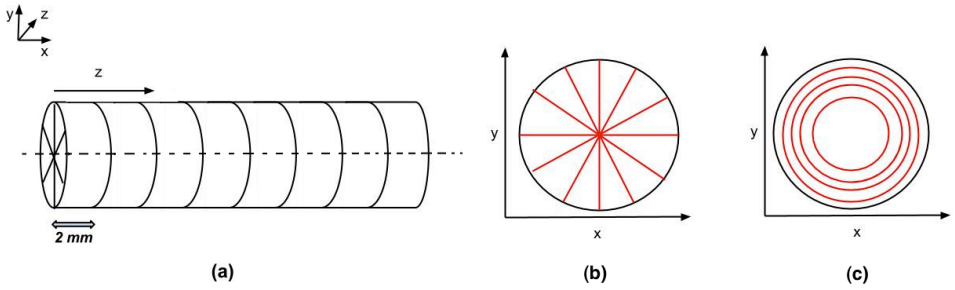

Figure 3.21. 3D grid to calculate the *CoV*: (a) division of cells in axial (*z*) direction; (b) division of cells on cross-section using sector cells;(c) division of cells on cross-section using circular cells.

Since the grid is defined according to a cylindrical reference system, it is necessary to transfer the original data from Cartesian to cylindrical, following Equation 3.15:

$$z_{cyl.} = z_{Cart.}$$
$$\theta = \arctan(\frac{y}{x}) \qquad \textbf{(Equation 3.15)}$$
$$r = \sqrt{(x^2 + y^2)}$$

Subsequently, after monitoring θ for all the particles, each particle is assigned to a sector according to its θ. The particles belonging to Groups 1 and 2 are counted in each sector, and the *CoV* is calculated for each slice following Equation 3.14.

The twist of the blade is taken into account by rotating the 2D grid for each cross-section with respect to the clockwise or anti-clockwise rotation of the blade. Considering the average length of the element as 76 *mm*, and the total twist per element as π, the amount of the rotation per unit of length (*rad/mm*) is ($\pi/76$). By adding this amount to the position of sectors on each slice, the new position of the sectors on the following slice could be calculated using Equation 3.16:

$$Sector_{(i+1)} = Sector_{(i)} \pm (\frac{\pi}{76}) \qquad \textbf{(Equation 3.16)}$$

where i represents the slice number. Adding or subtracting the rotation per unit of length ($\pi/76$) is a function of clockwise or anti-clockwise rotation of the blade.

The procedure described above is repeated for each cross-section on the grid to monitor the changes of the CoV along the mixer.

3.3.7 Changing the reference system

In order to approach the understanding of the mixing happening in the mixer, the reference system needs to be changed from the conventional Cartesian reference anchored to the wall of the mixer, to a moving reference system, where the blade of the geometry is the 0-plane (see Figure 3.22). This transformation allows the characterisation of the mixing due solely to the folding of the fluid elements, and not to the summation of the folding plus the displacement given by the rotation of the blade.

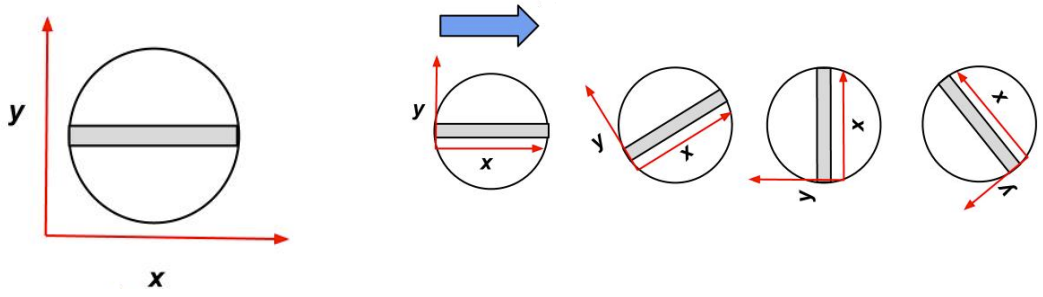

(a) **(b)**

Figure 3.22. Comparing different reference systems: (a) the conventional Cartesian reference system anchored to the wall; (b) the Cartesian reference anchored to the blade as it rotates.

The data was transferred using Equation 3.15, from Cartesian to cylindrical system. The degree of the rotation of the blade at each specific z was calculated by using the following equation:

$$\theta_{rotation} = \frac{z}{76} * \pi \qquad \textbf{(Equation 3.17)}$$

In order to find the new location of each particle (r, θ_{new}, z) in the moving reference system, the rotation angle of the blade at the axial position of the particle (z) was calculated according to Equation 3.17. Subsequently, by adding the $\theta_{rotation}$ to the angular position of the particle, the new position of the particle (r, θ_{New}, z) in the moving reference system could be found:

$$\theta_{new} = \theta_{old} \pm \theta_{rotation} \qquad \textbf{(Equation 3.18)}$$

where θ_{old} and θ_{new} are the angular position of the tracer before and after changing the reference system.

The new reference system was used to study the particle trajectories and study the effect of the distance of the particles to the solid boundaries on the velocity and residence time distribution.

Notation

Roman letters

a	Observed value of the sample	-
c_i	Concentration of particle in sector i	-
$\bar{c}$	Average concentration of c_i in one slice	-
d_p	Particle diameter	m
D	Mixer diameter	m
L_{150}	Length of the element in KM with 150° twist	m
L_{120}	Length of the element in KM with 120° twist	m
N	Number of sectors in each cross-section	-
$n_{1,i}$	Number of particles belong to Group 1, on sector i	-
$n_{2,i}$	Number of particles belong to Group 2, on sector i	-
r	Radial position in cylindrical coordinate	mm
S	Standard deviation of the samples	-
St	Stokes number	-
u	Velocity	m s^{-1}
$v_{avg.}$	Average Velocity	m s^{-1}
v_x	Velocity in x direction	m s^{-1}
v_y	Velocity in y direction	m s^{-1}

v_z	Velocity in z direction	m s^{-1}
v_i	Velocity at point i	m s^{-1}
$x(i)$	Position of point i in x direction	mm
$y(i)$	Position of point i in y direction	mm
$t(i)$	Recorded time for point i	mm

Greek letters

α	The angle between the line connecting p_1 and p_2 with the positive x-axis	degree
β	The angle between the line connecting p_1 and p_2 with the positive y-axis	degree
τ_p	Particle response time	s
τ_f	Fluid response time	s
$\theta_{rotation}$	Rotation angle of the blade	rad
θ	Angular position of the tracer	rad
ρ_p	Particle density	kg m^{-3}
μ	Viscosity	Pa s

Chapter 4 . MIXING OF NEWTONIAN FLUID USING THE KENICS STATIC MIXER

In this chapter the behaviour of glycerol as a Newtonian model fluid is investigated by using PEPT as the experimental technique. The Lagrangian and Eulerian velocity distributions are presented and compared to the previous numerical works. The residence time distribution function along each single element and the whole length of the mixer is calculated using the experimental data. The RTD curves calculated from the experimental data are compared with the one estimated from the convection model. Mixing performance is first characterised by coefficient of variance (CoV), and then by using the segregation index. The methodology that has been used in this chapter to investigate the flow behaviour and mixing performance in Kenics static mixer can be applied to other mixers with complex geometry as well.

4.1 Flow regime and development length

Glycerol with a purity of >98% and viscosity of 0.5 *Pa s* was chosen as the model Newtonian fluid in this work. The viscosity measurements were described in Chapter 3 and agree with literature values (Segur et al., 1951).

The Reynolds number for the flow through the mixer is calculated using the following equation:

$$N_{\mathrm{Re}} = \frac{\rho u D_h}{\mu} \qquad \textbf{(Equation 4.1)}$$

where ρ is the density of the fluid (1000 $kg\,m^{-3}$), u is the average velocity of the fluid in the pipe ($m.s^{-1}$), D_h is the hydraulic mean diameter of the Kenics static mixer (m), and μ is the viscosity of the fluid ($kg.m^{-1}.s^{-1}$). The hydraulic mean diameter can be calculated as the ratio of the wet surfaces to their perimeter:

$$D_h = \frac{4A}{p} \qquad \textbf{(Equation 4.2)}$$

Using Equation 4.2, The hydraulic mean diameter of a Kenics static mixer can be estimated by Equation 4.3 (Joshi et al., 1995) :

$$D_h = \frac{\pi D - 4w}{\pi + 2 - 2w/D} \qquad \textbf{(Equation 4.3)}$$

where D represents the diameter of the pipe (0.05 m), and w is the thickness of the blade (0.0038 m). Hence, D_h was calculated as 0.0288 m. The mean (superficial) velocity (u) is 0.1 m/s. Thus, the Reynolds number is calculated as 5.7, showing the flow is in a laminar regime.

For a fluid entering a pipe, the initial velocity profile at the inlet of the pipe is flat and will change gradually until it reaches to the fully developed condition. The distance that is required for the centre line velocity to reach 98% of its value for fully developed flow is called the development length. Assuming an initially uniform velocity profile entering the pipe the development length for Newtonian fluids in a laminar regime may be estimated as (C. A. Shook, 1991):

$$\frac{L_e}{D_h} = 0.062 N_{\mathrm{Re}} \qquad \textbf{(Equation 4.4)}$$

where L_e is called the development length. By substituting the value of N_{Re} and D_h in Equation 4.4, the entrance length is calculated as $0.353D_h$ or 0.01 m, which is taken into account during the design of the rig by keeping an empty length at the bottom of the pipe before the mixer elements.

4.2 Particle trajectories

The data from the PEPT experiment with the Newtonian fluid has been pre-processed as described in Chapter three, and presented in Cartesian coordinates. In this section, particle trajectories will be studied in order to get a better understanding of the behaviour of the fluid within the mixer.

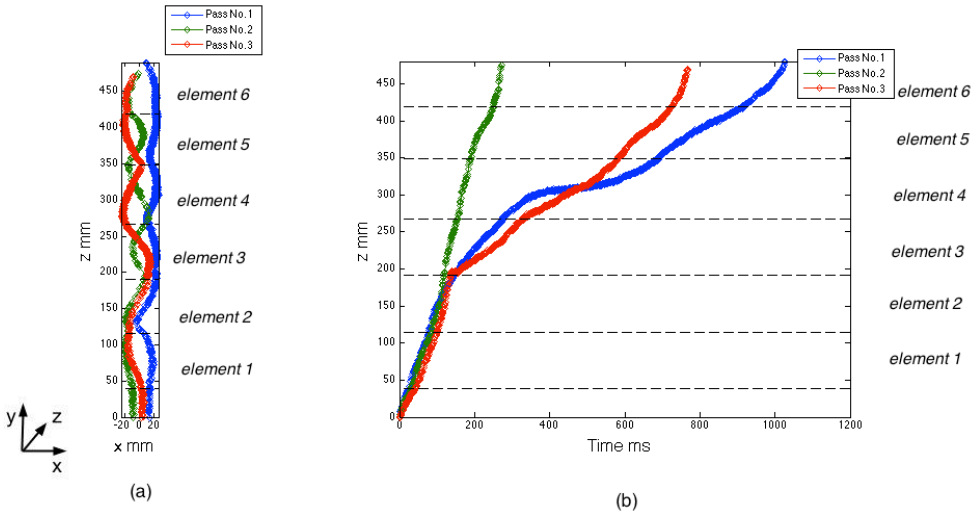

Figure 4.1. Particle trajectories of three randomly selected passes: (a) axial movement of the tracer vs. *x*. The black dash line indicates the position of the elements along *z*; (b) axial movement of the tracer vs. time.

There were around 2000 passes recorded for the experiment with the Newtonian fluid in Kenics static mixer. After monitoring all the particle trajectories, three passes were chosen for further Lagrangian analysis. Figure 4.1(a) shows how the particle movement of these three passes follow the shape of the elements along the axial length of the mixer. Figure 4.1 (b) represents the axial movement of the same three passes versus time. The graph shows that all the passes take a similar path until the end of the second element. On passing through the transition between the second and the third elements, the slope of pass number three (red) decreases suddenly, indicating a change in velocity. Further along the mixer, it is also observed that the slope of pass number one (blue) decreases within the fourth element. Thus, Figure 4.1 (b) shows the axial velocity of particles can change either at the transitional region between two consecutive elements, or within a single element. Since the fluid velocity is dependent on the radial and azimuthal location in the cross section due to the solid boundaries of the geometry (no-slip condition), the change in velocity implies a change in particle

location relative to these solid boundaries. Hence, the changes in the distance of the particles from the solid boundaries through the second, third and fourth element are monitored, and the effect of their position upon the axial velocity is studied further.

By finding the equation of the line representing the position of the blade, the distance of each of the recorded points from both the inner wall of the pipe and the blade was found for each of the three passes. It was assumed the closest solid boundary to each point has the most effect on the instantaneous velocity for each location, hence the minimum distance was chosen. Consequently, the axial velocity of each point was plotted versus this distance.

The data was processed using the de-rotational reference frame following the procedure described in §3.3.2 to ease the analysis. Figure 4.2 shows the particle trajectory of the same three passes on the cross-section of the second, third and fourth element, retaining the same colour labels as shown in Figure 4.1. The start and the end points for each pass are shown by black and magenta points. Along the second element, pass number three (red) is located between the blade and the inner wall of the pipe, and its position in the cross section is approximately constant. By passing through the transition between the second and third elements, pass number three (red) moves towards the inner wall of the pipe along the third element. Pass number one (blue) follows the shape of the inner wall of the pipe along the third element. When going through the fourth element, it is observed that pass number one (blue) moves towards the blade. Considering the density of the recorded points, it is possible to say that this movement towards the blade is very slow.

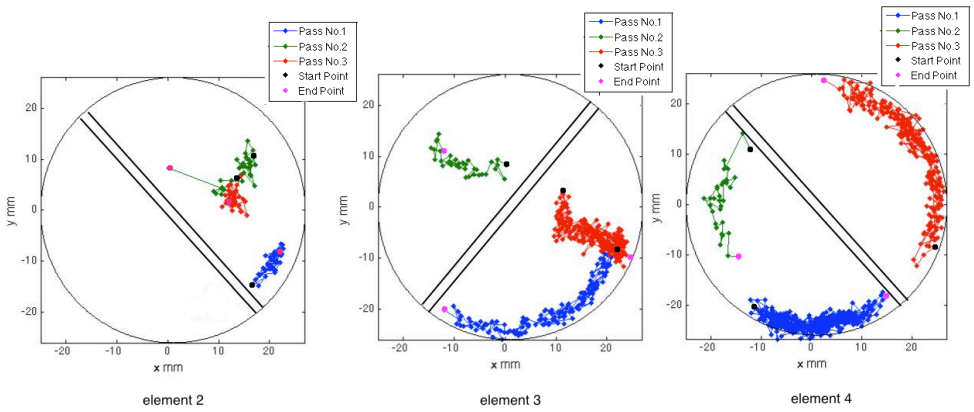

Figure 4.2. Particle trajectory of three passes on the cross-section of the mixer, located at the start of the 2nd element, 3rd element, and 4th element.

Figure 4.3 shows the effect of changing the distance to the closest solid boundary on the axial velocity for each pass along the second, third and fourth elements. Passes with the closer distance to the solid boundaries are expected to have a lower velocity. The error bars represent the spread of the recorded data point in distance and axial velocity for each pass.

As shown in Figure 4.3(a), the average distance to the solid boundaries is around 9 *mm* for pass number three (red) along the second element, with the average axial velocity around 0.13 *m/s*. However, by going through the third element, the average axial velocity of pass number three (red) decreases, due to its closer proximity to the solid boundary. Pass number one (blue) has an average distance of 2 *mm*, with the average axial velocity of 0.03 *m/s* along the third element.

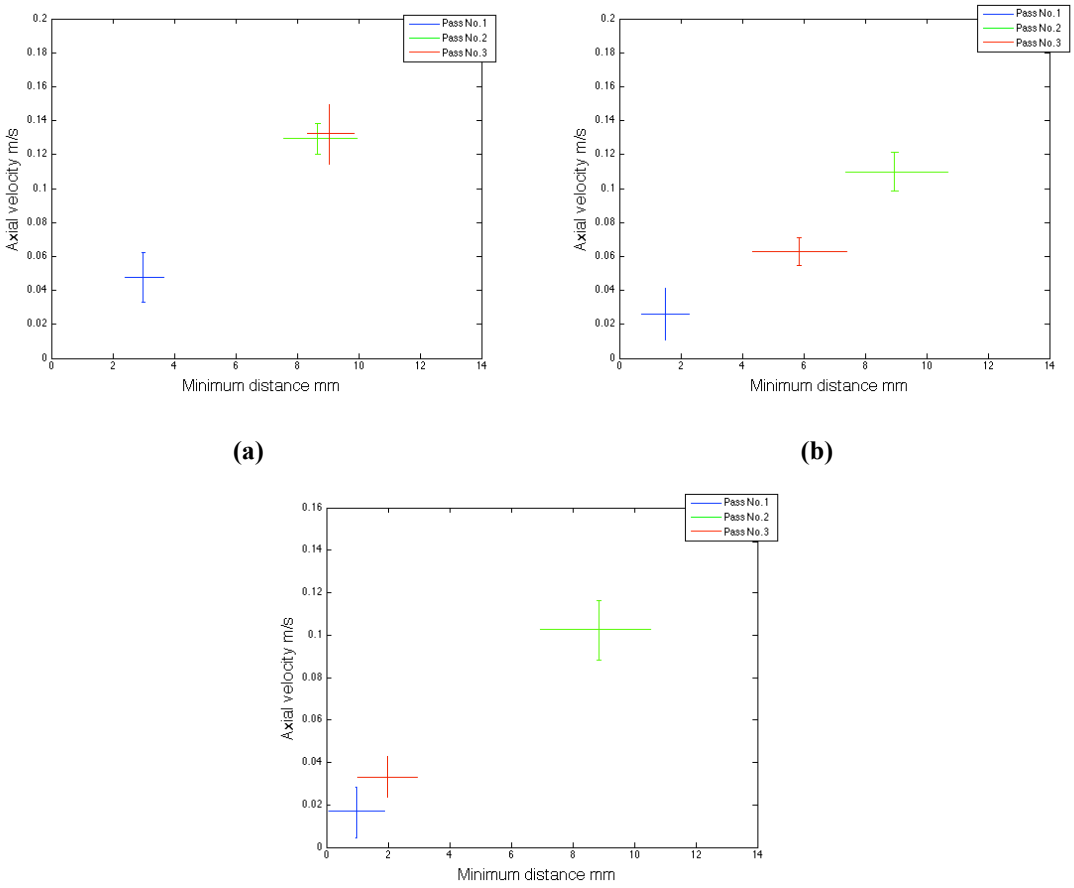

Figure 4.3. Axial velocity vs. the minimum distance to the solid boundaries for the same three passes for: (a) 2nd element; (b) 3rd element; (c) 4th element.

By passing through the fourth element, its average distance decreases to 1 *mm* with the average axial velocity around 0.02 *m/s*, which is lower than in the previous element. The results from Figure 4.2 and Figure 4.3 show that, by increasing the distance to the solid boundaries, the axial velocity of tracer increases as expected.

4.3 Studying the velocity

4.3.1 Choosing the grid

There are a number of factors which increase the possibility of breaking the tracer and causing the leakage of the radioactive material from the tracer to the fluid. During the

experiments, it was observed that, at a high gear pump speed, the tracer was smashed between the gears more often. Hence, the highest speed of the pump, at which the tracer would not be broken, was chosen to pump the fluid through the mixer. The superficial velocity of the fluid inside the mixer was measured as 0.1 *m/s*, which is the highest velocity at which the pump could have operated without damaging the tracer.

In this section, the Eulerian velocity maps, which are calculated according to the procedure as described in § 3.3.3, are presented.

The grid that is used to calculate the Eulerian velocities consists of 275 cells in the axial direction. This number is estimated by choosing different number of cells and comparing the results to find out the optimum number of cells at which the quality of the image is acceptable.

Figure 4.4 shows the normalised axial velocity map located in the transitional region between the second and third element, as a function of different cell size. The axial length of each cell is a function of the number of cells on the grid, and this could affect finding the exact location of the elements. For example, in Figure 4.4(e), the length of each cell in axial direction is 10 *mm*, meaning this graph shows the velocity changes within 10 *mm* in the axial direction. Hence, the transitional region between the second and third elements is located somewhere within a 10 *mm* long cell. Consequently, by decreasing the size of each cell, locating the exact position of the transitional region becomes more accurate.

The final value of velocity, which is assigned to each cell, is calculated§ from the average velocity of all the recorded points located in the cell. By decreasing the cell size, the final value of velocity would become closer to the real velocity in the system; therefore it is desirable to choose a cell with the minimum possible length. In this case,

considering the localisation error of positron emission particle tracking (PEPT), which is between 1-1.5 *mm* (Leadbeater et al., 2012) the smallest size for the cell would be 2 *mm*. However, if the number of passes is not high enough to cover the whole geometry, by decreasing the length of each cell, the quality of the final graph of the velocity map will be decreased, showing a high number of blank cells. This is a consequence of having cells which contain no recorded data points. This issue could be observed by comparing the number of blank cells in Figure 4.4(a), which has a cell size of 2 *mm*, with Figure 4.4(e) with the cell size of 10 *mm*. The comparison shows that, by increasing the length of the cell, the number of the blank cells decreases; therefore the quality of the image becomes better. Eventually, it was decided to choose the cell size of 4 *mm*, which is a compromise between accuracy and image quality.

A MATLAB code was then developed in order to interpolate the data in the axial direction. Going through all the data points, if the distance between each two consecutive point was more than 1 *mm,* a linear interpolation was used until the distance between the points decreases to 1 *mm*. After defining the grid and calculating the Eulerian velocities, it is possible to plot the velocity maps at any location along the mixer.

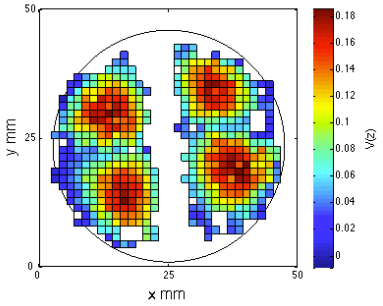

(a) Axial length of the cell =2 *mm*

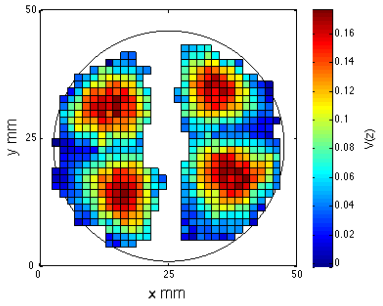

(b) Axial length of the cell =4 *mm*

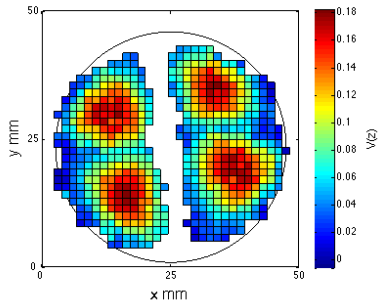

(c) Axial length of the cell = 6 *mm*

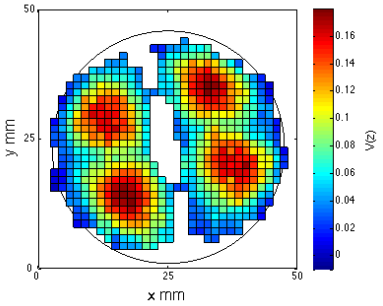

(d) Axial length of the cell = 8 *mm*

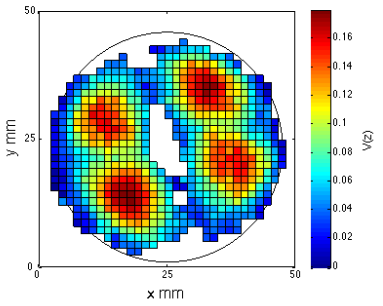

(e) Axial length of the cell = 10 *mm*

Figure 4.4. Effect of changing the axial length of the cell in the axial direction on the Eulerian velocity map. Normalised axial velocity at the cross-section of the start of the 3rd element with the axial cell size of (a) 2 *mm*; (b) 4 *mm*; (c) 6 *mm*; (d) 8 *mm*; (e) 10 *mm*.

4.3.2 Studying the existence of steady velocity through the cells

The final value of velocity assigned to each cell is calculated by getting the arithmetic average of the velocity of all the recorded data point in that certain cell. In this section, the relationship between the numbers of recorded location (data points) in each cell versus the final computed value of the velocity is investigated. The value of the velocity in each cell should be calculated over a sufficient number of locations, for it not to diverge if more locations are considered.

For this study, four representative cells have been chosen and are shown in Figure 4.5. Two of these cells are located in the area of high velocity of the flow; meanwhile another two are positioned near the wall, where the velocity is the lowest. Specifically shown in Figure 4.5, cell No.1 represents the area around the inner wall of the pipe, cell No.2 represents the area with highest velocity between the solid boundaries of the mixer, cell No.3 belongs to an area between the solid boundaries on the other side of the blade, and cell No.4 shows the area close to the inner wall of the pipe on the other side of the blade.

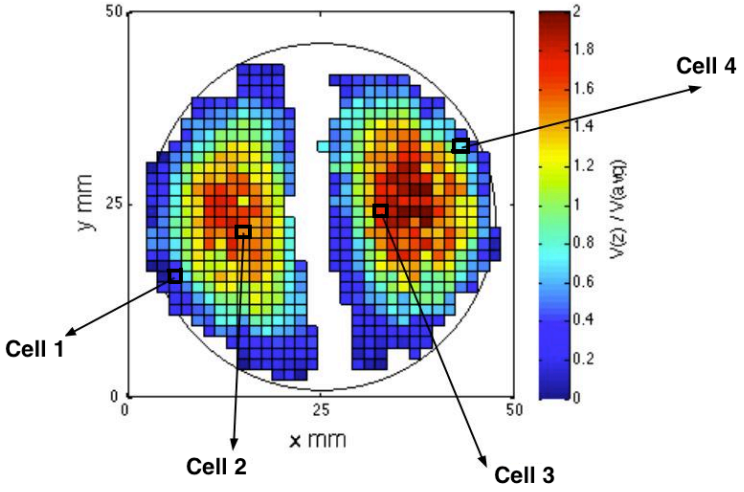

Figure 4.5. Location of four different cells with the cross-section of the mixer in the middle of the third element.

The running average of the velocity of all the passes though the selected cell is plotted versus the cumulative number of passes considered. If the number of locations used to calculate the velocity is sufficient, the average velocity should converge to a constant value.

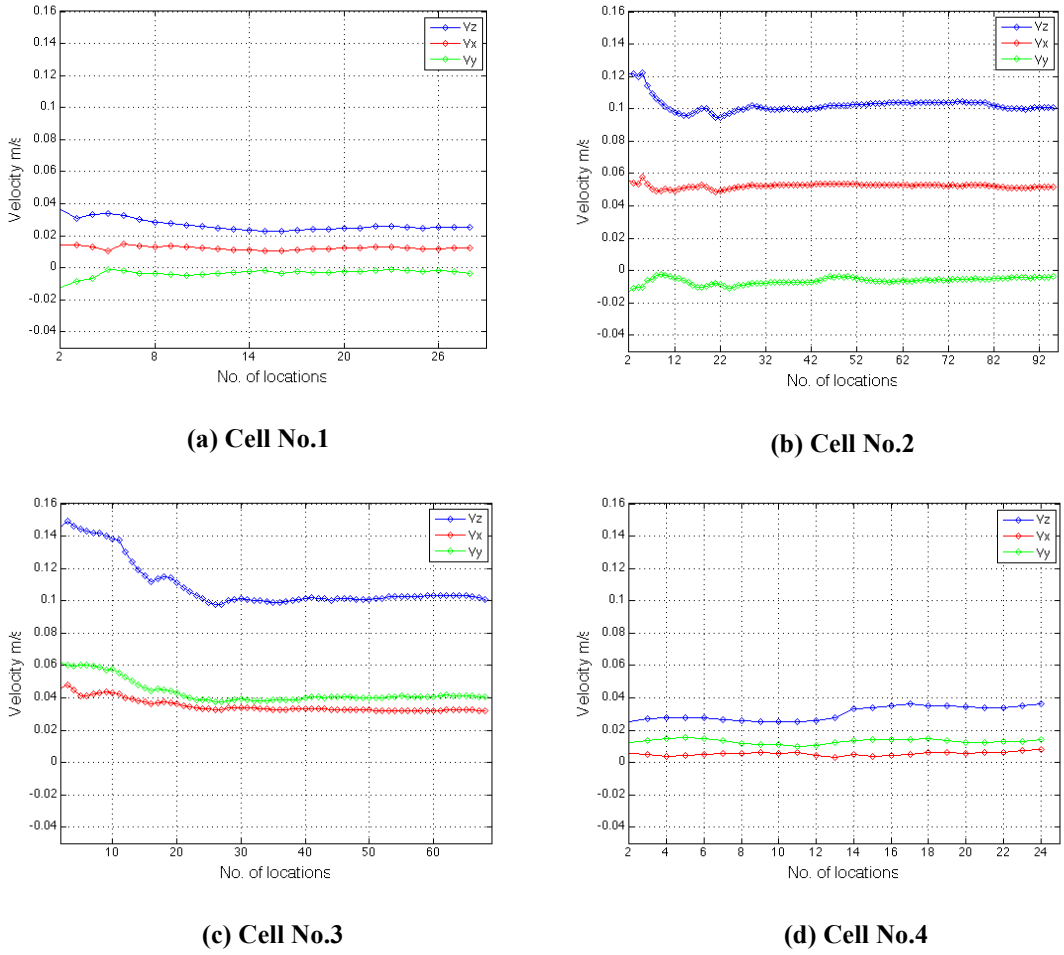

(a) Cell No.1

(b) Cell No.2

(c) Cell No.3

(d) Cell No.4

Figure 4.6. Effect of changing the number of locations on the calculated velocity in different directions for (a) cell No. 1; (b) cell No.2; (c) cell No.3; (d) cell No.4.

As shown in Figure 4.6(a), 28 locations are found within cell No. 1. The average value of the three velocity components appears to stabilise when > 14 locations are used. According to Figure 4.6(b), the average velocities are calculated over 93 locations, which is higher than the number of locations in Figure 4.6(a). This is due to the fact that the position of cell No.2 has a higher distance to the solid boundaries of

the system in comparison with cell one and, consequently, more fluid is passing through this area. Hence, the number of recorded location within cell No.2 is higher than cell No.1. Figure 4.6(b) shows that all the average velocities stabilise after 32 locations, which is higher than the minimum sufficient number of locations for cell o No.1. This is due to the existence of a higher velocity in cell No.2, which causes to calculate the value of the velocities for higher volume of fluid. Therefore, it is necessary to have a greater number of locations to reach a steady velocity. Using the same explanation for Figure 4.6(c) and (d), the standard deviation of the velocity components for each cell is shown in Table 4-1.

Table 4-1. Standard deviation of three velocity components for different cells.

Cell number	**Average u_z $m.s^{-1}$**	**Average u_y $m.s^{-1}$**	**Average u_x $m.s^{-1}$**	**u_z standard deviation**	**u_x standard deviation**	**u_y standard deviation**
Cell No.1	0.021	-0.01	0.019	0.0054	0.0014	0.0031
Cell No.2	0.1	-0.005	0.05	0.0052	0.0014	0.0023
Cell No.3	0.11	0.045	0.038	0.0026	0.0043	0.0073
Cell No.4	0.03	0.01	0.005	0.0037	0.0042	0.0041

Table 4-1 shows that the standard deviation of all the velocity components for all the cells is in the order of 10^{-3} *m/s*, which makes it possible to say that all the velocity components seems to be steady. Considering the results in Table 4-1 and Figure 4.6, it is concluded that the value of velocity in each cell is calculated over a sufficient number of locations, and increasing the number of passes would not change it.

4.3.3 Studying the velocity maps in the Cartesian reference system

Figure 4.7 shows the normalised axial velocity map in the cross-section at various axial locations along the elements of the mixer. Due to the manufacturing tolerances, the alignment of two consecutive elements is not always exactly 90^{o}, as discussed before (§3.2.1.1). The velocity maps produced in this work are therefore highly relevant to the common industrial applications of this type of mixer. As shown, after each transitional region, four velocity zones are created. These four velocity zones join together, creating two velocity zones by the middle of the element. Towards the end of the mixer, the quality of the image decreases significantly (Figure 4.7 (l)) as a consequence of the lack of recorded data points. This is due to the fact that the probability of a successful detection of the tracer is the highest in the centre of the camera, and it decreases further away from the centre of it (Guida et al., 2009).

Therefore, to study the development of the velocity profile along each element in more detail, it was decided to study the velocity maps along two consecutive mixing elements, representing the behaviour of the fluid in each mixing unit along the mixer. Subsequently, considering that the highest number of detected locations of the tracer belongs to the centre of the camera, where the third and the fourth elements are located, these elements were chosen for further study. The significant effect of developing the fluid along each element can be observed by examination of the velocity map at different cross-sections in Figure 4.8.

Figure 4.8 shows the normalised average axial velocity for the cross-section within the third and fourth mixing elements relative to their axial coordinates of z = 0, 1/8 L, 1/4 L, 1/2 L, 3/4 L, and L, with L being the element length. The value of the axial velocity is normalised by the value of the superficial velocity.

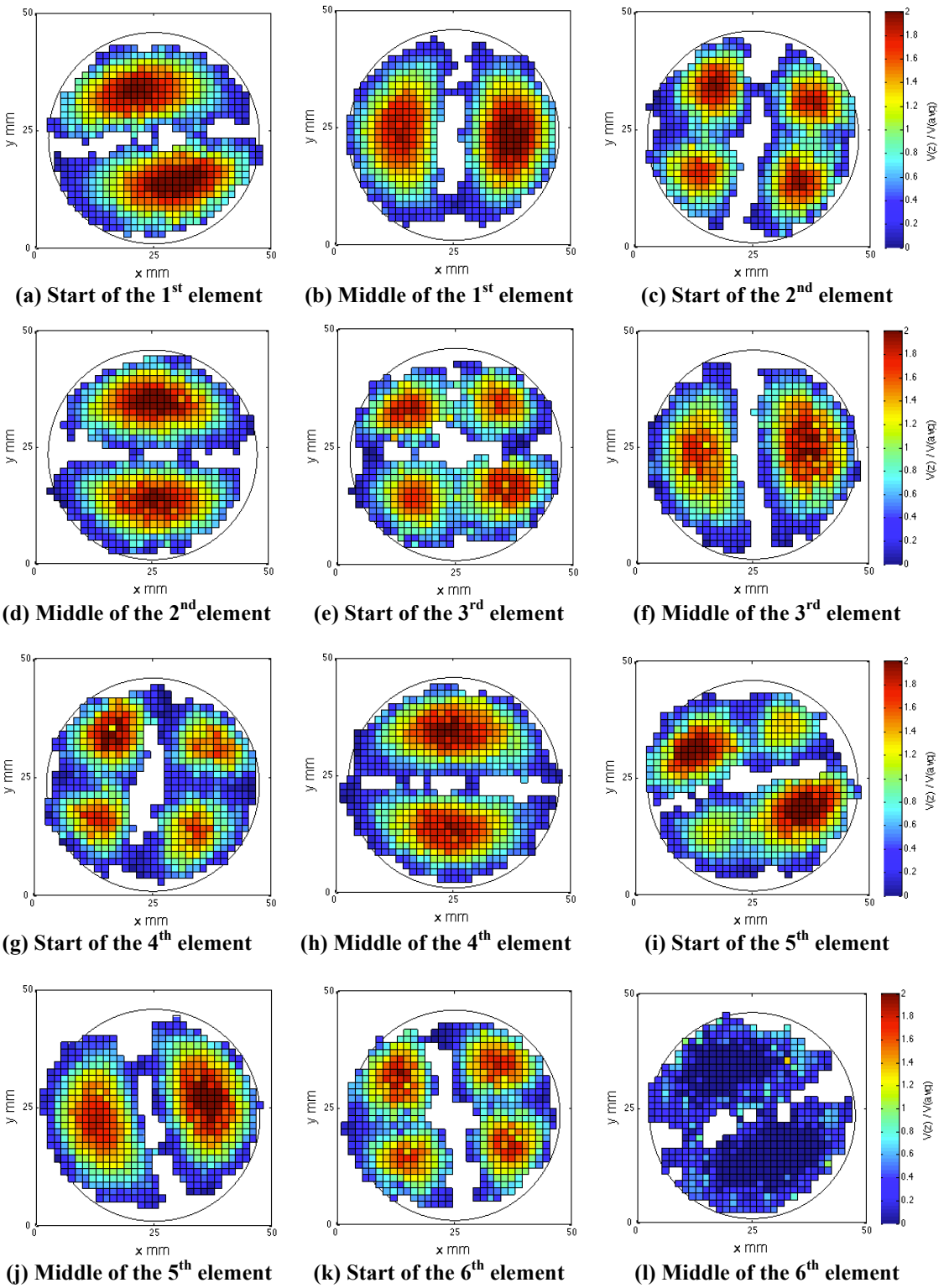

(a) Start of the 1st element (b) Middle of the 1st element (c) Start of the 2nd element

(d) Middle of the 2nd element (e) Start of the 3rd element (f) Middle of the 3rd element

(g) Start of the 4th element (h) Middle of the 4th element (i) Start of the 5th element

(j) Middle of the 5th element (k) Start of the 6th element (l) Middle of the 6th element

Figure 4.7. Normalised axial velocity map along the mixer at different cross-sections located at: (a) start of the 1st element; (b) middle of the 1st element; (c) start of the 2nd element; (d) middle of the 2nd element; (e) start of the 3rd element; (f) middle of the 3rd element; (g) start of the 4th element; (h) middle of the 4th element; (i) start of the 5th element; (j) middle of the 5th element; (k) start of the 6th element; (l) middle of the 6th element.

In the transitional region of both elements, the fluid is divided into four sections, which are diagonally symmetric. For $0 < z < 1/8\ L$, the velocity profile is still under the influence of the transitional region, i.e., the velocity profile looks flatter. By going further through the element, no significant change is observed for $1/4\ L < z < 3/4\ L$. For $z = 1/2\ L$ the fluid has a maximum peak in velocity at the furthest distance from the solid boundaries of the geometry (the inner wall of the pipe, and the blade). Towards the inner wall of the pipe, the velocity decreases significantly as expected. For $3/4\ L < z < L$, the shape of the velocity profile changes as a consequence of getting closer to the next transitional region.

The velocity profiles show the fluid on each side of the blade is dividing into two sections, which become completely separate in the transition region at $z = L$, which is also similar to $z = 0$ for the next mixing element. By comparing the velocity maps of element three and four, it is concluded that the behaviour that was described above is the same for both elements. Hence, the only difference between the velocity maps of these two elements is the opposite direction of the twist, which it does not seem to affect the velocity maps.

3rd element	4th element

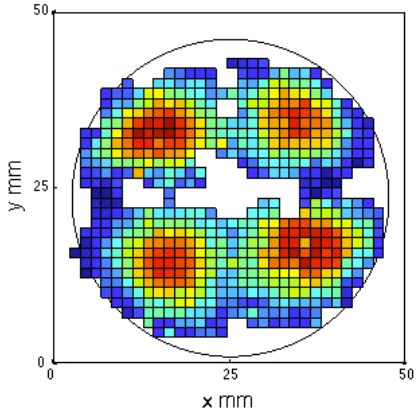

(a) $z = 0$

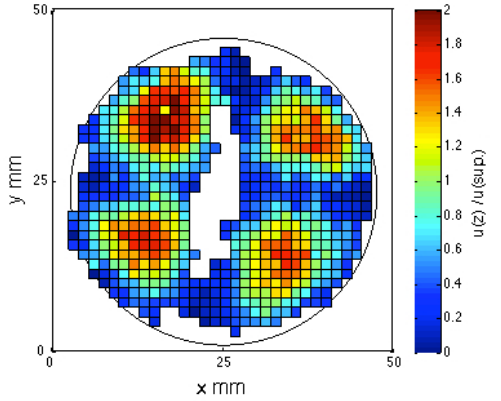

(g) $z = 0$

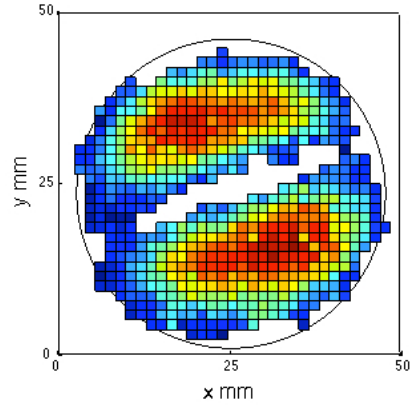

(b) $z = L/8$

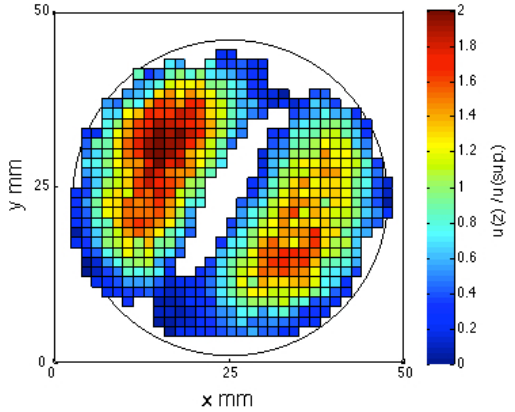

(h) $z = L/8$

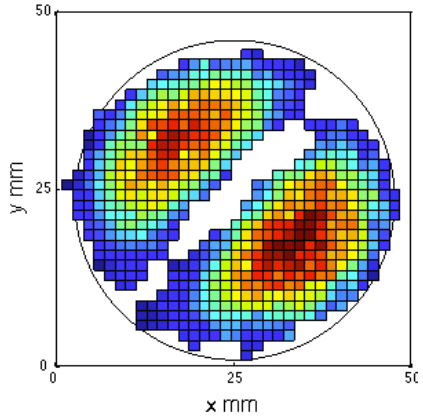

(c) $z = L/4$

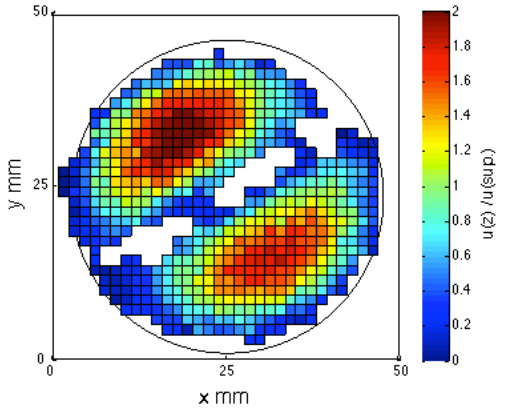

(i) $z = L/4$

Continued on the next page

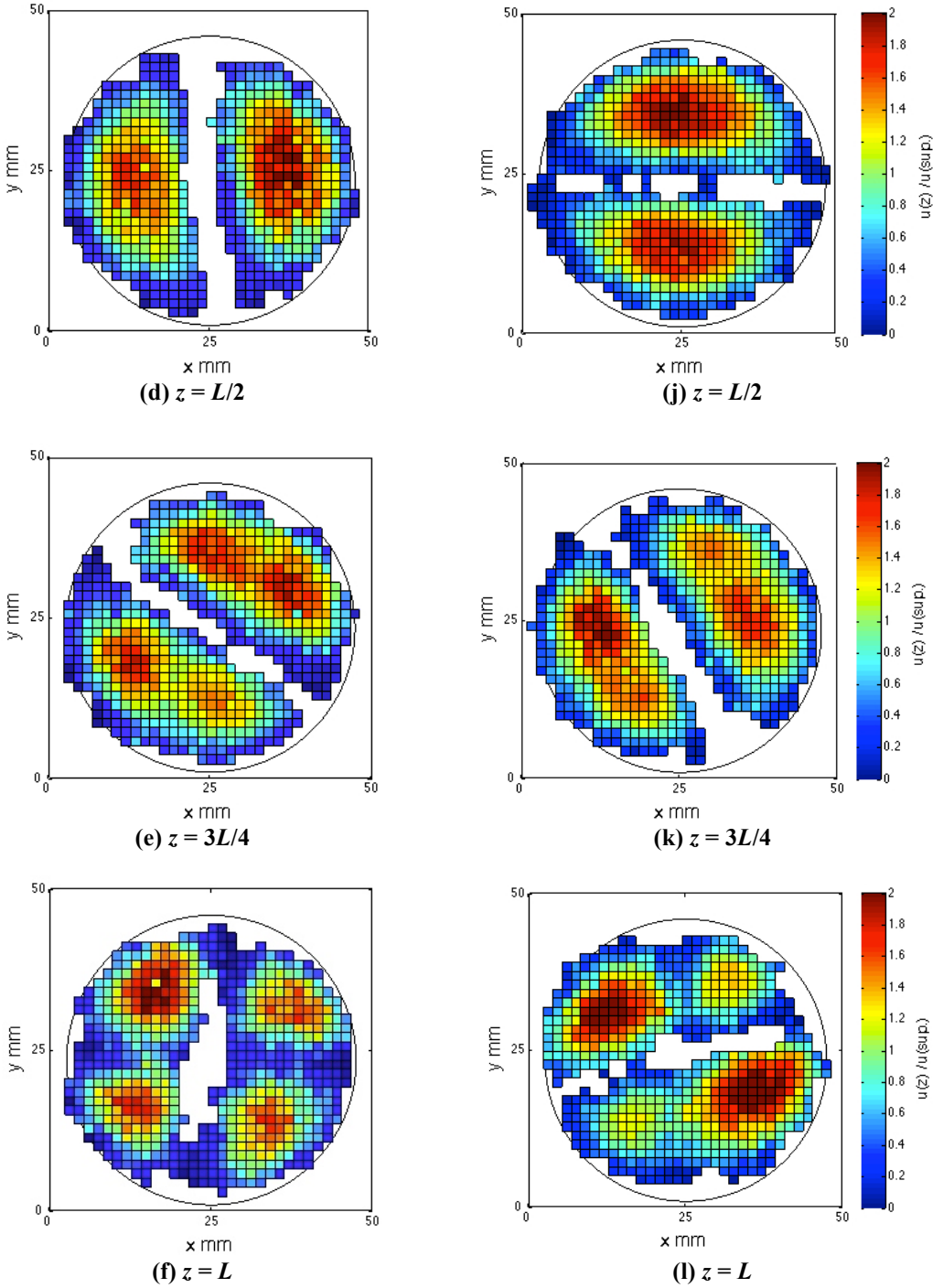

Figure 4.8. Normalised axial velocity map along the mixer at different cross-sections along (a-f) 3rd element; (g-l) 4th element. *L* is the length of the element.

Hobbs et al. (1998) showed a similar result using computational fluid dynamics with a Newtonian fluid and a similar viscosity to glycerol, using a lower axial velocity (0.002 *m/s*), with a Reynolds number of 0.15 (Figure 4.9).

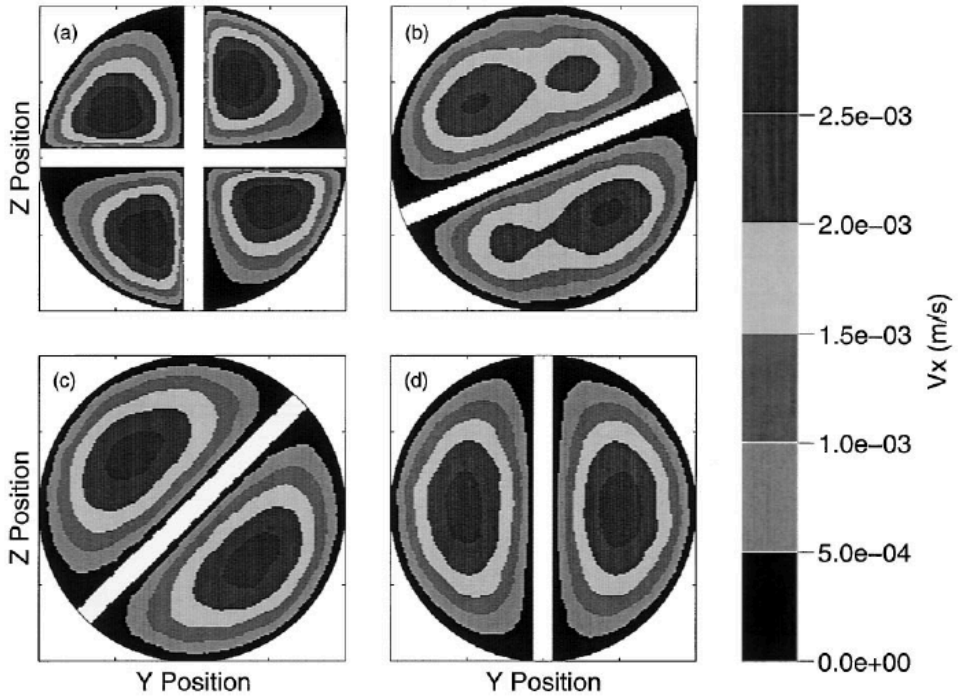

Figure 4.9. Contours velocity maps along the third element, from (Hobbs et al., 1998) at: (a) x = 0; (b) $x = L/8$; (c) $x = L/4$; (d) $x = L/2$. x is in the direction of the axial length of the mixer .

Since the Reynolds number in this work is larger than the one used by Hobbs et al. (1998), the scale of velocity on these graphs cannot be compared to the one from the PEPT experiment; however, it is possible to compare the general behaviour and development of the velocity profile along the third element in both cases. Figure 4.9 shows the contour velocity maps along the third element of a Kenics mixer with the same geometry design as the one used in this work. The location of the velocity maps is the same as the one in Figure 4.9 (with the x coordinate in the axial direction), located at $x = L/8$, $x = L/4$, and $x = L/2$. As shown in Figure 4.9(a), the fluid is divided into four sections on the transitional region, and the transitional region effect could be

observed at *L/8*. The asymmetric shape of the velocity zones at $x = L/8$ on each side of the blade in Figure 4.9(b) is similar to the result presented in Figure 4.8(b). A constant shape velocity profile could be seen between $L/4 < x < L/8$, as well as the maximum value of velocity in the middle of the area between two solid boundaries, which is in agreement with the results in Figure 4.8.

Figure 4.10 presents vector plots used to study the velocity fields relative to the x and y components. The vector plots are intended to provide a further understanding of the velocity field in both the x and y direction. The vector plots are overlapped with the contour maps of the velocity for all the fluids. The colour intensity on the contour plots therefore represents the length of the vectors, given by $|U|$, which is calculated using Equation 4.5:

$$|U| = \sqrt{\left(\frac{u_x}{u_{avg}}\right)^2 + \left(\frac{u_y}{u_{avg}}\right)^2} \qquad \textbf{(Equation 4.5)}$$

Considering the counter-clockwise twist of the blade, it is possible to observe the direction of the fluid movement in Figure 4.10, which shows a counter-clockwise movement as expected. The transitional region effect could be observed at $z = 0$, showing the higher velocity within two quarters of the cross-section. For $L/8 < z < L/2$, the length of the vectors increases by moving away from the solid boundaries, indicating increased velocity. The velocity vectors look symmetrical on each side of the blade. Towards the next transitional region, it could be observed that the vectors with higher velocity move towards the corner between the blade and the inner wall of the mixer.

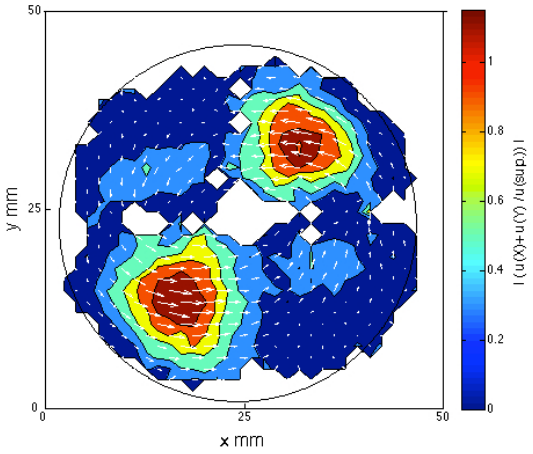

(a) $z = 0$

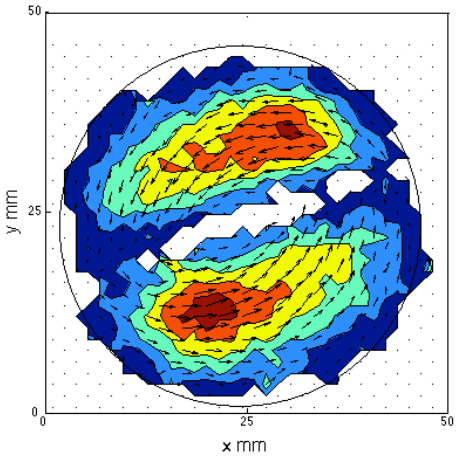

(b) $z = L/8$

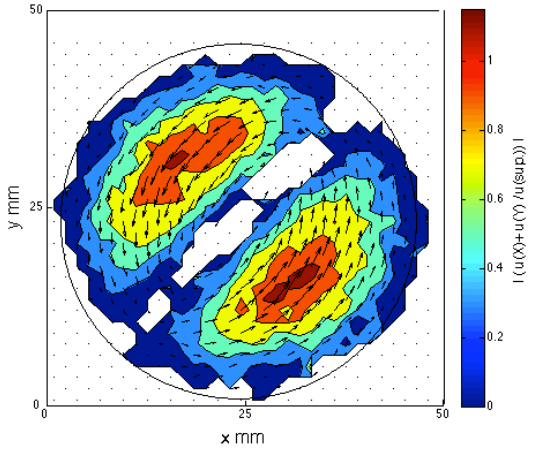

(c) $z = L/4$

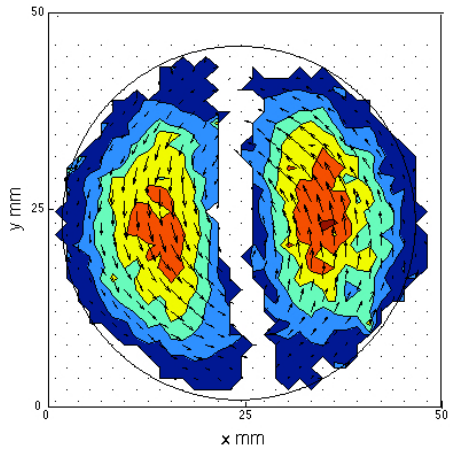

(d) $z = L/2$

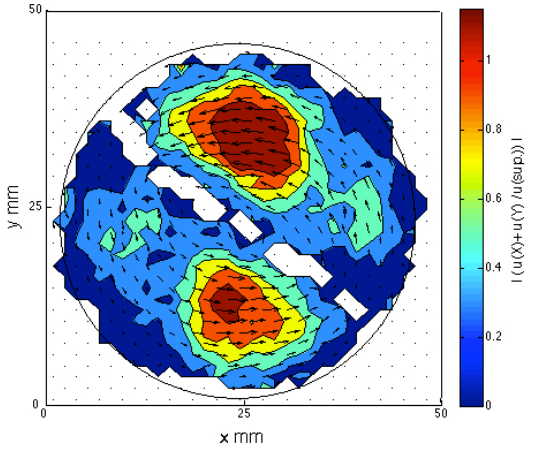

(e) $z = 3L/4$

Figure 4.10. Velocity vector plots of *x*- and *y*- velocity components along the 3rd element.

4.4 Shear rate

The shear rate is calculated from the velocity field, according to Equation 3.10, which was described in §3.3.4. Figure 4.11 shows the shear rate map through the third and fourth elements.

The effect of the transitional region could be observed by comparing the shear rate maps located at $z = 0$, and $L/4 < z < L/2$. For $L/4 < z < L/2$, the area around the solid boundaries of the mixer for both elements have the highest value of shear, which is between 25 to 40 s^{-1}. This is due to the high gradient of velocity close to the solid boundaries of the system. Consequently, the lowest value of shear rate is found in the area between the solid boundaries of the system, where the gradient of velocity is lower. Figure 4.11(g) and (h) show the shear rate map is become less uniform at $z = 3L/4$ as a result of the changes in the velocity when getting closer to the next transitional region.

3rd element	4th element

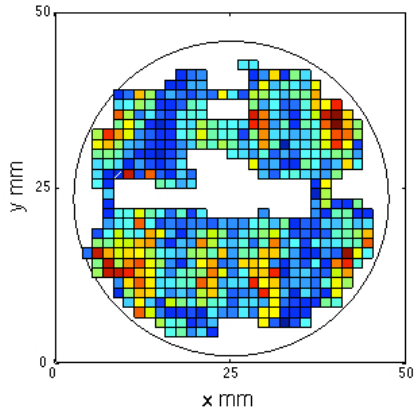

(a) $z = 0$

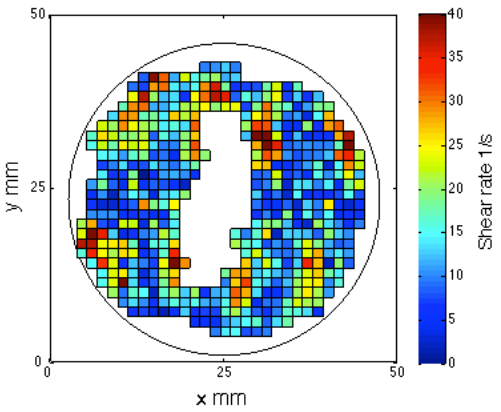

(b) $z = 0$

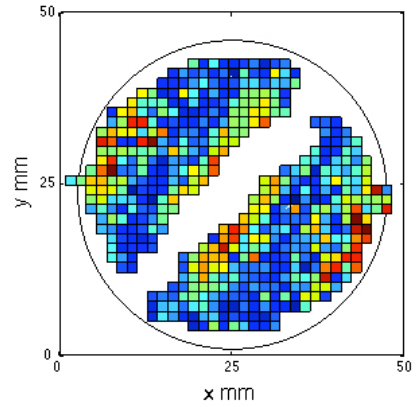

(c) $z = L/4$

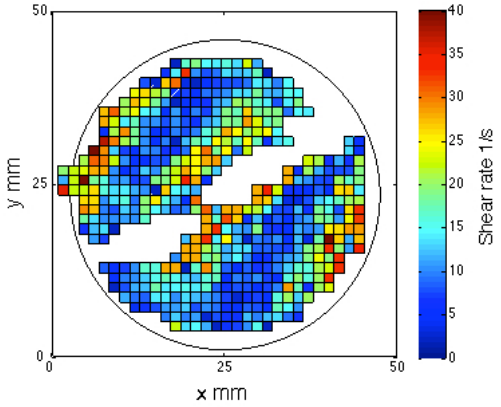

(d) $z = L/4$

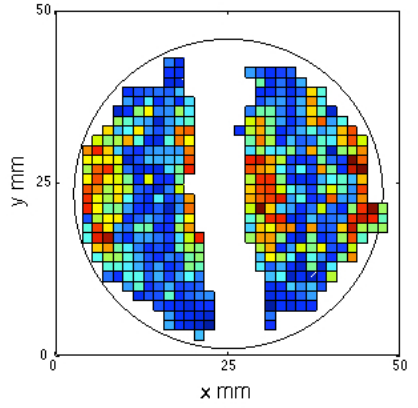

(e) $z = L/2$

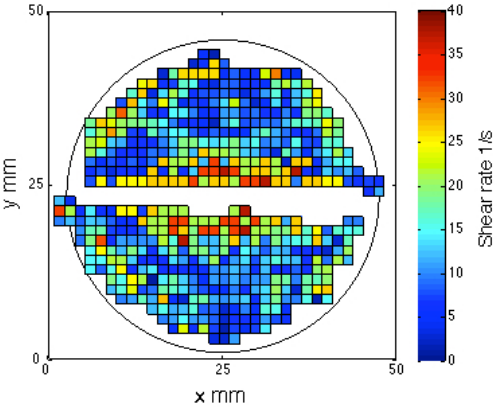

(f) $z = L/2$

Continued on the next page

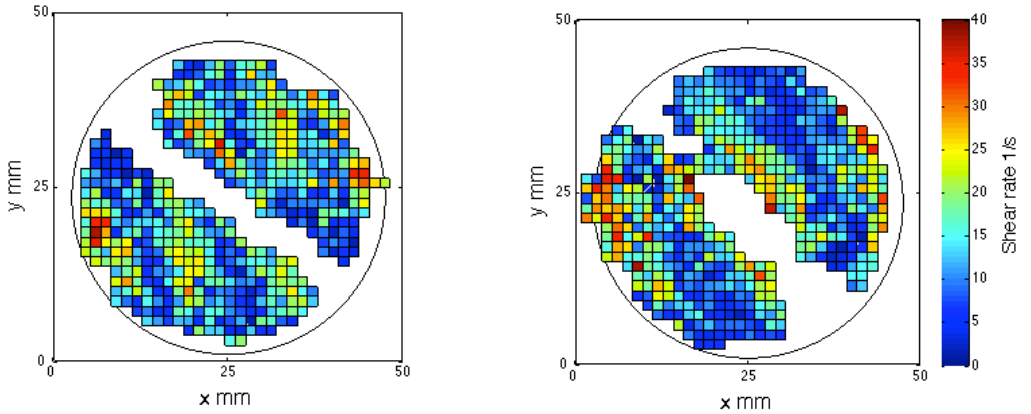

(g) $z = 3L/4$ **(h)** $z = 3L/4$

Figure 4.11. Shear rate maps along the 3rd and 4th elements located at: (a-b) $z = 0$**; (c-d)** $z = L/4$**; (e-f)** $z = L/2$**; (g-h)** $z = 3L/4$**.**

4.5 Studying the mixing performance

In this section, two different techniques are introduced to study the mixing performance of the system. In the first section, mixing is characterised by using the coefficient of variance (CoV). In the second part, the mixing performance is studied by using the concept of segregation index.

4.5.1 Characterisation of mixing by using the coefficient of variance

In this section, the result of characterising mixing by using the technique described in §3.3.1 is presented. As mentioned before, the particles are classified into two groups - blue and red - according to their entrance position. The movement of blue and red particles amongst each other and therefore the creation of striations are shown on the animation file *KM-180-Glycerol.mov* which can be found on the attached CD at the end of the thesis.

As mentioned before, the geometry was divided into a number of cells in order to calculate the CoV. Considering the localisation error of PEPT, which is around 1-1.5 *mm,* it was decided to choose the length of each cell in axial direction as 2 *mm*. The cross-section of the mixer is divided into six sectors, with a size of 30°.

Figure 4.12 shows the distribution of red and blue particles along the first element. It was decided to choose the feeding system normal to the blade, meaning the border between the blue and red groups is normal to the blade at the entrance of the mixer. This feeding system is one of the most common methods used in industry and in the literature.

Figure 4.12 (a) presents the distribution of blue and red particles at the entrance of the mixer. The borders of each sector are shown with a blue line. In order to follow the rotation of the grid along the first element, one of the borderlines is shown as black. By passing through the first element, the number of striations changes from two to four. Figure 4.12(b-d) shows the rotation of the striations for $L/4 < z < 3L/4$, with L being the length of the element. By entering the transitional region between the first and second element at $z = L$, the striations are getting cut by the blade of the second element.

Figure 4.13 presents the changes of the CoV with respect to the initial value of the CoV along the mixer (normalised CoV). The initial value of CoV is the value of CoV at the entrance of the mixer, and could be different than 1 considering some cells are located on the blade. The axial location of each point is being normalised by the length of the element. By passing through the first element, the CoV decreases continually, and by the end of the first element, the value of the CoV decreases by nearly 0.65, reaching to 0.35. From the second element, it is observed that the CoV

increases within the element, and decreases again by the end of the element. This behaviour can be seen for the rest of the elements as well. The reason for this behaviour will be described in §4.5.1.1.

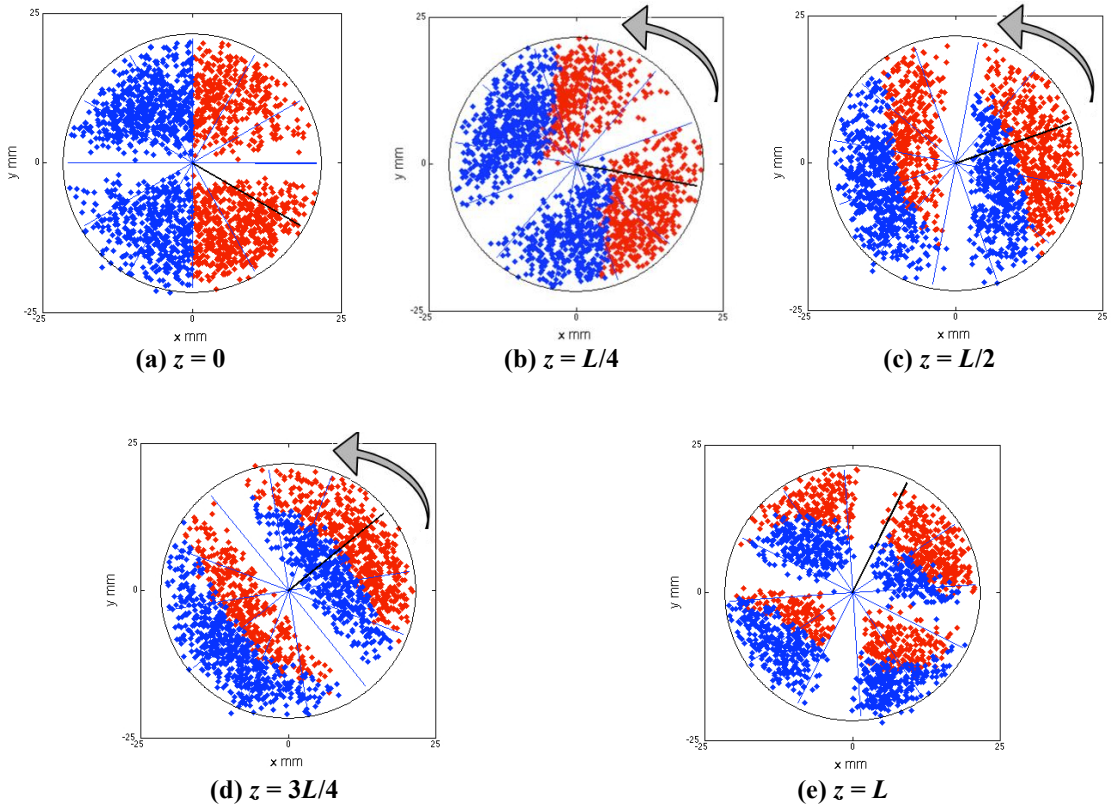

(a) $z = 0$ **(b) $z = L/4$** **(c) $z = L/2$**

(d) $z = 3L/4$ **(e) $z = L$**

Figure 4.12. Rotation of the fluid and the cells along the 1st element at: (a) $z = 0$; (b) $z = L/4$; (c) $z = L/2$; (d) $z = 3L/4$; (e) $z = L$. L is the length of the element. The blue lines indicate the border of the cells. The rotation direction along the element is shown with the grey arrow.

The rate of decreasing the value of the CoV through the first three elements is higher than the one for the last three elements. However, according to Figure 4.13, there are some locations along the mixer that despite being a distance from each other by one or two elements, have the same value of the CoV. This behaviour will be investigated in § 4.5.1.2.

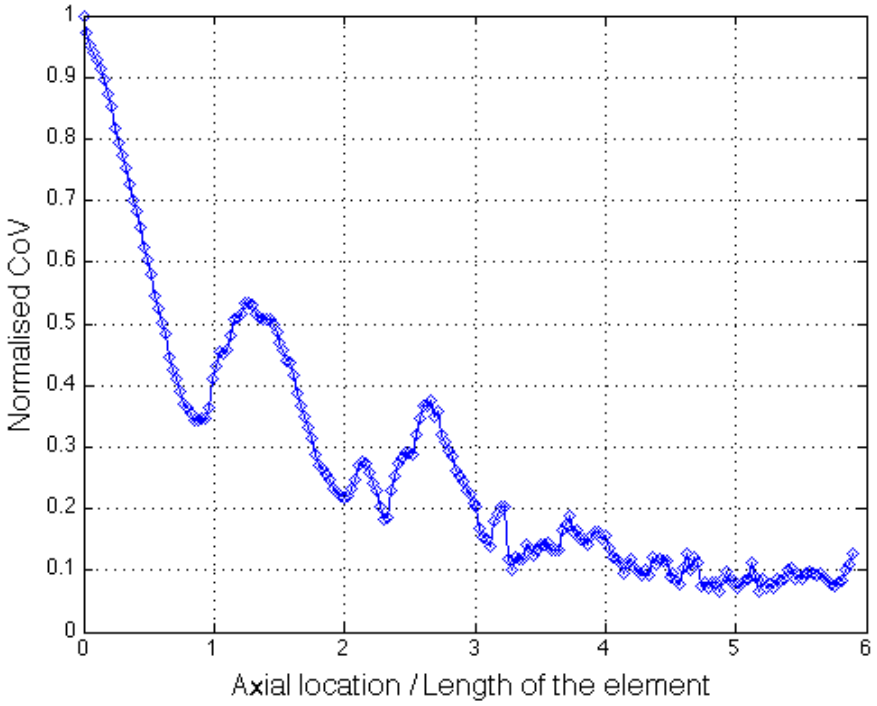

Figure 4.13. Changes of the normalised CoV along the mixer.

4.5.1.1 Investigating the changes of the CoV within one element

According to Figure 4.13, the values of the CoV oscillate, which is an unexpected phenomenon. A frame within the second element has been chosen to investigate this behaviour further. The range of the frame is chosen in a way that it contains both increases and decreases in the value of the CoV.

Figure 4.14(a) shows the changes of the CoV along the mixer, as presented before, by showing the area chosen to be investigated with the red rectangle.

The graph on the right hand side Figure 4.14(a) shows the area of the red rectangle with more detail. Considering the values of CoV spaced every 2 *mm* in the axial direction, it was decided to choose five points which could represent an increase and decrease in the value of the CoV within the chosen frame.

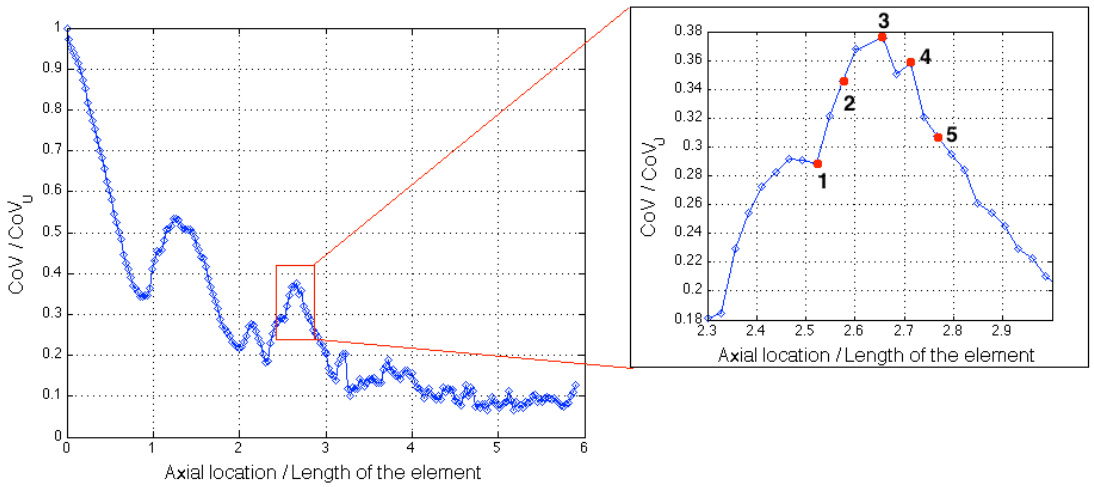

(a)

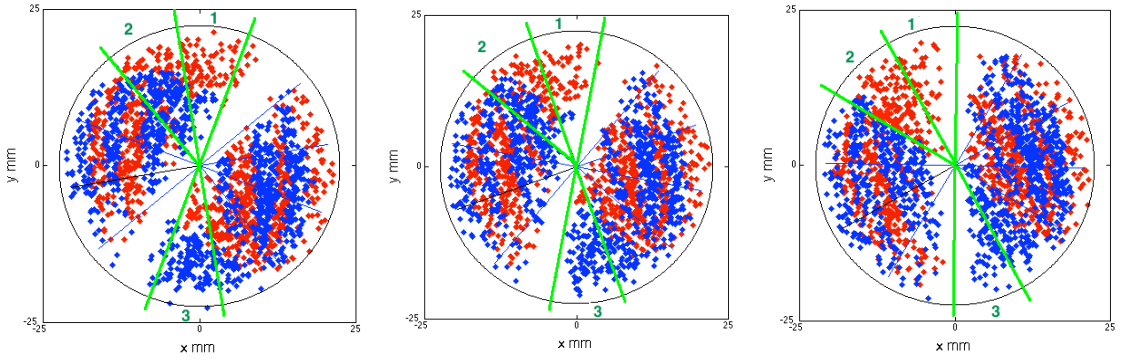

(b) **(c)** **(d)**

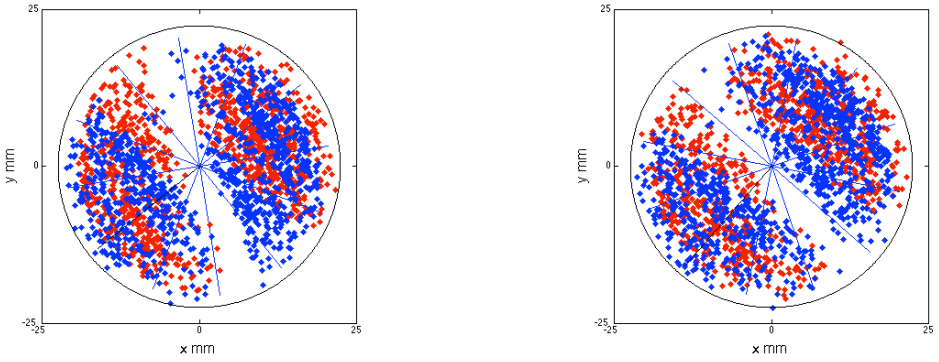

(e) **(f)**

Figure 4.14. Investigating increasing CoV between the 2nd and the 3rd element. (a) The red window frame indicates the area that has been investigated; five different points have been numbered; (b) Cross-section of the mixer located at point 1; (c) Cross-section of the mixer located at point 2; (d) Cross-section of the mixer located at point 3; (e) Cross-section of the mixer located at point 4; (f) Cross-section of the mixer located at point 5.

These points are numbered from one to five in Figure 4.14(a) with the distance of 4 *mm* between two consecutive points. The cross-section of the mixer at each point is then plotted in Figure 4.14(b-f).

Figure 4.14(b) shows the cross-section of the mixer at point one, and three specific sectors are labelled with a green border to highlight them. By moving to Figure 4.14(c), it can be observed that the number of blue particles within sectors one and two decreases, and the number of red particles decreases within sector three. Figure 4.14(d) shows the cross-section of the mixer at point three, which has the maximum value of the CoV. As it is shown, at this cross-section, sector one is completely red, most of sector two is red, and all the particles in sector three are blue. According to the CoV formula, a sector with a higher number of both blue and red particles is more mixed than the one which contains only blue or red particles. As a result, the value of the CoV increases for this cross-section. Following the same explanation, Figure 4.14(e) to (f) shows that the number of blue particles increases within the sectors which only contained red particles before and, consequently, the value of the CoV decreases for these cross-sections.

4.5.1.2 Investigating the locations with a similar CoV along *z*

Figure 4.15(a) shows the changes of the CoV along the mixer, with two red circles indicating the location of two points with the same CoV, but different locations along the axial length of the mixer. Point one is located within the first element, and point two is located within the third element. Figure 4.15(b) and (c) show the cross-section of the mixer located at points one and two. As shown, although the value of the CoV is similar for these two graphs, the striations thickness in Figure 4.15(c) are much smaller than the ones in Figure 4.15(b), showing a significantly better mixing of blue

and red particles. As mentioned before, the final value of the CoV in each cross-section is a function of the number of blue or red particles in all the sectors of each cross-section. The overall number of blue particles within each sector of these two cross-sections is plotted in Figure 4.15(d). In this figure, the number of the blue particles at different sectors of the cross-section of the mixer located at points one and two are shown as orange and green. For most of the sectors, the height of the orange and green columns are close to each other, indicating the number of blue particles in these sectors is similar within both cross-sections. Consequently, since the equation of the CoV is just a function of the number of particles in each sector, the final value of the CoV for these two different cross-sections becomes similar. This shows that characterising the mixing on PEPT experimental data by using the CoV does not include the changes of the scale of segregation or the striations thicknesses. Considering the localisation error of PEPT, it is not possible to have a quantitative measurement of the scale of segregation and striation thickness. It is, however, possible to observe the changes of striations by looking at the creation of red and blue striations along the mixer.

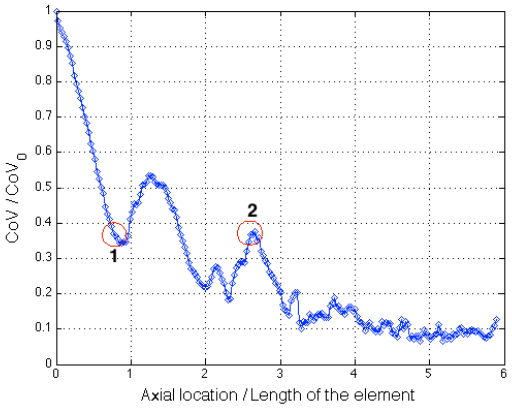

(a) The two points with the same CoV are shown with red circles.

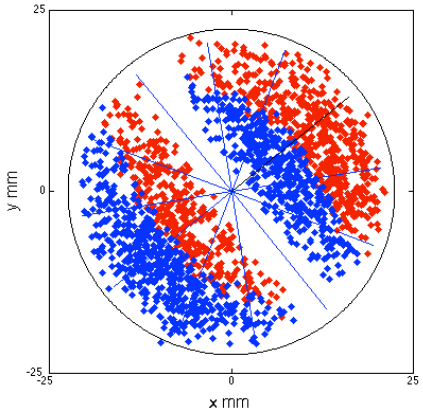

(b) Cross-section of the mixer located at point 1.

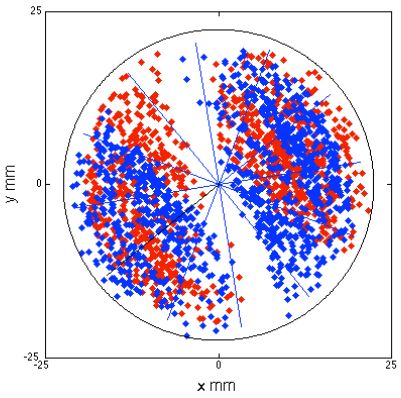

(c) Cross-section of the mixer located at point 2.

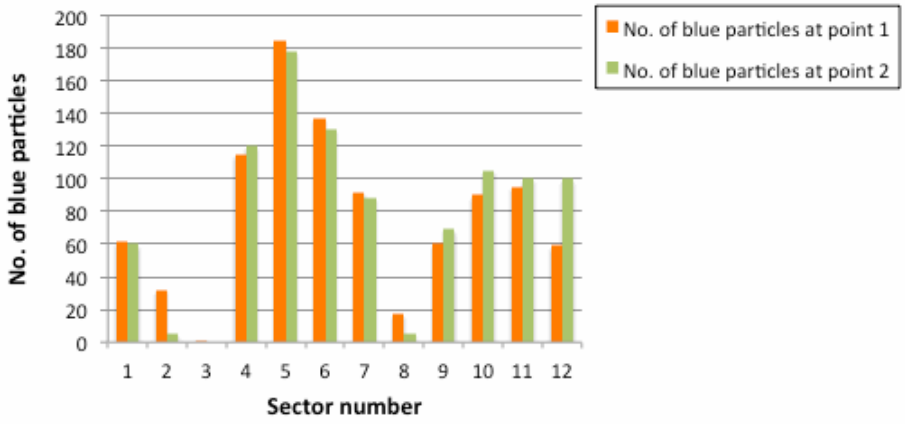

(d) Comparison between the number of the blue particles in each sector of the cross-section of the mixer located at point numbers 1 and 2.

Figure 4.15. Investigating different locations along the mixer with the same CoV.

Figure 4.15(a) also shows that the changes in the CoV after the fifth element are not as great as before, resulting in a nearly constant slope of the curve. It should be noted

that, towards the end of the mixer, the blue and red particles become more distributed. Hence, it is possible that the difference between the total number of the blue and red particles in each sector of two consecutive cross-sections is not as large as the ones in the first few elements, resulting in calculating two close values of the CoV.

In addition, another issue that should be considered is the effect of the PEPT localisation error on this analysis. As mentioned before, the location of all the particles is calculated within the range of ±1.5 *mm*. This variety in the location of the particles could become important at the borders of each sector towards the end of the mixer, where the blue and red particles are more distributed among each other. This means it is possible that some of the particles, which are considered to belong to one sector, should belong to the neighbouring sector.

4.5.1.3 Effect of different feeding configuration on CoV results

The effect of choosing different feeding and meshing configurations on the CoV was studied to investigate whether the before-mentioned issues also existed after these changes or not. The effect of choosing different feeding and meshing configurations on changes in the CoV along the mixer is shown in Figure 4.16. Two different feeding systems are considered: side-by-side feeding and circular feeding. For the circular feeding, blue and red particles are defined at the entrance of the mixer within circles with different radius. The change in the CoV along the mixer is calculated for each configuration, shown in Figure 4.16(a-d).

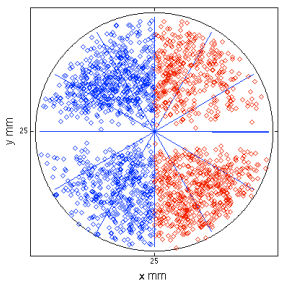

(a) Side-by-side feeding - sector cells

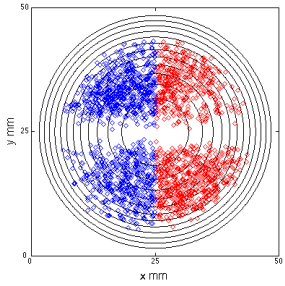

(b) Side-by-side feeding – circular cells

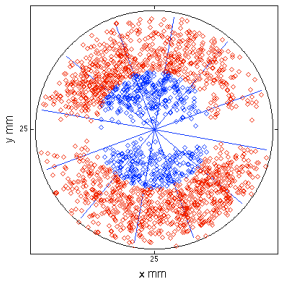

(c) Circular feeding – sector cells

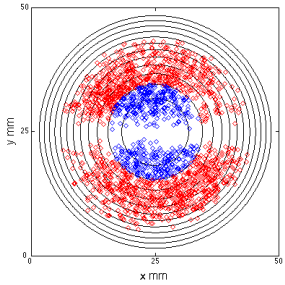

(d) Circular feeding – circular cells

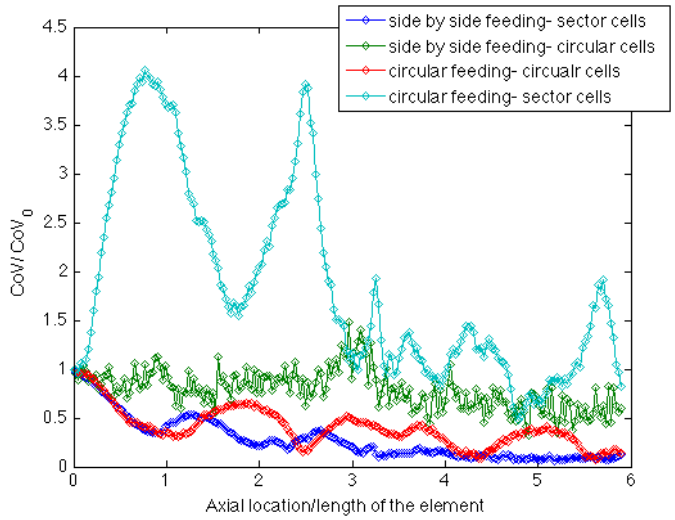

(e) Changes in the CoV for all the combinations of different feeding systems and cells

Figure 4.16. Effect of combining different meshing and feeding systems on the changes in the CoV along the mixer.

Both side-by-side feeding with sector cells and circular feeding with circular cells follow each other closely along the first element. The behaviour of side-by-side feeding with sector cells has been described before in detail. The value of the CoV

increases and decreases within a single element for circular feeding with circular cells, which was observed for side-by-side feeding as well. The final value of the CoV after six elements is the same for both configurations. Using the circular feeding with sector cells and side-by-side feeding with circular cells results in having cells which contain both blue and red particles at the start of the mixer. By going through the first element, some cells ended up containing just blue or red particles and, consequently, the value of the CoV increases for circular feeding with sector cells. Figure 4.16(e) shows that using circular feeding with sector cells and side-by-side feeding with circular cells does not change the existence of the two main issues mentioned regarding calculating the CoV.

Considering all the issues discussed in this section, using this technique with the PEPT data could have some limitations: not showing the effect of decreasing the striations thickness and scale of segregation, and being highly sensitive to the number of particles.

4.5.2 Characterising the mixing by using the segregation index

In this section, mixing is characterised by adopting a technique, which was previously used by Stambaugh et al. (2004) and Marigo et al. (2012) on DEM numerical simulation. In the first part of this section, a general description of this technique is presented, followed by the discussion of the results. In the second part, the effect of using different feeding arrangements on the changes of segregation is studied.

4.5.2.1 Description of the technique to calculate the segregation

The particles are classified into two different colours - blue and red - according to their entrance location as described in §4.5.1. Figure 4.18(a) presents the cross-section at the start of the mixer, showing the blue and red particles.

The MATLAB code, *segregation_index.m*, was written in order to calculate the changes of the segregation index through the mixer. First, the distances of all the particles from each other are calculated. For each particle, the closest neighbour is then chosen by comparing all the calculated distances from the rest of the particles. If a particle and its closest neighbour are both labelled as blue, they are counted as a 'blue-blue' contact and, if they are both red, they are counted as a 'red-red' contact. Using a similar definition, if the closest neighbour to a red particle is blue, they are counted as 'red-blue' contact and, if the closest neighbour to a blue particle is red, they are counted as 'blue-red' contact. By using the same definition as Stambaugh et al. (2004) and Marigo et al. (2012) segregation could be calculated by the following equation:

$$S = \frac{C_{RR}}{C_{RR} + C_{RB}} + \frac{C_{BB}}{C_{BB} + C_{BR}} \qquad \textbf{(Equation 4.6)}$$

where C_{RR}, C_{BB}, $C_{RB,}$ and C_{BR} are the red-red, blue-blue, red-blue, and blue-red contacts which have been counted from the previous stage. A group of particles are assumed to be uniformly mixed, when the number of the contacts between the particles of the opposite group starts to fluctuate around a constant number. For a completely segregated system, where C_{RB} or C_{BR} are equal to zero, the value of S is equal to two. For random mixtures, the value of S is assumed to be equal to one. For a specially ordered system, where there is no contact between the particles with the same colour (C_{RR}, C_{BB} = 0), the value of S is equal to zero. A schematic of all these

conditions is shown in Figure 4.18. $S > 1$ corresponds to an unstable state of segregation, and $S < 1$ indicates an ordered mixed system.

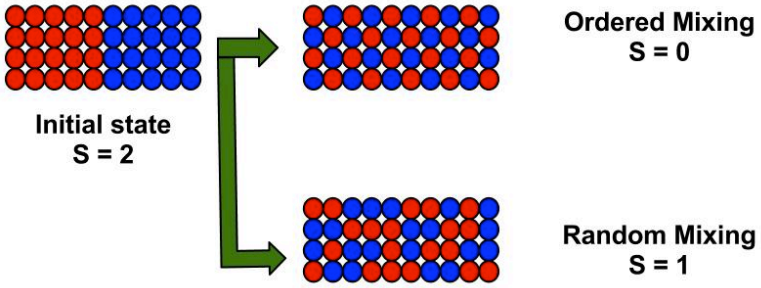

Figure 4.17.Graphical expression of different stages of segregation.

Figure 4.18(b) shows the changes in the segregation index along the mixer, calculated by Equation 4.6. The segregation index is decreasing from the first element until the end of the fifth element. By entering the sixth element, the segregation index starts fluctuating around one.

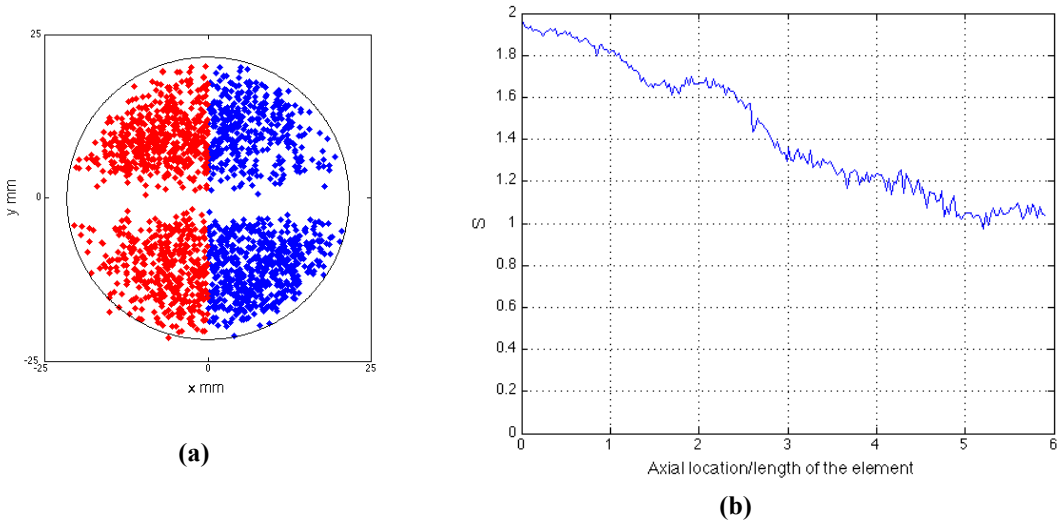

(a) **(b)**

Figure 4.18. (a) schematic of the feeding system used to calculate the segregation index; (b) changes of segregation along the mixer.

The effect of changing the number of passes on the segregation is shown in Figure 4.19.

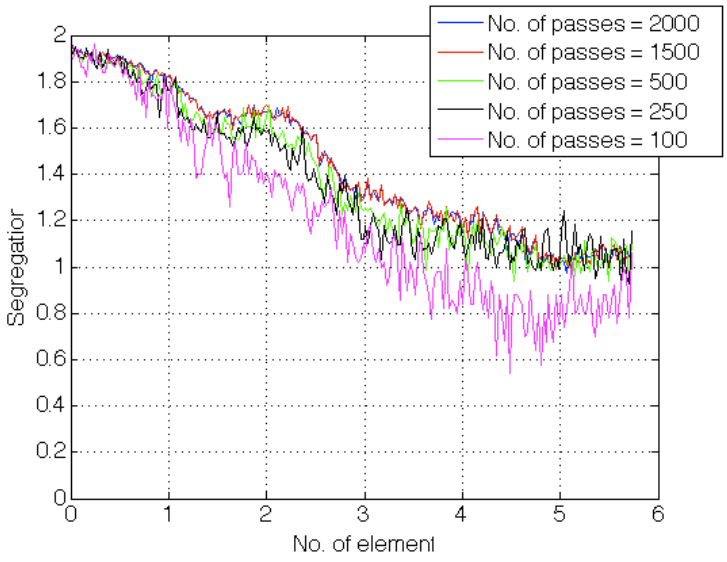

Figure 4.19. Effect of decreasing the number of passes on the changes of segregation along the mixer.

By decreasing the number of passes, the segregation curve shifts lower slightly, and the value of segregation decreases for the same axial location. However, this reduction in the value of segregation is not significant for using number of passes more than 250. This shows that calculating the segregation index using this method does not have a strong dependency on the total number of particles.

In order to get a better understanding about the changes of segregation along the mixer, the distance of all the particles to the closest blue and red particles are calculated. For each cross-section, all the distances between blue-blue, red-red, red-blue and blue-red particles are averaged, giving a single average distance to each contact group. The average distance value for each group is plotted versus the axial length of the mixer (Figure 4.20).

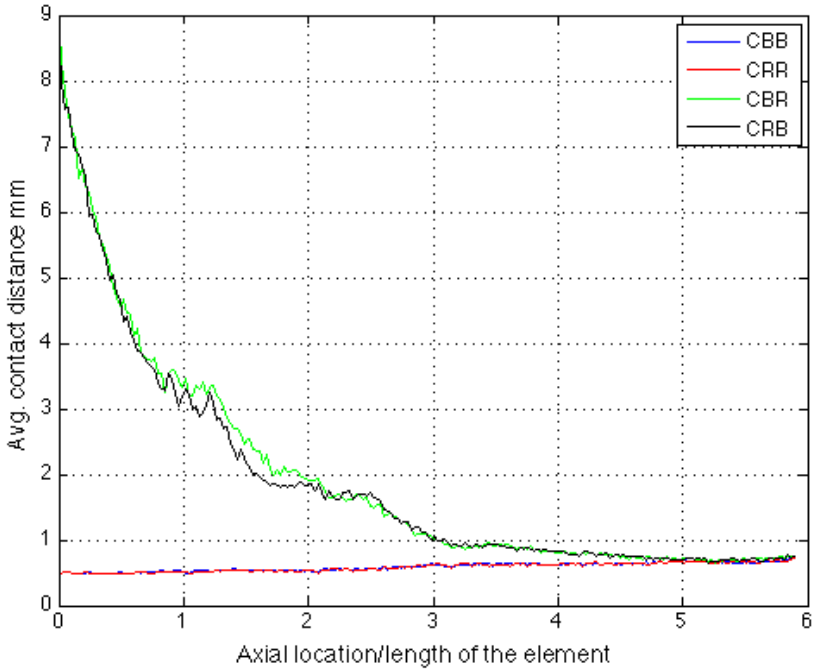

Figure 4.20. Average distance between the particles of each group vs. axial length of the mixer.

At the start of the mixer, the average distance between blue-red and red-blue contacts has its maximum value, which is decreasing by getting closer to the end of the mixer. This shows by passing through the elements, blue and red particles are becoming more distributed among each other and, as a result, the average distance between red-blue and blue-red particles decreases. On the other hand, the average distance between blue-blue and red-red particles is increasing and, by entering the sixth element, the value of the average distance between all the groups is becoming the same. At this point, one could say the average distance between the blue and red particles is becoming so small that it is not possible to say whether the closest neighbour to each particle is blue or red.

Figure 4.21 shows the number of the contact between the particles of each group. The curves, which show the changes of the blue-blue and red-red contacts, are symmetric to the ones which show the blue-red and red-blue contact. This is due to having equal

numbers of blue and red particles in the system. As shown, in the sixth element, the number of contacts between the particles of each group starts fluctuating around a constant number. Considering the constant segregation index after the sixth element in Figure 4.18(b), having the same averaged distance between the particles of each group after the sixth element, according to Figure 4.20, and the fluctuation of the number of contacts between the particles of each group, it could be concluded that the mixture reaches the randomly mixed stage after entering the sixth element.

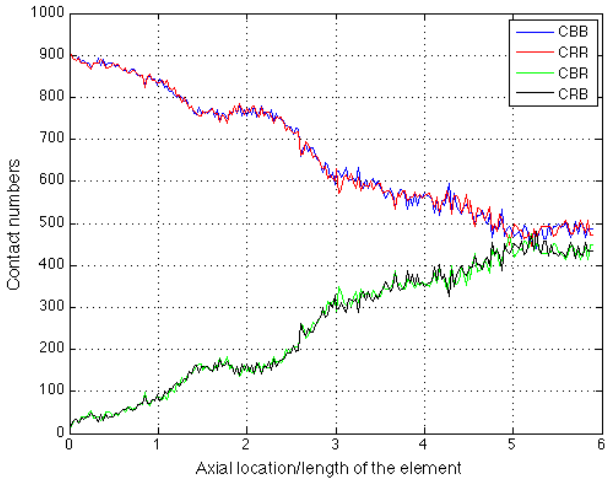

Figure 4.21. Changes in the counted contact numbers of the particles of each group vs. axial length of the mixer.

Figure 4.22 shows the distribution of red and blue particles through the mixer in the middle of each element. It should be mentioned that choosing a large marker size could affect the observation of the striations; therefore, all the particles are plotted with the minimum maker size. As mentioned before, no quantitative measurement of striation thickness is available in this work, due to the limitations of the PEPT resolution. However, it is possible to observe the changes of striations in Figure 4.22. During the first few elements, symmetric striations and patterns between the blue and

red particles on each side of the blade are observed. However, Figure 4.22(f) shows that, after the sixth element, it becomes difficult to see any pattern between the striations, which is in agreement with reaching the randomly mixed stage as described before.

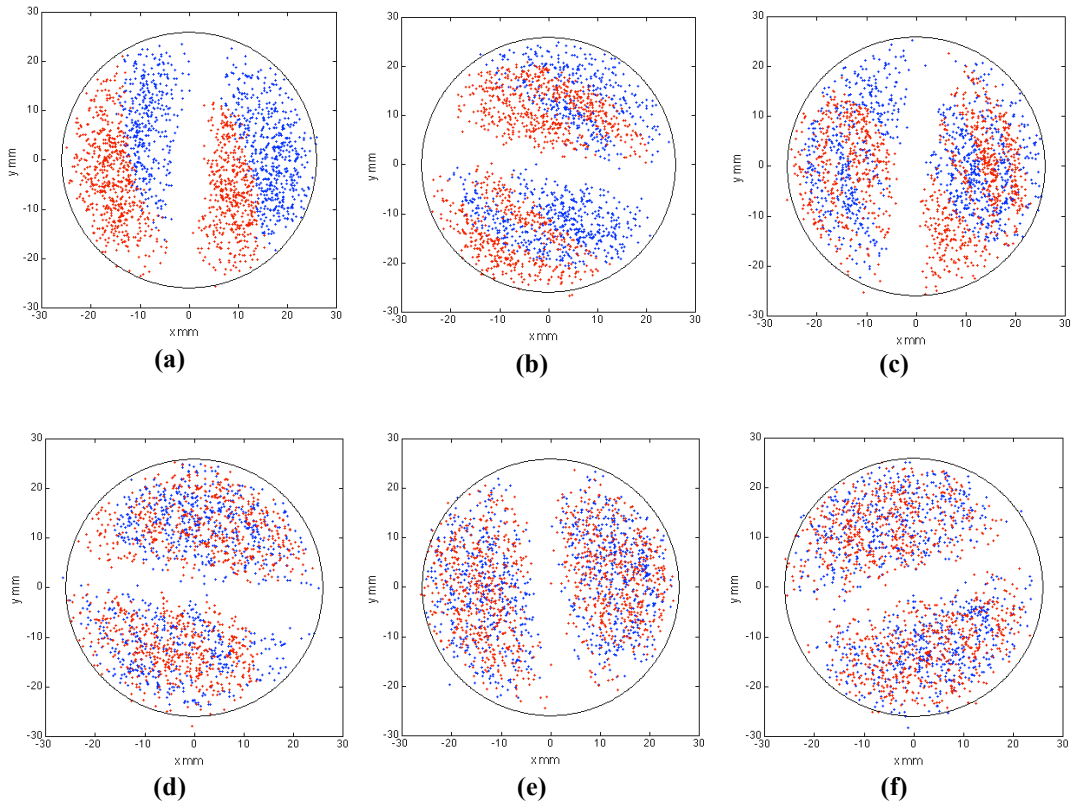

Figure 4.22. Distribution of blue and red particles along the mixer: (a) middle of the 1st element; (b) middle of the 2nd element; (c) middle of the 3rd element; (d) middle of the 4th element; (e) middle of the 5th element; (f) middle of the 6th element.

4.5.2.2 Effect of different feeding systems on changes of segregation

In order to study the effect of using different feeding systems on the segregation index, four different feeding configurations are defined, and the changes of segregation for each system is compared with the others. Figure 4.23 shows the cross-section of the mixer at the entrance, using different combinations for the injection of the blue and red particles. Figure 4.23(a) shows the side-by-side feeding configuration, in which the cross-section of the mixer is divided into two equal halves, and the particles

located in each half are labelled with the same colour. In Figure 4.23(b) and (c), by defining a smaller circle and square in the centre of the cross-section, the particles are labelled with different colours. Figure 4.23(d) shows a more complicated configuration, defining two rectangles containing red particles within the cross-section. It should be mentioned that all the configurations are chosen in a way that the overall number of blue and red particles for each system remains the same.

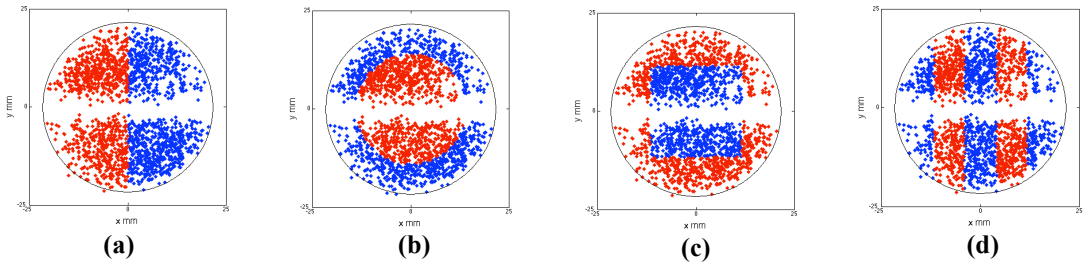

Figure 4.23. Cross-section of the mixer at the entrance using different feeding systems: (a) side-by-side feeding; (b) circular feeding; (c) square feeding; (d) rectangle feeding.

Using the same procedure as described in §4.5.2.1, the changes of the segregation for each feeding system is calculated, and the results are compared to each other in Figure 4.24.

The maximum value of segregation for circular, square, and three rectangles feeding configurations is 1.8, while this value is 1.97 for side-by-side feeding. The length of the interface between the blue and red groups for three rectangles, square, circular, and side by side is calculated as 145.9 *mm*, 108.52 *mm*, 102.93 *mm*, and 50 *mm*. It is observed that the circular and square feeding configurations look similar, with a final segregation value of 1.18.

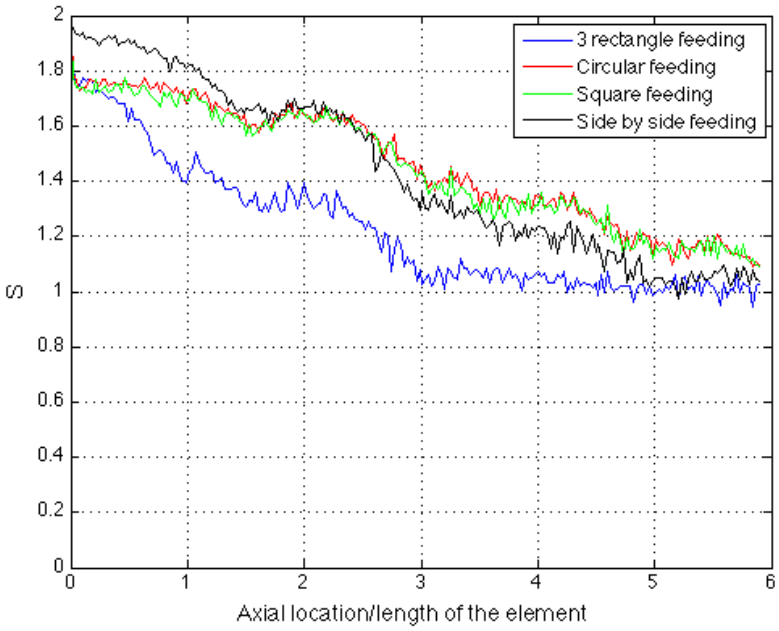

Figure 4.24. Comparison between the changes of the segregation for different feeding configurations.

For the side-by-side feeding, the value of segregation along the mixer is lower than the ones for circular and square feeding systems, and reaches 1 by the end of the sixth element, showing a better mixing in comparison with the circular and square feeding configurations. The three rectangle feeding configuration has the best performance in comparison with the three other feeding systems, reaching a segregation of 1 within the fourth element.

Using the same procedure described in §4.5.2.1, the averaged contact distance between the particles of each group is calculated for each feeding configuration, and the result is presented in Figure 4.25. As shown in Figure 4.25(a), the averaged contact distance between the particles with opposite colour becomes the same as the average distance between the particles with the same colour on the sixth element.

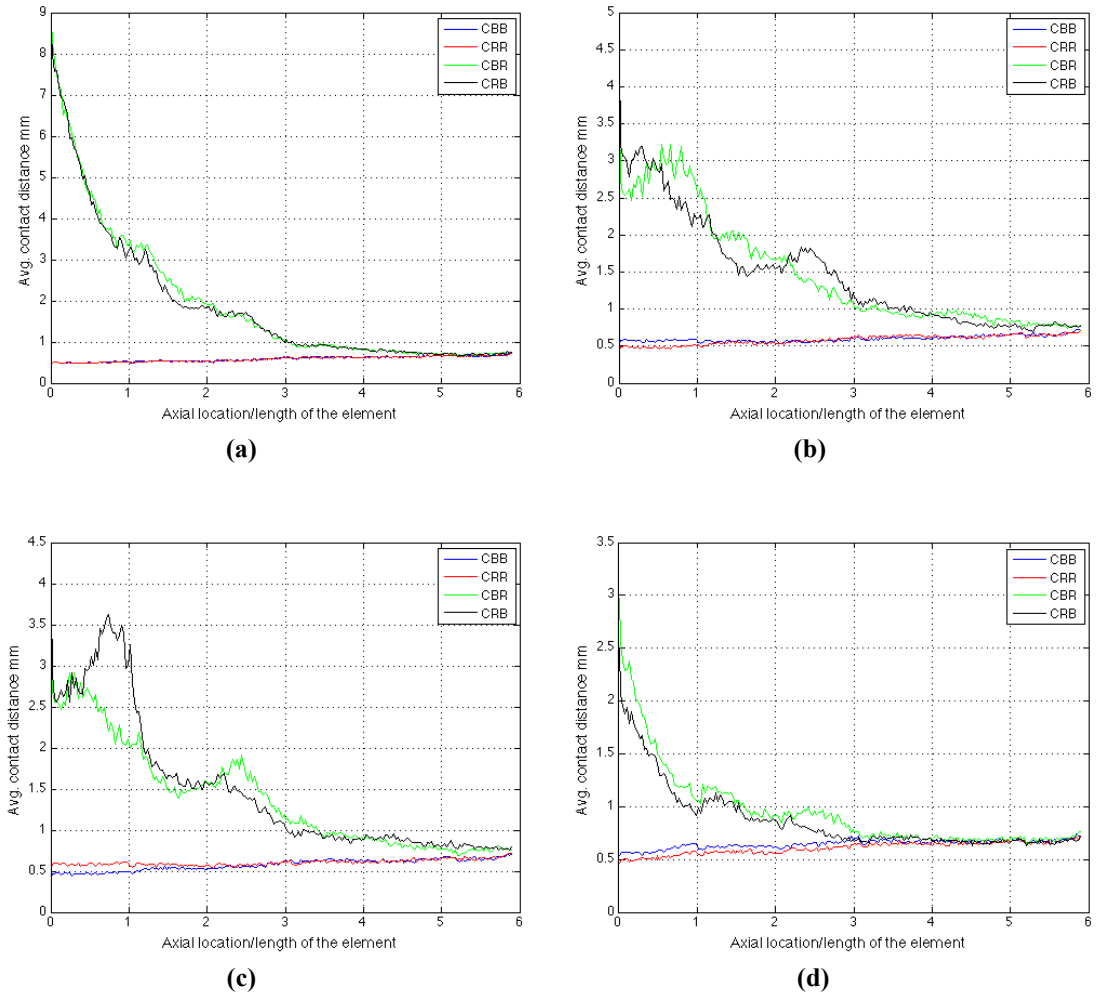

Figure 4.25. Changes of the average contact distance between the particles of each group for: (a) side-by-side feeding; (b) circular feeding; (c) square feeding; (d) three rectangles feeding.

As mentioned before, at this stage, the distance between blue and particles is so small that it is not possible to distinguish between red and blue particles, by considering the existence of the PEPT localisation error. By comparing Figure 4.25(b), (c), and (d), it is observed that the three rectangles feeding configuration reaches this stage sooner in comparison with the other feeding system.

Figure 4.26 shows the changes in the contact number between different groups of particles for all the feeding systems. As shown, for the three rectangle feeding system, the number of contacts between the particles of the opposite group starts fluctuating

around the same number within the fourth element. This behaviour could be observed within the sixth element for the side-by-side feeding, while the circular and square feeding systems could not be observed through the whole length of the mixer.

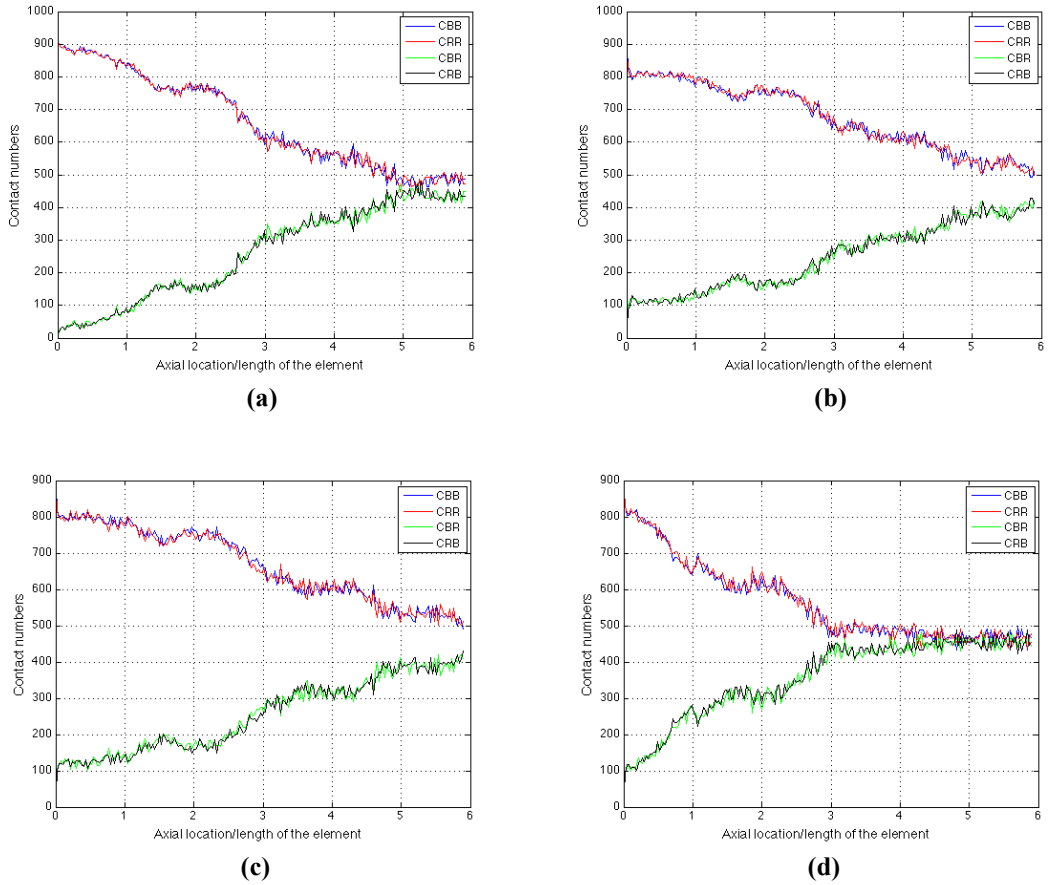

Figure 4.26. Changes in the counted contact numbers between the particles of each group for: (a) side-by-side feeding; (b) circular feeding; (c) square feeding; (d) three rectangles feeding.

By comparing the results from Figure 4.24, Figure 4.25 and Figure 4.26, it can be concluded that the three rectangles feeding system reaches the randomised mixing stage on the fourth element, showing the best mixing performance in comparison with the other systems. Hence, the feeding system with a larger interface between the blue and red groups reaches to the lowest value of segregation after six mixing element comparing with the other ones.

4.6 Residence time distribution

In this section, two subjects will be investigated. The first section studies the changes and characteristics of residence time distribution (RTD) within each single element of the mixer, and also through the whole length of the mixer. In the second part, a suitable model for RTD in the mixer will be investigated, and the experimental data will be compared with the RTD calculated from the model.

4.6.1 Studying residence time distribution within the elements

The residence time distribution function, measured from the response of the system to a pulse of tracer injection, is calculated using the following formula (Levenspiel, 1972):

$$E(t) = \frac{c(t)}{\int_0^\infty c(t)\,dt} \qquad \textbf{(Equation 4.7)}$$

where *c(t)dt* is the concentration of the tracer at the outlet between time *t* and *(t +dt)*. However, considering the discrete nature of the PEPT experimental data, Equation 4.7 is modified to a discrete function:

$$E(t) = \frac{n(t) \big/ \delta t}{\sum_{t=1}^{t=\infty} n(t)} \qquad \textbf{(Equation 4.8)}$$

where *n(t)* is the number of passes with residence time between *t* and *(t+δt)*. The mean residence time is then calculated from (Scott, 1992) :

$$\bar{t} = \frac{\int_{t=0}^{t=\infty} t.E(t)\,dt}{\int_{t=0}^{t=\infty} E(t)\,dt} \qquad \textbf{(Equation 4.9)}$$

By defining the normalised time as $\theta = t/\bar{t}$, the normalised RTD function is calculated from Equations 4.8 and 4.9:

$$E(\theta) = E(t).\bar{t} \qquad \textbf{(Equation 4.10)}$$

By normalising RTD in this way, it is possible to study the experimental data independently from the average residence time. The normalised RTD corresponding to each single element along the mixer is calculated according to Equation 4.10 (Figure 4.27(a)). The area under each curve in Figure 4.27(a) is equal to one. It is observed from Figure 4.27(a) that all the distribution curves have a similar shape, having a close standard deviation for the first five elements. Table 4-2 presents the minimum time that the tracer needs to go through each element along the mixer (θ_{min}), which is 0.5 for an empty pipe in the laminar regime. Considering the existence of the mixer elements inside the pipe, it is expected to observe some deviation from θ_{min} = 0.5 for each element. Table 4-2 also shows that, by getting further away from the centre of the field of view, the deviation from θ_{min} = 0.5 increases. The decrease in the quality of the data when getting further away from the centre of the field of view could affect the accuracy of the RTD observations.

Table 4-2. Minimum time for the tracer to go through each element along the mixer.

Element	**1st**	**2nd**	**3rd**	**4th**	**5th**	**6th**
θ_{Min}	0.41	0.48	0.5	0.5	0.49	0.3

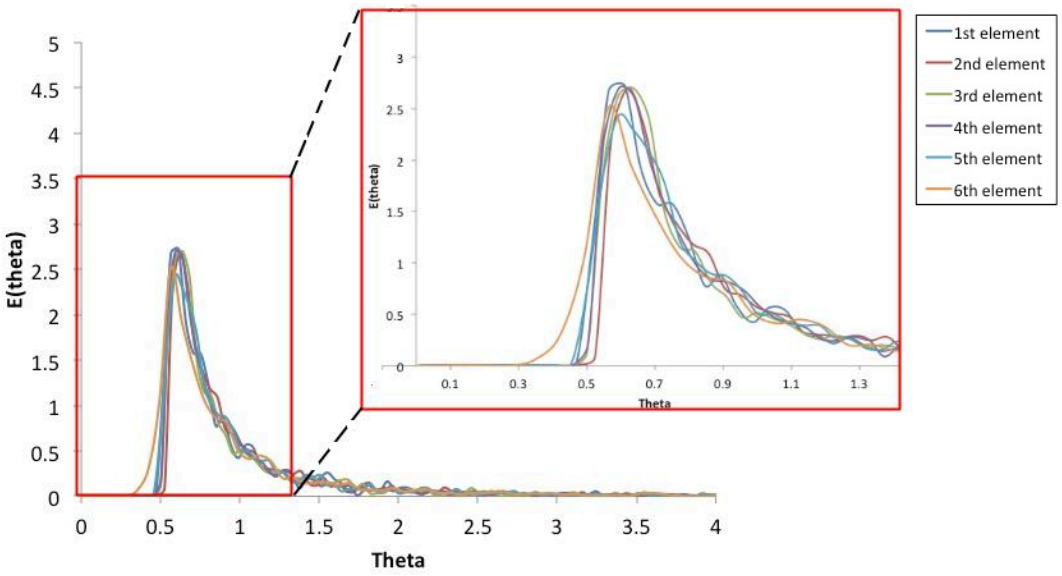

(a)

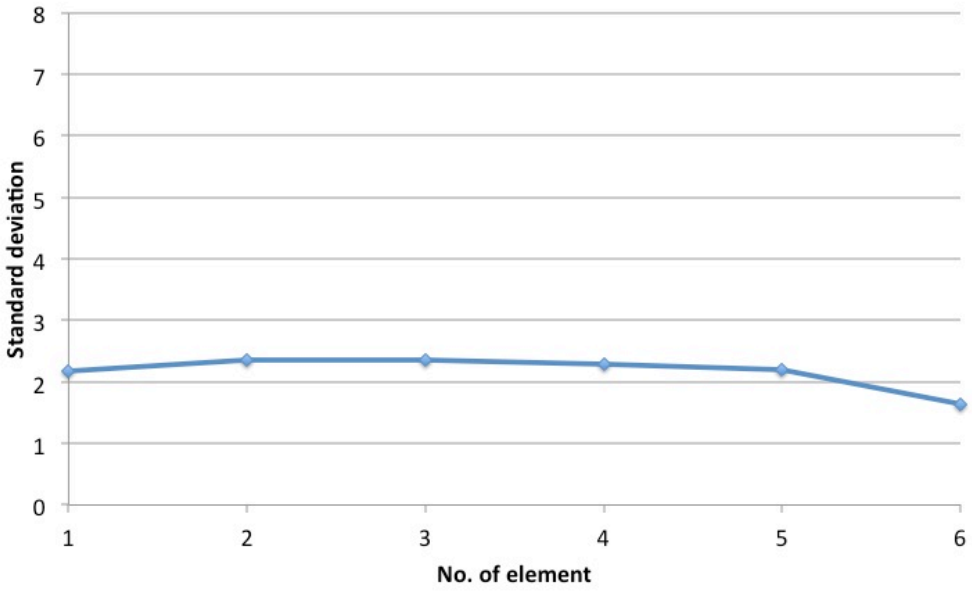

(b)

Figure 4.27. (a) normalised RTD along each single element; (b) changes of the standard deviation for each single element along the mixer.

Figure 4.27 (b) shows that, although there is no significant change in the standard deviation of each distribution for the first five elements, the six elements deviates more from the mean value. This could also be due to the low quality of the data

through the sixth element, as a result of the higher distance to the centre of the camera, as discussed before.

Figure 4.28 shows the RTD calculated from Equation 4.10 from the first to the sixth element. Figure 4.28(a) shows that, for the first two elements, the peak of the RTD curve is located at $\theta = 0.56$. However, when passing through an increased number of elements, it takes more time for the tracers to go through the elements and, subsequently, the peak of the RTD curve for the first six elements is located at $\theta = 0.68$. The mean residence time calculated from the experimental data was found to be close to the one estimated from the value of $u_{sup.}$ (Figure 4.28(b)). The value of the mean residence time is increasing in a linear fashion by going through a higher number of elements as expected.

The tail of the RTD curves in Figure 4.28(a) shows that it takes more than twice as long as the mean residence time for some passes to go through the mixer. To investigate the reason behind this behaviour, the particle trajectories of two passes representing the particles with high residence time are compared with the one which represents the particles with a residence time close to the mean residence time of the distribution.

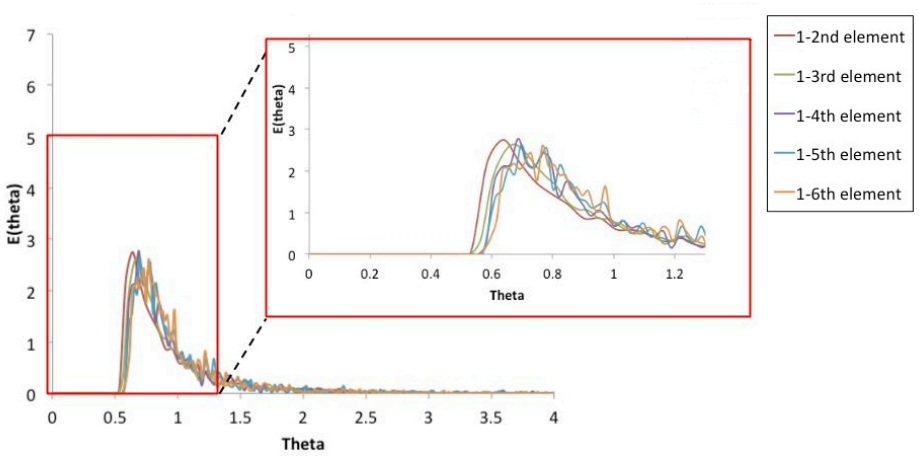

(a)

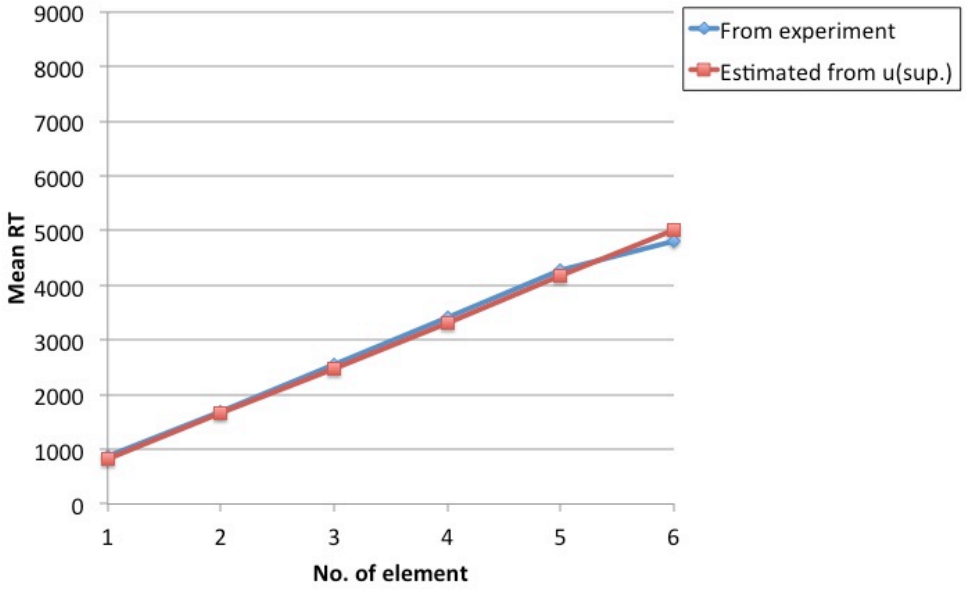

(b)

Figure 4.28. (a) RTD along the mixer starting from the 1st element; (b) changes of the mean residence time along the mixer.

Figure 4.29(a) shows the location of the residence time for these three passes on the RTD graph, indicated by blue, red, and green arrows. The curve shows RTD along the first five elements.

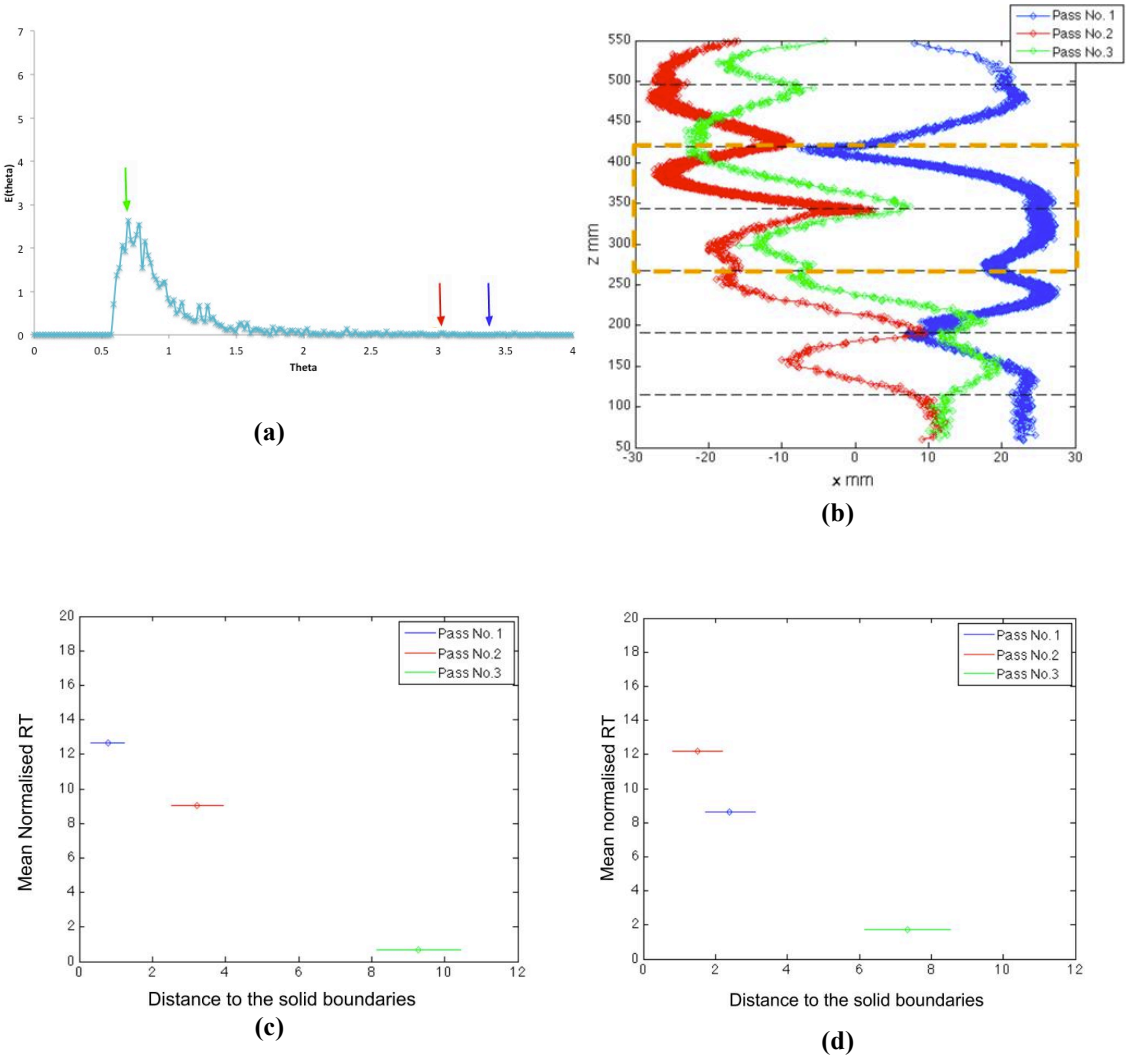

Figure 4.29. Investigating RTD along the mixer: (a) RTD for the first five elements -arrows indicate the residence time of the passes that will be investigated; (b) particle trajectory for three passes with the residence times indicated on (a); (c) effect of the distance to the solid boundaries on the mean residence time on each pass through the 3rd element; (d) effect of the distance to the solid boundaries on the mean residence time on each pass through the 4th element.

In Figure 4.29(b), the blue and red trajectories are the ones with the higher residence time, and the green trajectory represents the pass with the lower residence time. Considering the fact that the distance to the solid boundaries for each pass affects their total residence time, it was decided to study the effect of the changes in the distance to the solid boundaries on the residence time of the chosen three samples pass. Subsequently, the distance to the solid boundaries for the three passes was

monitored through the third and fourth elements (shown with orange rectangle in Figure 4.29(b)), using the same procedure as described before in §4.2. Figure 4.29(c) and (d) show the effect of the distance to the solid boundaries on the average residence time of each pass. As shown, pass numbers one and two (shown with blue and red) are closer to the solid boundaries of the mixer through elements three and four, and they have a higher value of mean residence time. Pass number three, which has a longer distance to the solid boundaries, also has a lower mean residence time, indicating the faster movement through the third and fourth elements in comparison with the other passes. These results are in agreement with the residence time observed in Figure 4.29(a) as expected, showing the higher residence time for pass numbers one and two in comparison with pass number three.

4.6.2 Choice of model for residence time distribution

There are different kinds of models for RTD, and a suitable model should be chosen depending on the type of flow and how close it is to the plug flow or mixed. Figure 4.30 shows the typical RTD curves for different models (Levenspiel, 1972). The dispersion model gives a more or less bell-shaped distribution, with the mean value located at $\theta = 1$.

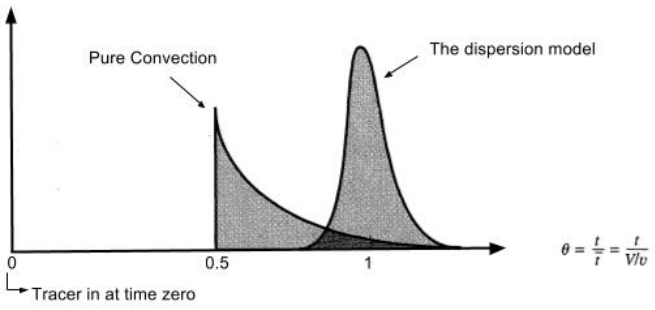

Figure 4.30. Comparison of the RTD of the three models (adapted from Levenspiel, 1972).

It is possible to choose the right model experimentally according to the changes of the standard deviation and variance within a certain distance. For a dispersion model, the variance is related to L using the following relation (Levenspiel, 1972) :

$$\sigma^2 = 2\left(\frac{D_d L}{u^3}\right) \quad \textbf{(Equation 4.11)}$$

where D_d is the axial dispersion coefficient, L is the length, and u is the velocity. Hence, for the dispersion model, the variance grows in a linear fashion with the distance:

$$\sigma^2 \propto L \quad \textbf{(Equation 4.12)}$$

On the other hand, for the convection model, the spread of the tracer grows in a linear fashion with distance (Levenspiel, 1972):

$$\sigma \propto L \quad \textbf{(Equation 4.13)}$$

By calculating the variance and the standard deviation of the experimental residence time, the changes in these two parameters versus the number of elements is plotted in Figure 4.31. The best-fitted line to each curve, shown with a red line, is calculated and the equation of each line is shown on the figures. The value for R^2 for Figure 4.31(a) is 0.94, and 0.97 for Figure 4.31(b).

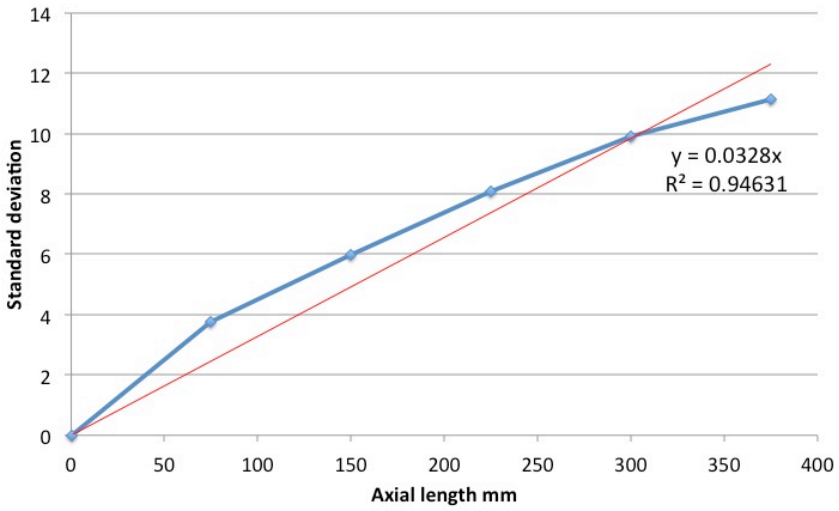

(a)

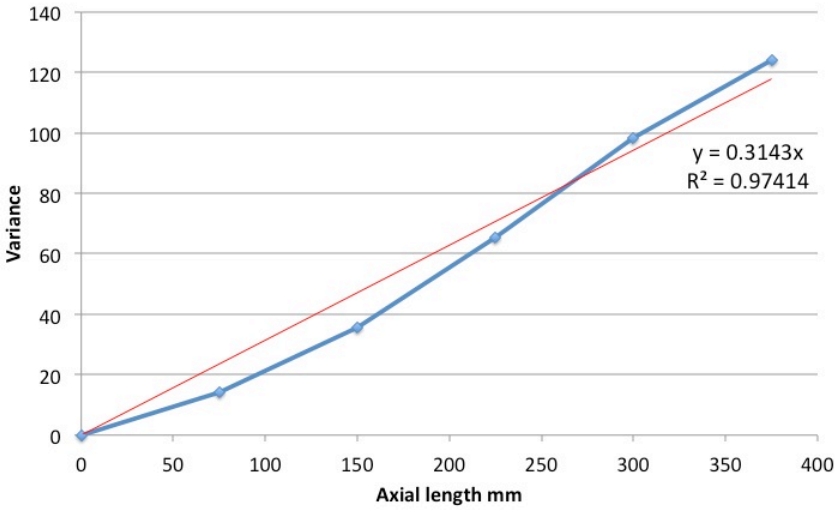

(b)

Figure 4.31. (a) changes of standard deviation along the mixer; (b) changes of the variance along the mixer.

However, for the viscous laminar fluid in a short pipe, it is suggested to use the convection model (Levenspiel (1972)). By comparing the shape of the experimental RTD curves in Figure 4.28 with the shape of the RTD models presented in Figure 4.30, it can be observed that there is more similarity between the shape of the

experimental RTD and the convection model, meaning the convection model might be a better fit in this case. Therefore, it was decided to investigate how close the convection model is to the experimental RTD.

For the convection model, the shape of the RTD curve is strongly affected by the way that the tracers are injected into the system. Considering the pulse injection of the tracers, Figure 4.32(a) and (b) shows the flux induction and the combination of the input-output methods that are being used during the experiment.

(a) **(b)**

Figure 4.32. (a) introducing and measuring the tracer; (b) combination of input-output (adapted from (Levenspiel, 1972)).

In this case, the RTD function can be derived using the equation of the velocity profile in a pipe for a laminar flow (Scott, 1992):

$$U = U_{\max}\left[1-\left(\frac{r}{R}\right)^2\right] = 2U_{avg}\left[1-\left(\frac{r}{R}\right)^2\right] = \frac{2\upsilon_0}{\pi R^2}\left[1-\left(\frac{r}{R}\right)^2\right] \qquad \textbf{(Equation 4.14)}$$

where U_{max} is the centreline velocity in a pipe with the outer radius of R, and U_{avg} is the average velocity through the pipe. The time passage of an element of fluid at radius r is:

$$t(r) = \frac{L}{U(r)} = \frac{\pi R^2 L}{\upsilon_0}\frac{1}{2[1-(r/R)^2]} = \frac{\tau}{2[1-(r/R)^2]} \qquad \textbf{(Equation 4.15)}$$

and by differentiating, it will be changed to:

$$dt = \frac{4}{\tau R^2}\left\{\frac{\tau/2}{[1-(r/R)^2]}\right\}rdr \qquad \textbf{(Equation 4.16)}$$

By considering the volumetric flow rate of the fluid out between *r* and *(r+dr)*, *dυ*, as *U(r)2πrdr*, the fraction of the total fluid passing between *r* and *(r+dr)* could be calculated by the following equation:

$$\frac{d\upsilon}{\upsilon_0} = \frac{U(r)2(\pi r dr)}{\upsilon_0} \qquad \textbf{(Equation 4.17)}$$

Hence, the fraction of the fluid between *r* and *(r+dr)* with a flow rate between *υ* and *(υ+dυ)* which spends a time between *t* and *(t+dt)* in the pipe can be calculated using the following equation:

$$E(t)dt = \frac{d\upsilon}{\upsilon_0} \qquad \textbf{(Equation 4.18)}$$

Combining Equations 4.17 and 4.18, and by using Equation 4.15 for *U(r),* the RTD function, *E*, can be calculated using the following relation:

$$E(t)dt = \frac{d\upsilon}{\upsilon_0} = \frac{L}{t}\left(\frac{2\pi r dr}{\upsilon_0}\right) = \frac{L}{t}\left(\frac{2\pi}{\upsilon_0}\right)\frac{\tau R^2}{4t^2}dt = \frac{\tau^2}{2t^3}dt \qquad \textbf{(Equation 4.19)}$$

$$E(t) = \frac{\tau^2}{2t^3}$$

And the minimum time that the fluid spends in the pipe is:

$$t = \frac{L}{U_{\max}} = \frac{L}{2U_{avg}}\left(\frac{\pi R^2}{\pi R^2}\right) = \frac{V}{2\upsilon_0} = \frac{\tau}{2} \qquad \textbf{(Equation 4.20)}$$

For laminar flow rector, $\tau = \overline{t}$, therefore, the equation to calculate the RTD within the pipe could be summarised as below:

$$E(t)=\begin{cases} 0 & t<\dfrac{\bar{t}}{2} \\ \dfrac{\bar{t}^2}{2t^3} & t\geq\dfrac{\bar{t}}{2} \end{cases}$$ **(Equation 4.21)**

and subsequently the dimensionless of RTD function is:

$$E(\Theta)=\begin{cases} 0 & \Theta<0.5 \\ \dfrac{1}{2\Theta^3} & \Theta\geq 0.5 \end{cases}$$ **(Equation 4.22)**

Figure 4.33 shows the comparison between RTD function calculated from Equation 4.22, and the experimental normalised RTD for the first to the second, first to fourth, and first to the sixth elements.

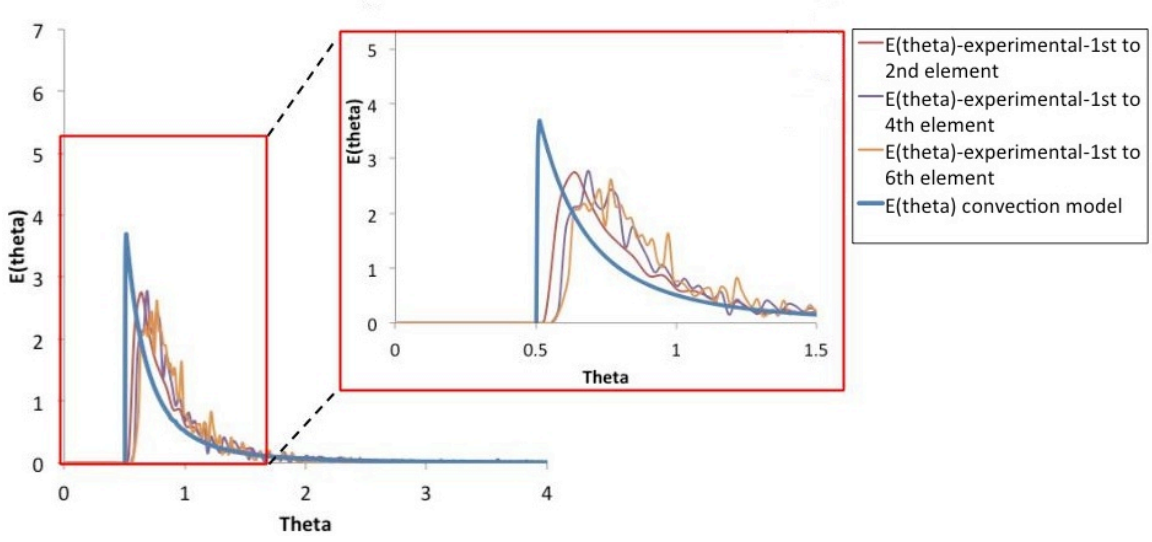

Figure 4.33. Comparison between the convection RTD model and the experimental data.

It can be observed that the RTD of the first to the second element is close to the RTD calculated from the model, with θ_{min} = 0.52. By going through a greater number of elements, the experimental $E(\theta)$ starts to deviate from the model, and the minimum required time for the tracer to go through the first six elements increases to 0.57. The

peak of each curve is also shifting towards $\theta = 1$ by going further towards the end of the mixer. The RTD calculated from the convection model, which has been used here, is developed for a laminar flow inside an empty pipe. Considering the geometry of the mixer, which includes number of elements installed inside an empty pipe, by passing through more number of elements, the experimental data deviates more from the convection model for an empty pipe. Considering the peak of the distribution curves is moving towards $\theta = 1$, and by comparing Figure 4.33 with Figure 4.30, it can be observed that the experimental RTD is moving away from the convection model RTD, and getting closer to the shape of the dispersion model RTD. This means the main changes in dispersion are happening within the transitional region between each two consecutive elements and, therefore, by passing through a greater number of elements, i.e., more transitional regions, the RTD becomes closer to the shape of the RTD on the dispersion model.

4.7 Conclusion

In this chapter, the behaviour of glycerol as a Newtonian model fluid is studied by using PEPT experimental data. The experimental data is processed using the procedure described in Chapter 3. The Eulerian velocity maps in the Cartesian reference system are calculated along the mixer. It is shown that the velocity in each cell is calculated over a sufficient number of locations. The maximum value of a normalised axial velocity is observed in the middle of the area between the blade and the inner wall of the pipe. It is also observed that, by going towards the solid boundaries of the system, the velocity decreases, as expected. The flow direction follows the direction of the twist in each element according to the velocity vector plots.

The shear rate maps are plotted along the third and fourth element, using the equations presented in Chapter 3. The highest value of shear rate is observed close to the solid boundaries of the system, due to the existence of high gradient of velocity in these areas. It has been demonstrated that the data from the PEPT experiment could be used to study the shear rate within the geometry.

Mixing is characterised by using two techniques. The geometry is divided into a number of cells, and the changes of the CoV along the mixer are calculated by counting the number of the blue and red particles within each cell. It is observed that the value of the CoV is highly dependent on the number of passes. It is shown that the value of the CoV is just a function of the total number of blue and red particles within each cell, and it does not track any changes in striation thickness within each cell. It should be mentioned that, due to the resolution of the PEPT experimental data, it is not possible to have a quantitative measurement of the scale of segregation and striation thicknesses along the mixer. Hence, the author does not suggest characterising mixing by the CoV using the PEPT experimental data. Consequently, the segregation index is calculated by finding the closest neighbour of each particle. It is observed that the value of segregation becomes constant within the sixth element. The value of the contact number between the particles of opposite groups is plotted versus distance, and it is observed that this value starts fluctuating for all the groups within the sixth element. Therefore, the system reaches the randomised stage within the sixth element.

RTD within the mixer is calculated using the experimental data. The effect of decreasing the quality of the data by getting further away from the centre of the field of view is observed on the RTD results. RTD for all the single elements look similar. The RTD curves along the mixer, starting from the first element, are also plotted. The

effect of passing through transition areas is observed by showing the increase of mean RT by going through a greater number of elements. Considering the use of a highly viscous Newtonian fluid in a laminar regime and, by comparing the shape of the RTD curves of the experimental data with the RTD of the convection and dispersion models, it is decided to compare the experimental data with the convection model. It is shown that the RTD of the first two elements have the closest shape to the RTD function of the convection model. However, by going further within the mixer, the deviation of the RTD curves from the convection model increases. By the end of the sixth element, the experimental RTD looks more similar to the dispersion model than the convection one. This shows the main changes in dispersion are happening within the transitional region between each two consecutive elements, while the changes within each element are mainly due to the convection forces.

In this chapter, it is demonstrated that the data from PEPT experiment could be used to study the flow motion and mixing performance of Newtonian fluid in Kenics static mixer.

Notation

Roman letters

C_{BB}	Contact number between blue-blue particles	-
C_{RR}	Contact number between red-red particles	-
C_{RB}	Contact number between red-blue particles	-
C_{BR}	Contact number between blue-red particles	-
$C(t)$	Concentration of the tracer at outlet	-
D_d	Axial dispersion coefficient	$m^2.s^{-1}$
D_h	Hydraulic mean diameter	m
D	Pipe diameter	m
$E(t)$	RTD function	s
$E(\theta)$	Dimensionless RTD function	-
L_e	Entrance length	m
L	Length of the element	m
N_{Re}	Reynolds number	-
$n(t)$	No. of passes with a residence time between t and (t+δt)	-
R	Radius	m
S	Segregation	-
t	Time	s
$\overline{t}$	Mean residence time	s
u_{avg}	Average velocity	$m.s^{-1}$
u_{max}	Centre line velocity in a pipe	$m.s^{-1}$
V	Total volume	m^3
v_z	Velocity in axial direction	$m.s^{-1}$
v_x	Velocity in *x*- direction	$m.s^{-1}$
v_y	Velocity in *y*- direction	$m.s^{-1}$
w	Thickness of the blade	m

Greek letters

ρ	Density of the fluid	$kg.m^{-3}$
μ	Dynamic viscosity of the fluid	$kg.\ m^{-1}s^{-1}$
τ	Shear stress	Pa
$\dot{\gamma}$	Shear rate	s^{-1}
θ	Normalised residence time	-
θ_{min}	Minimum time for the tracer to go through the mixer	-
ν	Volumetric flow rate	$m^3.s^{-1}$

Chapter 5 . MIXING OF NON-NEWTONIAN FLUIDS USING THE KENICS STATIC MIXER

The aim of this chapter is to obtain an understanding of the fluid motion and mixing performance within the Kenics mixer when non-Newtonian fluids are used. Two different concentrations of aqueous Carbopol solution are used as the non-Newtonian model fluids and the flow behaviour is obtained using PEPT. The data are then compared to results obtained with a Newtonian fluid, used as a base case to attempt to unpick the influence of non-Newtonian rheology.

5.1 Rheological properties of the fluid

The two different concentrations of Carbopol solution (0.1 wt% and 0.2 wt%) were prepared as described in §3.2.2.2. Their rheological properties were measured using the cone and plate rheometer (§3.2.1.1). The relation between the shear stress and the shear rate for the Carbopol 0.1 wt% and 0.2 wt% solutions at a temperature of 25°C is shown in Figure 5.1.

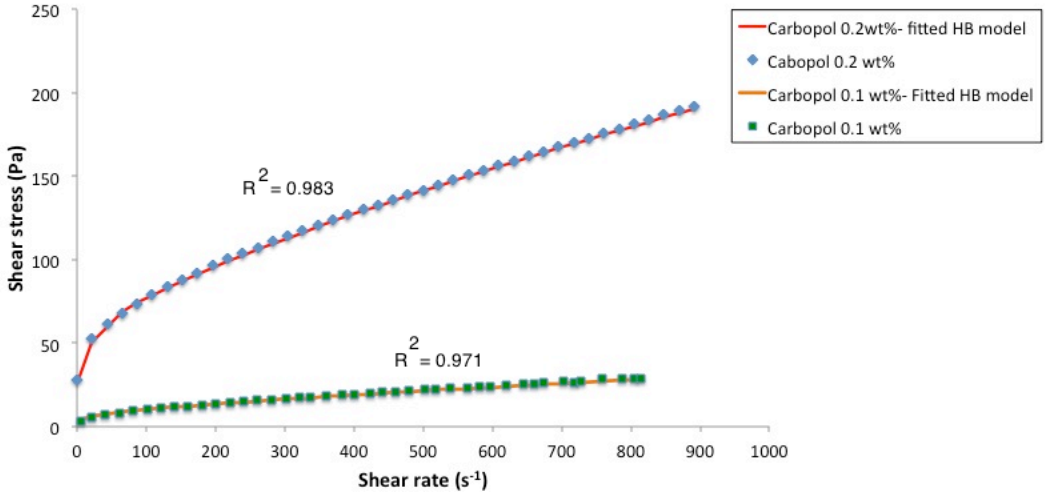

Figure 5.1. Shear stress vs shear rate for Carbopol 0.1 wt% and Carbopol 0.2 wt% solutions.

Figure 5.1 shows the shear-thinning nature of the fluids (Ferguson et al. (1991)) which can be represented by the Herschel-Bulkley model:

$$\tau = \tau_0 + k\dot{\gamma}^n \qquad \textbf{(Equation 5.1)}$$

where τ is the shear stress, τ_0 is the yield stress, and $\dot{\gamma}$ is the shear rate. k and n are the consistency index and flow indices respectively, which are calculated by fitting the model to the flow curves. Figure 5.1 also shows how close the flow curves are fitted to a Herschel-Bulkley model. Table 5-1 shows all the parameters of Equation 5.1 measured from Figure 5.1 for both fluids.

Table 5-1. Herschel-Bulkley parameters for Carbopol 0.1 wt% and Carbopol 0.2 wt% solutions.

Property / Solution	Consistency index, k (Pa. s^{n-1})	Flow index, n (-)	Yield stress, τ_0 (Pa)
Carbopol 0.1 wt%	0.26	0.7	3.7
Carbopol 0.2 wt%	2.25	0.62	34.79

The apparent viscosity of the Herschel-Bulkley model is then given by:

$$\mu = k\dot{\gamma}^{n-1} + \frac{\tau_0}{\dot{\gamma}} \quad ,for \quad \tau \geq \tau_0$$
$$\mu \to \infty \quad ,for \quad \tau < \tau_0 \qquad \textbf{(Equation 5.2)}$$

The average shear rate in the system is estimated using the predicted pipe flow velocity profile. For Herschel-Bulkley fluids, the velocity profile is given by Ferguson et al. (1991):

$$u(r) = \frac{nR}{n+1}\left(\frac{\tau_w}{k}\right)^{1/n}\left[\left(1-\phi\right)^{(n+1)/n} - \left(\frac{r}{R}-\phi\right)^{(n+1)/n}\right] \qquad \textbf{(Equation 5.3)}$$

where ϕ is the ratio of the yield stress to the wall shear stress, i.e. τ_0/τ_w. The value of radius (R) was assumed as half of the hydraulic mean diameter of the system, which was calculated in §4.1, as 0.0288 m. As mentioned in §3.2.3, the superficial velocities

for the Carbopol 0.1 wt% and 0.2 wt% solutions are 0.08 *m/s* and 0.15 *m/s*, respectively. The value of the wall shear stress is calculated by using the equation of the steady volumetric flow rate of a Herschel-Bulkley fluid in a laminar flow:

$$Q = \frac{\pi R^3 n}{\tau_w^3}\left(\frac{\tau_w - \tau_0}{k}\right)^{1/n}(\tau_w - \tau_0)\left[\frac{(\tau_w - \tau_0)^2}{3n+1} + \frac{2\tau_0(\tau_w - \tau_0)}{2n+1} + \frac{\tau_0^2}{n+1}\right] \qquad \textbf{(Equation 5.4)}$$

Knowing the value of the volumetric flow rate (Q) from the experiment and by substituting the value of n, k, and τ_0 from Table 5-1, τ_w is calculated as 7.149 *Pa* for Carbopol 0.1 wt% and 66.44 *Pa* for Carbopol 0.2 wt%. Subsequently, by putting the value of τ_w and ϕ into Equation 5.3, the velocity profile normalised by the superficial velocity for both solutions is plotted in Figure 5.2.

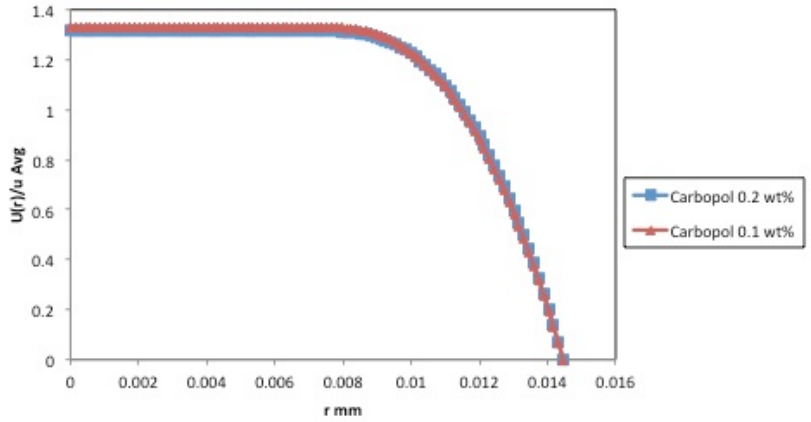

Figure 5.2. Predicted pipe flow velocity profile for the Carbopol solutions.

The average shear rate for both fluids is then estimated based on their predicted pipe flow velocity profiles:

$$\dot{\gamma}_{avg.} = \frac{\sum_{i=1}^{N} \dot{\gamma}(r) * Q(r)}{Q} \qquad \textbf{(Equation 5.5)}$$

$$Q(r) = u(r) * A(r)$$

where $\dot{\gamma}(r)$ is the shear rate at radius *r, Q(r)* is the volumetric flow rate at radius *r*, and *A(r)* is the area between each two consecutive radius. The value of average shear rate for Carbopol 0.1 wt% and Carbopol 0.2 wt% is calculated as 194 s^{-1} and 177 s^{-1}.

Subsequently, the apparent viscosity of Carbopol 0.1 wt% at a shear rate of 194 s^{-1} is found from the rheometer data as 0.06 *Pa.s*, and 0.45 *Pa.s* for Carbopol 0.2 wt% at the shear rate of 177 s^{-1}.

5.2 Flow regime and development length

Metzner et al. (1955) defined a generalised Reynolds number for time-independent fluids, using the equation below:

$$\mathrm{Re}_{MR} = \frac{\rho u^{2-n} D_h^n}{\mu_{app.}} \qquad \textbf{(Equation 5.6)}$$

where D_h is the hydraulic mean diameter, and $\mu_{app.}$ is the apparent viscosity of the fluid. Chilton et al. (1998) defined the Metzner-Reed Reynolds number using analytical solutions for a Herschel-Bulkley fluid in a pipe flow by Equation 5.6:

$$\mathrm{Re}_{MR} = \frac{\rho u D_h}{k\left(\frac{8u}{D_h}\right)^{n-1}\left(\frac{3n+1}{4n}\right)^n\left(\frac{1}{1-X}\right)\left(\frac{1}{1-aX-bX^2-cX^3}\right)^n} \qquad \textbf{(Equation 5.7)}$$

where:

$$a = \frac{1}{2n+1}, b = \frac{2n}{(n+1)(2n+1)}, c = \frac{2n^2}{(n+1)(2n+1)}, X = \frac{\tau_0}{\tau_w} \qquad \textbf{(Equation 5.8)}$$

Using Equations 5.6 and 5.7, the Reynolds number is calculated as 6.7 and 1.2 for the Carbopol 0.1 wt% and Carbopol 0.2 wt% solutions.

For a fluid entering a pipe, the initial velocity profile at the inlet of the pipe is flat and will change gradually until it reaches a fully developed condition. The distance required for the centre line velocity to reach to a fully developed flow is called the development length.

For a shear-thinning fluid, the fully developed velocity distribution is flatter than for a Newtonian fluid, therefore it is expected to have a shorter development length in comparison with the Newtonian fluids. The development length is calculated using the following equation (Steffe (1996)):

$$\frac{2L_e}{D_h} = \left(-0.25n + 0.35\right) * \left[\frac{D_h^n \bar{u}^{(2-n)} \rho}{k}\right] \qquad \textbf{(Equation 5.9)}$$

where L_e is the development length. Knowing the value of n and k from Table 5-1, the value of the development length for Carbopol 0.1 wt% and Carbopol 0.2 wt% is calculated as $1.063D_h$ (34 *mm*) and $0.03D_h$ (10 *mm*), which is taken into account by keeping an empty length at the bottom of the pipe before the mixer elements.

5.3 Eulerian velocity fields

Using the same data processing procedure as described in §3.3.3, the Eulerian velocity maps of both non-Newtonian fluids in Cartesian coordinates will be studied in this section. The results corresponding to non-Newtonian fluids will be also compared with the Newtonian fluid results from Chapter 4 at each stage.

5.3.1 Choosing the grid

As mentioned in §4.4.1, it is desirable to choose a cell size as small as possible to get accurate velocity maps; however, considering the PEPT localisation error, it is not possible to choose a cell size smaller than 2 *mm* in each direction. In order to choose the optimum cell size in the axial direction, the same procedure as described in §4.4.1

is used. The data file from the experiment is processed using different cell sizes in an axial direction, and the velocity maps are visually compared to choose the smallest cell size which would give sufficient image quality.

Figure 5.3 shows the normalised velocity map in an axial direction located at the start of the fourth element, using the Carbopol 0.1 wt% solution as the modelling fluid. For all the graphs, the cell size in *x* and *y* direction is considered as 2 *mm*.

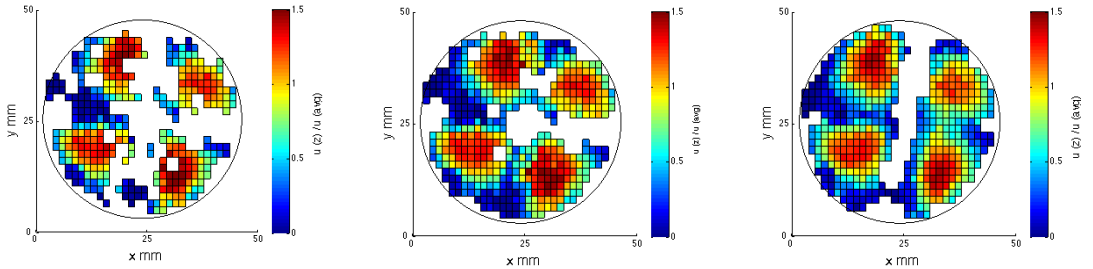

(a) Axial length of the cell = 2 *mm* **(b) Axial length of the cell = 4 *mm*** **(c) Axial length of the cell = 6 *mm***

(d) Axial length of the cell = 8 *mm* **(e) Axial length of the cell = 10 *mm***

Figure 5.3. Effect of changing the axial length of the cell in axial direction on the Eulerian velocity map. Normalised axial velocity at the cross-section of the start of the fourth element with the axial cell size of: (a) 2 *mm*; (b) 4 *mm*; (c) 6 *mm*; (d) 8 *mm*; (e) 10 *mm*.

As shown in Figure 5.3 (a), using the minimum size of the cell in an axial direction, which is 2 *mm*, results in a velocity map with many empty cells within the cross-section of the mixer, therefore, it is necessary to increase the cell size. This issue

exists for the velocity map corresponding to the axial cell size of 4 *mm* as well. As shown in Figure 5.3 (d) and (e), the number of the empty cells decreases by increasing the axial length of the cell. Consequently, it was decided to choose a 6 *mm* cell in an axial direction, which is the smallest cell size at which it is possible to have a uniform velocity map with the minimum number of empty cells within the cross-section of the mixer. The size of the cell in the *x*- and *y*- directions is kept as 2 *mm*. The data was then interpolated in an axial direction using the same method as described in §4.3.1.

5.3.2 Studying the existence of steady velocity through the cells

The value of the velocity in each cell should be calculated over a sufficient number of locations. It was shown in §4.4.2 that the average velocity of each cell was calculated over a sufficient number of locations for the experimental data using the Newtonian fluid (glycerol). However, considering the difference in data density of the non-Newtonian fluids and glycerol, it is necessary to investigate the existence of the steady velocity through the cells for the non-Newtonian experimental data as well.

Following the same procedure as described in §4.4.2, four cells with different locations were selected from the axial velocity map of the Carbopol 0.1 wt% solution, located in the middle of the third element (Figure 5.4).

Cell number one represents the area near the inner wall of the pipe; cell number two represents the area with a higher average velocity located between the blade and the inner wall of the pipe; cell number three is located close to the blade, and cell number four represents an area with the highest velocity within the cross-section.

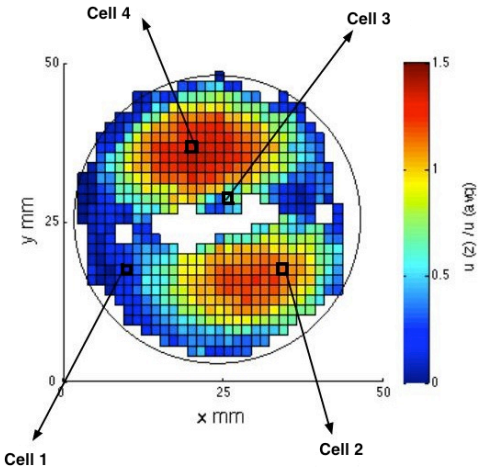

Figure 5.4. Location of four different cells with the cross-section of the mixer in the middle of the third element.

The running average of the velocity of all the passes though the selected cell is plotted versus the cumulative number of locations, and the result is shown in Figure 5.5. The number of locations refers to the number of the recorded data points within each cell.

As expected, the average velocity for the cells close to the solid boundaries of the system is calculated over fewer locations in comparison with the cells further away from the two solid boundaries of the system. Figure 5.5 (a) and (c) indicates that the velocities are steady after using around 14 locations. However, for Figure 5.5 (b) and (d), it seems that the velocity is not stable until after around 38 locations. The difference between the required number of locations between Figure 5.5 (a) and (b) is due to the higher axial velocity of Figure 5.5 (b), which causes the experiment to reach a steady velocity over a higher number of locations.

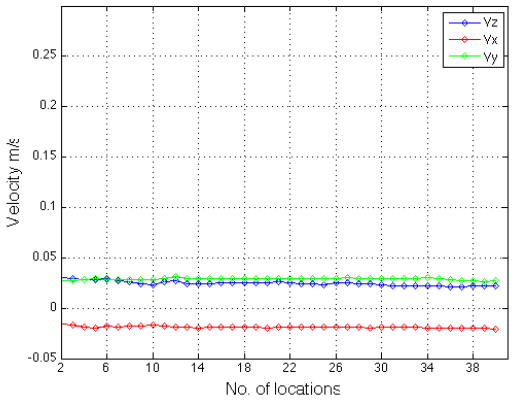

(a) Cell No.1

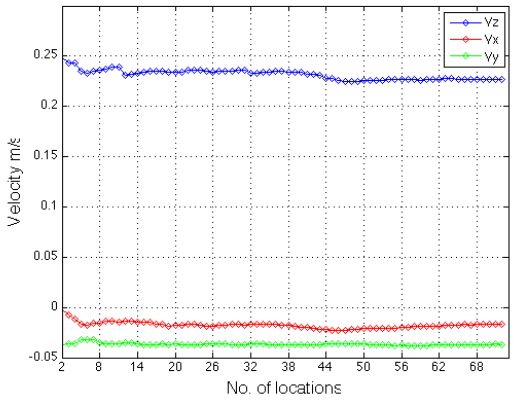

(b) Cell No.2

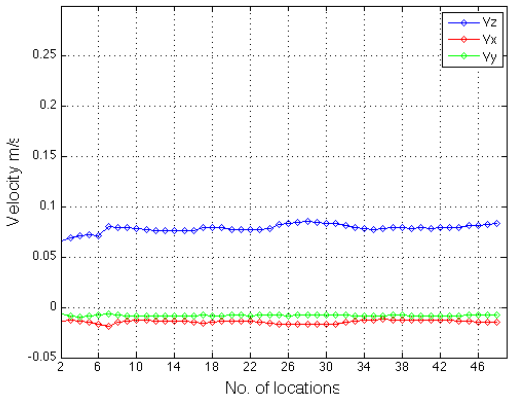

(c) Cell No.3

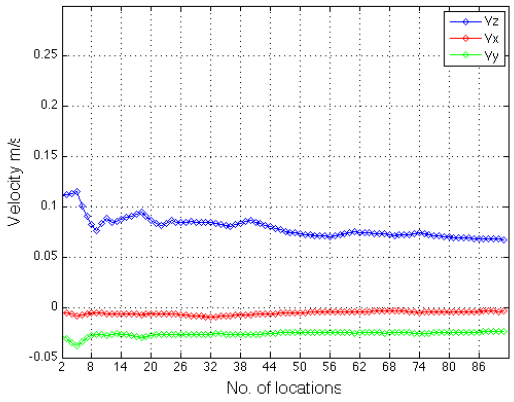

(d) Cell No.4

Figure 5.5. Effect of changing the number of locations on the calculated velocity in different directions for: (a) Cell No. 1; (b) Cell No.2; (c) Cell No.3; (d) Cell No.4.

The standard deviation of the velocity components for all the cells is found to be in the order of 10^{-3} *m/s* (Table 5-2). Considering the observation of steady velocity in each cell, according to Figure 5.5, and the small standard deviation of the average velocity calculated over the different number of points within each cell, it is concluded that the velocity is calculated over a sufficient number of locations.

Table 5-2. Standard deviation of three velocity components for different cells.

Cell number	Average u_z $m.s^{-1}$	Average u_x $m.s^{-1}$	Average u_y $m.s^{-1}$	u_z standard deviation	u_x standard deviation	u_y standard deviation
Cell No.1	0.025	-0.018	0.025	0.002	0.0009	0.0006
Cell No.2	0.22	-0.02	-0.04	0.005	0.003	0.001
Cell No.3	0.08	-0.02	-0.01	0.004	0.001	0.004
Cell No.4	0.02	-0.008	-0.03	0.001	0.001	0.002

5.3.3 Studying the velocity maps in a Cartesian reference system

The Eulerian velocity maps of both non-Newtonian fluids are plotted following the procedure of calculating the average velocity within each cell, as described in §4.3.3. In this section, the velocity maps of both non-Newtonian fluids will be compared with the maps of the Newtonian fluid. The velocity maps of the third element have the best resolution, in comparison with the other locations along the mixer, due to their closeness to the centre of the PEPT camera field of view. The comparison between the velocity maps will be focused on the third element in this section, due to the high number of graphs along both elements for both fluids.

Figure 5.6 shows the comparison between the velocity maps of Carbopol 0.1 wt%, Carbopol 0.2 wt% and the glycerol solutions along the third element, relative to their axial coordinates of $z = 0$, $z = L/8$, $z = L/4$, $z = L/2$, and $z = 3L/4$, with L being the length of the element. The value of axial velocity is normalised by the value of the superficial velocity for each fluid.

Carbopol 0.1 wt%	Carbopol 0.2 wt%	Glycerol
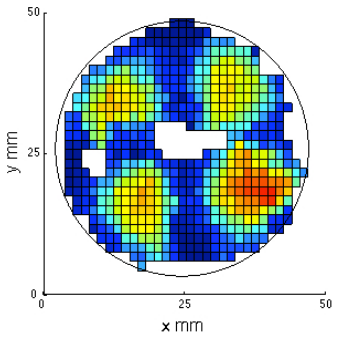	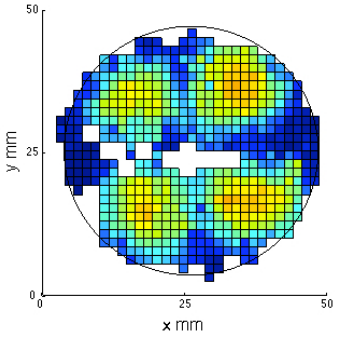	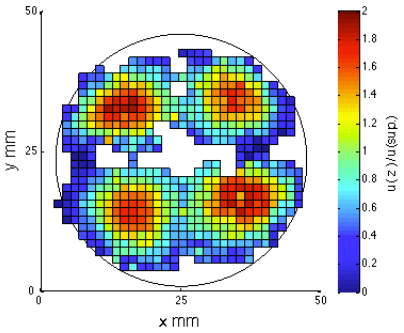
(a) z = 0	**(f) z = 0**	**(k) z = 0**
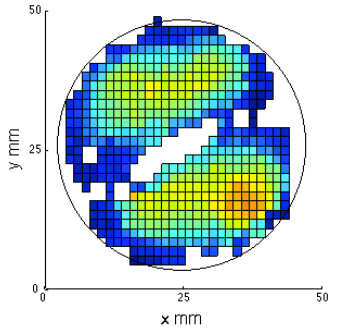	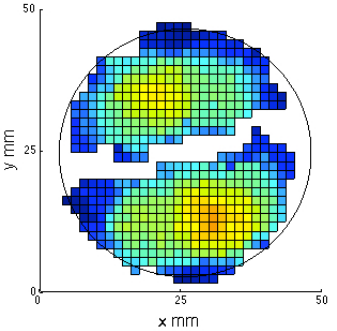	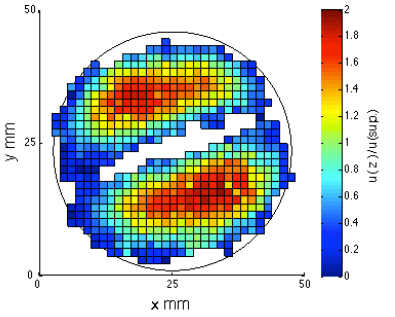
(b) z = L/8	**(g) z = L/8**	**(l) z = L/8**
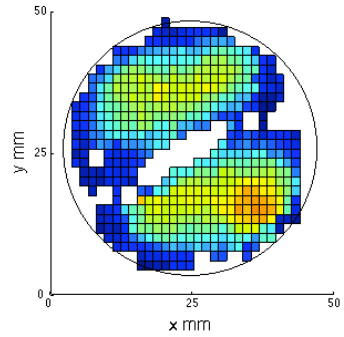	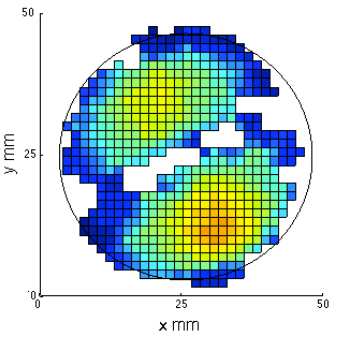	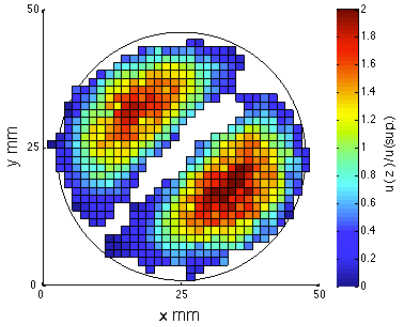
(c) z = L/4	**(h) z = L/4**	**(m) z = L/4**
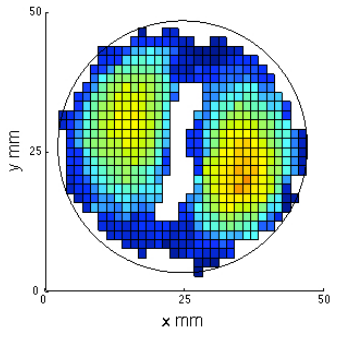	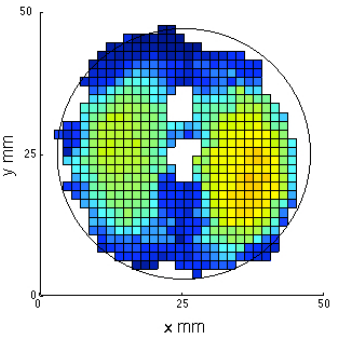	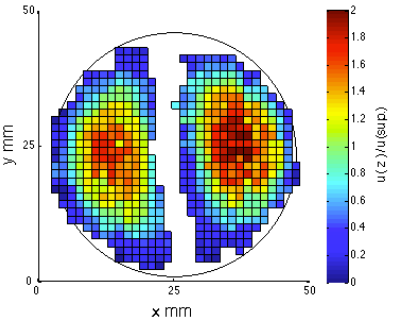
(d) z = L/2	**(i) z = L/2**	**(n) z = L/2**

Continued on the next page

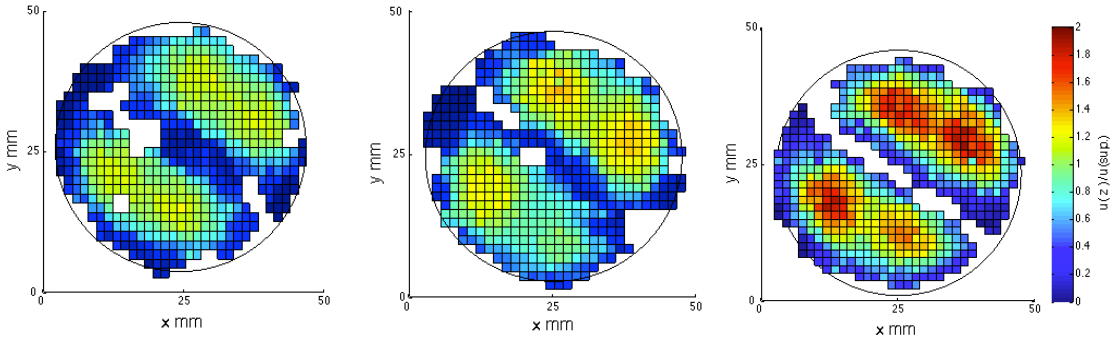

Figure 5.6. Normalised axial velocity map along the third element for: (a-e) Carbopol 0.1 wt%; (b-j) Carbopol 0.2 wt%, and (c-o) glycerol.

As shown in Figure 5.6 within each element ($L/8 < z < 3L/4$) there are two velocity zones, and each one of them is located on one side of the blade. Due to the orthogonal orientation of the downstream blade, each zone is split into two zones to create four velocity zones on the transition regions ($z = 0$) between the two consecutive elements. Each two velocity zones then merge on each side of the blade of the next element. For $L/4 < z < L/2$, the maximum peak of the velocity is located in the middle of the distance from the both solid boundaries of the system on each side of the blade. It is not possible to compare the thicknesses of the boundary layer around the inner wall of the pipe in each condition, due to the resolution and the difference in data density between the three fluids. However, comparing the velocity maps of both non-Newtonian and Newtonian fluids for $L/8 < z < 3L/4$ shows the high velocity area located between the blade and the inner wall of the pipe appears wider for non-Newtonian fluids than the Newtonian fluid. In order to investigate the differences between the shapes of the velocity profile for all these fluids, their predicted pipe flow velocity profiles are shown in Figure 5.7, using Equation 5.3 for non-Newtonian fluids, and Equation 4.2 for Newtonian fluids.

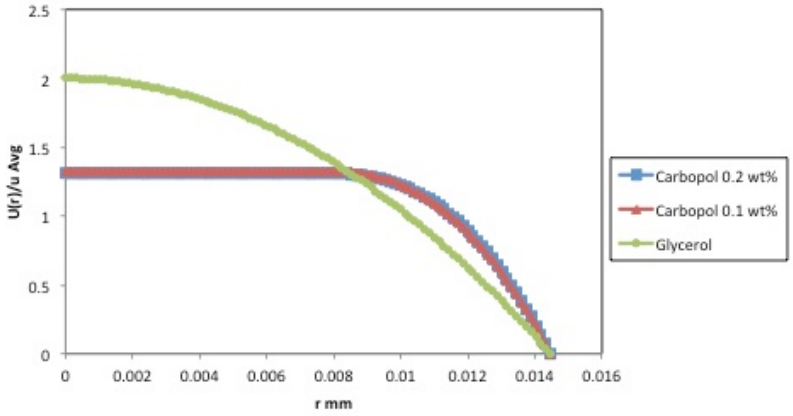

Figure 5.7. Predicted pipe flow velocity profile for Carbopol 0.1 wt%, Carbopol 0.2 wt%, and glycerol solutions.

Figure 5.7 shows the maximum velocity area is flatter for the non-Newtonian fluids in comparison with the Newtonian case, due to the shear-thinning property of the Carbopol solutions, with the maximum normalised velocity around 1.4 for non-Newtonian fluids, and 2 for the Newtonian fluid. This result is in agreement with the observation of the velocity maps in Figure 5.6, which showed the similarity between the velocity maps of the Carbopol solutions.

Figure 5.8 shows the vector plots used to study the velocity fields overlapped with the contour maps relative to the *x* and *y* components. The colour intensity on the contour plots, therefore, represents the length of the vectors, given by $|u(x)+u(y)|$, which represents the velocity in the cross-sectional plane.

Carbopol 0.1 wt%	Carbopol 0.2 wt%	Glycerol

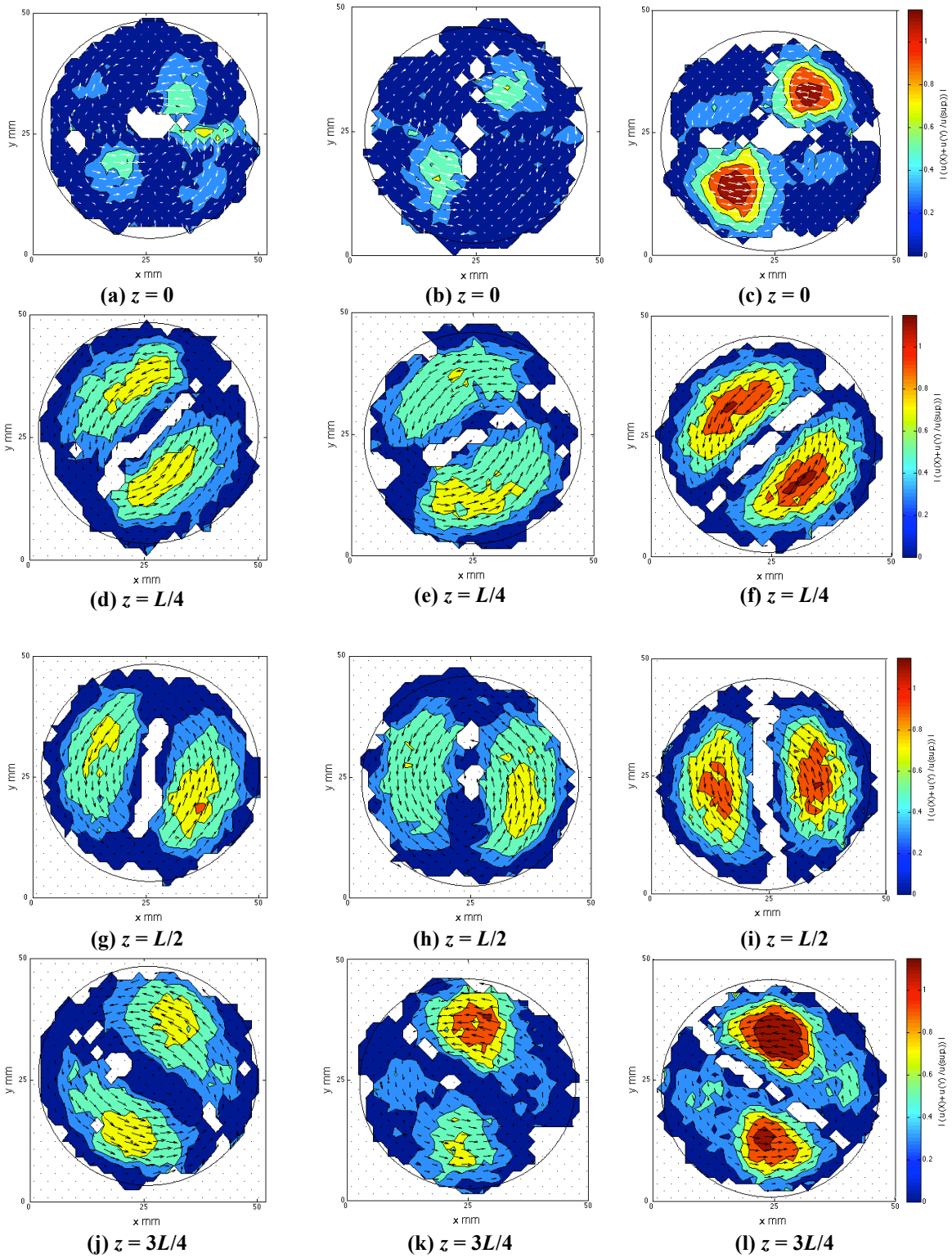

(a) $z = 0$ (b) $z = 0$ (c) $z = 0$

(d) $z = L/4$ (e) $z = L/4$ (f) $z = L/4$

(g) $z = L/2$ (h) $z = L/2$ (i) $z = L/2$

(j) $z = 3L/4$ (k) $z = 3L/4$ (l) $z = 3L/4$

Figure 5.8. Velocity vector plots of *x*- and *y*- velocity components of Carbopol 0.1 wt%, Carbopol 0.2 wt%, and glycerol solutions along the third element at (a-c) $z = 0$; (d-f) $z = L/4$; (g-i) $z = L/2$; (j-l) $z = 3L$-4.

The twist of the third element induces the flow to rotate anti-clockwise; this is shown in Figure 5.8 : (a), (b) and (c), referring to the plane crossing the transition between elements two and three. In this particular section, there are four velocity zones. The velocity zones are symmetric diagonally, and the value of normalised $|u(x)+u(y)|$ is higher for the second and third quadrant. In these quadrants of higher velocity, the flow direction - defined as the direction of the vectors - is anti-clockwise; while the ones located at the first and fourth quadrants are rotating clockwise with a smaller modulus. The opposite twist direction of the second and third elements is affecting the direction of the movement of the fluid, which is passing through the transitional region. From the immediate areas after the cross-section (shown in Figure 5.8 from $z = L/4$ to $z = 3L/2$) one velocity zone is created on each side of the blade for all the fluids. Towards the end of the element, at $z = 3L/4$, the velocity zones with a higher velocity are closer to the corner of the geometry as a result of getting closer to the next transitional region. The comparison between all the velocity maps shows the similarity between the non-Newtonian fluids, while a significant difference is observed between the non-Newtonian and Newtonian fluids. As shown in Figure 5.8 (c), (f), (i) and (l), the highest value of normalised cross-sectional velocity for glycerol is around 1.5, while this value is around 0.7 for non-Newtonian fluids. The area with the velocity greater than 0.7 (shown in yellow) for glycerol is much wider when compared with the Carbopol solutions. The tangential velocity for all the fluids is calculated to gain a better understanding of the rotation of the fluid within each cross-section. Figure 5.9 (a), (b) and (c) shows the tangential velocity maps of all fluids located at the middle of the third element. By selecting the row of cells located at $y = 25$, which is normal to the blade, the tangential velocity profile of all fluids is plotted at this plane, as in Figure 5.9 (d), (e) and (f).

Carbopol 0.1 wt%	Carbopol 0.2 wt%	Glycerol

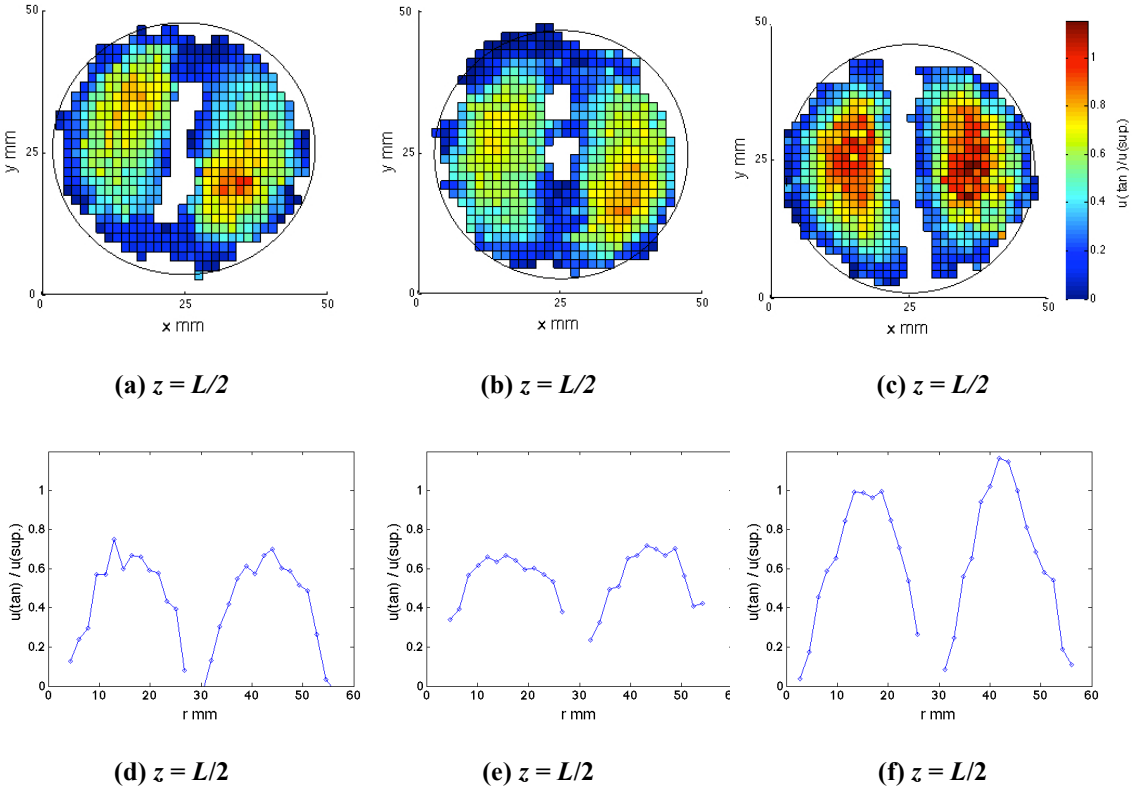

(a) $z = L/2$ **(b)** $z = L/2$ **(c)** $z = L/2$

(d) $z = L/2$ **(e)** $z = L/2$ **(f)** $z = L/2$

Figure 5.9. (a), (b) and (c) show the tangential velocity maps for the Carbopol solutions and glycerol located at the middle of the third element; (d), (e) and (f) show the tangential velocity profile for the Carbopol solutions and glycerol corresponding to the same location.

As shown in Figure 5.9 (d), (e) and (f), for all the fluids the minimum value of normalised tangential velocity is located next to the solid boundaries of the system, while the maximum value is located in the middle of the area between the blade and the inner wall of the pipe. The maximum value of the velocity for glycerol is around 1.5, which is higher than for the Carbopol solutions. By repeating the same procedure, it is possible to plot the axial velocity profile for all the fluids located at the plane normal to the blade (Figure 5.10). According to Figure 5.10 (d), (e) and (f), the maximum value of the normalised axial velocity is also higher for glycerol in

comparison with the Carbopol solutions. This is in agreement with the predicted pipe flow velocity profile in the laminar regime, as shown in Figure 5.7.

Carbopol 0.1 wt%	Carbopol 0.2 wt%	Glycerol

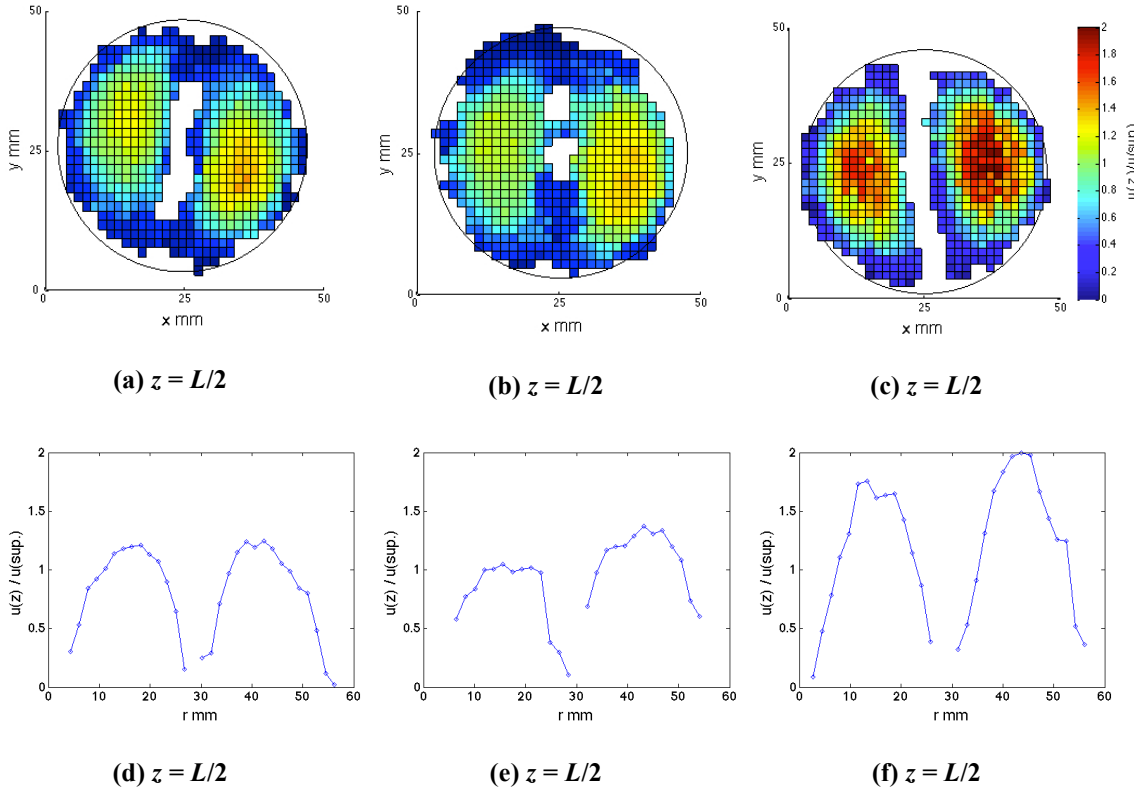

(a) $z = L/2$ (b) $z = L/2$ (c) $z = L/2$

(d) $z = L/2$ (e) $z = L/2$ (f) $z = L/2$

Figure 5.10. (a), (b) and (c) show axial velocity maps for the Carbopol solutions and glycerol located at the middle of the third element; (d), (e) and (f) show the axial velocity profile for the Carbopol solutions and glycerol corresponding to the same location.

Van Wageningen et al. (2004) investigated the flow in the KM, both numerically (FLUENT) and experimentally (Laser Doppler Anemometry), using glycerol solution as the fluid. They studied the velocity profiles for different Reynolds numbers through the KM. The smallest Reynolds number investigated was $N_{Re} = 20$, which is the closest one to the Reynolds numbers used in this work. Figure 5.11 presents the axial and tangential velocity profiles obtained with both numerical and experimental techniques. Figure 5.11 shows that the peak of the normalised axial velocity profile

for N_{Re} = 20 is located at u^* = 2, where u^* is the normalised velocity profile. This number reduces to one for the tangential velocity on the same plot. A comparison between Figure 5.11, and Figure 5.9(f) shows that the peak of both axial and tangential velocity profiles (peak of the parabola) calculated from the PEPT experiment for the glycerol solution matches the ones from the Van Wageningen et al. (2004) work presented in Figure 5.11.

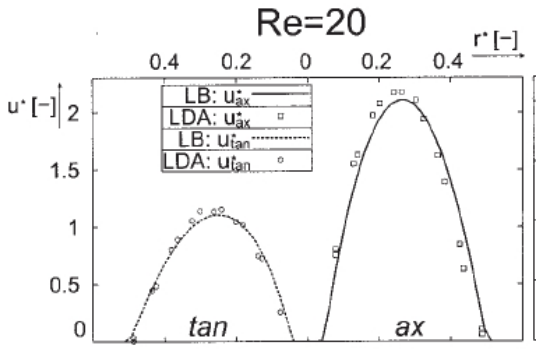

Figure 5.11. Comparison of the axial and tangential velocity profiles obtained with Laser Doppler Anemometry and the Lattice Bolzman method (a class of CFD methods for fluid simulations) at a Reynolds number of 20 (Van Wageningen et al., 2004*).*

The results from Figure 5.6 and Figure 5.8 show that the maximum normalised tangential and axial velocities are higher for the Newtonian fluid in comparison with the non-Newtonian solutions. Hence, the time taken by the fluid along the centreline, where the velocity is the highest, to travel through the element is less for the Newtonian fluid in comparison with the non-Newtonian ones. Consequently, it takes a shorter time for the Newtonian fluid to move 180° within the element, meaning the cross-sectional velocity of Newtonian fluid is higher.

Figure 5.9 confirms the same behaviour, by showing a higher velocity for Newtonian fluid in the middle of the area between the blade and the inner wall of the pipe.

5.4 Shear rate

The shear rate maps are calculated from the Eulerian velocities using Equation 3.10 for the various fluids. The shear rate, by definition, is the highest at the wall, and drops by getting further away from the solid boundaries, due to the decrease in the velocity gradient. Figure 5.12 shows the normalised shear rate maps of all the fluids, located at the same axial location along the third element. The value of the shear rate is normalised by the average shear rate of each system, which was calculated before in §5.1.

The value of normalised shear rate is highest close to the solid boundaries of the system for all the fluids along the mixer, as expected. As mentioned before, it is also possible to observe a wider high velocity area for Carbopol 0.1 wt% in comparison with the glycerol from Figure 5.6 and Figure 5.7, due to the shear-thinning behaviour of the Carbopol solution. Hence, it is expected to see a wider area with a lower shear rate between the solid boundaries of the system for non-Newtonian fluids than for glycerol. This difference could be observed by comparing with Figure 5.12(a), (c),(d),and (f), which shows specifically a wider area with a dimension-less shear rate as small as 0-1 between the blade and the inner wall of the pipe for Carbopol 0.1 wt% than for glycerol. There are also a number of cells with a normalised shear rate of >3 for Carbopol 0.2 wt% solution close to the inner wall of the pipe while, for glycerol, the maximum value of shear rate for some cells is around 2.5. This is due to the fact that the shear rate for highly yielding fluids is higher when compared to Newtonian fluids, or fluids with small yield stress. Figure 5.12 shows it is possible to investigate and compare the shear rate for both non-Newtonian and Newtonian fluids using the data from the PEPT experiment.

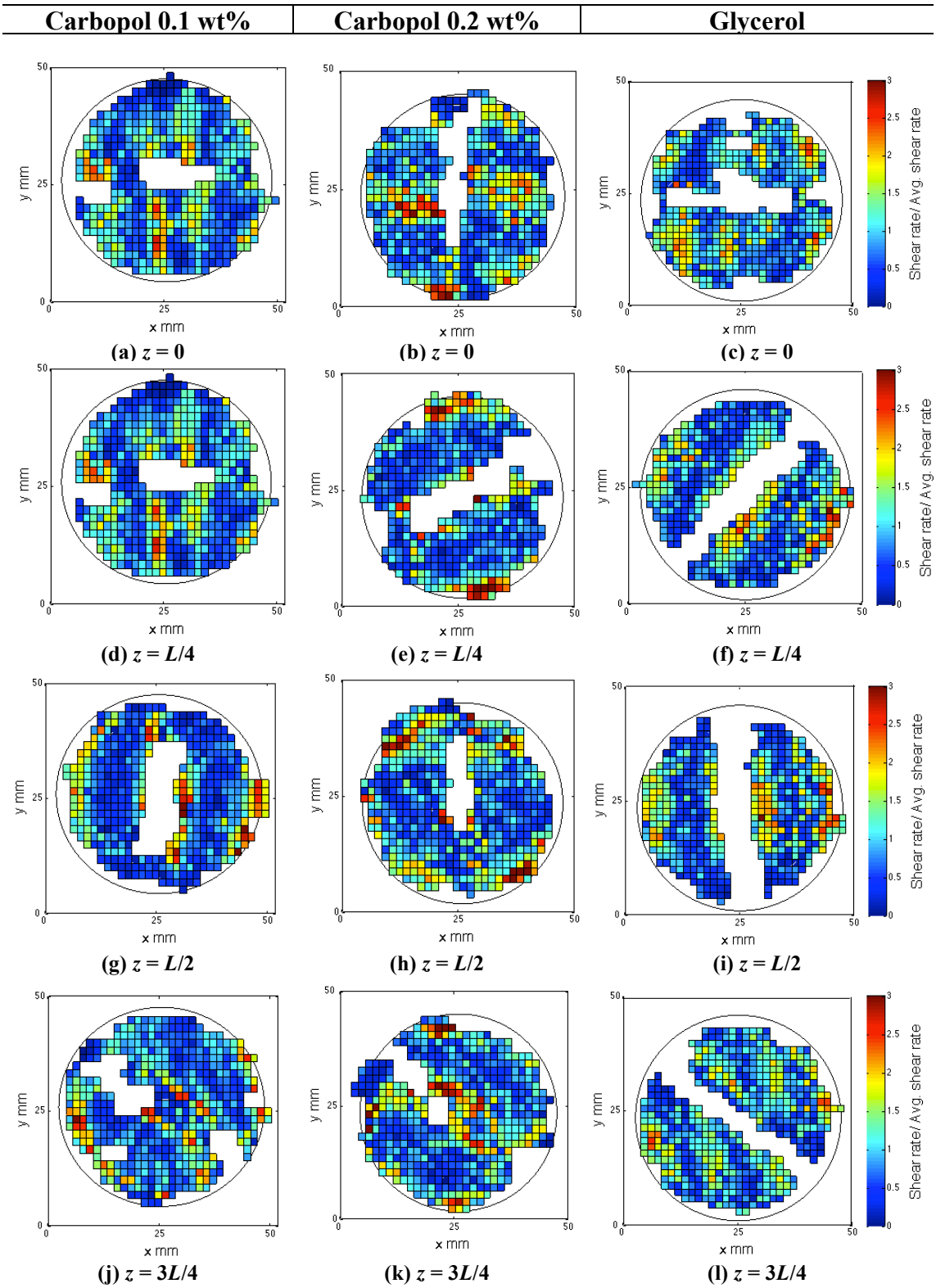

Figure 5.12. Shear rate maps of Carbopol 0.1 wt%, Carbopol 0.2 wt%, and glycerol solutions along the third element at (a-c) $z = 0$; (d-f) $z = L/4$; (g-i) $z = L/2$; (j-l) $z = 3L$-4.

5.5 Studying the mixing performance

Mixing of both non-Newtonian fluids is characterised by calculating the changes in segregation along the mixer. Using the same methodology described in §4.6.2, the particles are classified into two groups according to their entrance location at the start of the mixer. Figure 5.13 shows the distribution of red and blue particles for the Carbopol 0.1 wt% and 0.2 wt% solutions at the same location along the mixer. Figure 5.13 (b) and (i) shows that the shape of the striations for Carbopol 0.1 wt% and 0.2 wt% solutions is different at the middle of the first element. According to the mechanism of flow division and folding patterns in the KM, it is expected to see two striations on each side of the blade at this stage, with opposite colours. The Carbopol 0.2 wt% solution shows similar behaviour, having two striations on each side of the blade while, for the Carbopol 0.1 wt% solution, the shape of the striations is completely different with three striations on each side of the blade. By going further towards the end of the mixer, the particles look more distributed among each other for Carbopol 0.2 wt% while, for Carbopol 0.1 wt%, it is still possible to distinguish the striations, even at the middle of the sixth element.

The changes in the segregation for both non-Newtonian fluids are calculated along the mixer and the result shown in Figure 5.14. The segregation values along the first element are similar for both fluids, however, after going through the first transitional region, the value of segregation drops more for Carbopol 0.2 wt% than Carbopol 0.1 wt%. The value of the segregation is lower for Carbopol 0.2 wt% through the whole length of the mixer and, by the end of the mixer, the value of segregation for Carbopol 0.2 wt% reaches unity, which is nearly 0.4 units less than the final value of segregation for Carbopol 0.1 wt%.

Carbopol 0.1 wt%	Carbopol 0.2 wt%
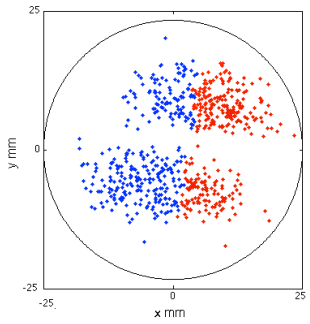	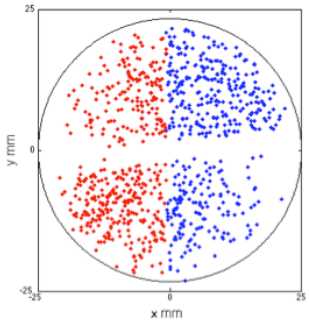
(a) Entrance of the mixer	(h) Entrance of the mixer
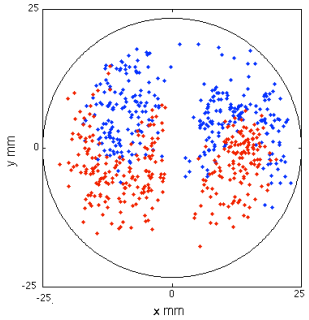	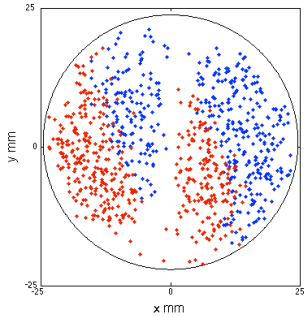
(b) Middle of the first element	(i) Middle of the first element
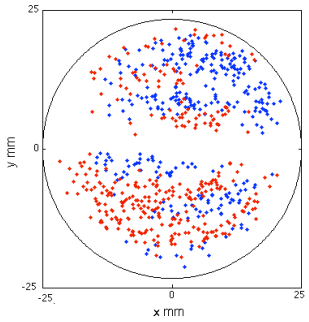	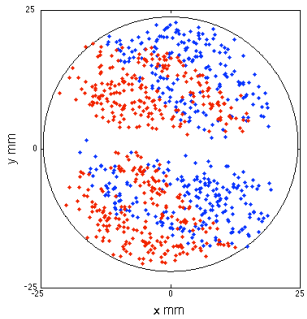
(c) Middle of the second element	(j) Middle of the second element
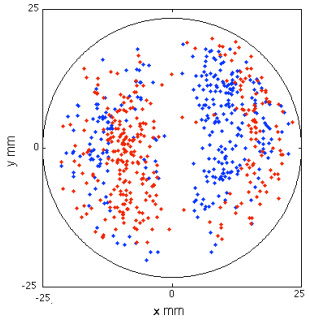	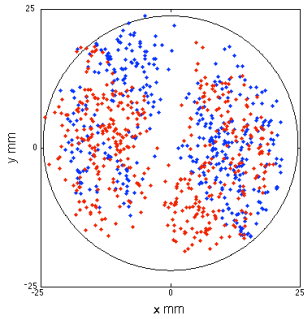
(d) Middle of the third element	(k) Middle of the third element

Continued on the next page

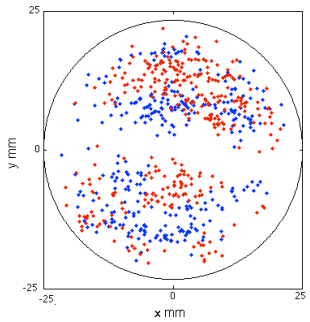

(e) Middle of the fourth element

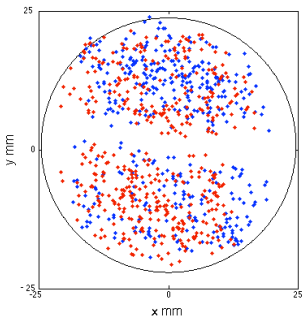

(l) Middle of the fourth element

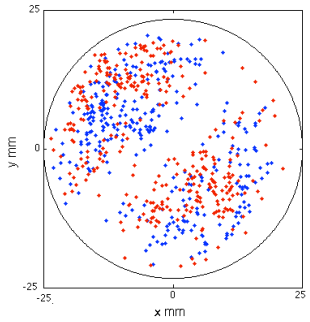

(f) Middle of the fifth element

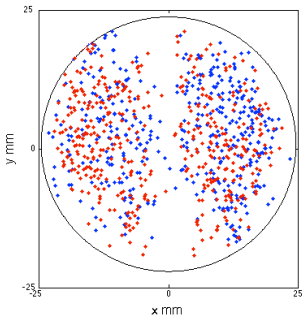

(m) Middle of the fifth element

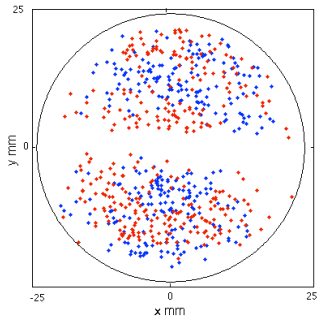

(g) Middle of the sixth element

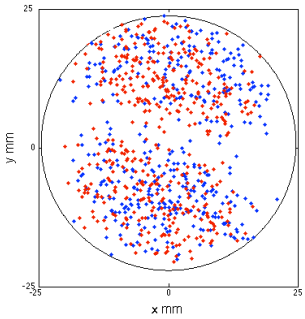

(n) Middle of the sixth element

Figure 5.13. Distribution of red and blue particles along the mixer for: (a-g) Carbopol 0.1 wt%; (h-n) Carbopol 0.2 wt%.

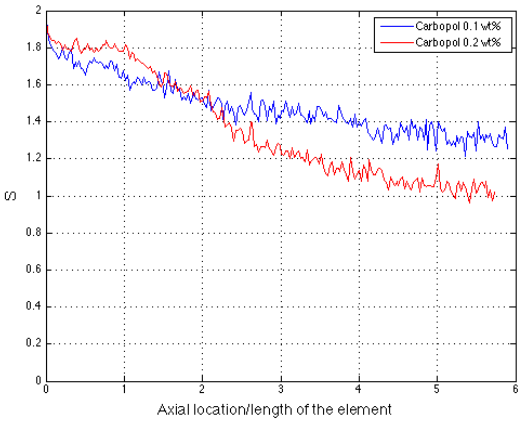

Figure 5.14. Changes in segregation along the mixer for both non-Newtonian fluids.

Changes in the contact numbers between the particles of each group in Figure 5.15(a) and (b) shows the contact number between the particles of all groups is fluctuating around a constant number along the sixth element of the mixer for the Carbopol 0.1 wt% solution. However, there is a large gap between the contact numbers of the particles of each group by the end of the mixer for the Carbopol 0.1 wt% solution. The changes in the average distance between the particles of each group in Figure 5.15(c) and (d) show the same result. By the sixth element, the particles become so close to each other that it is not possible to distinguish them for the Carbopol 0.2 wt% solution. However, for Carbopol 0.1 wt%, by the end of the sixth element, it is still possible to differentiate the red and blue particles from each other. These results show that, for Carbopol 0.2 wt%, the system reaches the randomised mixing stage by the end of the sixth element while, for the Carbopol 0.1 wt% solution, it does not. This difference between the mixing performances between both fluids is not expected, considering the similarity between their velocity profile (Figure 5.7), and the similar rheological properties of both fluids.

Carbopol 0.1 wt%	Carbopol 0.2 wt%

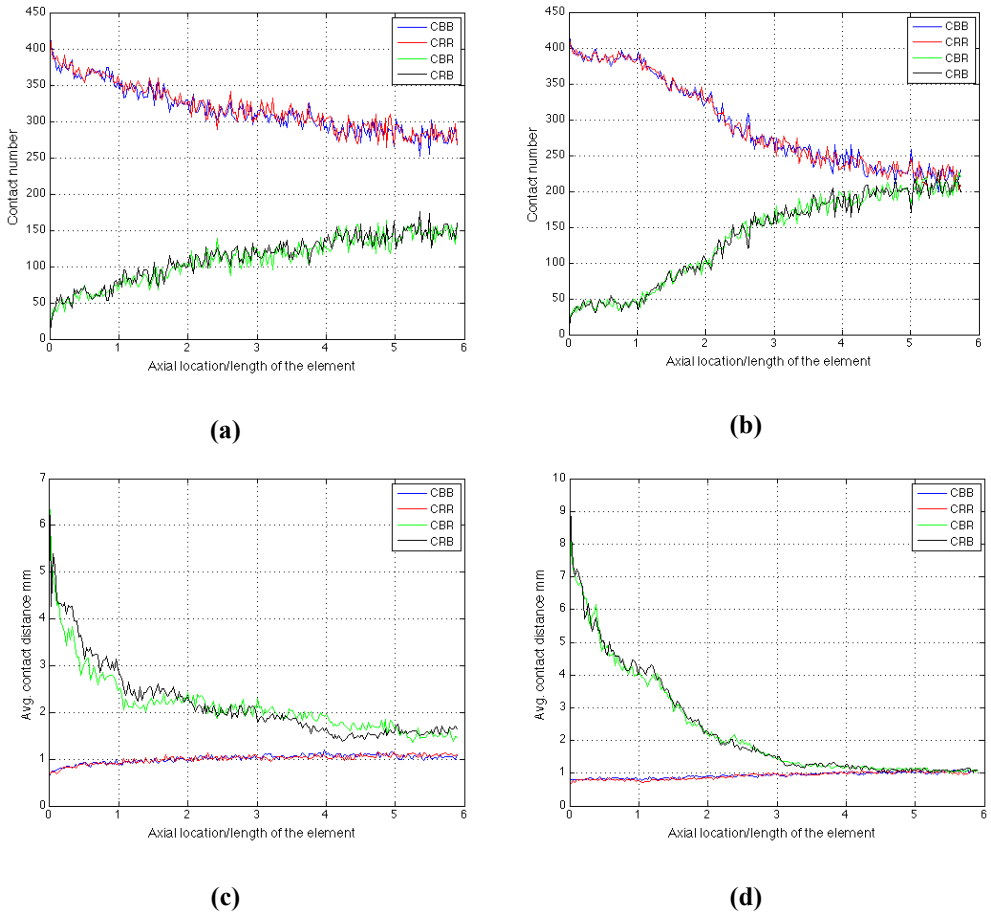

Figure 5.15. Changes in the contact number between the particles of each group for both non-Newtonian fluids (a) and (b); changes in the average contact distance between the particles of each group for both non-Newtonian fluids (c) and (d).

Figure 5.13 shows that, although the overall number of particles is the same for both fluids, the particles do not occupy the whole cross-section of the mixer at the entrance for the Carbopol 0.1 wt% solution. If the existence of some entrance effect is affecting the mixing performance of the Carbopol 0.1 wt% solution, by calculating the segregation starting from the middle of the first element, the changes in segregation for Carbopol 0.1 wt% should become similar to the one for Carbopol 0.2 wt%. Therefore, the change in segregation is calculated using two different locations as the

entrance: middle of the first element and middle of the third element. Figure 5.16 shows the different starting locations used to calculate the segregation.

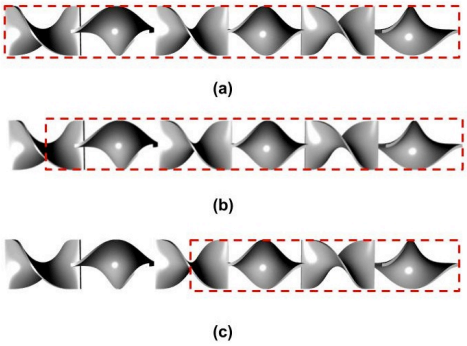

Figure 5.16. Calculating the segregation using different starting locations: (a) starting from the first element; (b) starting from the middle of the first element; (c) starting from the middle of the third element.

Figure 5.17 (a) and (b) shows the cross-section of the mixer at the middle of the first element, where the blue and red particles are defined. A comparison between Figure 5.17 (a) and Figure 5.13 (a) shows that, for Carbopol 0.1 wt%, the particles occupy a larger area of the cross-section in the middle of the first element rather than at the start of the mixer. Figure 5.17 (c) and (d) shows the cross-section of the mixer at the middle of the second element for both fluids. It is possible to observe two red striations on the upper half of the mixer for Carbopol 0.2 wt% while, for Carbopol 0.1 wt%, there are just a few red particles available in the same area, showing the particles are not distributed as much as for Carbopol 0.2 wt%. By calculating the changes in the segregation along the mixer for this case, it is observed in Figure 5.17 (e) that the mixing performance of Carbopol 0.2 wt% is still better than Carbopol 0.1 wt% along the mixer, by having a final value of segregation, which is nearly 0.2 units less than Carbopol 0.1 wt%.

Carbopol 0.1 wt%	Carbopol 0.2 wt%

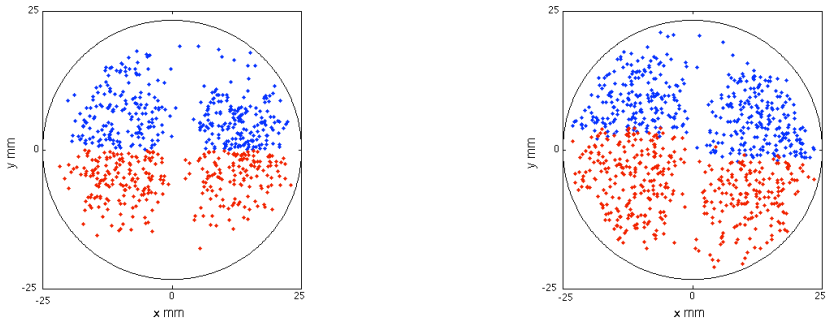

(a) **(b)**

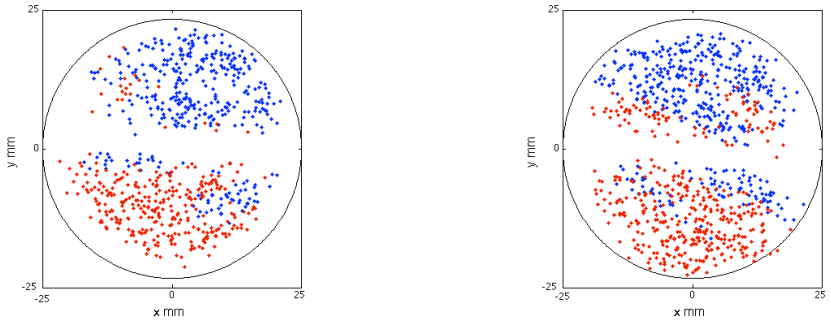

(c) **(d)**

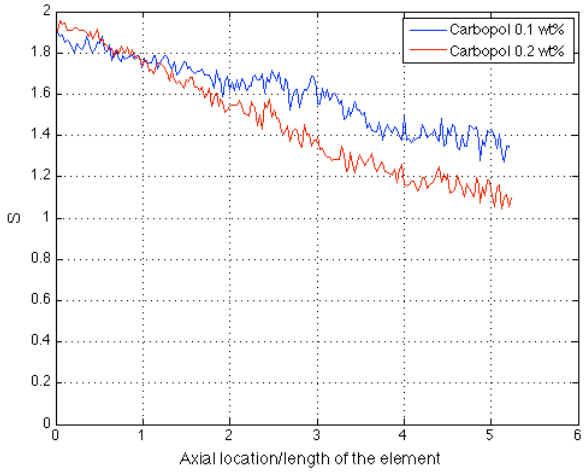

(e)

Figure 5.17. (a) and (b) define the red and blue particles at the middle of the first element; (c) and (d) show the distribution of red and blue particles at the middle of the second element; (e) shows the segregation changes along the mixer by defining the blue and red particles at the middle of the first element.

The same procedure is done by defining the entrance of the mixer at the start of the third element. Figure 5.18 (a) and (b) shows the position of the red and blue particles at the start of the third element. By going through one element, it is not possible to distinguish the exact shape of the blue striation on the lower half of the mixer for the Carbopol 0.1 wt% solution (Figure 5.18 (c)). Figure 5.18 (e) shows that, although the first three elements have not been considered in the calculations, the value of segregation is still 0.2 units smaller for Carbopol 0.2 wt%. This indicates that the reason behind having a lower mixing point for Carbopol 0.1 wt% cannot be the existence of any entrance effect on the fluid.

On the other hand, the theoretical development lengths of Carbopol 0.1 wt% and 0.2 wt%, which were calculated in § 5.2, showed the development length of Carbopol 0.1 wt% is almost three times more than Carbopol 0.2 wt%. The velocity distribution maps also showed that, by entering an element, the velocity profile gradually develops for both fluids by passing through each single element. The longer development length of Carbopol 0.1 wt% might have an effect on the stretching of the fluid along the element. The qualitative measurement of stretching is presented by visualising the changes in shape of the blue and red striations along the mixer. The common observation between Figure 5.13, Figure 5.17 and Figure 5.18 showed the blue and red striations look less stretched for Carbopol 0.1 wt% than for Carbopol 0.2 wt% along the elements. Further analysis can be carried out in the future as a quantitative measurement of stretching, by relating the changes in the number of blue and red particles on each side of the blade along the mixer to the stretching of the striations.

Carbopol 0.1 wt%	Carbopol 0.2 wt%

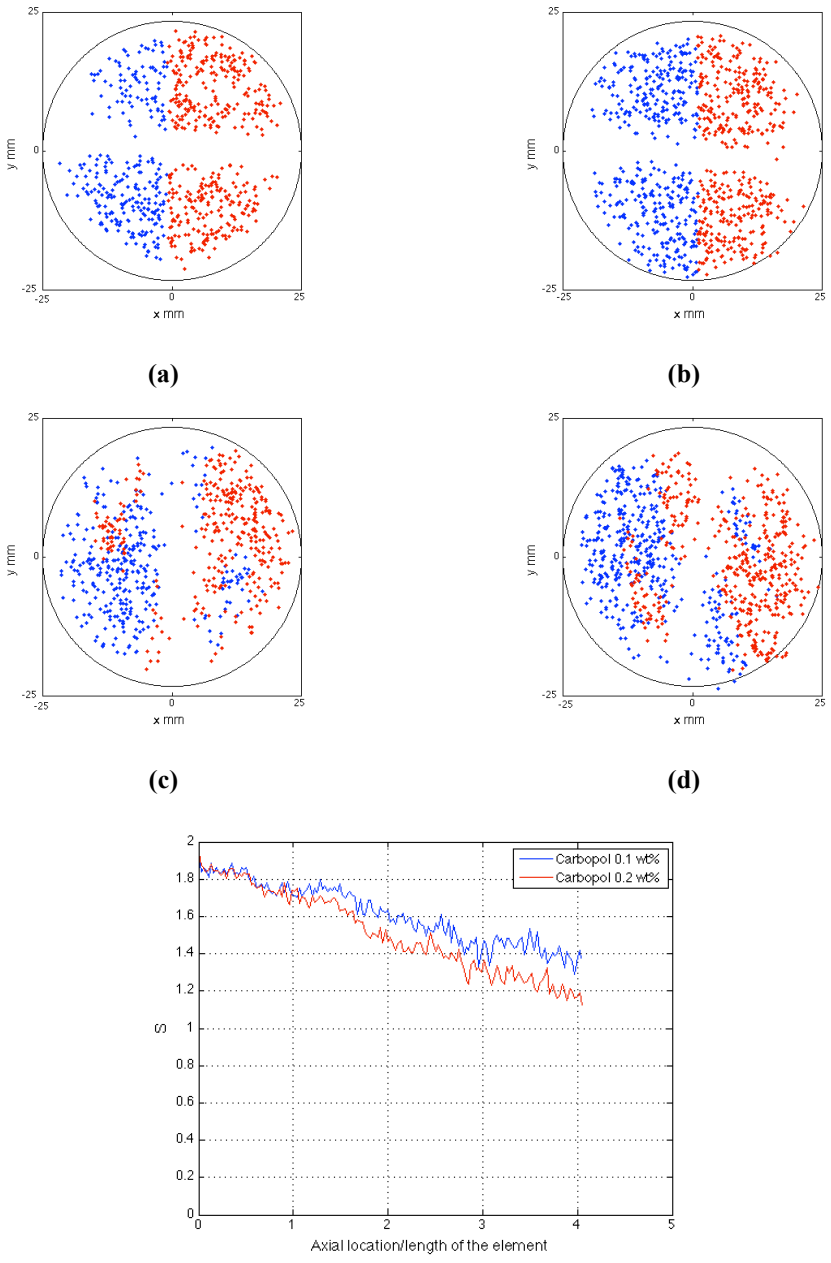

Figure 5.18. (a) and (b) define the red and blue particles at the middle of the second element; (c) and (d) show the distribution of red and blue particles at the middle of the third element; (e) shows the segregation changes along the mixer by defining the blue and red particles at the middle of the second element.

5.6 Residence time distributions

5.6.1 Studying the residence time distribution from the experimental data

The residence time distribution (RTD) function is calculated using Equation 4.9, following the same procedure described in § 4.6.1.

Figure 5.19 shows the RTD normalised by the mean residence time ($\theta = t/\bar{t}$) for both non-Newtonian fluids along each single element of the mixer. As mentioned in §4.7.1, the minimum time for the tracer to pass through an empty pipe is θ = 0.5 for Newtonian fluids. Since the centre line velocity for the non-Newtonian fluids is less than that for Newtonian, it should take a longer time than θ = 0.5 for the tracer to go through the mixer for non-Newtonian fluids. As shown in Figure 5.19 (a) and (b), the minimum time for the tracer to go through each single element is more than 0.5 for both non-Newtonian fluids, as expected, except for the first and sixth elements. A similar deviation for the first and the sixth elements was observed also for Newtonian fluids, as a result of the poor data quality at the elements located furthest from the centre of the field of view. Figure 5.19 (c) presents the changes in the mean residence time for each single element for both solutions, as well as the estimated value of mean residence time from the superficial velocity for each experiment. It is observed that the value of mean residence time, according to the experiment, is in agreement with those estimated from the superficial velocities of each fluid. The value of mean residence time does not change significantly for each single element along the mixer, as expected.

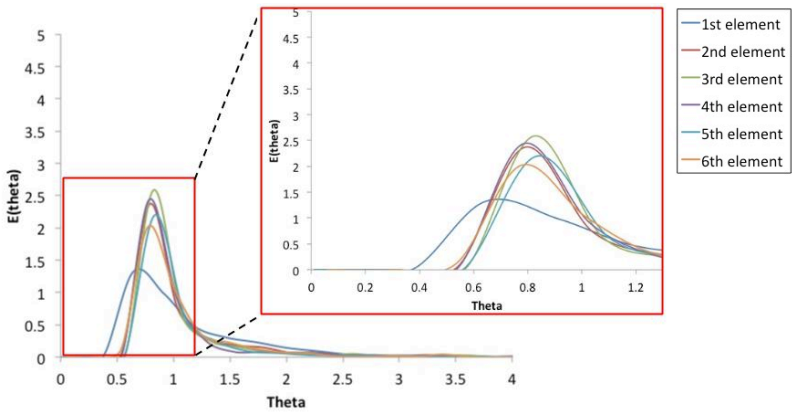

(a) Carbopol 0.1 wt%

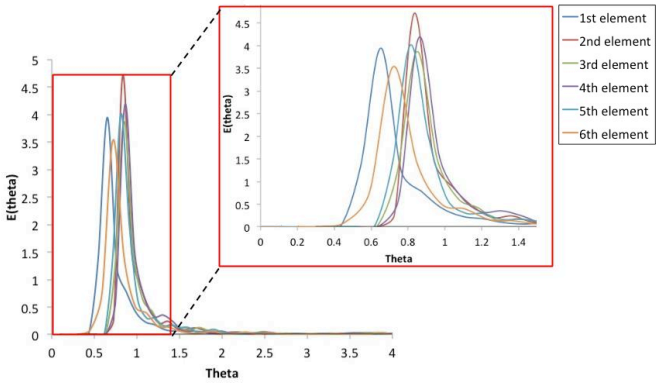

(b) Carbopol 0.2 wt%

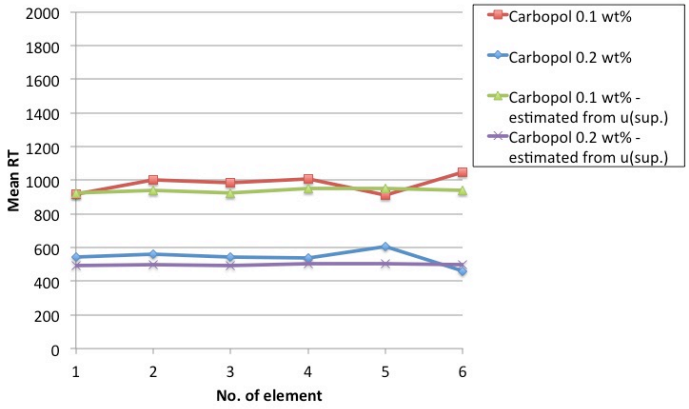

(c)

Figure 5.19. (a) shows normalised RTD for each single element for Carbopol 0.1%; (b) shows normalised RTD for each single element for Carbopol 0.2%; (c) shows mean residence time along each element for both solutions.

However, further from the centre of the field of view, i.e., getting closer to the start and end of the mixer, a small deviation from the value of mean residence time along

the second to the fourth elements could be observed. This indicates that the position of the first and the last elements also causes a deviation from the mean residence time of the rest of the elements, due to the poor quality of the data.

5.6.2 Choice of model for residence time distribution

Since the shear-thinning non-Newtonian fluids are very viscous, they should be treated by the convective model (Levenspiel, 1972), with diffusion being assumed as negligible. The analytical solution for convective model to calculate $E(\theta)$ is available for Newtonian fluids in §4.6.2. Although the analytical solution of $E(\theta)$ is also available for power-law and Bingham fluids, no available solution has been previously found for Herschel-Bulkley fluids (Levenspiel, 1972 and 1979). Hence, the normalised RTD model is directly derived from the equation of the velocity profile for Herschel-Bulkley fluids (Equation 5.3). Figure 5.20 shows the predicted pipe flow velocity profile of the Carbopol 0.2 wt% solution. To calculate the RTD function, the flow area between each two consecutive radii (shown as red area in Figure 5.20) is calculated for the whole cross-section:

$$A_{flow} = \pi(r_{j+1}^2 - r_j^2) \qquad \textbf{(Equation 5.10)}$$

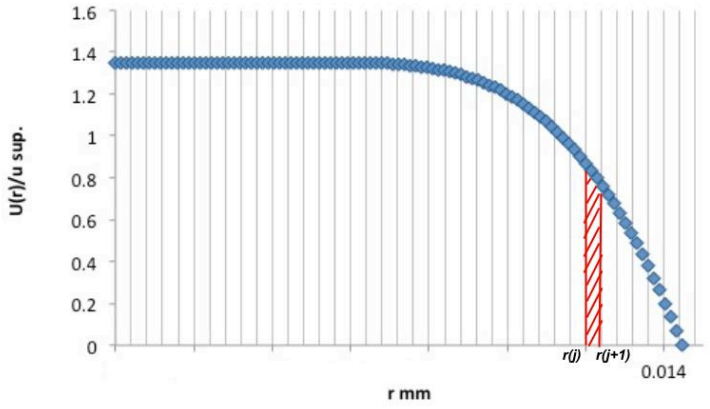

Figure 5.20. Calculating the RTD function from the velocity profile.

By multiplying the local mean velocity by the flow area of each section, the volumetric flow rate corresponding to each section is calculated as follows:

$$Q' = u(r) * A_{flow}$$
$$A_{flow} = \pi\left(\left(r + dr\right)^2 - r^2\right) \qquad \textbf{(Equation 5.11)}$$

For each annulus, the residence time is proportional to *1/Q′(r)* and, consequently, the fraction of passes with the residence time between *t* and (*t+dt)* is equal to $Q'(t)\Big/\sum Q$. The residence time between each two consecutive radii is then calculated by dividing the distance between them by the value of velocity corresponding to each radius. By dividing the fraction of passes into the value of the residence time between each two consecutive radii, the RTD function, or *E(t),* can be obtained:

$$E(t)_r = \frac{Q'(r)}{\sum Q} / \left(t(r + dr) - t(r)\right) \qquad \textbf{(Equation 5.12)}$$

Figure 5.21 shows the comparison between the RTD curves calculated from the velocity profile, and the experimental RTD curves for Carbopol 0.1 wt% and Carbopol 0.2 wt% solutions for each single element along the mixer. It can be observed that the shape of the RTD curves of each single element is similar to the one calculated from the model. The deviation between the RTD curve of the model and the one for the experimental data could be due to the fact that this model is calculated based on the velocity profile of an empty pipe, while the KM consists of a number of elements within the pipe, and the existence of these elements affects the RTD of the particles.

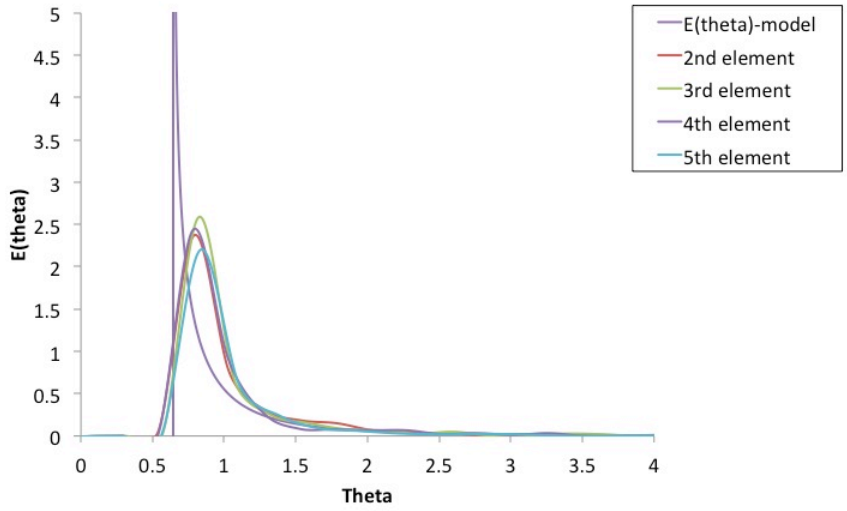

(a)

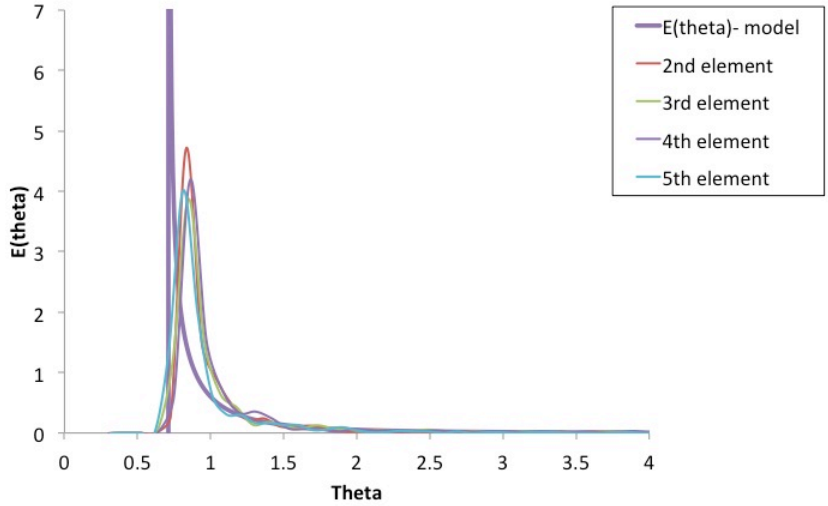

(b)

Figure 5.21. RTD of single elements of the KM in comparison with the model for (a) Carbopol 0.1 wt%; (b) Carbopol 0.2 wt%.

Figure 5.22 shows the experimental RTD for both solutions calculated from the first element along the mixer. For both solutions, the minimum time for the tracer to go through the mixer is more than 0.5, as expected. As shown in Figure 5.22 (a) and (b), by going through a higher number of elements, the value of the mean residence time increases. This indicates the peak of the RTD curve is shifting towards $\theta = 1$ by going through a higher number of elements.

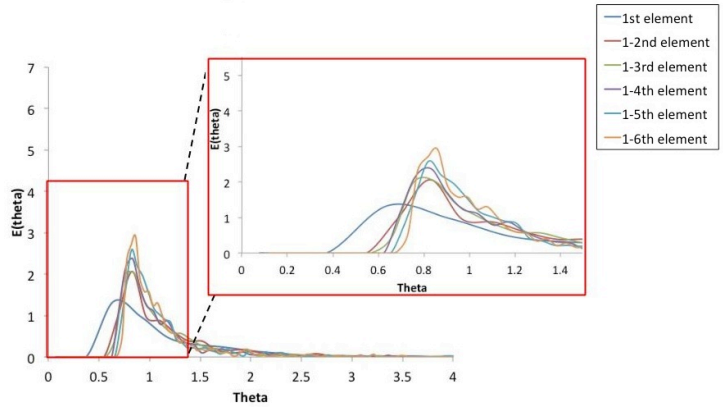

(a) Carbopol 0.1 wt%

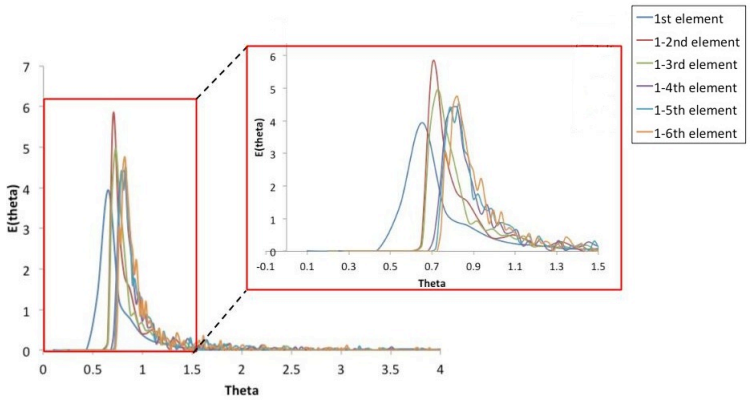

(b) Carbopol 0.2 wt%

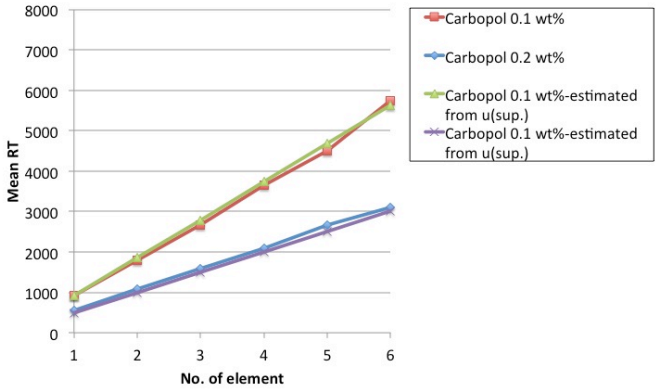

(c)

Figure 5.22. (a) shows normalised RTD along the mixer for Carbopol 0.1 wt%; (b) shows normalised RTD along the mixer for Carbopol 0.2 wt%; (c) shows mean residence time along the mixer for both solutions.

The lower value of the mean residence time for Carbopol 0.1 wt% in comparison with Carbopol 0.2 wt% is due to having a lower superficial velocity (Figure 5.22(c)).

Figure 5.22 (c) also shows that the mean residence time along the mixer calculated from the experimental data is close to the estimated one calculated when knowing the value of superficial velocity for each solution. The maximum value of $E(\theta)$ is higher for Carbopol 0.2 wt%. This could be justified by looking at the predicted pipe flow velocity profile of this solution, which shows a wider flat area on the centre line velocity. This indicates a higher volume of fluid is passing through the flat area of the velocity profile, causing it to have a higher fraction of tracers exiting before the mean residence time.

Figure 5.23 shows the comparison between the experimental RTD curves calculated from the start of the first element with the one from the model.

As shown in Figure 5.23 (a) and (b), the $E(\theta)$ calculated from the velocity profile looks similar for both fluids, as expected, considering the similarity between the shape of their velocity profiles (Figure 5.7). The normalised RTDs calculated from the experimental data are close to that the model predicted for both cases. As mentioned in §5.6.1, the value of θ at the peak of the curve is shifting towards one by going further through the mixer. This indicates that, by passing through a higher number of elements, the RTD curves are getting further away from the convection RTD model, and getting close to the shape of the RTD of the dispersion model, as discussed in §4.7.2. It was also shown in Figure 5.21 that the RTD curve of each single element was located close to the one used for the model and looked similar to it. This behaviour demonstrates also the main mechanisms of mixing in the KM.

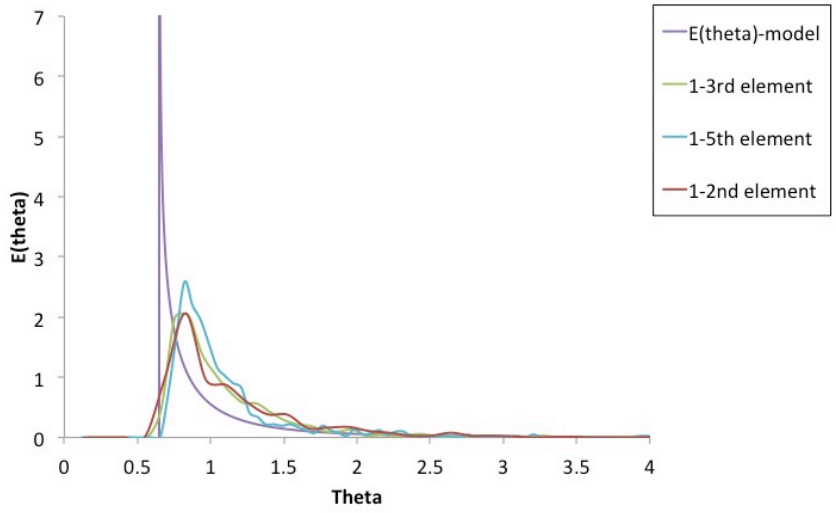

(a)

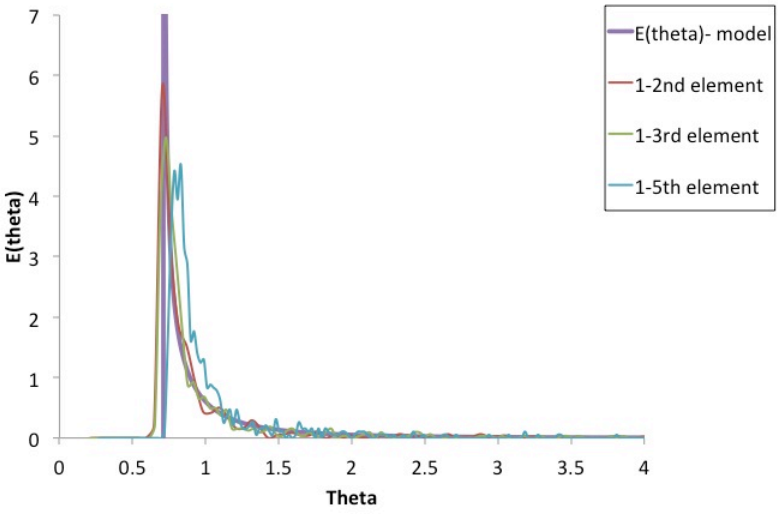

(b)

Figure 5.23. Comparison between the RTD model calculated from the velocity profile, and the RTD function calculated from the experimental data for (a) Carbopol 0.1 wt%; (b) Carbopol 0.2 wt%.

The main mechanism of mixing along each single element of the KM is distributive mixing, which can be observed in the similarity between the experimental RTD of each single element to the model calculated from the velocity profile. The dispersive mixing can be related to the shifting of the RTD curves towards the one for the dispersion model by going through a higher number of elements. The main changes in dispersion is happening within the transitional region between the elements and,

consequently, by passing through more transitional region, the RTD curves are getting closer to the shape of the one in the dispersion model.

5.7 Conclusion

In this chapter the results from PEPT experiments using two non-Newtonian fluids have been reported and compared. 0.1 wt% 0.2 wt% aqueous solutions of Carbopol 940 were chosen as the non-Newtonian model fluids whose rheology closely followed the Herschel-Bulkley model. The rheological properties of both solutions were studied, and the viscosity, flow behaviour index, and consistency index of both of them were reported. The Reynolds numbers of the solutions were calculated using the equation for generalised Metzner and Reed Reynolds number. The motion of the fluids within the KM is investigated by studying the velocity maps, RTD, and the shear rate maps.

The axial velocity maps of both non-Newtonian fluids looked similar to each other, as expected, which is in agreement with the similarity between their predicted pipe flow velocity profiles. The cross-sectional and tangential velocities of the Carbopol solutions were compared with the results for the Newtonian glycerol solution. The reason behind having a higher cross-sectional velocity for Newtonian fluid in comparison with the non-Newtonian ones was investigated. The tangential and axial velocity profiles of glycerol were found to be similar to the results from Van Wageningen et al. (2004). The cross-sectional velocity of the glycerol solution was found to be more than the one for non-Newtonian fluids, due to the higher centre line velocity of the Newtonian fluids. Hence, the time taken by the Newtonian fluid to travel 180° within an element is shorter than the non-Newtonian one.

The shear rate maps for all the solutions were studied. The area with a low shear rate was found to be wider for the non-Newtonian fluids. This was expected, considering the existence of the wide flat area on the velocity profile of both non-Newtonian fluids. The maximum value of the shear rate was observed next to the solid boundaries of the system, as expected. The results from the shear rate maps shows PEPT could be used to study the shear rate maps of the non-Newtonian fluids.

The mixing performance of both non-Newtonian fluids was characterised using the segregation index. It was observed that, by using the Carbopol 0.2 wt% solution, the system reached the randomised status of mixing at the sixth element while, in case of Carbopol 0.1 wt%, it did not. Bearing in mind the difference between the rheological properties of both fluids, and the similarity between their velocity maps, this difference was not expected. It was shown that this difference was not related to the existence of entrance effect. The observation from the distribution of the blue and red particles along the mixer showed a lower stretch in the striations of Carbopol 0.1 wt% along each element. The calculations of the development length of these fluids showed Carbopol 0.1 wt% solution has a development length at least three times more than the one for Carbopol 0.2 wt%. The higher development length of Carbopol 0.1 wt% could result in slower response to the changes of the geometry after passing through each transition region. Consequently, this difference could cause a reduction in stretching of the fluid elements for Carbopol 0.1 wt%. The author also suggests a quantitative measurement of stretching in the future by relating the stretching of the striations to the number of the blue and red particles on each side of the blade.

The RTD was studied for both fluids, using the related equations. It was shown in the previous chapter that the minimum time for a Newtonian fluid to go through the mixer is around $\theta = 0.5$. The experimental RTD curves for both non-Newtonian solutions

show that the minimum time for the tracer to go through the mixer is more than θ = 0.5. This was expected, due to the lower average velocity on the centre line of the non-Newtonian fluids in comparison with the Newtonian fluid. The values of mean residence time calculated from the experimental data were in agreement with the ones estimated from the superficial velocity for both solutions along the mixer. Since no analytical solution is available for the RTD function in Herschel-Bulkley fluids, the RTD model was estimated from the predicted pipe flow velocity profile of both fluids. It was shown that the shape of the RTD curves becomes closer to the one for the dispersion model by going through a higher number of elements along the mixer. This indicated that, by passing through a higher number of transition regions, the particles become more dispersed, which shows the existence of dispersive mixing on the transition regions within the KM.

The results presented in this chapter show the data from the PEPT experiment could be used to study the motion of the fluid, as well as characterising the mixing performance for the non-Newtonian fluids, as well as the Newtonian fluid.

Notation

Roman letters

A_{flow}	Flow area	m^2
D_h	Hydraulic mean diameter	m
$E(t)$	Residence time distribution function	-
$E(\theta)$	Normalised residence time distribution	-
k	Consistency index	Pa. s^{n-1}
k'	Apparent consistency index	Pa. s^{n-1}
L	Length of the element	m
L_e	Development length	m
N_{Re}	Reynolds number	-
n	Flow index	-
n'	Apparent flow index	-
t	Time	s
$\overline{t}$	Mean residence time	s
Q	Volumetric flow rate	m^3.s
Q'	Volumetric flow rate between two consecutive radii	m^3.s

R	Radius	m
Re_{MR}	Metzner & Reed Reynolds number	-
S	Segregation index	-
$u(r)$	Velocity in r direction	$m.s^{-1}$
$u_{sup.}$	Superficial velocity	$m.s^{-1}$
u^*	Velocity normalised by axial velocity (Van Wageningen et al., 2004)	-
u_x	Velocity in x direction	$m.s^{-1}$
u_y	Velocity in y direction	$m.s^{-1}$
u_z	Velocity in z direction	$m.s^{-1}$
u_{tan}	Tangential velocity	$m.s^{-1}$

Greek letters

τ	Shear stress	Pa
τ_0	Yield stress	Pa
τ_w	Wall shear stress	Pa
$\dot{\gamma}$	Shear rate	s^{-1}
$\dot{\gamma}_{avg.}$	Average shear rate	s^{-1}

ϕ	Ratio of yield stress to the wall shear stress	Pa
ρ	Density of the fluid	kg. m^{-3}
θ	Normalised residence time	-
θ_{min}	Minimum time for the tracer to go through the mixer	-

Chapter 6 . KENICS STATIC MIXER: EFFECT OF TWIST ANGLE

In this chapter, the effect of changing the twist angle of the blades in Kenics static mixer (KM) on the flow behaviour and mixing performance are studied. The effect of the twist angle of the blade on the KM mixing performance has been previously studied in the literature (Hobbs et al. (1998), Byrde et al. (1999), Galaktionov et al. (2003)). Hobbs et al. (1998) calculated the change in variation coefficient along the mixer for different twist angles in a range of 30 to 210°, and showed that the KM with a 150° twist angle gave the best mixing performance in comparison with the others. Galaktionov et al. (2003) studied the optimised twist angle of a KM in the range of 90° to 270° using the intensity of segregation to characterise the mixing performance. They also showed that, by considering the change in the intensity of segregation along the 12 element mixer, the KM with 150° twist angle had the optimised design. It was also shown that, by plotting the changes in the intensity of segregation versus the pressure drop, the KM with 140° twist angle had the highest efficiency. All of these works have been described more detail in §2.2.1. To the authors' knowledge, there has never been any experimental work on the effect of twist angle to support the previous numerical works. Therefore, the objective of this chapter is to study experimentally the mixing performance and flow characteristics of a KM with a 120° and a 150° twist angle.

The standard KM with a 180° twist was modified by changing the twist angle of the elements to 150° and 120° . A detailed description of both geometries is given in § 3.2.1.1.

6.1 Flow regime and rheological properties of the fluid

Glycerol with a purity of >98% was chosen as the model Newtonian fluid for KM 150° and 120°. The glycerol solution used for the experiments in KM 150° and 120° is the same as the one used for the experiments in the KM 180°.

The superficial velocity used during the experiments with both geometries is the same as the one used for the KM 180° , which is 0.09 *m/s*. Since the diameter, the superficial velocity, and the fluid (glycerol solution) are the same as those used for the experiment with KM 180°, the Reynolds number is calculated as the same as for KM 180° (N_{Re} = 5.6).

The development length for Newtonian fluids in a laminar regime is estimated as a function of the Reynolds number from (Shook, 1991):

$$\frac{L_e}{D_h} = 0.062 N_{\mathrm{Re}} \qquad \textbf{(Equation 6.1)}$$

Considering the same Reynolds number and hydraulic mean diameter for both experiments in KM 150° and 120°, the entrance length is calculated as $0.347D_h$ or 0.01 *m*, which is taken into account by keeping an empty length at the bottom of the pipe before the mixer elements.

6.2 Studying the velocity

As mentioned at the start of this chapter, the effect of changing the twist angle of the blade in the KM had been previously studied numerically by Hobbs et al. (1997b), Hobbs et al. (1998), Szalai et al. (2003), and Galaktionov et al. (2003). The velocity distribution maps of the KM with different twist angles were not presented in these

works. The results of the velocity maps in the different modified geometries of the KM are presented here.

6.2.1 Choosing the grid

2000 passes are recorded during each experiment with the KM 150° and 120° geometries, the same as for KM 180°. In § 4.3.1, the analysis of choosing the right cell size for Eulerian velocity maps using the glycerol solution was presented. The same analysis and results of finding the right cell size for the experiment with KM 180° is valid for the experiments in KM 150° and 120°, considering the similarity between the fluids, superficial velocity, and total number of passes. The geometry is meshed using cells with the length of 2 *mm* in x and y direction, and 4 *mm* in z direction.

It was shown in § 4.3.2, that the value of the average velocity assigned to each cell is calculated over a sufficient number of locations within the cell. Since the fluid, number of cells, number of passes, and the value of superficial velocity for the experiments in KM 150° and 120° are same as the ones used in Chapter 4 for KM 180 with glycerol, the same result is valid here as well.

6.2.2 Studying the velocity maps in the Cartesian reference system

The Eulerian velocity maps of both geometries are plotted following the procedure of calculating the average velocity within each cell, as described in § 3.3.3. In this section, the velocity maps along the third element for both modified geometries are presented and compared with each other. The third element for all geometries is located close to the centre of the field of view, and therefore has the best data quality. Figure 6.1 presents the velocity maps along the third element for the KM with 120°, 150° and 180° twist angles, relative to their axial coordinates of $z = 0$, $z = L/8$, $z = L/4$,

$z = L/2$, and $z = 3L/4$, with L being the length of the element. The value of axial velocity is normalised by the value of the superficial velocity.

Four velocity zones are created in the transitional region at $z = 0$ for all the geometries. For KM 180° , the four velocity zones join together, creating two velocity zones on each side of the blade at $z = L/8$. However, for KM 120° and 150°, it is still possible to distinguish the two velocity zones on each side of the blade at $z = L/8$. For $L/4 < z < L/2$, the velocity maps of KM 180° look similar to each other, showing the flow is already developed after $z = L/4$. The two high velocity cores on each side of the blade look slightly wider at $z = L/4$ than at $z = L/2$ for both KM 150° and 120°.

The shortest length of the element (L) is for KM 120° (51 *mm*) and the longest one is for KM 180° (75 *mm*). The fluid goes through a shorter distance at $z = L/4$ in KM 120° and KM 150°, in comparison with KM 180°.

KM 120 °	KM 150 °	KM 180 °
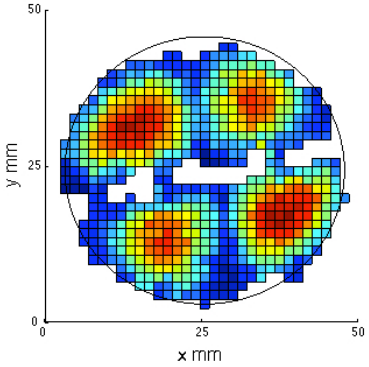	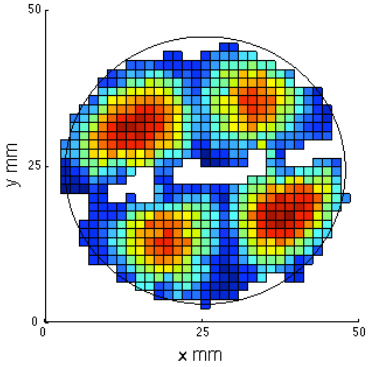	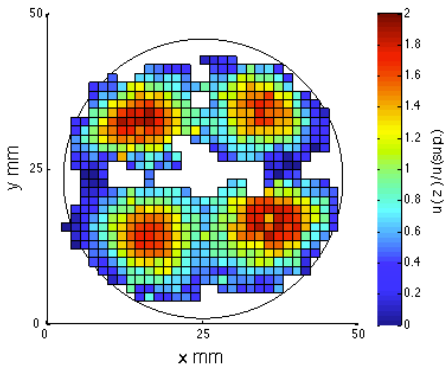
(a) z = 0	**(f) z = 0**	**(k) z = 0**
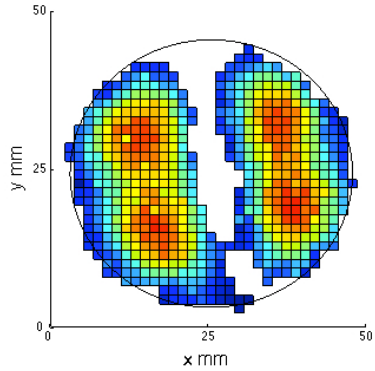	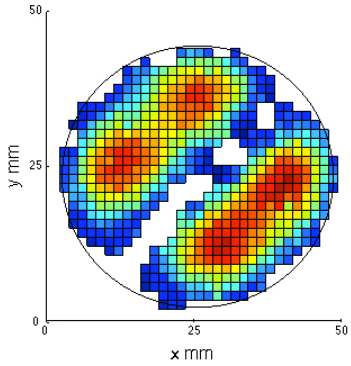	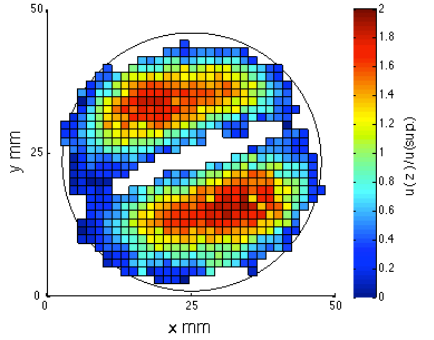
(b) z = L/8	**(g) z = L/8**	**(l) z = L/8**
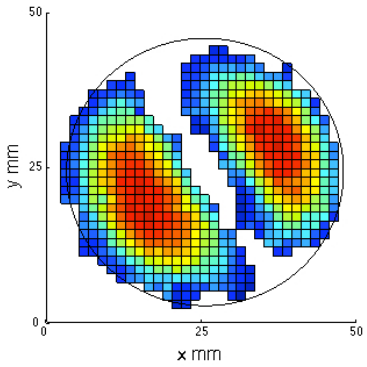	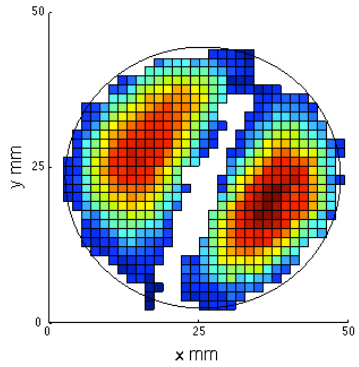	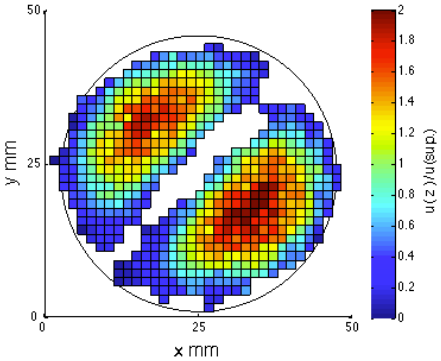
(c) z = L/4	**(h) z = L/4**	**(m) z = L/4**
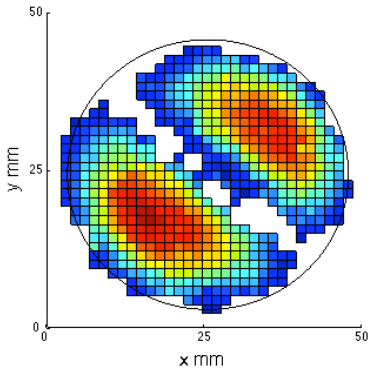	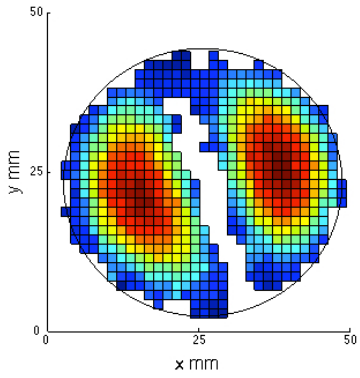	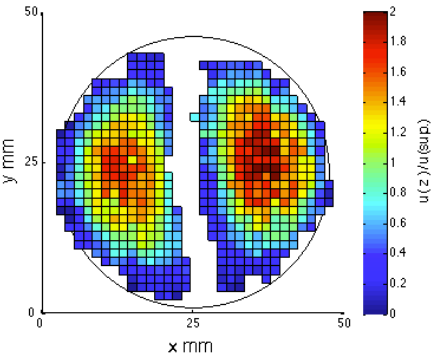
(d) z = L/2	**(i) z = L/2**	**(n) z = L/2**

Continued on the next page

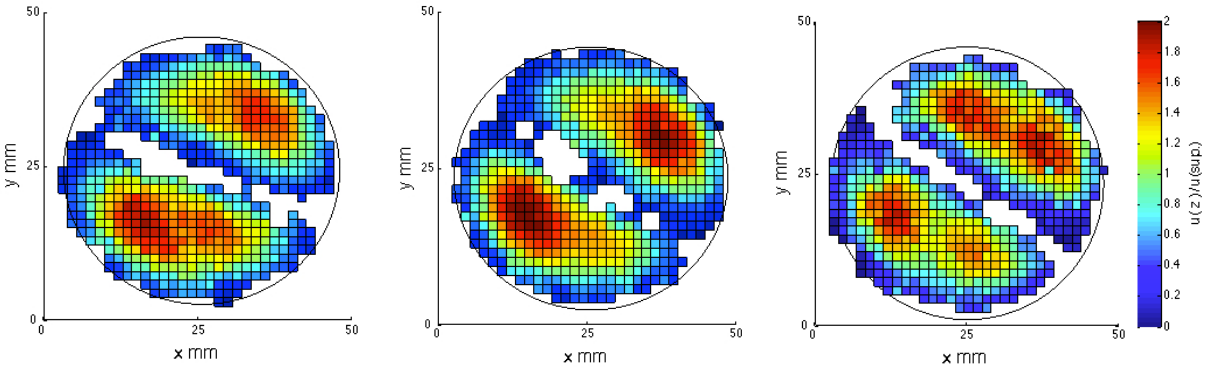

Figure 6.1. Normalised axial velocity map along the third element for: (a-e) KM 120°; (f-j) KM 150°, and (k-o) KM 180°. The blade is rotating anti-clockwise.

Consequently, the flow looks less developed at $z = L/4$ in KM 120° and 150° in comparison with KM 180°, which is observable by the difference between the shape of their velocity maps between $z = L/4$ and $z = L/2$. At $z = L/2$ the maximum value of velocity is located in the middle of the area between the blade and the inner wall of the pipe for KM 120°, 150°, and 180°. The value of velocity decreases when going towards the solid boundaries of the system for all the geometries, as expected. By getting closer to the next transitional area, the high velocity zones are moving towards the corner of the geometry on each side of the blade as a result of getting closer to the next transitional area for all the geometries.

Figure 6.2 presents the vector plots used to study the velocity fields relative to the x and y components. The vector plots are overlapped to the contour maps of the velocity for all the fluids. The colour intensity on contour plots represents the length of the vectors, given by $|u(x)+u(y)|$.

KM 120 °	KM 150 °	KM 180 °
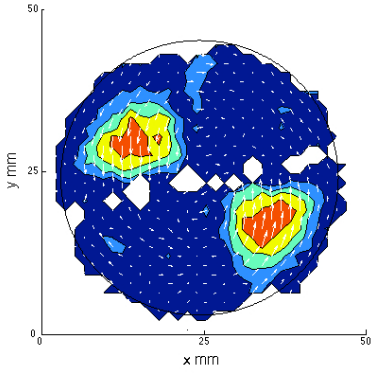	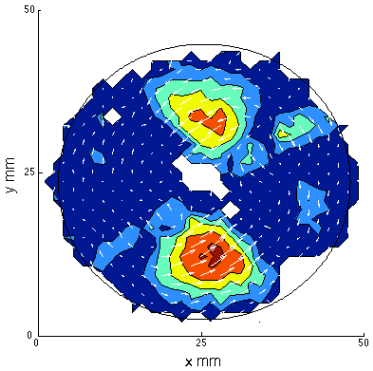	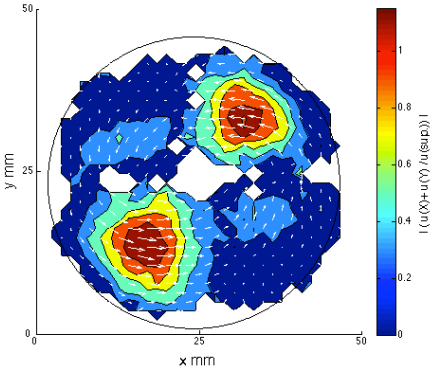
(a) $z = 0$	**(f)** $z = 0$	**(k)** $z = 0$
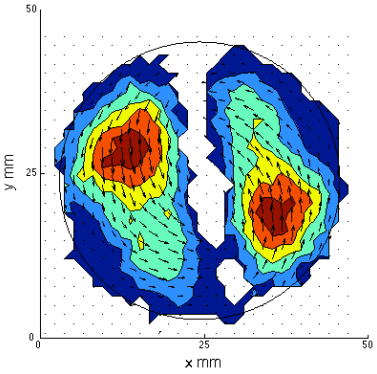	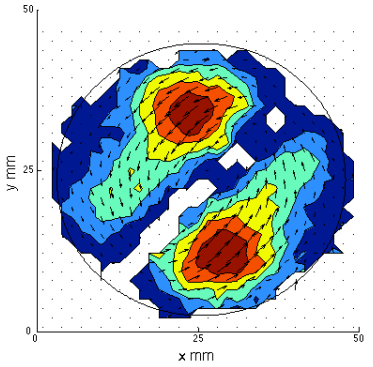	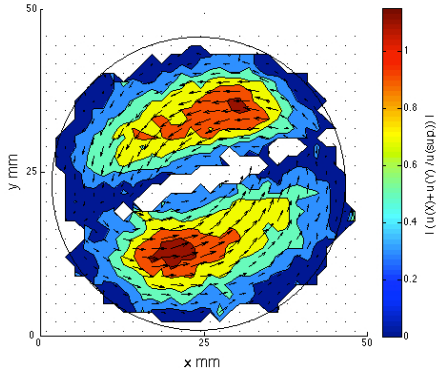
(b) $z = L/8$	**(g)** $z = L/8$	**(l)** $z = L/8$
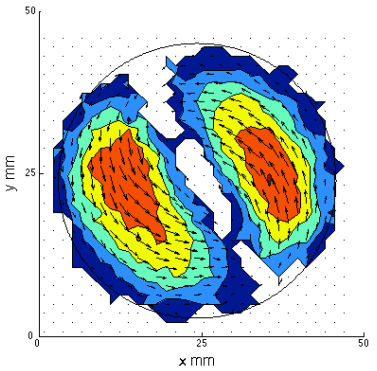	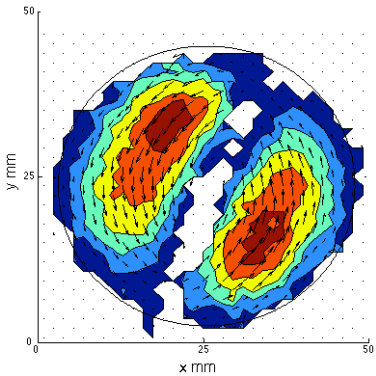	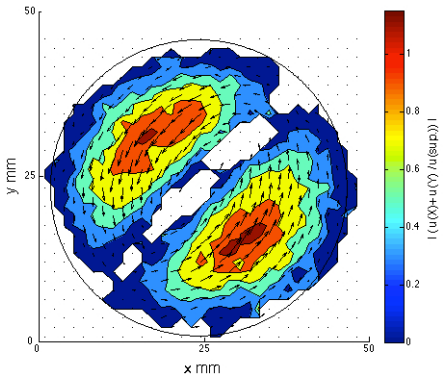
(c) $z = L/4$	**(h)** $z = L/4$	**(m)** $z = L/4$
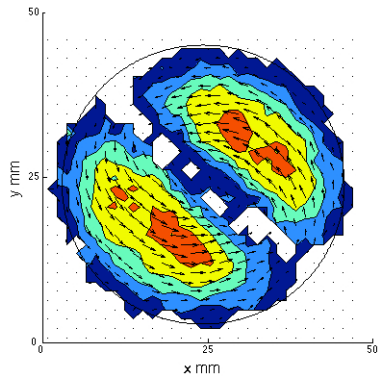	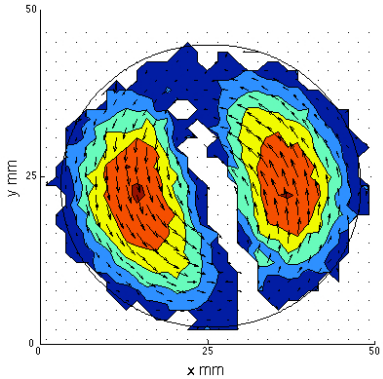	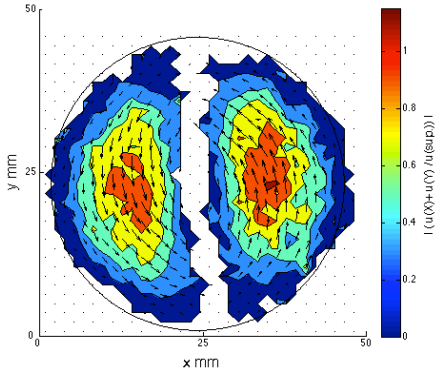
(d) $z = L/2$	**(i)** $z = L/2$	**(n)** $z = L/2$

Continued on the next page

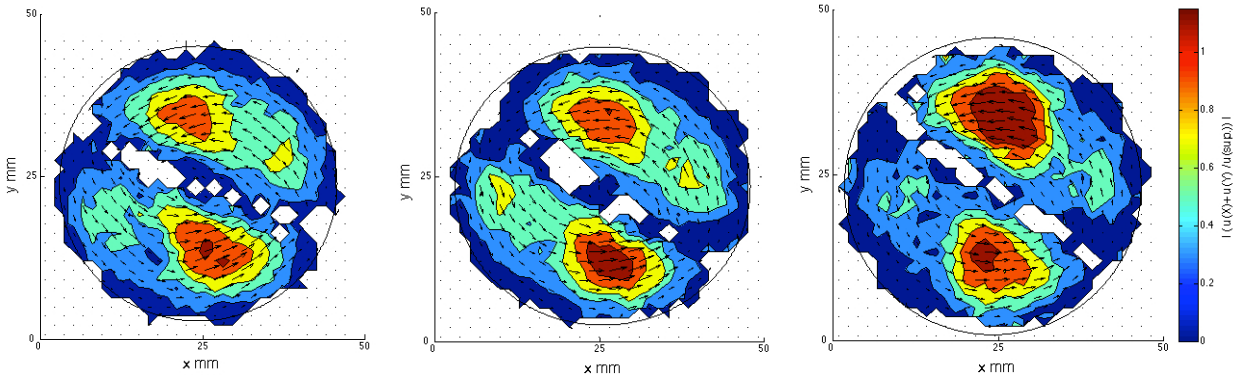

(e) $z = 3L/4$ (j) $z = 3L/4$ (o) $z = 3L/4$

Figure 6.2. Cross-sectional velocity map along the third element for: (a-e) KM 120 °; (f-j) KM 150 °, and (k-o) KM 180 °.

At $z = 0$, all the geometries show a higher velocity within two quarters of the cross-section as a consequence of passing from the transitional area between two elements. For $L/8 < z < 3L/4$, it is possible to observe the direction of the fluid movement on the velocity maps, which shows the counter-clockwise rotation of the twist as expected. The magnitude of $|u(x)+u(y)|$ decreases by moving towards the solid boundaries of the system for all the geometries, showing the symmetric velocity vectors on each side of the blade. At $z = L/8$, the high velocity zones are concentrated in the corner of the geometry for KM 120° and KM 150°, while they look more stretched for KM 180°. Similar behaviour was observed in Figure 6.1 for the axial velocity maps. For $z = 3L/4$, the vectors with higher velocities move towards the corner of the geometry as a result of getting close to the next transitional area. It can be observed that two high velocity zones are created within the cross-section. In order to get a better understanding of the flow direction between $z = 3L/4$, and the following transition region, the cross-sectional velocity maps are plotted between $z = 3L/4 + 4$ *mm* and $z = 3L/4 + 8$ *mm*, where the following transition region is located. Figure 6.3 shows the cross-section of the mixer at $z = 3L/4 + 4$ *mm* on the third element of KM 180°, at $z = 3L/4 + 8$ *mm,*

and at the entrance of the 4th element. The approximate position of the blade on the third element is shown with a grey bar, while the position of the blade at the start of the following element (i.e., the fourth element) is shown with a black bar. The four velocity zones created between the blades are numbered from one to four. Figure 6.3(a) shows the flow direction is following the counter-clockwise twist of the third element. The fast velocity zones (zones two and four) are located behind the third element blade, while the slow velocity zones (zones one and three) are located in front of the third element blade. The zooming window shows the flow direction is counter-clockwise within the slow and fast velocity zones. Moving to the next cross-section at $z = 3L/4 + 8$ *mm*, it can be observed that the fast velocity zones are still located behind the blade of the third element. However, by zooming into the velocity map, it is observed the flow direction is not the same for all the zones. While zones two and four are still rotating counter-clockwise, zones three and one start following the twist direction of the following element (i.e., the fourth element), and therefore rotating in a clockwise direction. The interesting observation from Figure 6.3(b) is the existence of regions of 'stagnant flow' (zones one and three in Figure 6.3(b)) and 'twisting flow' (zones two and four in Figure 6.3(b)). The creation of these regions is due to the combined effect of the residual twist and the new twist of the following element in the opposite direction, which squeezes the fluid within zones two and four. The arrangement of the velocity zones stays the same as Figure 6.3(b), and it changes in Figure 6.3(c) at the entrance of the following element. This behaviour was observed in a similar way for all the geometries, and therefore only the velocity maps of KM 180 ° are presented here.

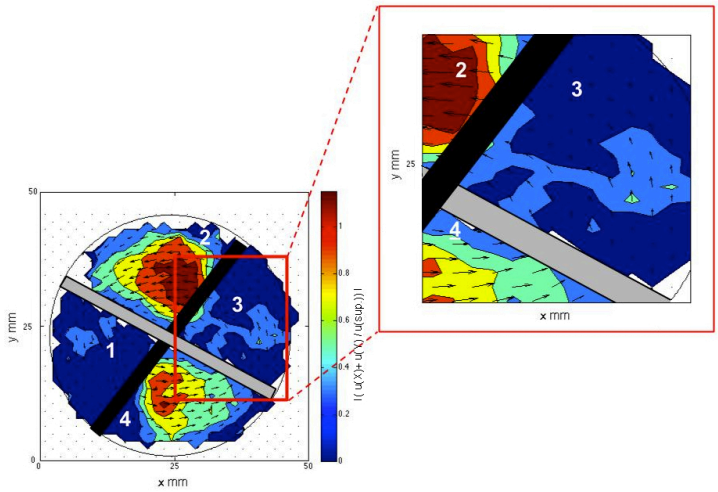

(a) $z = 3L/4 + 4$ *mm*

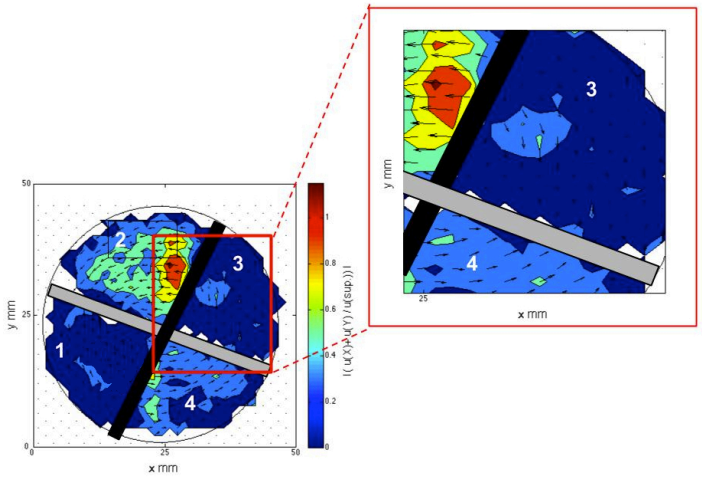

(b) $z = 3L/4 + 8$ *mm*

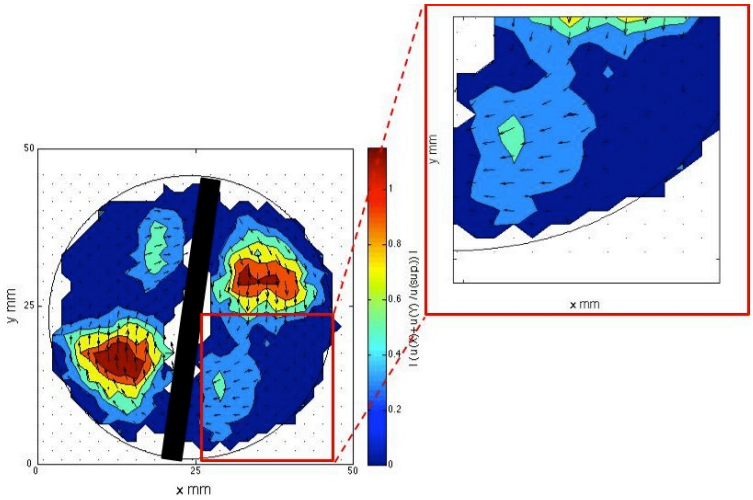

(c) $z = 0$ (4^{th} element)

Figure 6.3. Cross-sectional velocity map towards the end of the third element between z = 3L/4 and the transition region for KM 180° located at: (a) z = 3L/4 + 4 *mm*, and (b) z = 3L/4 + 8 *mm*;(c) start of the 4^{th} element.

Figure 6.4 shows the tangential velocity maps located at the middle of the third element for all the geometries. As shown, the tangential velocity maps of all the geometries look similar to each other, having the same maximum magnitude of velocity between the solid boundaries of the mixer for all the modified geometries.

KM 120°	KM 150°	KM 180°

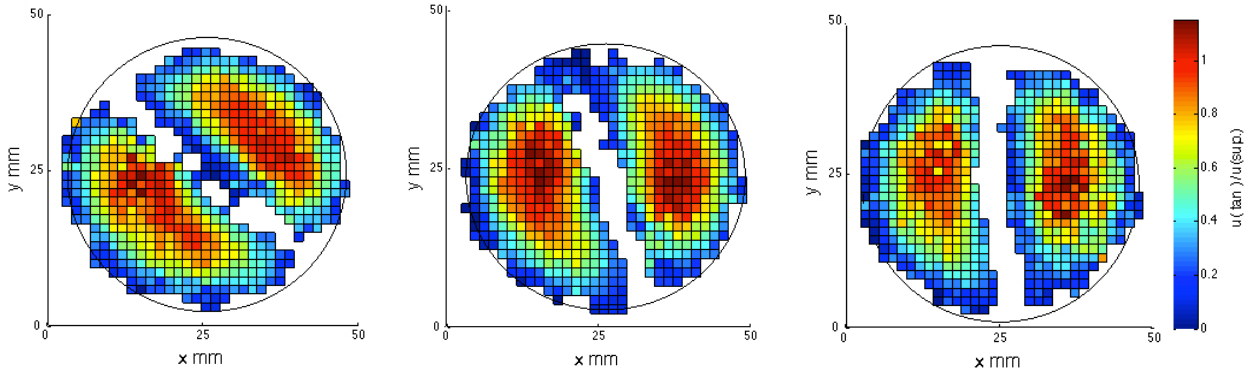

(a) $z = L/2$ (b) $z = L/2$ (c) $z = L/2$

Figure 6.4. Tangential velocity map located at the middle of the third element for: (a) KM 120°; (b) KM 150°, and (c) KM 180°.

6.3 Shear rate

The shear rate maps are calculated from the Eulerian velocities using Equation 3.10 for the various fluids.

Figure 6.5 shows the normalised shear rate maps for all the modified geometries, located at the same axial location along the third element. In order to find the average shear rate from the experimental data, a number of cross-sections are selected along the mixer, and the average shear rate for each cross-section is estimated by getting an average from the values of shear rate assigned to each cell of the map. The final value

of the average shear rate is then calculated as 15 s^{-1} by getting an average from the average shear rate assigned to each cross-section.

For z = 0, the effect of passing through the previous transitional area could be observed on the shear rate map, by having the highest value of shear rate close to the location of the blades of the second and third elements which are normal to each other. The value of the shear rate is the highest close to the solid boundaries of the system for all the geometries, as expected.

For $z = L/4$ and $z = L/2$, the area with the lowest shear between the solid boundaries of the system for KM 120° and KM 150° look flatter in comparison with KM 180°. Considering using the same glycerol solution for all the experiments, a similarity between the shear rate maps is expected. By getting closer to the next transition area at $z = 3L/4$, the areas with the lowest shear rate are moving towards the corner of the geometry and getting separated from each other by an area with a higher shear rate. As shown in Figure 6.5 (d), (h), and (i), the location of the area with a higher shear rate is close to normal to the middle of the blade on the third element, which is where the blade on the fourth element is located on the following transitional area. The results from Figure 6.5 show that changing the twist angle of the blades does not affect the distribution of the shear rate within the elements using glycerol as the Newtonian model fluid.

KM 120 °	KM 150 °	KM 180 °

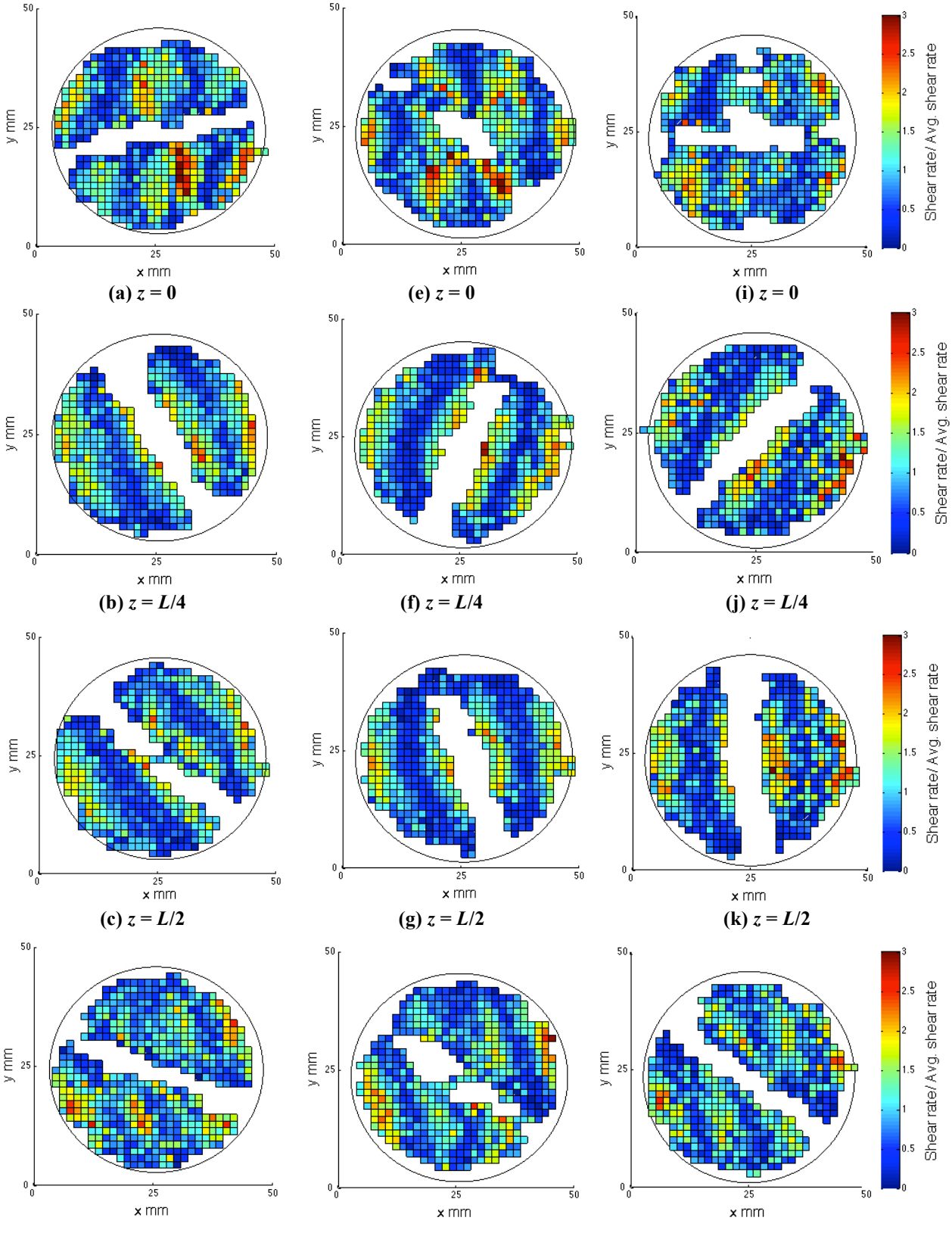

(a) $z = 0$ (e) $z = 0$ (i) $z = 0$

(b) $z = L/4$ (f) $z = L/4$ (j) $z = L/4$

(c) $z = L/2$ (g) $z = L/2$ (k) $z = L/2$

(d) $z = 3L/4$ (h) $z = 3L/4$ (l) $z = 3L/4$

Figure 6.5. Normalised shear rate maps for: (a-d) KM 120° ;(e-h) KM 150°

6.4 Studying the mixing performance

For all the modified geometries, mixing is characterised by calculating the changes in segregation along the mixer. As described in § 4.5.2.1, particles are classified into two groups (blue and red) according to their entrance position. By finding the closest neighbour particle to each one, the change in segregation is calculated along the mixer by the following equation:

$$S = \frac{C_{RR}}{C_{RR} + C_{RB}} + \frac{C_{BB}}{C_{BB} + C_{BR}} \qquad \textbf{(Equation 6.2)}$$

where C_{RR}, C_{BB}, $C_{RB,}$ and C_{BR} are the red-red, blue-blue, red-blue, and blue-red contacts. The procedure of calculating segregation changes along the mixer was described in detail in § 4.5.2.1.

Figure 6.6 shows the segregation changes along the mixer for all the modified geometries. The value of segregation is calculated over the same number of passes for all the geometries. Because of the different number of elements and length of the elements across the different geometries, the segregation is presented here both versus the element number in Figure 6.6 (a) and versus the axial distance in Figure 6.6 (b).

As is shown in Figure 6.6 (a), the segregation index in KM 150° approaches unity faster than other geometries (KM 150° > KM 180° > KM 120°). It is, however, important in identifying optimal mixing performance to take into account the head loss. Under the assumption that the pressure drop increases linearly with the length of the mixer, as described by the Darcy–Weisbach equation, we consider pressure drop as a function of the overall mixer length. This is shown in Figure 6.6 (b), where KM 150° is confirmed as having the lowest value of segregation already after a distance of 100 *mm* from the beginning of the mixer, reaching 1 asymptotically after 300 *mm*.

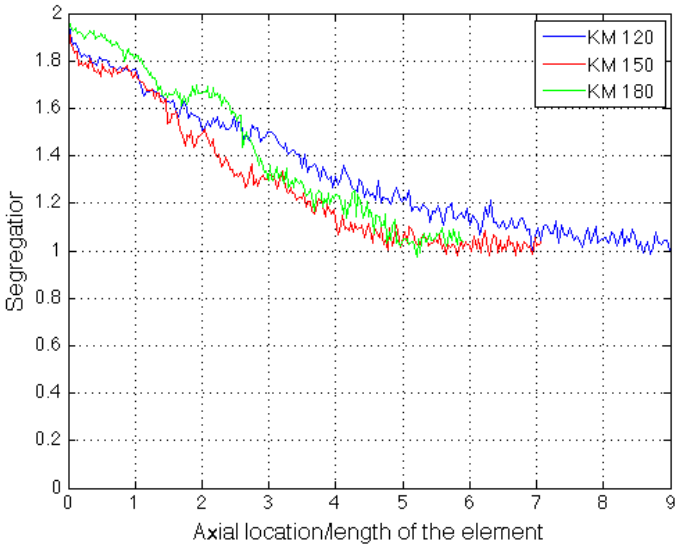

(a)

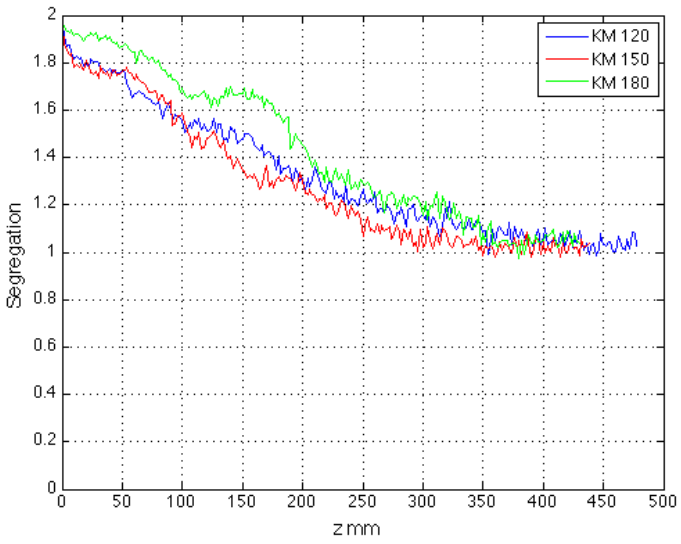

(b)

Figure 6.6. Changes in segregation for the modified geometries vs. (a) number of elements and (b) axial location.

Meanwhile, both KM 180° and 120° require mixer lengths of 400 *mm* to reach a value of segregation of 1. It is also observed from Figure 6.6 (b) that the value of segregation for KM 180° is always higher than for KM 120° and KM 150° for $0 < z < 350$ *mm*. In conclusion, the mixing performance per unit length along the mixers can be summarised as: KM 150° > KM 120° > KM 180°.

Galaktionov et al. (2003) previously studied numerically the effect of changing the twist angle of the blades on the mixing performance of a Kenics Static Mixer by calculating the intensity of segregation (§2.2.1). The result of this work is in agreement with their result, which shows KM with 150° twist has the best mixing performance in comparison with other twist angles. Another numerical work by Hobbs et al. (1998) also studied the effect of changing the twist angle on the perofrmance of the Kenics mixer (§2.2.1). They calculated the changes of coefficient of variance along the mixer for a range of twist angles from 30° to 210°. According to their work, the mixing performance per number of elements of Kenics mixer with different twist angles can be summarised as: KM 150° > KM 180° > KM 120°. This result is also in agreement with the results presented in the current work.

6.5 Residence time distribution

The previous section characterises the cross-sectional mixing of all the geometries by using the segregation index. Studying the residence time distribution (RTD) curves, on the other hand, can reveal lots of information about the axial mixing along the mixer. In this section, the RTD of the modified geometries is presented and compared to each other.

The RTD function is calculated using Equation 4.9, following the same procedure used for KM 180°, described in §4.6.1.

Figure 6.7 (a) and (b) show the normalised RTD function calculated over each single element along each modified geometry. The first and last elements for both geometries are not plotted, due to the low data quality. The shapes of the RTD curves are similar to each other for both geometries.

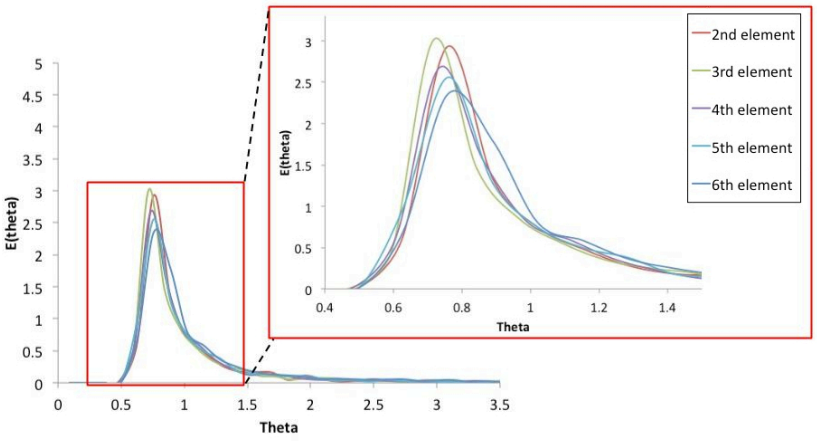

(a)

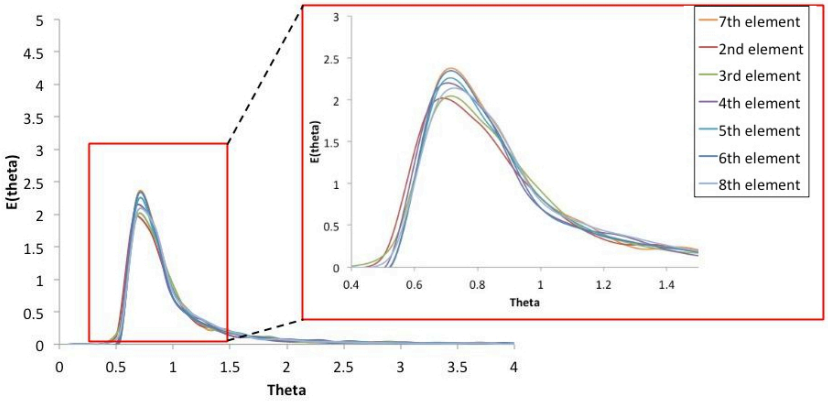

(b)

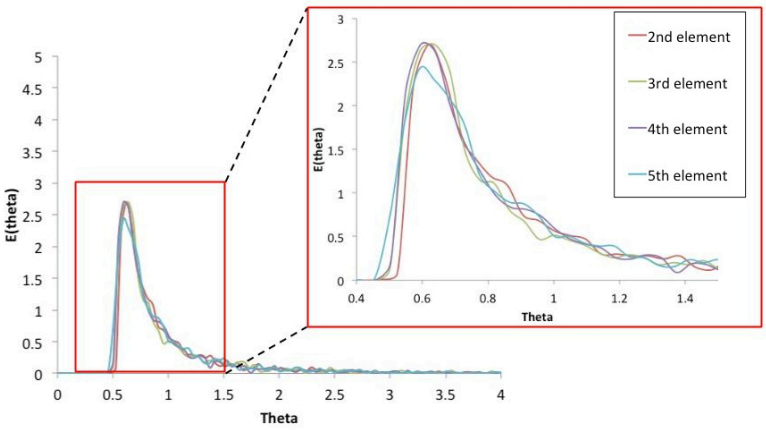

(c)

Continued on the next page

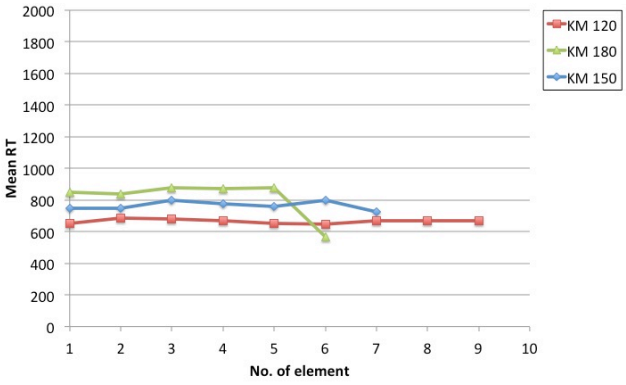

(d)

Figure 6.7. The normalised RTD function of each single element for: (a) KM 150°; (b) KM 120°; (c) KM 180°, and (d) comparing the mean residence time for all the modified geometries.

The minimum time for the tracer to go through each element is around 0.5 which, as described previously, is expected, due to the Newtonian nature of the fluid. Figure 6.7 (d) presents the comparison between the average residence times for each single element for all the modified geometries. Except for the deviation of KM 180° on the sixth element, the value of mean residence time does not change significantly for each single element along the geometries. The value of average mean residence time is highest for KM 180°, which has the longest element, and lowest for KM 120°, which has the shortest one, as expected.

Considering the high viscosity of the glycerol solution and it being in the laminar regime, the experimental data has been fitted to the RTD function calculated from the convection model. The reason behind this choice and the explanation of the convection model was discussed in detail in § 4.6.2.

The dimensionless RTD for the convection model could be calculated by the following equation:

$$E(\theta) = \begin{cases} 0 & \theta < 0.5 \\ \dfrac{1}{2\theta^3} & \theta \geq 0.5 \end{cases}$$ **(Equation 6.3)**

where θ is the residence time normalised by the averaged residence time ($t / \bar{t}$). Figure 6.8 shows the comparison between the normalised RTD function from the experimental data for single elements and the one calculated from Equation 6.3 for the convection model. In order to avoid a high number of curves within the graph, only a selected number of elements are shown for each mixer.

Figure 6.8 shows that, for all the geometries, the experimental RTD curves of the single elements are located close to the one from the model. The deviation of this curve from the convection model curve might be related to the existence of the elements inside the pipe. The shape of the RTD curves of the single elements in KM 180° looks closer to the RTD calculated from the convection model in comparison with the other mixers. At the next stage, the effect of passing through the transition regions on RTD is studied by plotting the RTD curves calculated from the first element along the mixer.

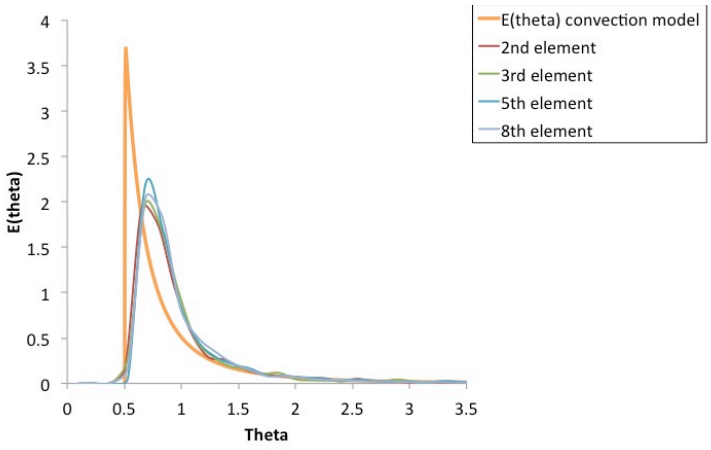

(a)

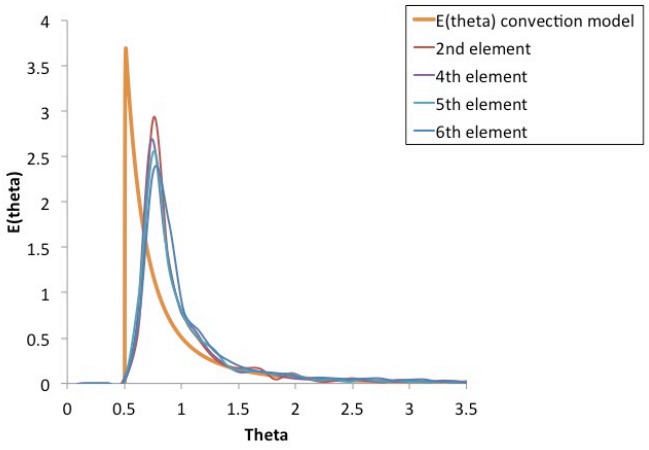

(b)

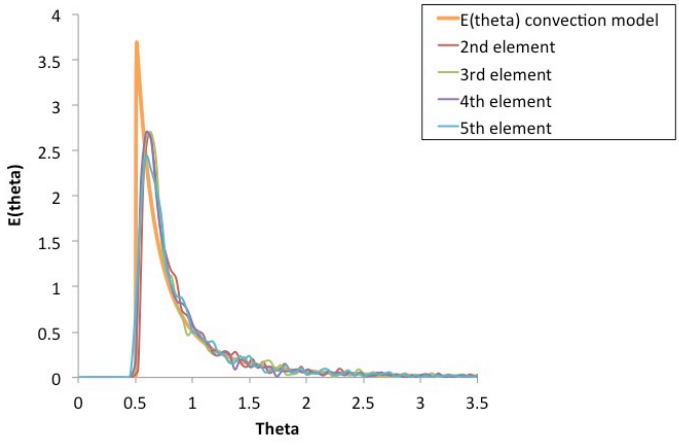

(c)

Figure 6.8. Comparison between the experimental RTD and the convection model along single elements for: (a) KM 120 °; (b) KM 150 °, and (c) KM 180 °.

Figure 6.9 presents the experimental RTD function calculated from the start of the first element along the mixer, in comparison with the one from the convection model. Although the length of the elements are different for each geometry, normalisation of the residence time by the value of average residence time along each element makes it possible to compare the RTD curves of all the modified geometries. KM 180° has the minimum number of elements among the modified geometries (six elements), and therefore it was also decided to compare the RTD along the first six elements for all the geometries (Figure 6.9 (c)). As shown in Figure 6.9 (b), the peak of the RTD curve shifts towards the right by going through a higher number of elements and, consequently, a higher number of transition regions for all the geometries. It is easier to understand this shift by looking at particle trajectories within a single element. Along a single element, each particle follows a streamline, keeping a constant velocity mostly, and therefore the RTD would not be changed along the length of the element by passing through that single element again.

Having two consecutive elements with opposite twist directions is similar to having two mixers in series with two different blades. There is a probability that the particle changes position relative to the blade of the new element, resulting in a change of velocity hence a change in RT (§4.2 and §4.6.1) in comparison with the previous element. This has the effect of narrowing the distribution of the residence time, since particles that were fast in the first element may now be slow, or vice versa. By passing through an *infinite* number of elements, each particle would be expected to experience the same distribution of trajectories (not necessarily in the same order), and would have the same total residence time. Hence, the shape of the overall RTD of an infinite mixer would look like plug flow.

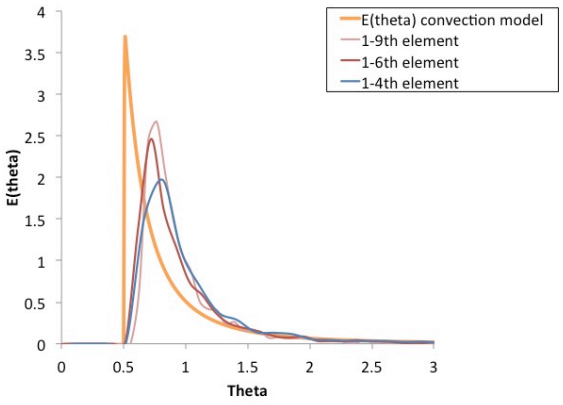

(a)

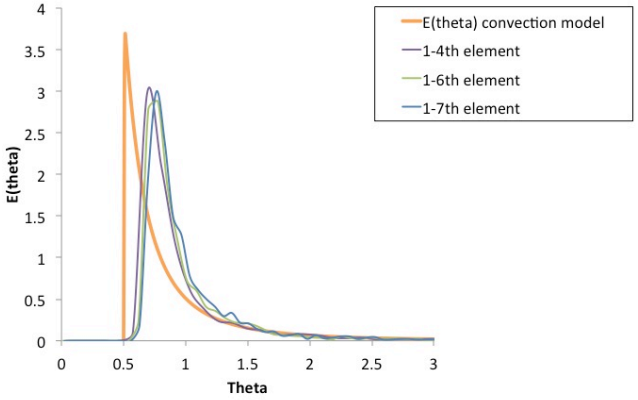

(b)

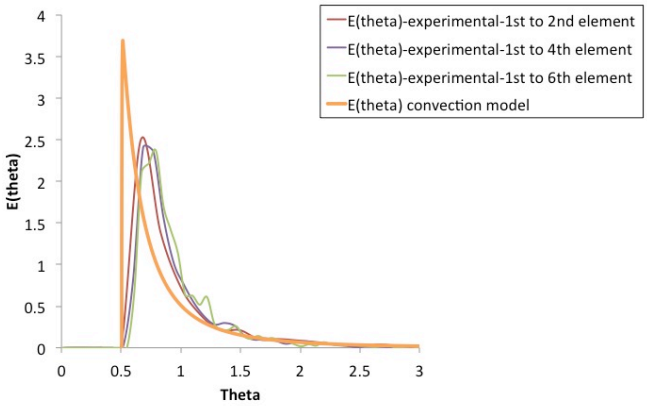

(c)

Continued on the next page

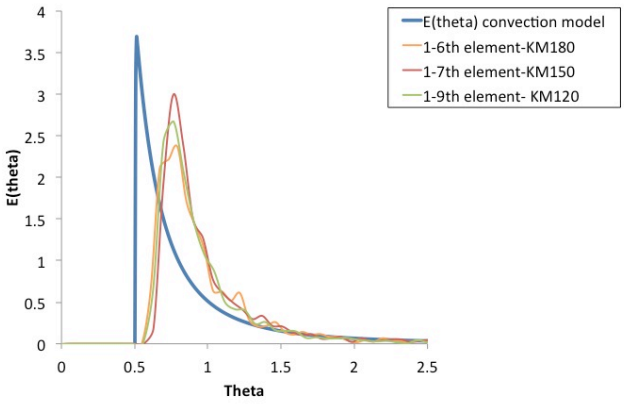

(d)

Figure 6.9. Comparing the normalised RTD function from the experimental data with the convection model: (a) KM 120 °; (b) KM 150 °; (c) all the modified geometries along the first six elements, and (d) all the modified geometries along the whole length of the mixer.

As discussed in § 4.6.2, for the dispersion model, the peak value of residence time is located at $\theta = 1$. It can be observed from Figure 6.9 that, by going through a higher number of elements for each geometry, the peak value of residence time is getting further away from $\theta = 0.5$, and getting closer to $\theta = 1$. This indicates that, by going through more transition regions where the main dispersion in the KM is happening, the shape of the RTD function moves closer to that of the dispersion model.

It can be observed from Figure 6.9 (d) that, by considering all nine elements of KM 120°, the RTD curve of KM 120° becomes closer to the RTD curves of KM 150° and KM 180°. This is related to the fact that nine elements of KM 120° have a total length equivalent to six elements of KM 180° and seven elements of KM 150° (around 450 *mm*). Therefore, by passing through the same length as KM 150° and KM 180°, the RTD curve of KM 120° becomes closer to the RTD curve of KM 150°.

Another characteristic that could be considered in comparing the RTD of each geometry is the wideness of the distributions. Full width at half maximum (FWHM) is an expression, which can be used to compare the RTD curves of each geometry. In

this method, the wideness of the distribution is measured at half of the maximum value of it (Figure 6.10). As discussed before, after an *infinite* number of elements, the shape of the RTD curve is expected to become same as the plug flow. Hence, an RTD curve that has the smallest wideness can represent a better axial mixing.

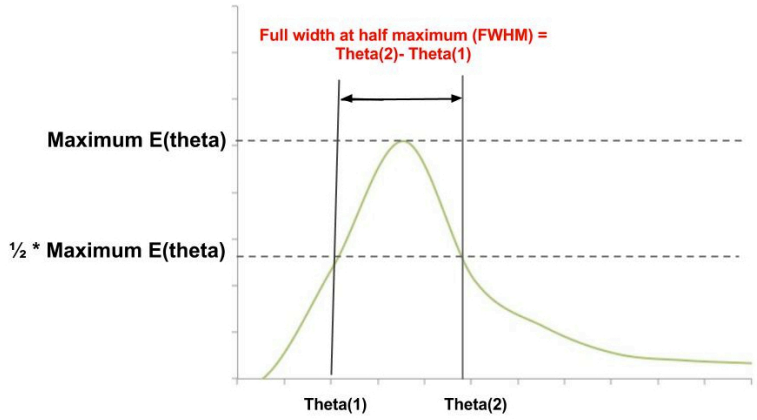

Figure 6.10. Full width at half maximum method (FWHM).

For all the geometries, the value of FWHM was measured according to the RTD curves presented in Figure 6.9. Figure 6.11 shows the changes of the measured FWHM for all the geometries versus number of mixing element (a) and also the axial length along the mixer (b).

For all the geometries, the value of FWHM decreases significantly before entering the second element, which shows the effect of passing through the first transition region on the residence time distribution curves. It can be observed that the value of FWHM decreases by going through the mixer, which indicates the improvement in axial mixing by passing through more number of mixing elements. The final value of FWHM after going through all the mixing elements for each geometry is calculated and compared.

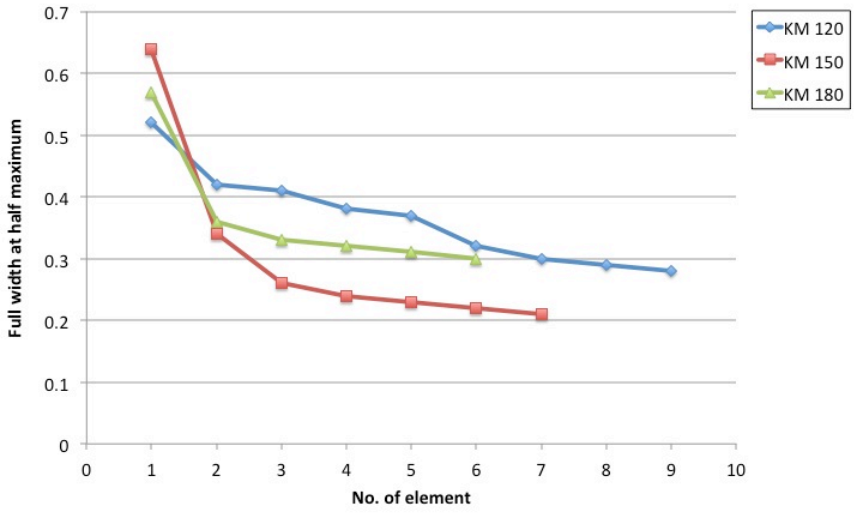

(a)

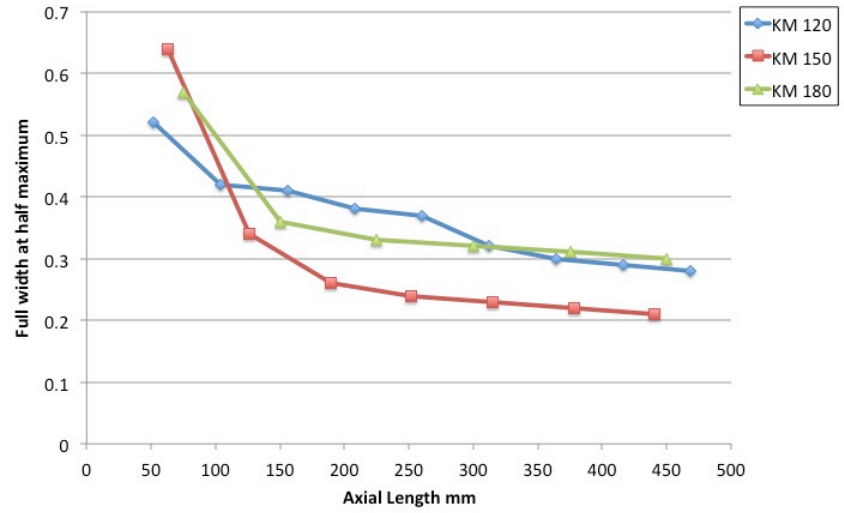

(b)

Figure 6.11. Changes of the value of full width at half maximum (FWHM) for all the geometries vs. (a) number of mixing elements; (b) axial length.

As shown in Figure 6.11(a) the maximum value of FWHM after going through six mixing elements belongs to KM 180° (0.3), while the value of FWHM for KM 150° and KM 120° are found to be 30% and 7% less than the one for KM 180°. Hence, KM 150° has the lowest value of FWHM, which indicates a narrower RTD comparing with other geometries and therefore a better axial mixing. This result is in agreement with the observation from the RTD curves in Figure 6.9, which showed the shape of the RTD curve of KM 150° is the closest one to the dispersion model, meaning the

fluid elements become more dispersed among each other for this geometry. Therefore, the comparison between the axial mixing of these geometries can be summarised as : KM 150° > KM 120° > KM 180°, where KM 150° has the best axial mixing.

6.6 Conclusion

In this chapter, the effect of changing the twist angle of the blade on flow behaviour and mixing performance was investigated experimentally for the first time, by modifying the elements of a standard KM into twisting angles of 150° and 120°.

The axial velocity maps along the third element for all the geometries were plotted and compared. It was shown based on the cross-sectional velocity maps that the reversing twist of consecutive elements results in the creation of stagnant regions within the transitional region between the elements. By looking at the velocity maps of all the geometries close to the transitional region ($z = L/8$), it was observed that the flow looks less developed for KM 120° in comparison with KM 150° and KM 180°, due to the shorter length of the element. It is observed that changing the twist angle of the blade does not affect the velocity distribution within the KM significantly. No significant effect of twist angle is observed on the shear rate distribution.

The mixing performance is characterised using the segregation index for all the modified geometries. It was observed that the segregation in KM 150° approaches unity faster than the other geometries, and therefore KM 150° has a better mixing performance per number of elements (KM 150° > KM 180° > KM 120°). This result is in agreement with the findings from Hobbs et al. (1998) and Galaktionov et al. (2003). Considering the importance of achieving the optimum performance with the lowest head loss, the mixing performance per unit length along the mixer was calculated as well. It was also observed that KM 150° has the best mixing

performance per unit length along the mixer in comparison with the other geometries. Although KM 180° has a higher value of segregation than KM 120° until $z = 350\ mm$, their value of segregations becomes very close to each other after this distance. The mixing performance per unit length along these geometries can be summarised as: KM 150° > KM 120° > KM 180°.

The RTD curves for each single element for all the modified geometry looked similar. It was shown that the peak value of θ moves towards one by passing through a higher number of elements for all the geometries. The RTD curves are compared with the RTD from the convection model. It is shown that, for all the geometries, by passing through a higher number of elements, the RTD curves deviate more from the convection model, and get closer to the dispersion, for which the peak value of the residence time distribution is located at $\theta = 1$. By passing through six elements, KM 150° has the closest peak value of θ to 1, while KM 120° is furthest away from this value. This shows that, by going through same number of elements, the amount of dispersion happening in the transition regions for KM 150° is more than KM 180°, while KM 120°shows the lowest dispersion in comparison with the others. The wideness of the distributions were compared with each other by calculating the FWHM value for all of them after going through the whole length of the mixer. It was observed the wildness of KM 150° and KM 120° residence time distribution curves is 33% and 7% less than the one for KM 180°. Hence, KM 150° has the best axial mixing in comparison with the other geometries (KM 150° > KM 120° > KM 180°).

By using the PEPT experimental data, it has been shown in this chapter that changing the twist angle of the KM using a Newtonian fluid does not affect the velocity and shear rate distributions significantly along the mixer. However, the mixing

performance and RTD are highly affected by decreasing the twist angle of the KM, observing the best performance for a Kenics Static Mixer with a 150° twist in blades.

Notation

Roman letters

C_{BB}	Contact number between blue-blue particles	-
C_{RR}	Contact number between red-red particles	-
C_{RB}	Contact number between red-blue particles	-
C_{BR}	Contact number between blue-red particles	-
D	Axial dispersion coefficient	$m^2.s^{-1}$
D_h	Hydraulic mean diameter	m
D	Pipe diameter	m
$E(\theta)$	Dimensionless RTD function	-
L_e	Entrance length	m
L	Length of the element	m
N_{Re}	Reynolds number	-
N	Number of cells	-
S	Segregation	-
t	Time	s
$\overline{t}$	Mean residence time	s
$u_{sup.}$	Superficial velocity	$m.s^{-1}$
u_z	Velocity in axial direction	$m.s^{-1}$
u_x	Velocity in x- direction	$m.s^{-1}$
u_y	Velocity in y- direction	$m.s^{-1}$
u_{tan}	Tangential velocity	$m.s^{-1}$
w	Thickness of the blade	m

Greek letters

ρ	Density of the fluid	$kg.m^{-3}$
μ	Dynamic viscosity of the fluid	$kg.\ m^{-1}s^{-1}$
θ	Normalised residence time	-

θ_{min}	Minimum time for the tracer to go through the mixer	-
σ	Standard deviation	-

Chapter 7 . MIXING THE NON-NEWTONIAN FLUID USING THE SMX-PLUS STATIC MIXER

7.1 Rheological and fluid dynamics properties of the fluid

Carbopol 0.1 wt% was chosen as the non-Newtonian modelling fluid for the experiment with SMX-plus. The rheological properties of the solution has been described before in §5.1. The Herschel-Bulkley parameters for Carbopol 0.1 wt% solution are presented in Table 7.1.

Table 7.1. Herschel-Bulkley parameters for Carbopol 0.1 wt% solution.

Property / Solution	Consistency index (k) (Pa. s^{n-1})	Flow index (n) (-)	Yield stress (τ_0) (Pa)
Carbopol 0.1 wt%	0.26	0.7	3.7

The average shear rate in the system is approximated using the predicted pipe flow velocity profile of Herschel-Bulkley fluids in an empty pipe (Ferguson et al., 1991) :

$$u(r) = \frac{nR}{n+1}\left(\frac{\tau_w}{k}\right)^{1/n}\left[\left(1-\phi\right)^{(n+1)/n} - \left(\frac{r}{R}-\phi\right)^{(n+1)/n}\right] \qquad \textbf{(Equation 7.1)}$$

where ϕ is the ratio of the yield stress to the wall shear stress, i.e. τ_0/τ_w. The value of radius (r) used in this equation is calculated from the hydraulic mean diameter of the geometry. Considering the complex geometry of the SMX-plus mixer, which includes different configuration of the blades along the mixer (Figure 7.1), calculating a single value of hydraulic mean diameter in this mixer is not as clear as with the KM.

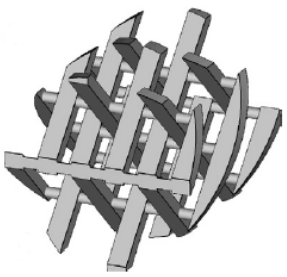

Figure 7.1. Arrangements of the bars for a single element in SMX-plus mixer (Hirschberg et al., 2009).

According to the literature, there is no unique definition for the hydraulic mean diameter in SMX-plus. Hirschberg et al. (2009) used the pipe inner diameter as an estimation of the hydraulic mean diameter in SMX-plus mixer. There are a number of other works on SMX mixer, which has a similar complex geometry to SMX-plus, at which the authors used the diameter of the pipe as the hydraulic mean diameter of the system ((Liu et al., 1994), (Meijer et al., 2011)). In this work, the hydraulic mean diameter of the SMX-plus mixer is estimated by finding the perimeter of the wetted surfaces for a number of cross-sections along a single element. Theoretically, the hydraulic mean diameter can be calculated from the following equation:

$$D_h = \frac{4A}{p} \qquad \textbf{(Equation 7.2)}$$

where A is the flow cross-sectional area (m^2), and p is the wetted perimeter of the cross-section (m). Considering the change in the arrangement of the blades along a single element of the mixer, the wetted perimeter varies along an element. Therefore, the hydraulic mean diameter is calculated over four different cross sections along a single element (Figure 7.2), and by averaging them a single estimated value of D_h was found. The final value of hydraulic mean diameter was estimated as 0.026 m.

Knowing the value of the volumetric flow rate, which was measured during the experiment, and using the value of the parameters presented in Table 7.1, the value of wall shear stress is calculated as 7.5 Pa. After calculating the predicted pipe flow velocity profile of an empty pipe for Herschel-Bulkley fluids, the value of the average shear rate is then estimated as 20 s^{-1} by calculating the gradient of the velocity in different radius. The procedure of this calculation is described in more detail in § 5.1. Subsequently, the apparent viscosity of Carbopol 0.1 wt% solution at this shear rate is found from the rheometer data (Figure 5.1) to be equal to 0.08 *Pa.s.*

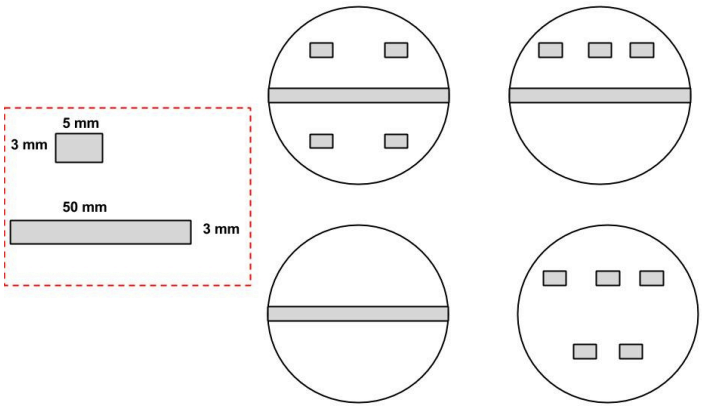

Figure 7.2. Four chosen cross-sections along a single element of SMX-plus used to estimate the hydraulic mean diameter.

The value of wall shear stress is calculated using the following formula for the pipe flow:

$$Q = \frac{\pi R^3 n}{\tau_w^3}\left(\frac{\tau_w - \tau_0}{k}\right)^{1/n}(\tau_w - \tau_0)\left[\frac{(\tau_w - \tau_0)^2}{3n+1} + \frac{2\tau_0(\tau_w - \tau_0)}{2n+1} + \frac{\tau_0^2}{n+1}\right] \quad \textbf{(Equation 7.3)}$$

After measuring the flow rate during the experiment and dividing it by the area of the cross section of the pipe, the value of superficial velocity is measured as 0.15 *m/s* for this set of experiment. The Metzner-Reed Reynolds number for Herschel-Bulkley fluids is calculated following the same procedure that was described before in § 5.2 using Equation 1.4 (Chilton et al. (1998)):

$$\mathrm{Re}_{MR} = \frac{\rho u D_h}{k\left(\frac{8u}{D_h}\right)^{n-1}\left(\frac{3n+1}{4n}\right)^n\left(\frac{1}{1-X}\right)\left(\frac{1}{1-aX-bX^2-cX^3}\right)^n} \quad \textbf{(Equation 7.4)}$$

where:

$$a = \frac{1}{2n+1}, b = \frac{2n}{(n+1)(2n+1)}, c = \frac{2n^2}{(n+1)(2n+1)}, X = \frac{\tau_0}{\tau_w} \quad \textbf{(Equation 7.5)}$$

By substituting the value of all the parameters in Equation 7.4 and Equation 7.5, the Reynolds number is calculated as 16.1, which means the flow is in Laminar regime. It should be mentioned Equation 7.4 and 7.5 are developed for an empty pipe, while the SMX-plus geometry contains a number of solid blades within the pipe. The Reynolds number for an empty pipe by considering the actual diameter of the pipe rather than the hydraulic mean diameter is calculated as 18.

7.2 Studying the mixing performance

The mixing performance of Carbopol 0.1 wt% solution in the SMX-plus mixer is characterised by calculating the segregation along the mixer, following the procedure described in § 4.6.2. The particles are classified into two groups according to their entrance position in the mixer (Figure 7.3). Segregation is calculated along the mixer by finding the closest neighbour to all the particles. Figure 7.4 shows the changes of segregation for SMX-plus in comparison with the other solutions used in KM, which were discussed in the previous chapters.

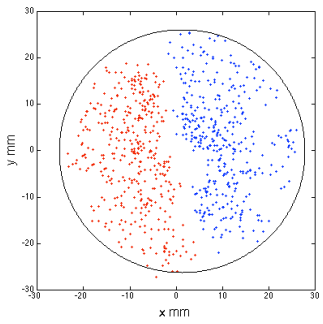

Figure 7.3. Blue and red particles distribution at the entrance of the mixer.

In order to be able to compare the changes of segregation along all the experiments, the total number of passes for all of them should be the same. Since the minimum number of recorded passes belongs to the experiment with SMX-plus (800 passes), a

number of passes are removed randomly from the other experimental data in order to be able to compare their mixing performance with each other.

As shown in Figure 7.4, although the first value of segregation for all the experiments starts from the same number as expected, the difference between the reduction of segregation for SMX-plus is observable even from the first element. It can be observed that the value of segregation of SMX-plus reaches unity around the third element.

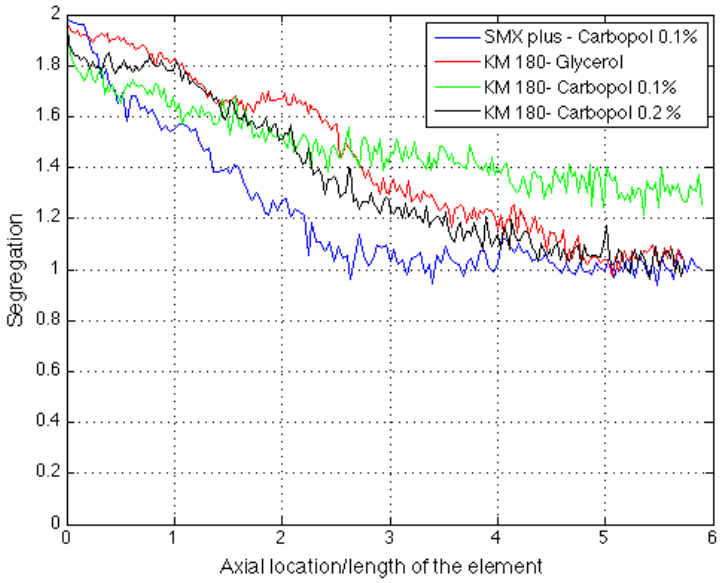

Figure 7.4. Changes of segregation for SMX – plus in comparison with KM vs. number of elements.

The observation based on the changes of the contact number between particles of each group also shows the better performance of SMX-plus. Figure 7.5 shows also the value of the contact number between particles of opposite groups starts fluctuating around a constant number at the third element. Similar behaviour is observed for the changes of the average distance between the particles of each group (Figure 7.5(b)). It is shown that by the end of the third element, the blue and red particles are so well

distributed among each other, that it becomes hard to distinguish them from each other by the end of the sixth element.

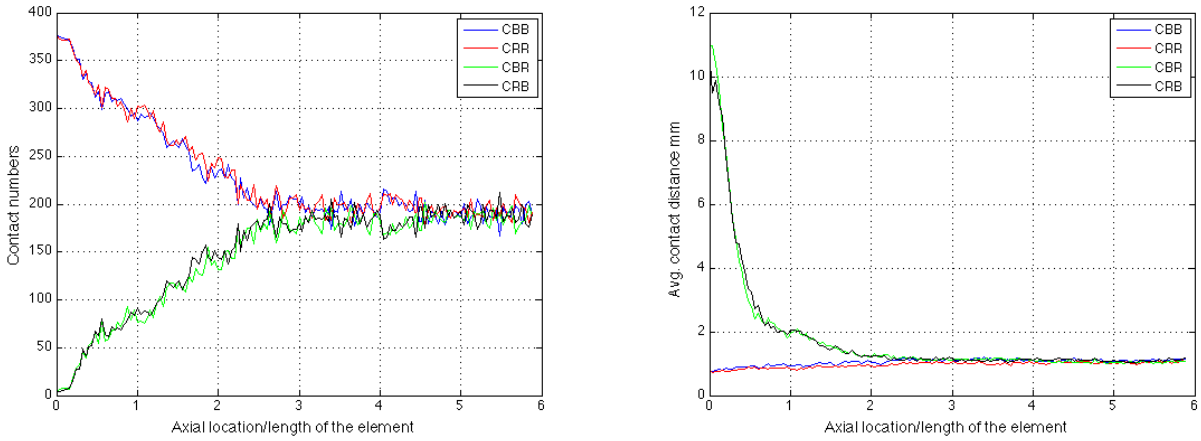

(a) **(b)**

Figure 7.5. (a) Changes of the contact number between the particles of each group; (b) changes of the average contact distance between the particles of each group.

It is also possible to show the significant difference between the mixing performance of SMX-plus and KM by visualising the distribution of blue and red particles along the mixer (Figure 7.6). Figure 7.6 presents the distribution of blue and red particles for SMX-plus and KM at the cross section of the mixer located in the middle of the first to the fourth element. The total number of particles for each case is considered as 800, which is the same as the number of recorded passes for SMX-plus. The distribution of blue and red particles along the mixer is also animated using a MATLAB code, which is available in the attached DVD (*SMX-plus.mov*). It can be observed how well distributed the blue and red particles are in SMX-plus right after the first mixing element comparing with the other experiments (Figure 7.6(e-f-g-h)). The comparison between SMX-plus, and KM with glycerol, which has the best mixing performance in comparison with the other experimental fluids in KM, shows the striation thicknesses are much smaller for SMX-plus even from the middle of the second element. As mentioned before, it is not possible to have a quantitative

measurement about the striation thicknesses with PEPT data; however, visualising the striations makes it possible to have a qualitative measurement about this matter. At the middle of the third element (Figure 7.6(i-j-k-l)), it is still possible to distinguish the striations and their symmetry on each side of the blade for all the experiments with KM.

SMX-plus, Carbopol 0.1%	KM 180°, Glycerol	KM 180°, Carbopol 0.1%	KM 180°, Carbopol 0.2 %

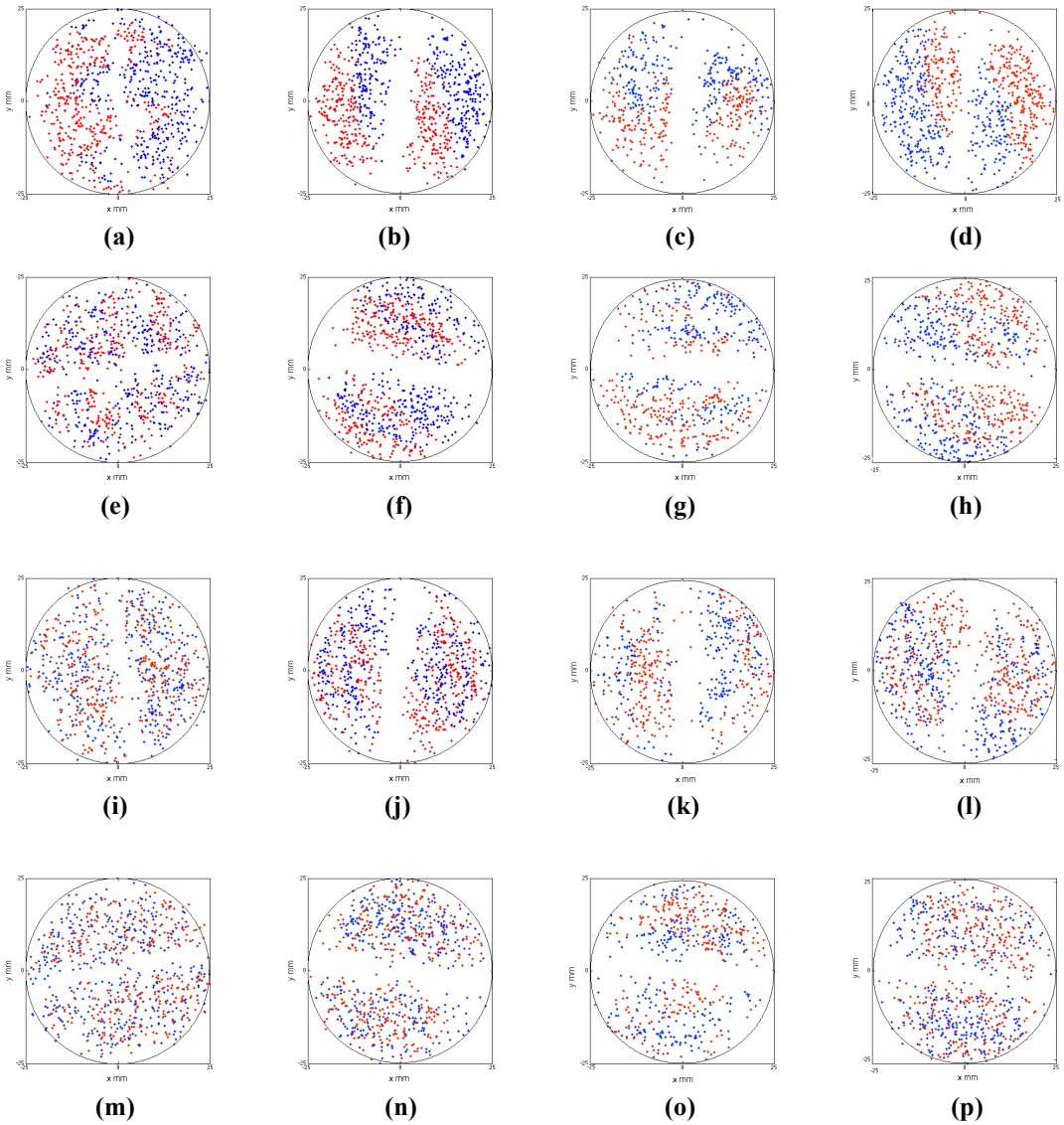

Figure 7.6. Comparing the distribution of blue and red particles in SMX-plus with KM at: (a-b-c-d) middle of the first element; (e-f-g-h) middle of the second element; (i-j-k-l) middle of the third element; (m-n-o-p) middle of the fourth element.

However, for SMX-plus, it is not possible to differentiate the striations from each other or finding any symmetric pattern on each side of the blade from the middle of the third element to the end. This is where according to Figure 7.4 and Figure 7.5 the system reaches to the randomised stage of mixing for SMX-plus. Hence, the distribution of blue and red particles is completely random at this stage, which is also observable from Figure 7.6. The results presented in this section show SMX-plus has significantly better mixing performance in comparison with Kenics static mixer. In terms of mixing performance per unit length it was observed SMX-plus reaches to the randomised stage of mixing within the one third of the required distance for KM. By considering the mixing performance per number of mixing elements, randomised stage of mixing was observed on the third element of SMX-plus and on the sixth element of KM. This result is in agreement with the work from Rauline et al. (2000), which numerically compared the mixing performance of KM and SMX. Using the stretching histories and intensity of segregation to characterise the mixing performance, they showed one mixing element of SMX is equivalent to three mixing elements of KM. This work was discussed in more detail in § 2.2.2.

7.3 Studying the velocity

In this section, velocity distribution within the SMX-plus mixer is studied. As mentioned before, the water-based nature of the Carbopol solution causes the reduction of the activity of the tracer after shorter period of time in comparison with using glycerol as the experimental fluid. Therefore, the number of the recorded passes after five days of experiment was much less than the ones recorded with glycerol. The data presented in this chapter are based on 800 passes. Considering the difference in number of passes and also using a different geometry than Kenics mixer, the

investigation of finding the right cell size for meshing the geometry and the related error analysis is repeated for this experiment again.

7.3.1 Choosing the grid

Due to the use of different geometry and also lower data density of the experiment with SMX-plus mixer, the qualitative measurement to find the optimum cell size of the Eulerian velocity map is investigated. This procedure was described before in detail in § 4.3.2. By considering the PEPT localisation error, and also the data density, choosing a cell size smaller than 2 *mm* in any direction would not give an accurate velocity map. Therefore, the length of the cell in x and y direction is considered as 2 *mm*, which is same as the one chosen for the velocity maps on the previous chapters. The velocity map in one cross-section is calculated by using different cell sizes in axial direction to investigate which cell size gives the best image quality. Figure 7.7 shows the velocity distribution at the middle of the third element calculated over different axial cell size.

As shown in Figure 7.7(a), choosing the minimum cell size of 2 *mm*, does not give a good image quality of the velocity distribution. There are a number of empty cells, which are located everywhere within the map and not just where the blades are. By increasing the length of the cell to 4 and 6 *mm*, it is observed that the number of the empty cells within the cross-section decreases. The best image quality is observed for the cell size of 8 *mm*. However, it should be noted although by increasing the length of the cell the quality of the map improves, the accuracy of the results decreases. This is due to the fact that the value of the average velocity in each cell is calculated over a longer length and therefore it might deviate from the actual value of velocity in each point.

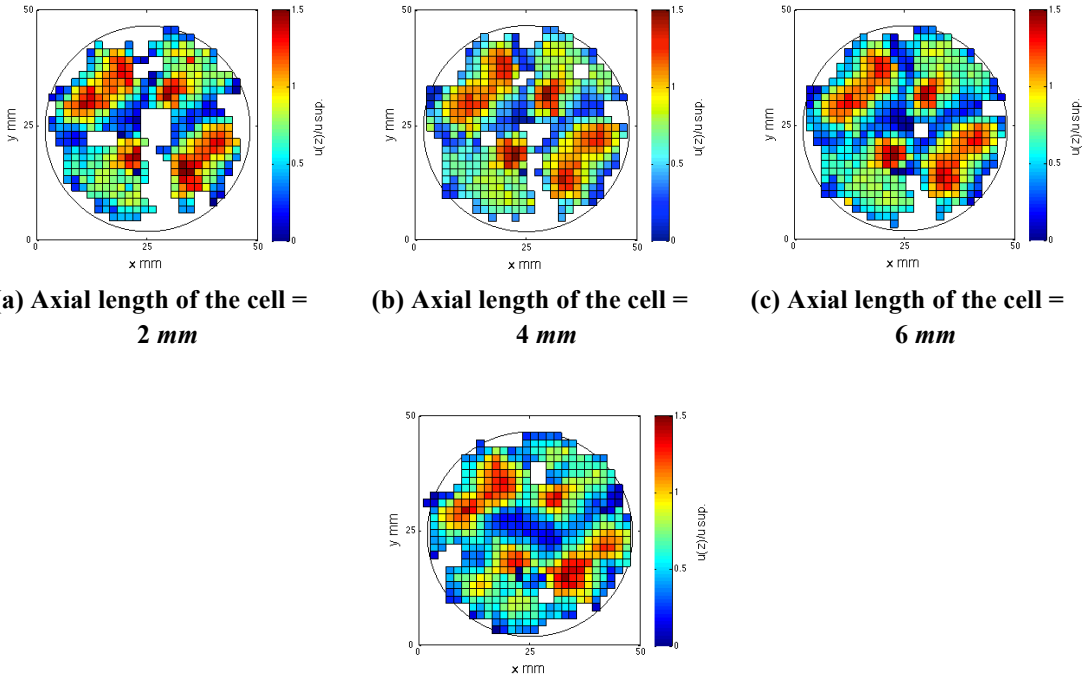

(a) Axial length of the cell = 2 *mm*

(b) Axial length of the cell = 4 *mm*

(c) Axial length of the cell = 6 *mm*

(d) Axial length of the cell = 8 *mm*

Figure 7.7. Effect of changing the length of the cell in axial direction on the Eulerian velocity map. Normalised axial velocity at the cross-section of the mixer located in the middle of the third element with axial cell size of: (a) 2 *mm*; (b) 4 *mm*; (c) 6 *mm; (d) 8* mm.

Considering all these issues, after this qualitative measurement, it is decided to choose the cell size of 6 *mm* in axial direction, since it is the smallest cell size at which the quality of the velocity map is good enough to be investigated.

7.3.2 Study the existence of steady velocity through the cells

As discussed before in §4.4.2 and §5.3.2, it is necessary to investigate whether the value of average velocity assigned to each cell is calculated over sufficient number of data points or not. Four representative cells are selected from the axial velocity map located in the middle of the third element.

As shown in Figure 7.8, cell one represents the area close to the inner wall of the pipe, cell two represents the area between the blades with the highest velocity, cell three

represents the area between the blades and the inner wall of the pipe, and cell four represents another area between the other blades with a high value of velocity.

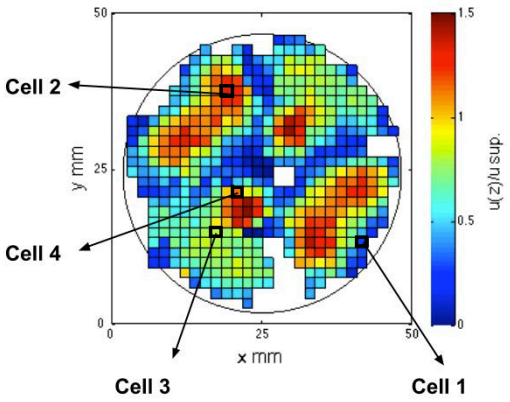

Figure 7.8.Location of four different cells within the cross-section of the mixer in the middle of the third element.

The running average of the velocity of all the passes through the selected cells are plotted versus the considered cumulative number of locations. If the number of locations used to calculate the velocity is sufficient, it is expected to observe the value of the velocity converging on a certain number.

As shown in Figure 7.9(a), the value of velocity in cell one is calculated over total 39 locations, and after using 14 locations it seems to become steady. For cell two, the average velocity is calculated over more number of locations, around 80, which is higher than cell two. This difference is due to the different position of these cells. Cell one is located next to the inner wall of the pipe, and consequently there is less fluid passing through that area in comparison with the location of cell two.

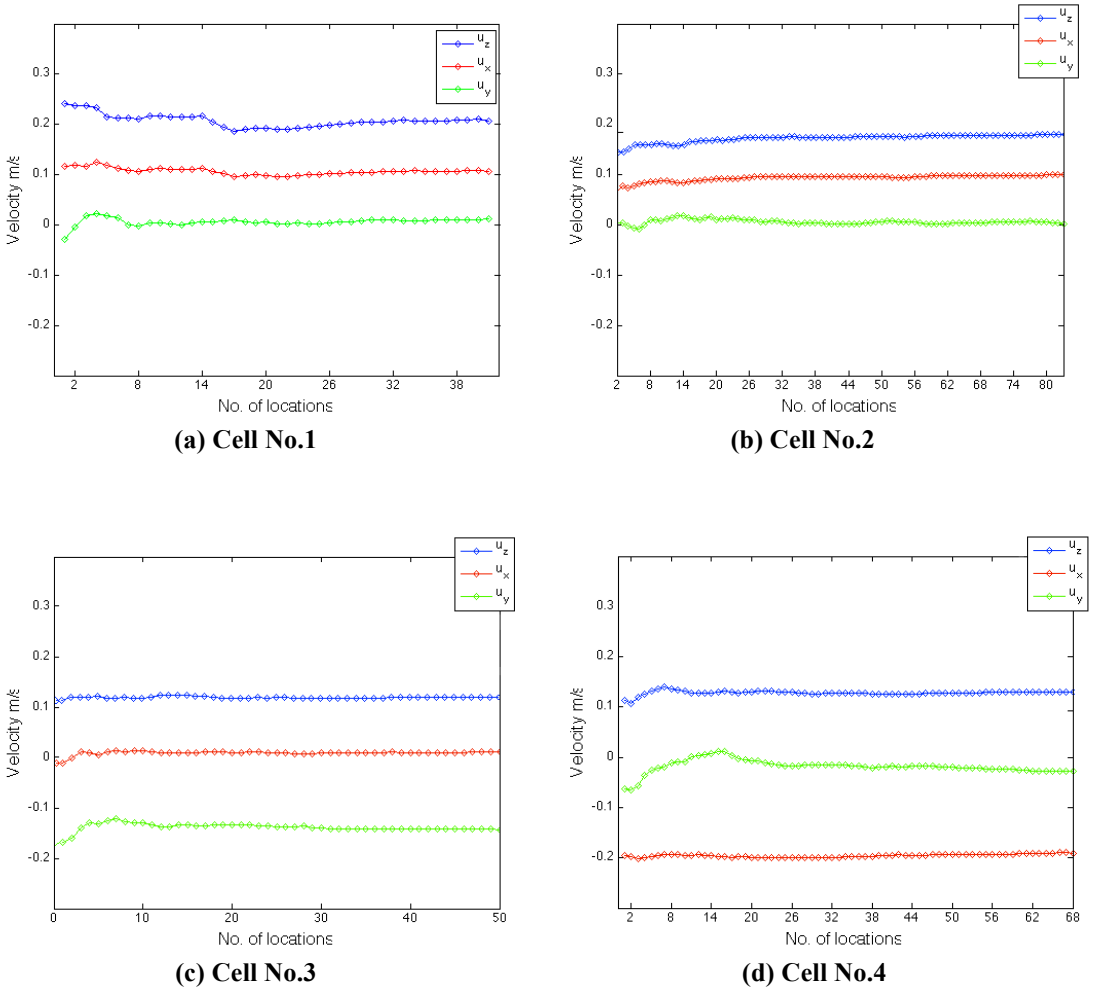

(a) Cell No.1 **(b) Cell No.2**

(c) Cell No.3 **(d) Cell No.4**

Figure 7.9. Effect of changing the number of locations in each cell on the calculated velocity in different directions for (a) cell No.1; (b) cell No.2; (c) cell No.3; (d) cell No.4.

It is observed that the average velocity for the cells located close to the solid boundaries of the system is calculated over fewer locations in comparison with the ones far from the solid boundaries. For all of these cells, it seems that the value of velocity becomes steady by the end of using the total number of locations in each cell.

Table 7.2 shows the standard deviation of all the velocity components for all the cells. Same as the result from using Carbopol 0.1 wt% in KM (§5.3.2.), the standard deviations of all the velocity components are in the order of 10^{-3} *m/s,* which is similar to the ones from Kenics mixer, except for u_x and u_z of cell number one and four.

Table 7.2. Standard deviation and mean values of three velocity components for different cells.

Cell number	Average u_z $m.s^{-1}$	Average u_x $m.s^{-1}$	Average u_y $m.s^{-1}$	u_z standard deviation	u_x standard deviation	u_y standard deviation
Cell No.1	0.201	0.108	0.003	0.0116	0.0081	0.0142
Cell No.2	0.186	0.989	0.001	0.0032	0.0011	0.0019
Cell No.3	0.102	0.001	-0.0189	0.0045	0.0022	0.0036
Cell No.4	0.113	-0.201	-0.182	0.0094	0.0064	0.0198

However, even for cell one and four it can be observed that by reaching to the total number of locations used in each cell, the velocity components becomes steady, which indicates the value of average velocity in each cell is calculated over sufficient number of locations.

7.3.3 Studying the velocity maps in Cartesian reference system

The Eulerian velocity maps along the SMX-plus mixer are plotted after calculating the average velocity in each cell. Figure 7.10 shows the third and fourth elements of the mixer, with the red dash lines indicating different axial locations. This picture helps to get a better understanding about the location of the blades, and axial and cross-sectional velocity maps, which will be presented later.

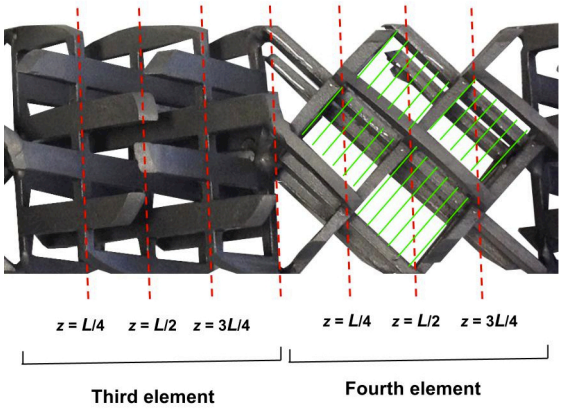

Figure 7.10. Arrangement of the blades along the third and fourth element of SMX-plus, with *L* as the length of the element.

Figure 7.11 represents the axial velocity maps normalised by the value of superficial velocity (0.15 *m/s*) along the third and fourth elements, relative to their axial coordinates of $z = 0$, 1/4 L, 1/2 L, 3/4 L, with L being the element length.

As shown in Figure 7.11(a) and (b), at $z = 0$ the cross-section of the mixer is divided into half by a blade passing horizontally and vertically from the middle of the cross section. For $L/4 < z < 3L/4$, it can be observed that velocity is the highest in the middle of the distance between each two neighbouring blades. To get a better understating about the position of these high velocity areas, they are shaded green in Figure 7.10. The velocity decreases by going towards the inner wall of the pipe and the solid boundaries of the system, as expected. The velocity maps along the third and fourth element look similar to each other, with the only difference being 90° geometry rotation. For the presented velocity maps of KM, which were discussed in the previous chapters, the position of the blade was marked by the existence of the empty cells within the map. However, for SMX-plus no empty cell could be observed where the blades are located due to the axial length of the cells, but their estimated positions could be seen where the velocity is lowest. This inaccuracy might be due to two reasons. First, the low data density and therefore choosing the longer cells on the Eulerian map; and second the complicated configurations of the blades, which leads to the existence of small empty spaces between each neighbouring blades. Considering 1.5-2 *mm* PEPT localisation error, the small area between each neighbouring blades and the thickness of them, there is a high chance that the PEPT algorithm recorded a position for the tracer where the blade is actually located.

3rd element	4th element

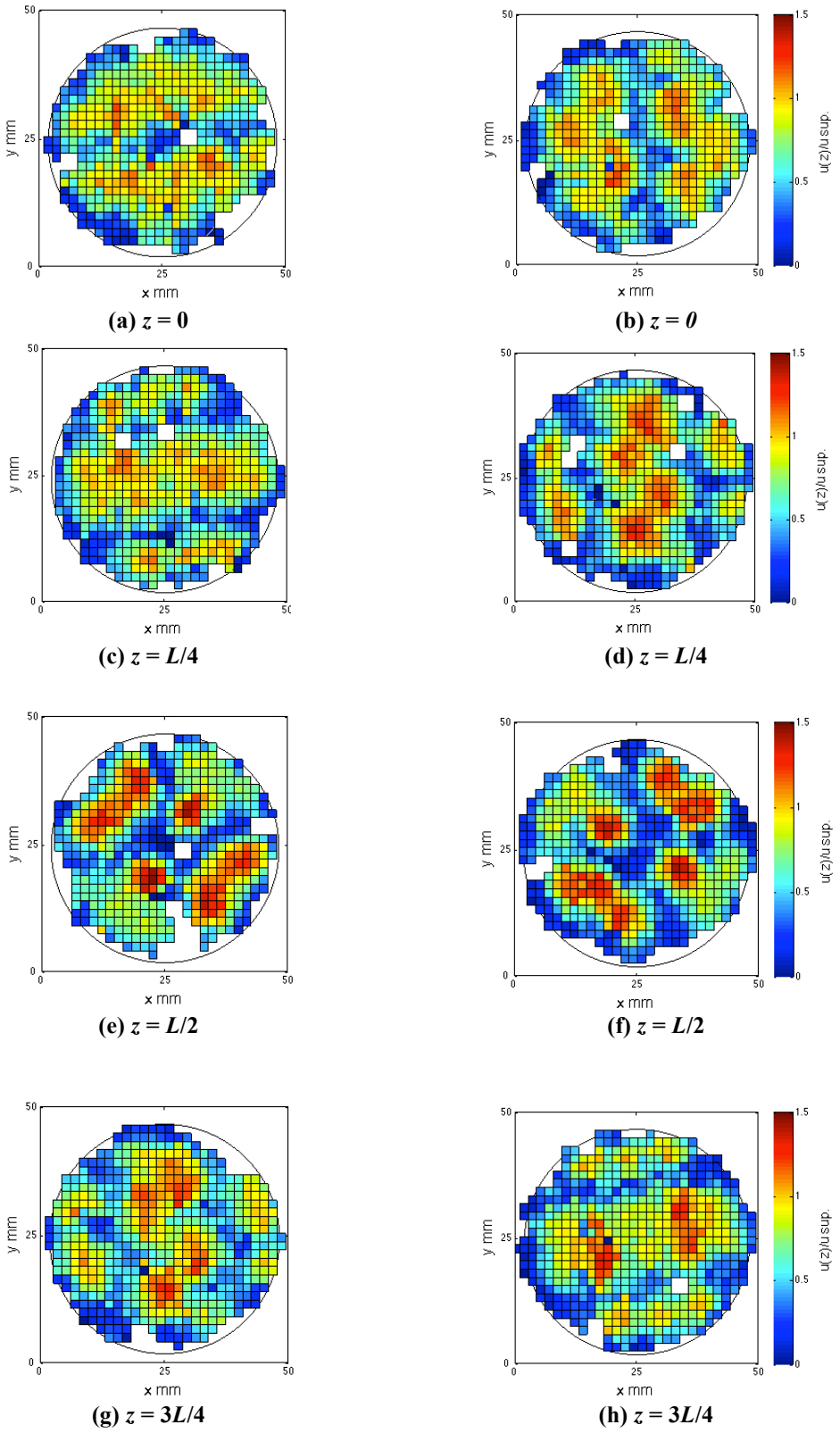

Figure 7.11. Normalised axial velocity map along the mixer at different cross-sections along (a-c-e-g) 3rd element; (b-d-f-h) 4th element. *L* is the length of the element.

7.3.3.1 Particle trajectories and arrangement of the blades

In order to get a better understanding about the effect of the gap between each neighbouring blade on the particle paths, the particle trajectories of six random passes are plotted in Figure 7.12.

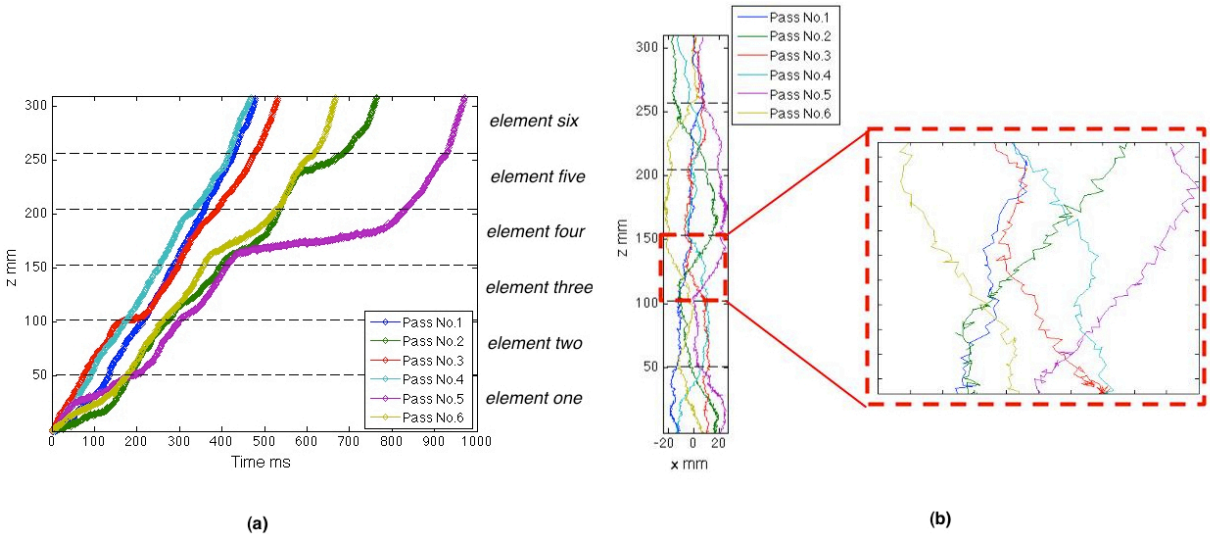

Figure 7.12. Particle trajectories of six random passes along the mixer. (a) z vs. time; (b) z vs. x.

It can be observed from Figure 7.12(a) that the slope of the curve, which represents the axial velocity along the mixer, does not change significantly within an element for pass number one, three, and four. The slope of the curve of pass number two, five, and six in Figure 7.12(a) however decreases within the fourth element. By looking at Figure 7.12(b), it can be observed that these particles are moving close to the inner wall of the pipe, which explains the sudden decrease in axial velocity of these passes along the fourth element. Figure 7.12(b) also shows the deviation of the particle trajectories from each other along the elements, which can be related to the arrangement of the blades. Although it is not possible to show the exact position of the blade, the general picture from Figure 7.12(b) shows how the passage of particles

through different gaps between the blades within an element could change their position relative to each other.

It was shown in Figure 7.12(b) the particle trajectories follow the gaps between the blades within each element. However, there is still a chance that due to the PEPT localisation error and also the high number of blades within each cross section, the position of the particle is recorded where the blade is actually located. As discussed before in §4.3.3, this might be one of the reasons that it is not possible to have a clear observation about the location of the blades from the velocity distribution maps.

7.3.3.2 Cross-sectional velocity distribution maps in SMX-plus

To get more information about the movement of the fluid between the blades in SMX-plus, the cross-sectional velocity maps are plotted. Figure 4.10the vector plots used to study the velocity fields relative to the x and y components along the third element. The vector plots are overlapped with the contour maps of the velocity for all the fluids. The colour intensity on the contour plots therefore represents the length of the vectors, given by $|u(x)+u(y)|$. Figure 4.10 shows for $0 < z < L/4$, there are velocity zones created between the vertical solid boundaries with a high magnitude of velocity. At $z = L/2$, it can be observed that the cross-sectional velocity is significantly lower within the whole cross-section. By comparing this velocity map with the axial one on Figure 7.11(e), it can be concluded that at this specific location along the element the movement of the fluid is mainly in the axial direction, and therefor there is a higher velocity in axial direction rather than the cross-sectional one. This could be due to the arrangement of the blades at $z = L/2$, which is also observable in Figure 7.10.

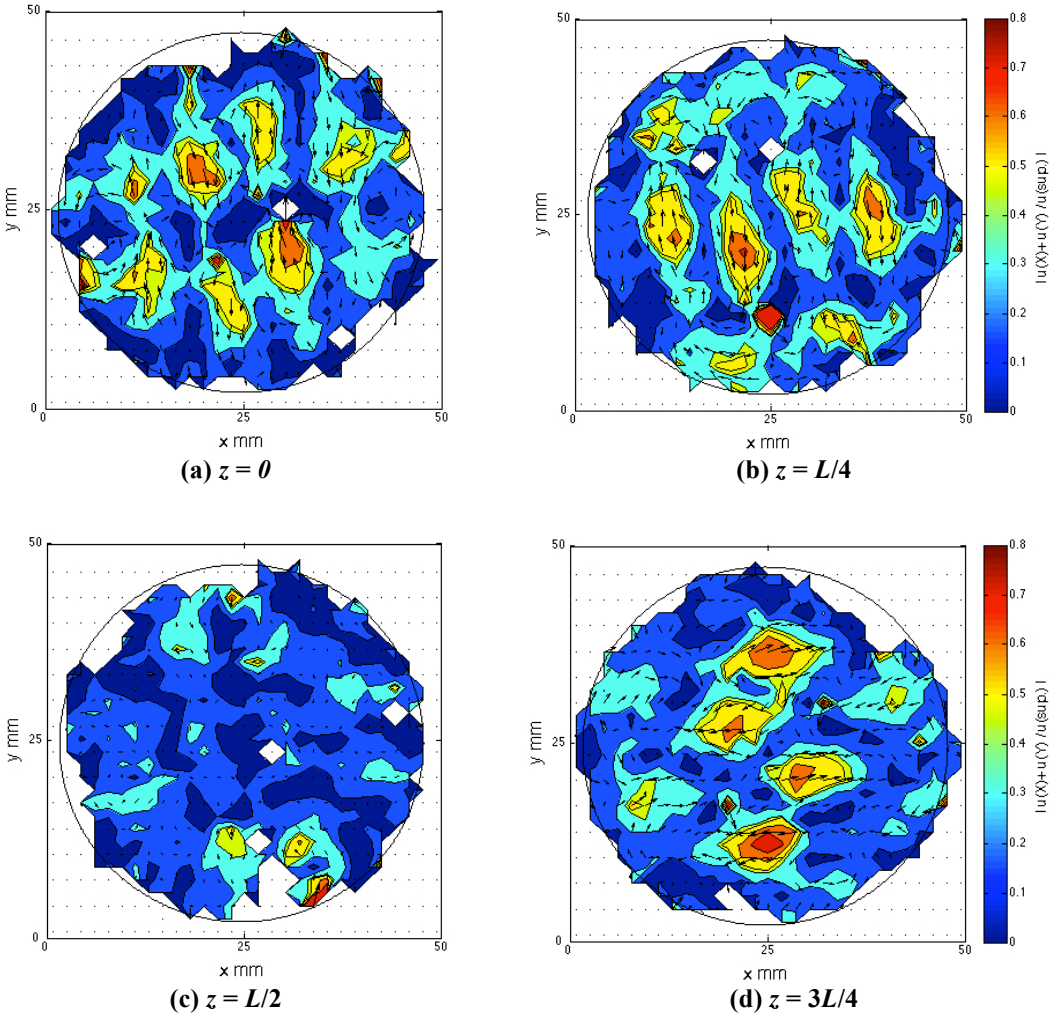

(a) $z = 0$ **(b) $z = L/4$**

(c) $z = L/2$ **(d) $z = 3L/4$**

Figure 7.13. Velocity vector plots of *x*- and *y*- velocity components along the 3rd element at (a) $z = 0$; (b) $z = L/4$; (c) $z = L/2$; (d) $z = 3L/4$.

Two of the cross-sectional velocity maps presented in Figure 4.10are selected and by zooming in on their vector plots, the direction of the fluid within the cross-section is investigated (Figure 7.14). Figure 7.14 (a) shows the cross section of the mixer on the third element at $z = 0$, with a window frame covering the right half of the mixer. It can be observed that the arrangement of the vertical blades causes the anticlockwise and clockwise movement of the fluid in the area between each two neighbouring blades.

For $z = 3L/4$, as a result of getting closer to the next transition region, the direction of the vectors changes and they become more or less parallel to the x axes, showing still

the opposite direction of movement for each two neighbouring areas separated by a blade.

Figure 7.15(a) and (b) show the axial and cross-sectional velocity maps at $z = L/4$ on the third element. It can be seen that on the axial velocity map it is just possible to observe the horizontal blade passing from the middle of the cross-section, and not the vertical ones which are observable on Figure 7.15(a). The movement of the fluid in x and y directions on the cross-sectional velocity maps makes it possible to observe the vertical blades as well as the horizontal one. The reason that the vertical blades are not observable in Figure 7.15(a) as good as in Figure 7.15(b) is due to the fact that the length of the cells in x and y directions are shorter than the z direction. Consequently, the velocity maps on x and y direction have more accuracy in terms of detecting all the solid-boundaries within the cross section, while the ones for axial velocity are less accurate since the length of the cells are longer in the axial direction. As discussed before, by increasing the data density it might be possible to get a better resolution in all the directions for such a complex geometry. Figure 7.15(b) also shows the direction of the flow in each neighbouring area separated by vertical blades is opposite to each other. This behaviour is demonstrated in Figure 7.15(c).

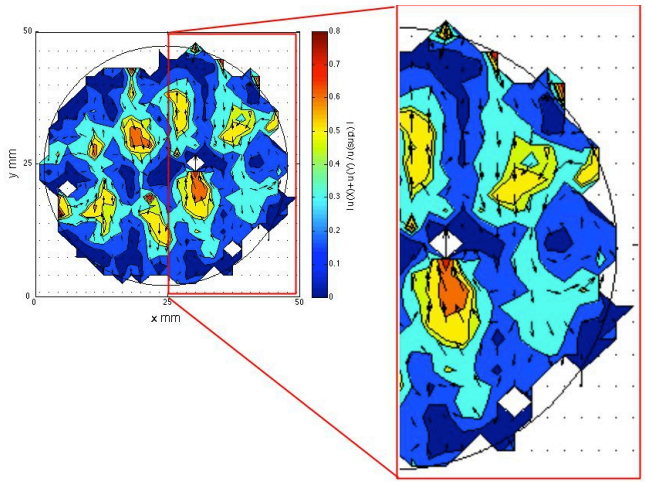

(a) $z = 0$

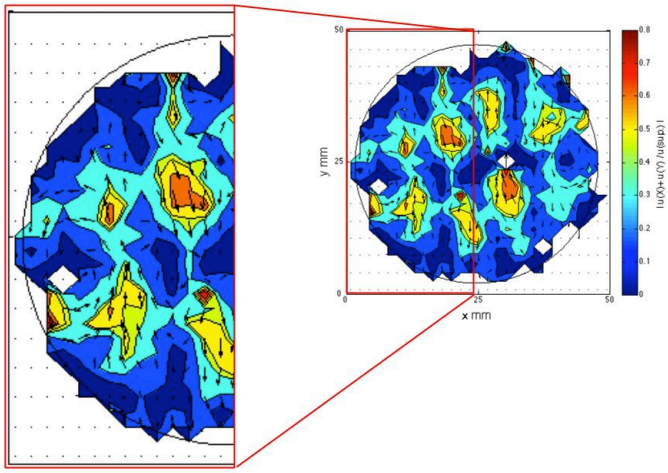

(b) $z = 0$

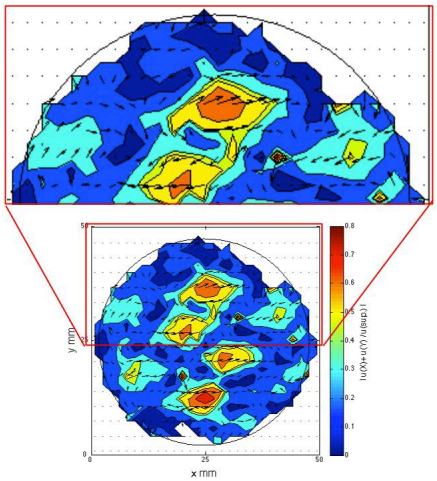

(c) $z = 3L/4$

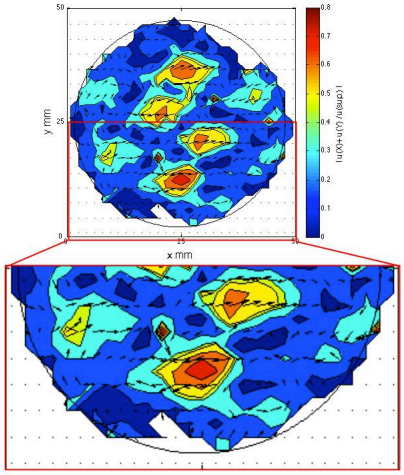

(d) $z = 3L/4$

Figure 7.14.Velocity vector plots located at (a,b) $z = 0$; (c,d) $z = 3L/4$.

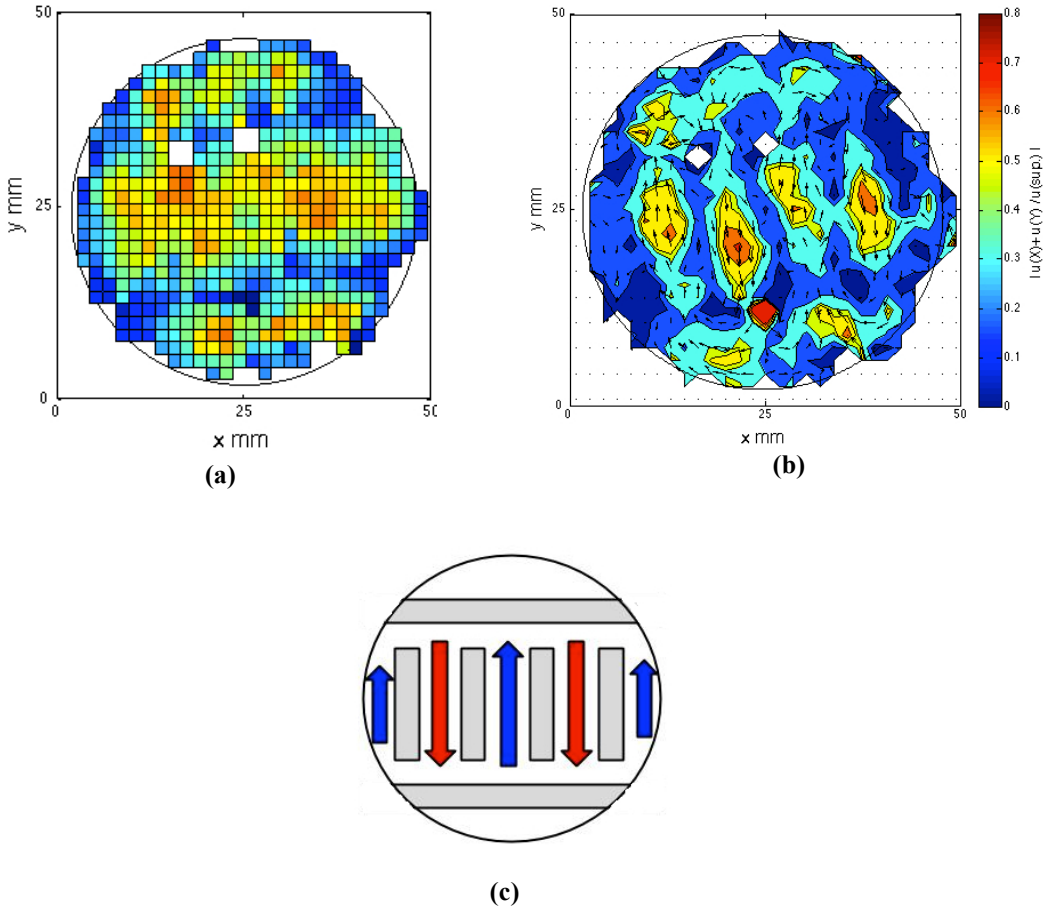

Figure 7.15. (a) Normalised axial velocity map at $z = L/4$ on the third element; (b) normalised cross-sectional velocity map at $z = L/4$ on the third element; (c) schematic of the flow direction and he position of the blades at at $z = L/4$ on the third element.

It is shown that the configuration of the blades in SMX-plus, has a significant effect on the movement of the fluid in x and y direction within the element and between each two neighbouring blades. For Kenics mixer, the particles follows the twist of the blade along each element, and upon reaching the transition region they can go either to the right or left side of the following blade. However for SMX-plus, six blades are located within an element, and by reaching to each one of them the particle can either goes through the right or left side of the blade. This special arrangement of the blades increases the chance for the particle to change its location in x and y direction continuously along each element. The cross-sectional velocity maps in Figure 4.10

showed the cross-sectional movement of the fluid within each element of SMX-plus is significantly more than the one for KM mixer, due to the arrangement of the blades in SMX-plus. This characteristic behaviour of fluid in SMX-plus, leads the particles to distribute better among each other within the cross-section of each single element and not just in the transition areas in comparison with KM. This behaviour could have a major effect on the cross-sectional mixing of SMX-plus in comparison with KM. The lower value of segregation and therefore the better mixing performance of SMX-plus confirm the better distribution of particles for this mixer.

7.4 Residence time distribution

7.4.1 Studying the residence time distribution from the experimental data

The residence time distribution is calculated using the following formula (Levenspiel, 1972):

$$E(t) = \frac{c(t)}{\int_0^\infty c(t)\,dt} \qquad \textbf{(Equation 7.6)}$$

where *c(t)dt* is the concentration of the tracer at the outlet between time *t* and *(t +dt)*. Equation 7.6 is modified to a discrete function:

$$E(t) = \frac{n(t) \diagup \delta t}{\sum_{t=1}^{t=\infty} n(t)} \qquad \textbf{(Equation 7.7)}$$

where *n(t)* is the number of passes with residence time between *t* and *(t+δt)*. The mean residence time is then calculated from (Scott, 1992) :

$$\bar{t} = \frac{\int_{t=0}^{t=\infty} t.E(t)\,dt}{\int_{t=0}^{t=\infty} E(t)\,dt} = \int_{0}^{\infty} tE(t)\,dt \qquad \textbf{(Equation 7.8)}$$

By defining the normalised time as $\theta = t/\bar{t}$, the dimensionless RTD function is calculated from Equations 7.7 and 7.8:

$$E(\theta) = E(t) \times \bar{t} \qquad \textbf{(Equation 7.9)}$$

Figure 7.16(a) shows the residence time distribution curves for each single element of SMX-plus. The area under each curve is equal to one, and it can be seen that the peak of all the curves located around the same θ, which means the mean residence time for all the curves is similar. Figure 7.16(b) shows the value of the mean residence time for each single element. As shown, mean residence time does not change significantly along the mixer for each element. By dividing the length of each element by the value of the superficial velocity, the expected mean RT for each single element can be calculated. As it is shown in Figure 7.16(b), the mean residence time calculated form the experimental data is constant and in good agreement with that calculated from the superficial velocity.

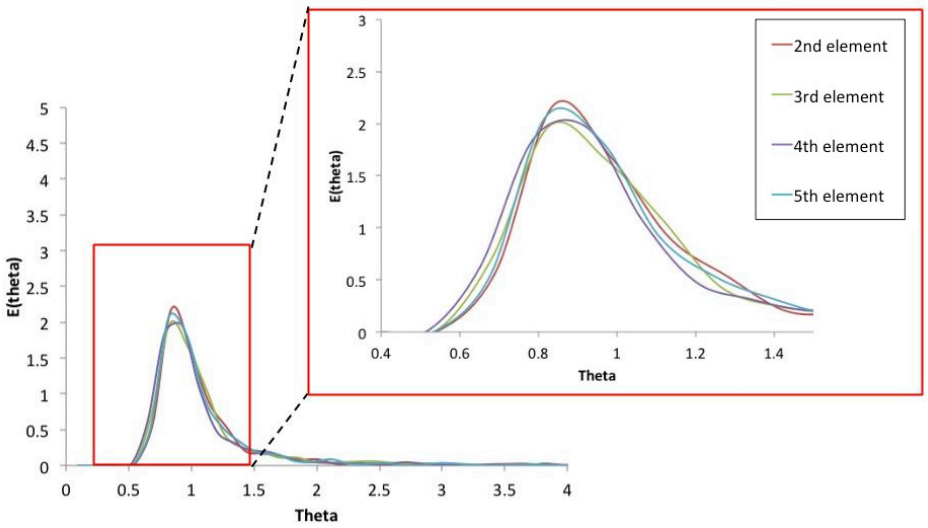

(a)

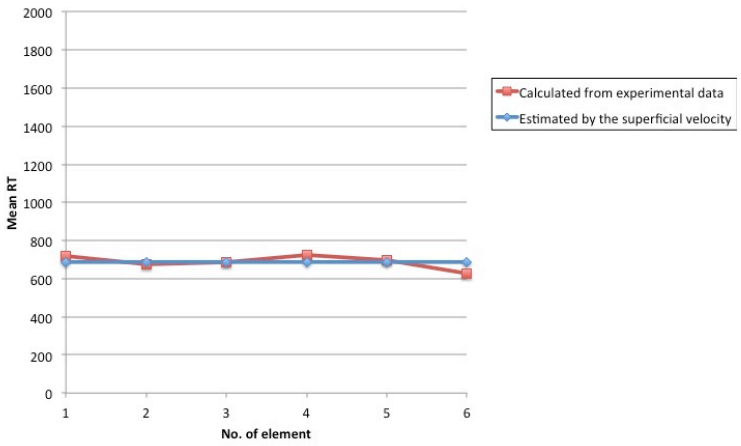

(b)

Figure 7.16. (a) normalised RTD along each single element; (b) changes of the mean RT for each single element along the mixer.

Figure 7.17(a) presents the RTD calculated from the start of the first element along the mixer. It can be see that by going further towards the end of the mixer, the peak of the residence time is moving towards $\theta = 1$.

Figure 7.17(b) shows the comparison between the residence time distributions along the first six elements of Kenics static mixer and SMX-plus, at which Carbopol 0.1wt% solution used as the model fluid. The peak of the RTD curve is shifted towards the right hand side for SMX-plus in comparison with the one for KM.

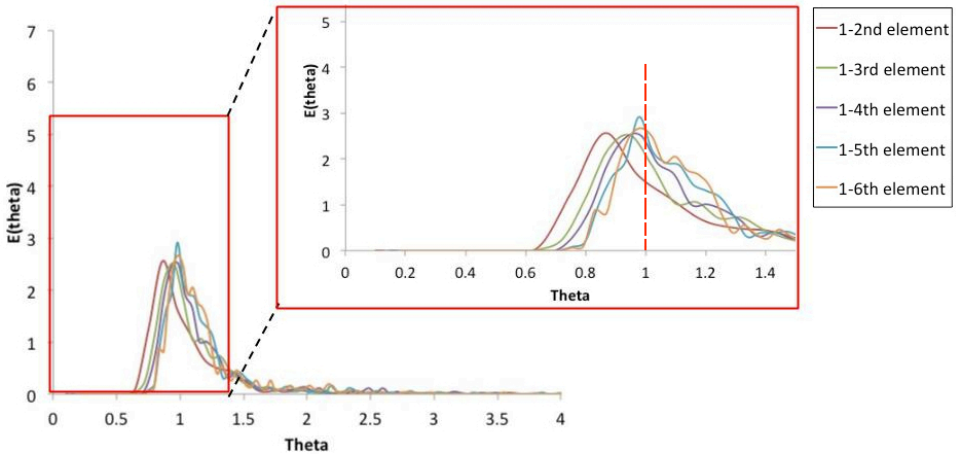

(a)

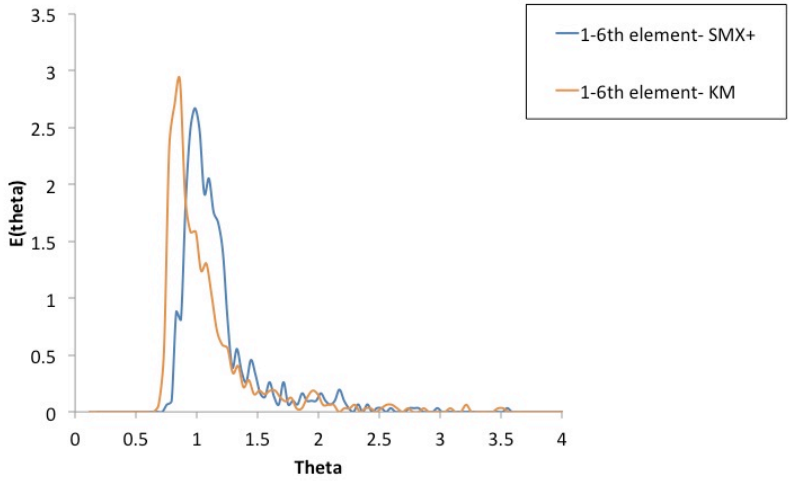

(b)

Figure 7.17.(a) RTD along the mixer starting from the 1st element; (b) comparison between KM and SMX-plus.

7.4.2 Choice of the model for residence time distribution

As discussed before in Chapter five, the analytical solution for the convection model of RTD is not available for Herschel-Bulkley fluids ((Levenspiel, 1979), Levenspiel (1972)). Therefore, the dimensionless residence time distribution function ($E(\theta)$) is directly derived from the equation of the laminar velocity profile of an empty pipe for the Herschel-Bulkley fluids. This procedure was described before in detail in §5.6.2.

Figure 7.18(a) shows the residence time distribution function along first two, three, and five elements for SMX-plus mixer in comparison with the one estimated from the predicted pipe flow velocity profile of the Carbopol 0.1 wt% solution.

Figure 7.18(a) shows the minimum time for the tracer in the non-Newtonian fluid to go through the mixer is more than 0.5. Since the RTD model is calculated from the velocity profile of an empty pipe, the deviation of the residence time distribution curve at the start of the mixer from the one calculated from the model is expected.

By comparing the shape of the experimental RTD and the ones for convection and dispersion model from Levenspiel (1972) in Figure 7.18(b), it can be observed by going through more number of elements in SMX-plus, the RTD curve deviates more from convection model, and getting closer to the dispersion model. This indicates the main changes in dispersion is happening within the transitional areas between the elements, and by passing through more number of elements the RTD is getting closer to the shape of the residence time distribution for dispersion model.

Figure 7.19 shows the RTD curves along the first six elements for both KM and SMX-plus mixer, using Carbopol 0.1 wt% as the model fluid. The peak of the RTD curve for SMX-plus is closer to $\theta = 1$ in comparison with the one for KM, and therefore closer to the dispersion model. This shows the fluid is getting much more dispersed in SMX-plus in comparison with KM, after going through the same number of elements.

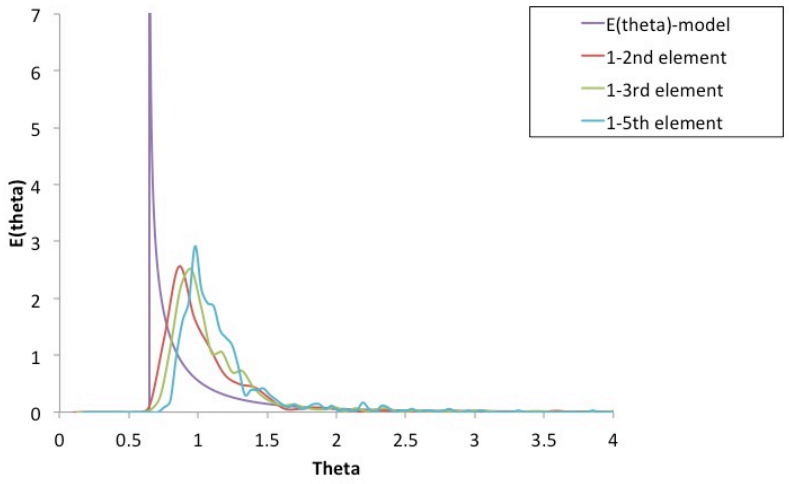

(a)

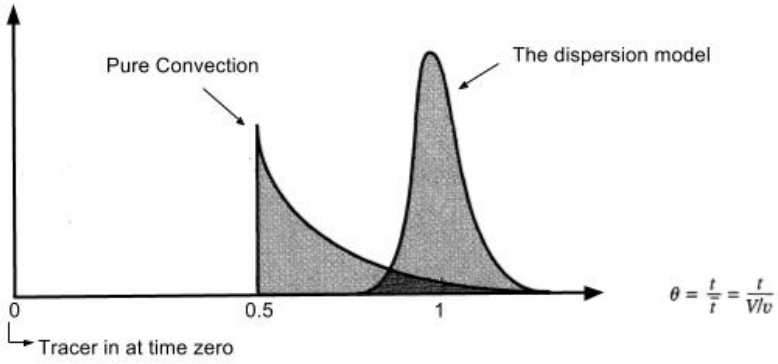

(b)

Figure 7.18. (a) Comparison between the RTD calculated from the model and the experimental data; (b) RTD curves for convection and dispersion models (adapted from Levenspiel (1972)).

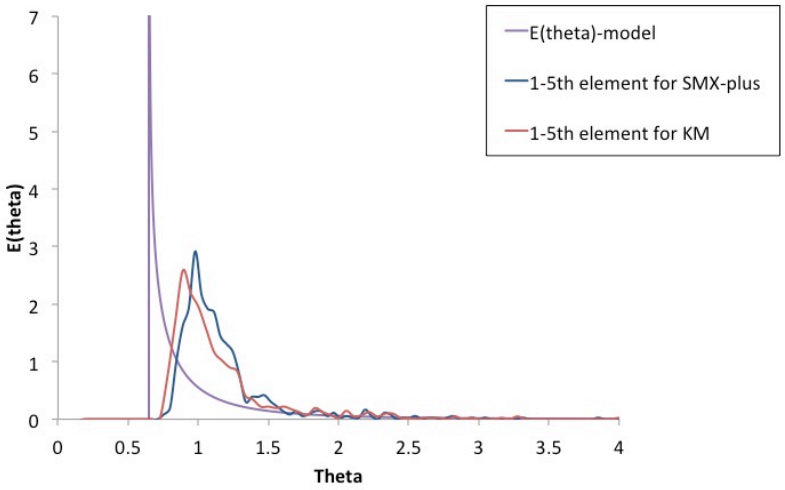

Figure 7.19. Comparing the RTD calculated from the model and experimental data for SMX-plus and Kenics static mixer.

The results from Figure 7.18 and Figure 7.19 show the experimental RTD function of SMX-plus looks closer to the dispersion model, due to the higher amount of dispersion in comparison with Kenics mixer. Therefore, it is decided to fit the experimental data to the dispersion model for SMX-plus mixer.

7.4.2.1 Dispersion model

The amount of the dispersion within a system can be characterised by calculating the dimensionless Peclet number (Scott (1992)):

Pe = (Rate of transport by advection) / (Rate of transport by dispersion)

$$= \frac{uL}{D_{disp.}} \qquad \textbf{(Equation 7.10)}$$

where u is the velocity ($m.s^{-1}$), L is the characteristic length (m), and $D_{disp.}$ is the dispersion coefficient (s^{-1}). By treating the boundary condition of the mixer as the open-open system, at which the flow is undistributed as it passes the entrance and the exit boundaries (Figure 7.20), the following equation has been derived (Scott (1992)):

$$\frac{\sigma^2}{\bar{t}^2} = \frac{2}{Pe} + \left(\frac{8}{Pe}\right)^2 \qquad \textbf{(Equation 7.11)}$$

where σ and $\bar{t}$ are the standard deviation and the mean of the distribution which can be calculated from the experimental data.

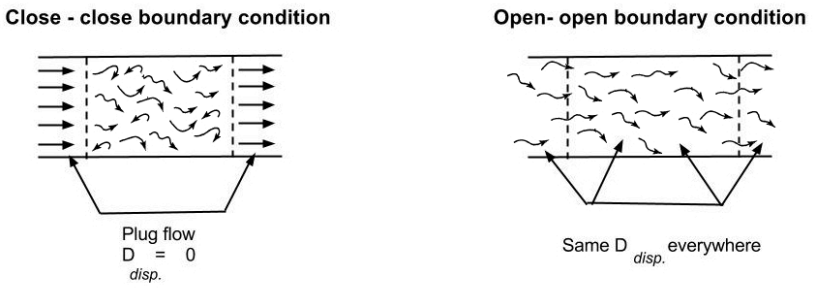

Figure 7.20. Different boundary conditions used with the dispersion model (from Levenspiel (1972)).

By measuring the standard deviation and mean of the residence time distribution from the experimental data, the value of Peclet number for the first six elements of the mixer is calculated as 110. For Pe > 100, the equation of the normalised residence time distribution for the dispersion model can be calculated by the following equation (Scott (1992)):

$$E(\theta) = \frac{1}{2\sqrt{\pi\theta/Pe}} \exp\left[\frac{-(1-\theta)^2}{4\theta/Pe}\right] \qquad \textbf{(Equation 7.12)}$$

where θ is the normalised residence time from the experiment. By calculating the RTD of the dispersion model using Equation 7.12, the experimental data is fitted to the model, and the result is shown in Figure 7.21.

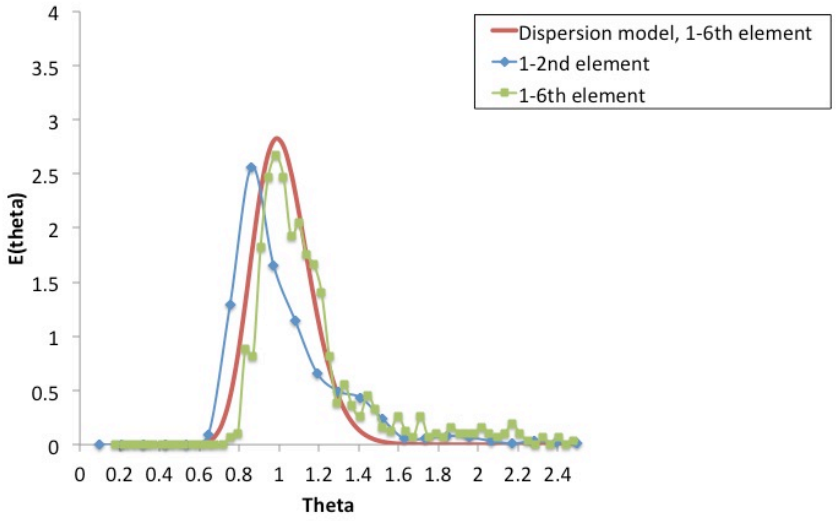

Figure 7.21. Comparing the experimental RTD and the dispersion model.

As shown in Figure 7.21, by passing through six mixing elements, the RTD becomes significantly close to the one from the dispersion model. It can be observed that the experimental data does not fit closely to the dispersion model in two regions: close to the start of the tail of the distribution (θ = 1.3-1.6) and around $\theta \approx 0.8$, where it represents the minimum time required by the tracers to go through the whole length of

the mixer. This deviation might be related to the fact that this model is derived for an empty pipe, while the SMX-plus structure contains a number of blades and solid boundaries within the mixer.

Finally, the value of R-squared (coefficient of determination) is calculated as 0.911, which indicates the experimental data fits the dispersion model closely. The arrangement of the blades in SMX-plus forces the particles to have a large displacement along each single element of the mixer, and therefore they become more dispersed among each other. By going through more number of elements (referring to Figure 7.21, comparison between the RTD of the first element and the RTD of the first to the sixth element) the shape of the RTD curve becomes closer to the dispersion model.

7.5 Conclusion

In this chapter, the behaviour of the non-Newtonian fluid in SMX-plus mixer is investigated by using the data from PEPT experiment. Carbopol 0.1wt% solution was used as the non-Newtonian model fluid. This mixer has been introduced by Sulzer company since just a few years ago, and the first work on it is dated for 2009 (Hirschberg et al., 2009). Hence, the number of the available previous works on this mixer is limited. The results presented in this chapter cover a whole new range of studies on SMX-plus from investigating the velocity maps to the residence time distribution and mixing performance of this mixer in comparison with KM.

The Eulerian velocity maps are studied after meshing the geometry into a number of cells and assigning a value of average velocity to each one of them. It is shown that the average velocity in each cell is calculated over sufficient number of locations, and therefore the value of velocity assigned to each cell represents the average velocity in

that specific location. The normalised axial velocity maps show the value of velocity decreases by going towards the solid boundaries of the system, as expected. The cross-sectional velocities and the fluid rotation within each cross-section are investigated by plotting the velocity vector plots. It is shown that the fluid elements are moving in clockwise and anti-clockwise directions within the space between each neighbouring blades in the cross-section of the mixer. The movement of the fluid within each cross section is significantly more than the one in KM due to the special configuration of the blades. One of the issues observed on the velocity maps of SMX-plus is the resolution of the map. Due to the special configuration of the blades in SMX-plus with the small space between each two neighbouring blade and by considering 1.5 - 2 *mm* PEPT localisation error, there is a high possibility that the PEPT algorithm records a position for the tracer where the blade is actually located. Due to this reason and also the low data density, some of the blades are just observable from the cross-sectional velocity maps and not on the axial velocity maps. Consequently, the shear rate maps are not presented in this chapter, due the low resolution of the graphs. The author suggests for complex geometries such as SMX-plus, which consists of a higher number of solid boundaries within the cross-section, it is necessary to have a higher data density than geometries such as KM, to have an accurate velocity map with a good resolution. It can be suggested to use at least 2000 passes for this kind of geometry.

The mixing performance in SMX-plus mixer is characterised by calculating the changes of segregation index along the mixer. It is shown that for SMX-plus the system reaches to the randomised stage of mixing on the third element, while for KM this was happening on the sixth element. The value of segregation is lower along each single element for SMX-plus than KM, which indicates the better distribution of

particles within each element for SMX-plus. According to the cross-sectional velocity maps, the movement of the fluid within each cross section is significantly more for SMX-plus than KM due to the special configuration of the blades in this mixer. Consequently, the particles distributed more among each other along each single element in SMX-plus rather than KM, and therefore the value of segregation would be lower along the SMX-plus. The changes of striations thicknesses are visualised by plotting the distribution of the blue and red particles among each other for all the experiments with KM and SMX-plus. The significant better performance of SMX-plus in comparison with KM could be observed visually just after going through one element. This analysis shows PEPT could be used as a powerful experimental technique to characterise and compare the mixing performance of different mixers with complex geometries.

The residence time distribution function is calculated from the experimental data along the mixer. The RTD curves for each single element look similar to each other, as expected. The dimensionless RTD function of Herschel-Bulkley fluid is estimated from its predicted pipe flow velocity profile, since there is no analytical solution available for the RTD of the convection model for this group of fluids. It is shown by going through more number of elements, the residence time distribution curves calculated from the experimental data are getting further away from the convection model, and getting closer to the dispersion model. The experimental residence time distribution is also fitted to the dispersion model, and it is observed the RTD after going through six elements is a close fit to the dispersion model. The arrangement of the blades in SMX-plus mixer causes the particles to become more dispersed within each other, and therefore results in having a better axial mixing.

The results presented in this chapter showed for complex geometries such as SMX-plus, it is necessary to have a high data density to get a good resolution on the velocity maps. It is also shown that PEPT could be used as a powerful experimental technique to study and compare the flow behaviour and mixing performance within the mixers with different configurations.

Notation

Roman letters

A_{flow}	Flow area	m^2
$c(t)dt$	Concentration of the tracer at the outlet between time t and $(t + \delta t)$	mol dm^{-3}
D_h	Hydraulic mean diameter	m
$D_{disp.}$	Dispersion coefficient	s^{-1}
$E(t)$	Residence time distribution function	-
$E(\theta)$	Normalised residence time distribution	-
k	Consistency index	Pa. s^{n-1}
k'	Apparent consistency index	Pa. s^{n-1}
L	Length of the element	m
N_{Re}	Reynolds number	-
n	Flow index	-
$n(t)$	No. of passes with RT between t and $(t + \delta t)$	-
n'	Apparent flow index	-
Pe	Peclet number	-
t	Time	s
$\overline{t}$	Mean residence time	s
Q	Volumetric flow rate	m^3.s
Q'	Volumetric flow rate between two consecutive radius	m^3.s
R	Radius	m
Re_{MR}	Metzner & Reed Reynolds number	-
S	Segregation index	-
$u(r)$	Velocity in r direction	$m.s^{-1}$
$u_{sup.}$	Superficial velocity	$m.s^{-1}$
u_x	Velocity in x direction	$m.s^{-1}$

u_y	Velocity in y direction	$m.s^{-1}$
u_z	Velocity in z direction	$m.s^{-1}$
u_{tan}	Tangential velocity	$m.s^{-1}$

Greek letters

τ	Shear stress	Pa
τ_0	Yield stress	Pa
τ_w	Wall shear stress	Pa
$\dot{\gamma}$	Shear rate	s^{-1}
ϕ	ratio of yield stress to the wall shear stress	Pa
ρ	Density of the fluid	$kg.\ m^{-3}$
θ	Normalised residence time	-
θ_{min}	Minimum time for the tracer to go through the mixer	-

Chapter 8 .CONCLUSIONS AND FUTURE WORK

In this chapter are reported the overall conclusions of the results presented in this work. The chapter is divided in sections according to the order in which the result chapters are presented. The conclusions finish with the future recommendations.

8.1 Newtonian and non-Newtonian fluids in Kenics static mixer

- *The flow behaviour of Newtonian and non-Newtonian fluids has been studied using PEPT as the experimental technique.*

Glycerol and Carbopol solutions were used as the Newtonian and non-Newtonian model fluids to study the flow behaviour within the standard design of KM with 180° twist angle. Different methodologies have been developed using MATLAB computer codes to investigate and characterise both the motion of the flow and the performance of the mixer.

PEPT has been used for the first time to generate a wealth of data sufficient to validate current numerical simulations and those to come. However, it has been found challenging to compare the results of Lagrangian simulations where the difference between the data density obtained from numerical simulations exceeds the one achievable by PEPT at least by one order of magnitude. For instance, the numerical works on KM used at least 20000 tracer particles, injecting them through a circle with diameter of 0.1 *cm,* which covers an area that presents 1% of the volumetric flow. Using numerical software, the velocity distribution, mixing performance, and stretching histories were studied along the mixer on these numerical works. While the maximum number of particle passes obtained with PEPT in this work was around 2000 passes after five days of experiment.

The Eulerian velocity distribution maps have been used to show the nature of the Kenics mixer. These maps have revealed the flow split at the transition regions between consecutive elements, and the re-blending of this along each element. The results from axial, tangential and cross-sectional velocity maps of glycerol were found in agreement with the literature. It was observed that the value of axial velocity decreases towards the solid boundaries of the system, as expected. The axial velocity maps of both non-Newtonian fluids found to be similar to each other, which was in agreement with the similarity between the predicted pipe flow velocity profiles of them.

Shear rate was calculated using PEPT data for both Newtonian and non-Newtonian fluids. It has already been described in this thesis that, in the same way as all other experimental techniques, PEPT by nature has a localization error. In addition, the mathematical transformation which generated the Eulerian velocity maps inevitably adds to the uncertainty in localization and therefore velocity. In this work, special care was taken in sampling sufficient data points per mesh cell, in order to have statistically significant differences between neighbouring cells. Nevertheless, upon calculating the derivatives for the shear rate from the Eulerian velocity maps, these uncertainties are amplified and produce a noisy shear rate map. The author believes that although it is difficult to infer a clear shear rate profile for some cross sections, the overall value of shear is indicative of the fluid dynamic conditions present in the mixer. This statement is also supported by shear rate estimation for the current flow rates. The highest value of the shear rate was observed close to the solid boundaries due to the existence of the high gradient of velocity in these areas for all the experimental conditions.

- *The effect of the two main mixing mechanisms in Kenics mixer - distributive and dispersive mixing - on the residence time distribution was shown along the mixer for Newtonian and non-Newtonian fluids.*

The residence time distribution function was calculated along each single element of the mixer, and the similarity between the shapes of the RTD curves for each single element was observed as expected. Each mixing element along the mixer can act as individual mixing units, and therefore the combination of six mixing elements is similar to having six mixers in series. It was shown that the shape of the RTD curve for the first two elements of the mixer is close to the convection model for laminar flow in pipes, but at the end of the mixer, it is closer to the shape of the RTD function for the dispersion model. The similarity between the shape of the RTD curves of each single element to the one for the convection model shows the distributive mixing is happening along the single elements. It was also demonstrated the dispersive mixing happens mainly on the transition regions, showing the effect of passing through the transition regions on the RTD curves by getting closer to the dispersion model.

- *The data from PEPT measurements can be used to characterise the cross-sectional mixing performance in Kenics mixer for Newtonian and non-Newtonian fluids.*

The mixing performance was characterised using two techniques, the analysis of the variability in concentration of labelled passes in discrete sections of the fluid (CoV) and by a closest neighbour technique (segregation index). It was shown that the use of a number based coefficient of variance alone is not enough to fully characterise the mixing performance in Kenics mixer using the discrete data. It was demonstrated that CoV does not show any sensitivity to the arrangement of the particles next to each

other within a cell, but just to the total number of them in each cell. Due to the resolution of the PEPT data, it was not possible to have a quantitative measurement about the scale of segregation and striation thicknesses. However, it was observed the number of striations changes according to the theoretical relation for the first three elements, before it becomes hard to distinguish the striations by eye. Considering all the above-mentioned issues, the author does not suggest the use of CoV on the PEPT experimental data to characterise the mixing performance in continuous mixers. An alternative way was suggested to characterise the mixing performance in KM by means of a segregation index. In this method, the segregation index is calculated based on finding the closest neighbouring particle for each tracer particle. The results from the Newtonian fluid in KM showed the system reaches to a randomised state of mixing within the sixth element of the mixer.

- *Carbopol 0.2 wt% solution mixes better than Carbopol 0.1 wt% solution.*

The comparison between the mixing performances of non-Newtonian fluids used in this work showed the mixing performance of KM using Carbopol 0.1 wt% solution is poorer than Carbopol 0.2 wt% solution. The analysis showed the difference in their mixing performances was not due to the existence of entrance effect in the mixer using Carbopol 0.1 wt% solution. A qualitative measurement based on the distribution of blue and red particles along the mixer showed the fluid elements of Carbopol 0.1 wt% solution have a lower stretching and folding along the mixer in comparison with Carbopol 0.2 wt%. The calculations of the theoretical development length for these two fluids reveals that Carbopol 0.1wt% solution has a development length at least three times more than the one for Carbopol 0.2 wt% solution. The difference in the development length of these two fluids might cause a reduction in stretching of the fluid elements for Carbopol 0.1 wt% as a result of having slower response to the

changes of geometry after going through each transition region. This behaviour could affect the mixing performance, and results in a poorer mixing performance of Carbopol 0.1wt% solution. A quantitative measurement of stretching and folding of the fluid elements within the mixer for Carbopol 0.1 wt% might reveal more information about this matter in the future.

8.2 Effect of twist angle of the blade on performance of KM

- *Although changing the twist angle of the blades does not have a significant effect on the velocity and shear rate distribution maps, it affects the mixing performance within the Kenics mixer.*

The geometry of the Kenics mixer was modified by changing the twist angle of the standard design to 150° and 120°, and the performance of these configurations were compared to each other using glycerol as the Newtonian model fluid. The comparison between velocity and shear rate distribution maps revealed the twist angle of the blade does not have a significant effect on the Eulerian velocities and the shear distribution within KM, since the amount of the twist per unit length for all the geometries is the same. The main effect of twist angle was observed on the mixing performance and residence time distribution.

It was shown that KM with 180°, 150°, 120° twist in blades reaches the randomised state of mixing on the sixth, fifth, and the ninth element. The mixing performance per mixing element can be summarised as: KM 150° > KM 180° > KM 120°. This result is in agreement with the numerical results in literature. Under the assumption of a linear increase of pressure drop with length, the changes of segregation versus axial distance along the modified geometries were also plotted. It was shown that also in this case the KM with 150° of twist retains the best mixing performance. Although

KM 180° has a lower value of segregation than KM 120° along most of the length of the mixer, the value of segregation of these two geometries becomes really close to each other by the end of the mixer. The mixing performance per unit length along the modified geometries can be summarised as KM 150° > KM 120° > KM 180°.

- *Studying the residence time distribution curves showed the Kenics mixer with 150° twist has the best axial mixing both per element and per axial length.*

It was shown by going through the six mixing elements, the shape of the RTD curve of KM 150° becomes the closest one to the dispersion model RTD curve. It was discussed that, after an infinite number of elements, the shape of the RTD curve is expected to become same as the plug flow, which has a sharp peak. It was observed that KM 150° has the best axial mixing in comparison with the other geometries (KM 150° > KM 180° > KM 120°).

8.3 Non-Newtonian fluid in SMX-plus

- *For complex geometries such as SMX-plus, it is necessary to have a high data density to observe an accurate velocity distribution map.*

In this work the flow behaviour of non-Newtonian fluids in the novel SMX-plus mixer was also studied. Due to the recent introduction in the market of this type of mixer (2009), very little is known regarding its mixing performance. In order to be able to observe all the solid boundaries and the blades within a complex geometry such as SMX-plus, it is necessary to choose a grid size as small as possible. The smallest grid size which can be used with PEPT data should not be smaller than the PEPT localisation error, which is around 1 - 1.5 *mm*. However, choosing the small

grid size requires a high data density. The author suggests the use of high data density (at least 2000 passes) in case of investigating complex geometries such as SMX-plus.

- *Each element of SMX-plus is equivalent to three mixing element of the Kenics mixer, and consequently SMX-plus has a better performance than Kenics mixer.*

The axial and cross-sectional velocity maps showed the existence of a movement similar to contra flow within the cross-section of the SMX-plus is more intense than KM, due to the special arrangement of the blades. Hence, the fluid elements move significantly more in radial direction than Kenics mixer, resulting in better mixing within each single element of SMX-plus. It was shown that the system reaches a randomised state of mixing on the third element in SMX-plus, and on the sixth element in Kenics mixer. This significant difference in the mixing performance of SMX-plus and KM was also shown by visualizing the creation of striations along both mixers.

- *The RTD curves of SMX-plus found to be a close fit to the dispersion model.*

The comparison between the residence time distribution curves of SMX-plus and KM revealed the RTD of SMX-plus is closer to the one for dispersion model than KM. By fitting the experimental data to the dispersion model after calculating the Peclet number, it was shown that the RTD of the first six elements along the mixer fits closely to the dispersion model.

8.4 Strengths and weaknesses of PEPT

Other quantification techniques, which are mainly optical ones, have been used widely in different system to study the flow and characterising mixing performance.

A high number of numerical works also investigated the flow behaviour and mixing performance of Kenics mixer. The strengths and weaknesses of PEPT in comparison with both experimental and numerical techniques are discussed in this section.

One of the most important advantages of PEPT is that the use of it is not limited to transparent fluids like the optical techniques; PEPT also makes it possible to study opaque systems. This technique provides unique Lagrangian data, which can be used to visualise the Lagrangian trajectories and the 3D flow structure within the mixing device. Different flow characteristics such as velocity distributions, residence time distribution, shear rate maps, and intensity of segregation can be all studied with this technique, whereas the other common techniques such as PLIF and PIV cannot provide information about all these characteristics together at the same time. According to the literature, the use of other experimental techniques on Kenics mixer has been limited to a selected range of elements, while with PEPT it is possible to access the information about the flow at any point through the mixer and also within each single element of it.

Same as any other experimental technique, there is always expected to see a deviation from the results found by numerical simulations and the ones from experiment, due to the existence of certain experimental errors. The agreement between the results of PEPT on velocity distribution and the mixing performance and the ones from the numerical works showed the reliability of the results from PEPT. However, it should be mentioned that the validation of the results such as velocity distribution and mixing performance depends also on the use of the same operating conditions.

On the other hand, PEPT also has some limitations. Although the amount of the information that can be obtained from the PEPT data is much more than from other

experimental techniques, the cost of the use of this technique is significantly higher as well. The fragility of the tracer makes it sensitive to the mechanical stress that can be applied by the equipment used in the rig. It was observed during the experiments that the use of gear pumps that have inner dimensions smaller than size of the particle, can damage and break the tracer. The breakage of the tracer results in the leakage of its radioactivity and contamination of the entire fluid batch. Consequently it is often necessary to flush out the whole system and re-start the experiment, which is a time consuming process. Using a high flow rate gear pump is not also recommended due to the high shear imposed by the pump, which will result in high stress to the tracer.

Another limitation is the fact that water can leach out the radioactivity of the tracer. Although this problem can be partially solved by using extra coating layer on the tracer, it was shown in this work that the amount of the recorded data within the same number of days using a water-based solution would be less than when using a non-water based solution.

An extra caution should also be taken about using PEPT in small geometries and in systems that impose a sudden change in direction of the flow. Considering the minimum possible size of tracer at which the activity of the tracer is high enough for experiments (200 μm), and the PEPT localisation error, this technique might not work perfectly in the geometries with inner dimensions close to the localisation error.

8.5 Future recommendations

In this work, a methodology has been developed for analysis of the Lagrangian data obtained from PEPT experiments to study the flow and mixing performance in Kenics and SMX-plus static mixers in Laminar regime. The structure of the MATLAB computer codes used for the Lagranian and Eulerian analysis in this work has been

developed in a flexible way, which makes it possible to be applied to other mixing systems by changing the input parameters. The experimental data presented in this work opened a new chapter in understanding the flow behaviour in static mixers. The data can be also used to validate future numerical works using the same operating conditions of this work.

Depending on the financial resources, the author suggests obtaining as many passes as possible for continuous systems such as static mixers. It is suggested to use at least 2000 passes for continuous mixers which have a similar dimensions to the ones used in this work. The duration of the experiment to get 2000 passes depends on the velocity used during the experiment, however, for this experiment it took around thirty five hours to generate 2000 passes with the Newtonian fluid. Generating a similar number of passes for the water-based Carbopol solutions required around fifty hours of experiment. The effect of velocity on the flow behaviour and mixing performance can be studied in the future by applying the same methodology that has been developed in this work to study the flow. The use of higher velocities however, depends on using a tracer that is more resistant to the mechanical stress imposed by the pump, which is currently under development by School of Physics and Astronomy of University of Birmingham. Studying the chaotic behaviour of the fluid in Kenics mixer is highly sensitive to the initial conditions such as the position of the tracer at the entrance of the mixer. It is therefore necessary to improve the resolution and also the PEPT localisation error to be able to study the characteristics that are highly sensitive to the initial location of the tracer. It is also possible to study the effect of scaling up the mixer dimensions on the performance and flow behaviour in KM, by applying the same methodology developed in this work. Considering the ability of PEPT in working with opaque systems and non-transparent fluids, other materials

such as suspensions and polymer melts can also be studied in static mixers by using this technique. The author suggests using other experimental techniques such as PLIF under the same operating conditions to compare the obtained results on mixing performance with the one from PEPT. The effect of shear thinning property of the fluid can also be investigated in more depth using a wider range of flow and consistency indexes. This can provide some more information, which might help to get a better understanding about the observed difference in the mixing performance of the two Carbopol solutions used in this work. The author also suggests a quantitative measurement on stretching the fluid elements, based on the changes in the number of the blue and red particles at each side of the blade along the mixer. In this work, a number of methodologies have been presented to study the motion related properties of the flow such as velocity distributions, shear rate maps, and residence time distribution, as well the characterising the mixing performance in static mixers. The author believes the Lagrangian three-dimensional PEPT data can provide a wealth of information about the flow behaviour in both dynamic and static mixers. Hence, there is always a potential for developing new methodologies to study different flow characteristics.

Knowledge of the limitations of PEPT is fundamental in order to plan and handle the experiments correctly and also the data analysis of continuous systems in Laminar regime. Despite the limitations described, PEPT remains a powerful tool for studying opaque systems, providing a unique experimental 3D Lagrangian data. The methodological approach used in this work can be use as the basis of other works that are intended to study the Laminar flow in other continuous mixing devices.

Chapter 9 . REFERENCES

ADAMIAK I., J. Z. 2001. An experimental investigations of non-Newtonian liquid flow in a static Kenics mixer. Chemical and Process Engineering, 22, 175-180.

ADRIAN, R. J. 1991. Particle-imaging techniques for experimental fluid mechanics. Annual review of fluid mechanics, 23, 261-304.

ALBERINI, F., SIMMONS, M. J., INGRAM, A. & STITT, E. H. 2012. A combined criterion to identify mixing performance for the blending of non-Newtonian fluids using a Kenics KM static mixer.

ALLOCCA, P. 1982. Mixing efficiency of static mixing units in laminar flow. Fiber Producer, 8, 12-19.

ALVAREZ, M., ZALC, J., SHINBROT, T., ARRATIA, P. & MUZZIO, F. 2002. Mechanisms of mixing and creation of structure in laminar stirred tanks. AIChE Journal, 48, 2135-2148.

ALVAREZ, M. M., ARRATIA, P. E. & MUZZIO, F. J. 2002. Laminar mixing in eccentric stirred tank systems. The Canadian Journal of Chemical Engineering, 80, 546-557.

ARMENIADES, C. D. 1966. Mixing device. US patent application.

ARRATIA, P., KUKURA, J., LACOMBE, J. & MUZZIO, F. 2006. Mixing of shear-thinning fluids with yield stress in stirred tanks. AIChE Journal, 52, 2310-2322.

ARRATIA, P. E. & MUZZIO, F. J. 2004. Planar laser-induced fluorescence method for analysis of mixing in laminar flows. Industrial & Engineering Chemistry Research, 43, 6557-6568.

AUBIN, J., FLETCHER, D. F., BERTRAND, J. & XUEREB, C. 2003. Characterization of the mixing quality in micromixers. Chemical engineering & technology, 26, 1262-1270.

AUBIN, J., LE SAUZE, N., BERTRAND, J., FLETCHER, D. F. & XUEREB, C. 2004. PIV measurements of flow in an aerated tank stirred by a down-and an up-pumping axial flow impeller. Experimental thermal and fluid science, 28, 447-456.

AVALOSSE, T. & CROCHET, M. 1997. Finite-element simulation of mixing: 2. Three-dimensional flow through a kenics mixer. AIChE Journal, 43, 588-597.

BAKALIS, S., FRYER, P. J. & PARKER, D. J. 2004. Measuring velocity distributions of viscous fluids using positron emission particle tracking (PEPT). AIChE journal, 50, 1606-1613.

BAKALIS, S., FRYER, P. J. & PARKER, D. J. 2004. Measuring velocity distributions of viscous fluids using positron emission particle tracking (PEPT). AIChE journal, 50, 1606-1613.

BAKKER, A., LAROCHE, R. D. & MARSHALL, E. M. 1998. Laminar flow in static mixers with helical elements. The online CFM Book, http://www. bakker. org/cfm.

BARIGOU, M. 2004. Particle tracking in opaque mixing systems: An overview of the capabilities of PET and PEPT. Chemical Engineering Research and Design, 82, 1258-1267.

BARIGOU, M., FAIRHURST, P., FRYER, P. & PAIN, J.-P. 2003. Concentric flow regime of solid–liquid food suspensions: theory and experiment. Chemical Engineering Science, 58, 1671-1686.

BEMROSE, C., FOWLES, P., HAWKESWORTH, M. & O'DWYER, M. 1988. Application of positron emission tomography to particulate flow measurement in chemical engineering processes. Nuclear Instruments and Methods in Physics Research Section A: Accelerators, Spectrometers, Detectors and Associated Equipment, 273, 874-880.

BERGEN, J., CARRIER, G. & KRUMHANS, J. 1958. Criteria for Mixing and the Mixing Process.

BOSS, J. & CZASTKIEWICZ, W. 1982. Principles of scale-up for laminar mixing processes of Newtonian fluids in static mixers. Int. Chem. Eng, 22, 362-367.

BYRDE, O. & SAWLEY, M. L. 1999. Optimization of a Kenics static mixer for non-creeping flow conditions. Chemical engineering journal, 72, 163-169.

CHILTON, R. A. & STAINSBY, R. 1998. Pressure loss equations for laminar and turbulent non-Newtonian pipe flow. Journal of hydraulic engineering, 124, 522-529.

CHITI, F. 2008. Lagrangian studies of turbulent mixing in a vessel agitated by a rushron turbine: positron emission particle tracking (PEPT) and computational fluid dynamics (CFD). Ph.D., University of Birmingham.

CHITI, F., BAKALIS, S., BUJALSKI, W., BARIGOU, M., EAGLESHAM, A. & NIENOW, A. W. 2011. Using positron emission particle tracking (PEPT) to study the turbulent flow in a baffled vessel agitated by a Rushton turbine: Improving data treatment and validation. Chemical Engineering Research and Design, 89, 1947-1960.

CHUNG, K., BARIGOU, M. & SIMMONS, M. 2007. Reconstruction of 3-D flow field inside miniature stirred vessels using a 2-D PIV technique. Chemical Engineering Research and Design, 85, 560-567.

COOPER JR, A. R. 1966. Diffusive mixing in continuous laminar flow systems. Chemical Engineering Science, 21, 1095-1106.

COUPLAND, J. M. & HALLIWELL, N. A. 1992. Particle image velocimetry-Three-dimensional fluid velocity measurements using holographic recording and optical correlation. Applied optics, 31, 1005-1007.

COX, P. W., BAKALIS, S., ISMAIL, H., FORSTER, R., PARKER, D. J. & FRYER, P. J. 2003. Visualisation of three-dimensional flows in rotating cans using positron emission particle tracking (PEPT). Journal of Food Engineering, 60, 229-240.

DANCKWERTS, P. 1952. The definition and measurement of some characteristics of mixtures. Applied Scientific Research, 3, 279-296.

DEVELLIAN, R. 1972. Continuous, Predictable Performance with Motionless Mixers. Automation, February, 46-48.

DOUCET, J., BERTRAND, F. & CHAOUKI, J. 2008. A measure of mixing from Lagrangian tracking and its application to granular and fluid flow systems. Chemical Engineering Research and Design, 86, 1313-1321.

ETCHELLS, A. W. & MEYER, C. F. 2004. Mixing in Pipelines. Handbook of Industrial Mixing. John Wiley & Sons, Inc.

FAIRHURST, P. G., BARIGOU, M., FRYER, P. J., PAIN, J. P. & PARKER, D. J. 2001. Using positron emission particle tracking (PEPT) to study nearly neutrally buoyant particles in high solid fraction pipe flow. International journal of multiphase flow, 27, 1881-1901.

FAN, X., PARKER, D. J. & SMITH, M. D. 2006. Enhancing 18F uptake in a single particle for positron emission particle tracking through modification of solid surface chemistry. Nuclear Instruments and Methods in Physics Research Section A: Accelerators, Spectrometers, Detectors and Associated Equipment, 558, 542-546.

FAN, X., PARKER, D. J. & SMITH, M. D. 2006. Enhancing 18F uptake in a single particle for positron emission particle tracking through modification of solid surface chemistry. Nuclear Instruments and Methods in Physics Research Section A: Accelerators, Spectrometers, Detectors and Associated Equipment, 558, 542-546.

FANGARY, Y., BARIGOU, M., SEVILLE, J. & PARKER, D. 2000. Fluid trajectories in a stirred vessel of non-Newtonian liquid using positron emission particle tracking. Chemical Engineering Science, 55, 5969-5979.

FANGARY, Y. S., BARIGOU, M., SEVILLE, J. P. & PARKER, D. J. 2002. A Langrangian study of solids suspension in a stirred vessel by positron emission particle tracking (PEPT). Chemical engineering & technology, 25, 521-528.

FERGUSON, J. & KEMBLOWSKI, Z. 1991. Applied fluid rheology, Cambridge, Elsevier Applied Science.

GABRIELE, A. 2011. Fluid Gels: formation, production and lubrication. PhD thesis, University of Birmingham.

GALAKTIONOV, O. S., ANDERSON, P. D., PETERS, G. W. M. & MEIJER, H. E. H. 2003. Mixing and Compounding-Analysis and Optimization of Kenics Static Mixers. International Polymer Processing, 18, 138-150.

GALAKTIONOV, O. S., MEIJER, H. E. H. & BAAIJENS, F. P. T. 2002. Optimization of distributive mixing: from prototype flows to industrial devices.

GHARIB, M., RAFFEL, M., RONNEBERGER, O. & KOMPENHANS, J. 1995. Feasibility study of three-dimensional PIV by correlating images of particles within parallel light sheet planes. Experiments in fluids, 19, 69-77.

GODFREY, J. C. 1997. Chapter 12 - Static mixers. In: HARNBY, N., EDWARDS, M. F., A.W. NIENOWA2 - N HARNBY, M. F. E. & NIENOW, A. W. (eds.) Mixing in the Process Industries. Oxford: Butterworth-Heinemann.

GOKUL CHANDRA, K. & KALE, D. 1992. Pressure drop for laminar flow of viscoeleastic fluids in static mixers. Chemical Engineering Science, 47, 2097-2100.

GRACE, C. D. 1971. Static mixing and heat transfer. Chem. Proc. Eng, 52, 57.

GUIDA, A., FAN, X., PARKER, D. J., NIENOW, A. W. & BARIGOU, M. 2009. Positron emission particle tracking in a mechanically agitated solid-liquid suspension of coarse particles. Chemical Engineering Research and Design, 87, 421-429.

GUIDA, A., NIENOW, A. W. & BARIGOU, M. 2010. PEPT measurements of solid-liquid flow field and spatial phase distribution in concentrated monodisperse stirred suspensions. Chemical Engineering Science, 65, 1905-1914.

GUIDA, A., NIENOW, A. W. & BARIGOU, M. 2011. Mixing of dense binary suspensions: Multi-component hydrodynamics and spatial phase distribution by PEPT. AIChE Journal, 57, 2302-2315.

HALL, J. F., BARIGOU, M., SIMMONS, M. J. & STITT, E. H. 2004. Mixing in unbaffled high-throughput experimentation reactors. Industrial & Engineering Chemistry Research, 43, 4149-4158.

HAWKESWORTH, M., O'DWYER, M., WALKER, J., FOWLES, P., HERITAGE, J., STEWART, P., WITCOMB, R., BATEMAN, J., CONNOLLY, J. & STEPHENSON, R. 1986. A positron camera for industrial application. Nuclear Instruments and Methods in Physics Research Section A: Accelerators, Spectrometers, Detectors and Associated Equipment, 253, 145-157.

HEYWOOD, N., VINEY, L. & STEWART, I. Mixing efficiencies and energy requirements of various motionless mixer designs for laminar mixing applications. Fluid Mixing II Symposium, 1984. 147-176.

HIRSCHBERG, S., KOUBEK, R., MOSER, F. & SCHÖCK, J. 2009. An improvement of the Sulzer SMX static mixer significantly reducing the pressure drop. Chemical Engineering Research and Design, 87, 524-532.

HOBBS, D. M. & MUZZIO, F. J. 1997a. The Kenics static mixer: a three-dimensional chaotic flow. Chemical engineering journal, 67, 153-166.

HOBBS, D. M. & MUZZIO, F. J. 1997b. Effects of injection location, flow ratio and geometry on kenics mixer performance. AIChE Journal, 43, 3121-3132.

HOBBS, D. M. & MUZZIO, F. J. 1998. Optimization of a static mixer using dynamical systems techniques. Chemical Engineering Science, 53, 3199-3213.

HOBBS, D. M. & MUZZIO, F. J. 1998. Reynolds number effects on laminar mixing in the kenics static mixer. Chemical Engineering Journal, 70, 93-104.

HOBBS, D. M., SWANSON, P. D. & MUZZIO, F. J. 1998. Numerical characterization of low Reynolds number flow in the Kenics static mixer. Chemical engineering science, 53, 1565-1584.

ILIEVSKI, D., RUDMAN, M. & METCALFE, G. 2001. The separate roles of shear rate and mixing on gibbsite precipitation. Chemical engineering science, 56, 2521-2530.

JAFFER, S. A. 1998. Experimental Studies of Static Mixers and Twin Screw Extruders. PhD thesis, McMaster.

JAFFER, S. A. & WOOD, P. E. 2009. Quantification of laminar mixing in the kenics static mixer: an experimental study. The Canadian Journal of Chemical Engineering, 76, 516-521.

JAWORSKI, Z., DYSTER, K. & NIENOW, A. 2001. The effect of size, location and pumping direction of pitched blade turbine impellers on flow patterns: LDA measurements and CFD predictions. Chemical Engineering Research and Design, 79, 887-894.

JAWORSKI, Z., NIENOW, A. & DYSTER, K. 1996. An LDA study of the turbulent flow field in a baffled vessel agitated by an axial, down-pumping hydrofoil impeller. The Canadian Journal of Chemical Engineering, 74, 3-15.

JOSHI, P., NIGAM, K. D. P. & NAUMAN, E. B. 1995. The Kenics static mixer: new data and proposed correlations. The Chemical Engineering Journal and The Biochemical Engineering Journal, 59, 265-271.

KEMBLOWSKI, Z. & PUSTELNIK, P. 1988. Residence time distribution of a power-law fluid in kenics static mixers. Chemical engineering science, 43, 473-478.

KUKUKOVA, A., AUBIN, J. & KRESTA, S. M. 2009. A new definition of mixing and segregation: Three dimensions of a key process variable. Chemical Engineering Research and Design, 87, 633-647.

KUMAR, V., SHIRKE, V. & NIGAM, K. D. P. 2008. Performance of Kenics static mixer over a wide range of Reynolds number. Chemical Engineering Journal, 139, 284-295.

LA FONTAINE, R. & SHEPHERD, I. 1996. Particle image velocimetry applied to a stirred vessel. Experimental thermal and fluid science, 12, 256-264.

LAMBERTO, D., ALVAREZ, M. & MUZZIO, F. 1999. Experimental and computational investigation of the laminar flow structure in a stirred tank. Chemical Engineering Science, 54, 919-942.

LARACHI, F., CHAOUKI, J. & KENNEDY, G. 1995. 3-D mapping of solids flow fields in multiphase reactors with RPT. AIChE Journal, 41, 439-443.

LAWSON, N. & WU, J. 1997. Three-dimensional particle image velocimetry: experimental error analysis of a digital angular stereoscopic system. Measurement Science and Technology, 8, 1455.

LEADBEATER, T. W., PARKER, D. J. & GARGIULI, J. 2012. Positron imaging systems for studying particulate, granular and multiphase flows. Particuology.

LEHWALD, A., THÉVENIN, D. & ZÄHRINGER, K. 2010. Quantifying macro-mixing and micro-mixing in a static mixer using two-tracer laser-induced fluorescence. Experiments in fluids, 48, 823-836.

LEVENSPIEL, O. 1972. Chemical reaction engineering, Wiley New York etc.

LEVENSPIEL, O. 1979. The chemical reactor omnibook Corvallis, OR.

LI, M., WHITE, G., WILKINSON, D. & ROBERTS, K. J. 2004. LDA measurements and CFD modeling of a stirred vessel with a retreat curve impeller. Industrial & Engineering Chemistry Research, 43, 6534-6547.

LIU, M., PESKIN, R. L., MUZZIO, F. J. & LEONG, C. W. 1994. Structure of the stretching field in chaotic cavity flows. AIChE Journal, 40, 1273-1286.

LIU, S., HRYMAK, A. N. & WOOD, P. E. 2006. Design modifications to SMX static mixer for improving mixing. AIChE Journal, 52, 150-157.

MARIGO, M., CAIRNS, D., DAVIES, M., COOK, M., INGRAM, A. & STITT, E. 2010. Developing Mechanistic Understanding of Granular Behaviour in Complex Moving Geometry using the Discrete Element Method. Part A: Measurement and Reconstruction of Turbula Mixer Motion using Positron Emission Particle Tracking. Computer Modeling in Engineering & Sciences(CMES), 59, 217-238.

MARIGO, M., CAIRNS, D. L., DAVIES, M., INGRAM, A. & STITT, E. H. 2012. A numerical comparison of mixing efficiencies of solids in a cylindrical vessel subject to a range of motions. Powder Technology, 217, 540-547.

MARIGO, M., DAVIES, M., LEADBEATER, T., CAIRNS, D. L., INGRAM, A. & STITT, E. H. 2013. Application of Positron Emission Particle Tracking (PEPT) to validate a Discrete Element Method (DEM) model of granular flow and mixing in the Turbula mixer. International Journal of Pharmaceutics, 446, 46-58.

MEIJER, H. E., SINGH, M. K. & ANDERSON, P. D. 2011. On the performance of static mixers: A quantitative comparison. Progress in Polymer Science.

METZNER, A. B. & REED, J. C. 1955. Flow of non-newtonian fluidscorrelation of the laminar, transition, and turbulent-flow regions. AIChE Journal, 1, 434-440.

MICKAILY-HUBER, E. S., BERTRAND, F., TANGUY, P., MEYER, T., RENKEN, A., RYS, F. S. & WEHRLI, M. 1996. Numerical simulations of mixing in an SMRX static mixer. The Chemical Engineering Journal and the Biochemical Engineering Journal, 63, 117-126.

MISHRA, V. P., DYSTER, K. N., NIENOW, A. W., MCKEMMIE, J. & JAWORSKI, Z. 1998. A study of an up-and a down-pumping wide blade hydrofoil impeller: Part I. LDA measurements. The Canadian Journal of Chemical Engineering, 76, 577-588.

MOHR, W. D., SAXTON, R. L. & JEPSON, C. H. 1957. Mixing in Laminar-Flow Systems. Industrial & Engineering Chemistry, 49, 1855-1856.

MUZZIO, F., MENEVEAU, C., SWANSON, P. & OTTINO, J. 1992. Scaling and multifractal properties of mixing in chaotic flows. Physics of Fluids A: Fluid Dynamics, 4, 1439.

MUZZIO, F., SWANSON, P. & OTTINO, J. 1991. The statistics of stretching and stirring in chaotic flows. Physics of Fluids A: Fluid Dynamics, 3, 822.

MUZZIO, F., SWANSON, P. & OTTINO, J. M. 1992. Mixing distributions produced by multiplicative stretching in chaotic flows. International journal of bifurcation and chaos, 2, 37-50.

NAUMAN, E. 1982. Reactions and residence time distributions in motionless mixers. The Canadian Journal of Chemical Engineering, 60, 136-140.

NAUMAN, E. B. 1991. On residence time and trajectory calculations in motionless mixers. The Chemical Engineering Journal, 47, 141-148.

NG, K., FENTIMAN, N., LEE, K. & YIANNESKIS, M. 1998. Assessment of sliding mesh CFD predictions and LDA measurements of the flow in a tank stirred by a Rushton impeller. Chemical Engineering Research and Design, 76, 737-747.

NIGAM, K. D. P. & VASUDEVA, K. 1980. Residence time distribution in static mixer. The Canadian Journal of Chemical Engineering, 58, 543-544.

NOBEL, L. 1962. PROCESS AND APPARATUS FOR MIXING. US patent application.

OLMICCIA, J., HENICHE, M. & BERTRAND, F. 2011. A Particulate Method for Determining Residence Time in Viscous Flow Processes. Macromolecular Materials and Engineering, 296, 362-372.

OSELEDETS, V. I. 1968. A multiplicative ergodic theorem. Characteristic Ljapunov, exponents of dynamical systems. Trudy Moskovskogo Matematicheskogo Obshchestva, 19, 179-210.

OTTINO, J. 2000. Chaotic mixing in a bounded three-dimensional flow. J. Fluid Mech, 417, 265-301.

PAHL, M. & MUSCHELKNAUTZ, E. 1982. Static mixers and their applications. Int. Chem. Eng, 22, 197-205.

PARKER, D., HAWKESWORTH, M. & BEYNON, T. 1995. Process applications of emission tomography. The Chemical Engineering Journal and the Biochemical Engineering Journal, 56, 109-117.

PARKER, D. J., BROADBENT, C. J., FOWLES, P., HAWKESWORTH, M. R. & MCNEIL, P. 1993. Positron emission particle tracking-a technique for studying flow within engineering equipment. Nuclear Instruments and Methods in Physics Research Section A: Accelerators, Spectrometers, Detectors and Associated Equipment, 326, 592-607.

PARKER, D. J., DIJKSTRA, A. E., MARTIN, T. W. & SEVILLE, J. P. K. 1997. Positron emission particle tracking studies of spherical particle motion in rotating drums. Chemical Engineering Science, 52, 2011-2022.

PARKER, D. J., LEADBEATER, T. W., FAN, X., HAUSARD, M. N., INGRAM, A. & YANG, Z. 2008. Positron imaging techniques for process engineering: recent developments at Birmingham. Measurement Science and Technology, 19, 4004.

PIANKO-OPRYCH, P., NIENOW, A. W. & BARIGOU, M. 2009. Positron emission particle tracking (PEPT) compared to particle image velocimetry (PIV) for studying the flow generated by a pitched-blade turbine in single phase and multi-phase systems. Chemical Engineering Science, 64, 4955-4968.

PUST, O., STRAND, T., MATHYS, P. & RÜTTI, A. Quantification of laminar mixing performance using Laser-Induced Fluorescence. 13th International Symposium on Applications of Laser Techniques to Fluid Mechanics, Lisbon, Portugal, 2006.

PUSTELNIK, P. 1986. Investigation of residence time distribution in Kenics static mixers. Chemical Engineering and Processing: Process Intensification, 20, 147-154.

R.DERBY 1976. Viscoelastic Fluids, An Introduction to Their Properties and Behaviour,, Marcel Dekker Inc.

RAMMOHAN, A. R., KEMOUN, A., AL-DAHHAN, M. H. & DUDUKOVIC, M. P. 2001. A Lagrangian description of flows in stirred tanks via computer-automated radioactive particle tracking (CARPT). Chemical engineering science, 56, 2629-2639.

RAULINE, D., LE BLÉVEC, J. M., BOUSQUET, J. & TANGUY, P. A. 2000. A comparative assessment of the performance of the Kenics and SMX static mixers. Chemical Engineering Research and Design, 78, 389-396.

RAULINE, D., LE BLÉVEC, J. M., BOUSQUET, J. & TANGUY, P. A. 2000. A comparative assessment of the performance of the Kenics and SMX static mixers. Chemical Engineering Research and Design, 78, 389-396.

RAULINE, D., TANGUY, P. A., LE BLÉVEC, J. M. & BOUSQUET, J. 1998. Numerical investigation of the performance of several static mixers. The Canadian Journal of Chemical Engineering, 76, 527-535.

ROM-KEDAR, V., LEONARD, A. & WIGGINS, S. 1990. An analytical study of transport, mixing and chaos in an unsteady vortical flow. Journal of Fluid Mechanics, 214, 347-394.

RUTHERFORD, K., LEE, K., MAHMOUDI, S. & YIANNESKIS, M. 1996. Hydrodynamic characteristics of dual Rushton impeller stirred vessels. AIChE Journal, 42, 332-346.

SAATDJIAN, E., RODRIGO, A. J. S. & MOTA, J. P. B. 2012. A study of mixing by chaotic advection in two three-dimensional open flows. Chemical Engineering Science.

SCOTT, F. H. 1992. Elements of chemical reaction engineering. Fluidized Bed Reactor the Methylchlorosilane Reaction and Determination of the Fate of Oxygen, silicon chemistry, 1, 23-33.

SHAH, N. F. & KALE, D. D. 1991. Pressure drop for laminar flow of non-Newtonian fluids in static mixers. Chemical engineering science, 46, 2159-2161.

SHENG, J., MENG, H. & FOX, R. O. 1998. Validation of CFD simulations of a stirred tank using particle image velocimetry data. The Canadian Journal of Chemical Engineering, 76, 611-625.

SHOOK, C. A. 1991. Slurry flow: principles and practice, London, Butterworth-Heinemann.

SIMMONS, M., ZHU, H., BUJALSKI, W., HEWITT, C. & NIENOW, A. 2007. Mixing in a model bioreactor using agitators with a high solidity ratio and deep blades. Chemical Engineering Research and Design, 85, 551-559.

SINGH, M. K., ANDERSON, P. D. & MEIJER, H. E. 2009. Understanding and optimizing the SMX static mixer. Macromolecular rapid communications, 30, 362-376.

SPENCER, R. S. & WILEY, R. M. 1951. The mixing of very viscous liquids. Journal of Colloid Science, 6, 133-145.

STAMBAUGH, J., SMITH, Z., OTT, E. & LOSERT, W. 2004. Segregation in a monolayer of magnetic spheres. Phys Rev E Stat Nonlin Soft Matter Phys, 70, 031304.

STEFFE, J. F. 1996. Rheological methods in food process engineering, Freeman press.

STEWART, R. L., BRIDGWATER, J., ZHOU, Y. C. & YU, A. B. 2001. Simulated and measured flow of granules in a bladed mixer--a detailed comparison. Chemical Engineering Science, 56, 5457-5471.

SZALAI, E., ARRATIA, P., JOHNSON, K. & MUZZIO, F. 2004. Mixing analysis in a tank stirred with Ekato Intermig< sup>®</sup> impellers. Chemical Engineering Science, 59, 3793-3805.

SZALAI, E. S. & MUZZIO, F. J. 2003. Fundamental approach to the design and optimization of static mixers. AIChE journal, 49, 2687-2699.

TANGUY, P. A., BERTRAND, J. & XUEREB, C. 2005. Handbook of Industrial Mixing, Science and Practice, E.L. Paul, V.A. Atiemo-Obeng, S.M. Kresta (Eds.). John Wiley & Sons, Hoboken, NJ (2003), ISBN: 0-471-26919-0. Chemical Engineering Science, 60, 2533.

TAUSCHER, W. & SCHUTZ, G. 1973. Static mixing elements. Sulzer Tech Rev, 55, 157.

TUNG, T. T. 1976. Low Reynolds number entrance flows: a study of a motionless mixer.

VAN DER MOLEN, K. & VAN MAANEN, H. 1978. Laser-Doppler measurements of the turbulent flow in stirred vessels to establish scaling rules. Chemical Engineering Science, 33, 1161-1168.

VAN WAGENINGEN, W. F. C., KANDHAI, D., MUDDE, R. F. & VAN DEN AKKER, H. E. A. 2004. Dynamic flow in a kenics static mixer: An assessment of various cfd methods. AIChE journal, 50, 1684-1696.

VISSER, J. E., ROZENDAL, P. F., HOOGSTRATEN, H. W. & BEENACKERS, A. A. 1999. Three-dimensional numerical simulation of flow and heat transfer in the Sulzer SMX static mixer. Chemical Engineering Science, 54, 2491-2500.

WILKINSON, W. & CLIFF, M. An investigation into the performance of a static in-line mixer. Second European Conference on Mixing, A2-15-29, 1977.

WILLERT, C. & GHARIB, M. 1991. Digital particle image velocimetry. Experiments in fluids, 10, 181-193.

WITTMER, S., FALK, L., PITIOT, P. & VIVIER, H. 1998. Characterization of stirred vessel hydrodynamics by three dimensional trajectography. The Canadian Journal of Chemical Engineering, 76, 600-610.

WONG, Y. S. 2006. Particle motion in relatively thin fluidised bed models. Chemical Engineering Science, 61, 6234-6238.

WU, H. & PATTERSON, G. 1989. Laser-Doppler measurements of turbulent-flow parameters in a stirred mixer. Chemical Engineering Science, 44, 2207-2221.

ZALC, J., ALVAREZ, M., MUZZIO, F. & ARIK, B. 2001. Extensive validation of computed laminar flow in a stirred tank with three Rushton turbines. AIChE Journal, 47, 2144-2154.

ZALC, J., SZALAI, E., ALVAREZ, M. & MUZZIO, F. 2002. Using CFD to understand chaotic mixing in laminar stirred tanks. AIChE Journal, 48, 2124-2134.

ZALC, J. M., SZALAI, E. S., MUZZIO, F. J. & JAFFER, S. 2002. Characterization of flow and mixing in an SMX static mixer. AIChE Journal, 48, 427-436.

APPENDIX A. ADDITIONAL FIGURES

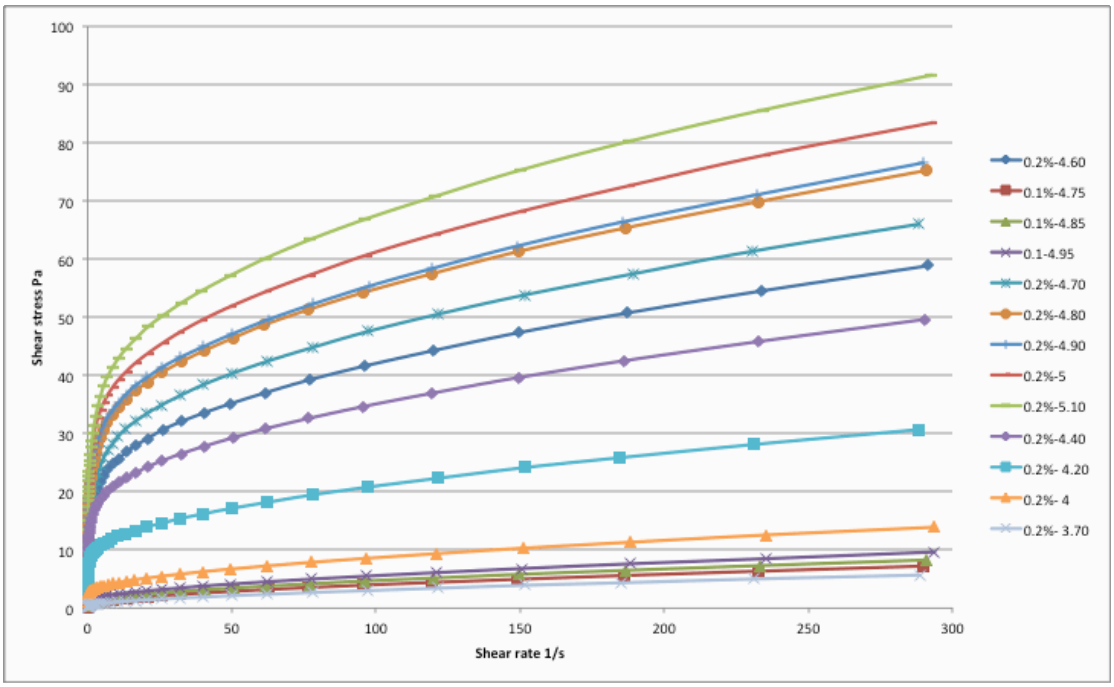

Figure A.1. Shear table of Carbopol 0.1 wt% and Carbopol 0.2 wt% solutions for different pH.

APPENDIX B. MATLAB SCRIPTS

Base.m

```
%%%% 'M' contains the data of the whole experiment.

%%%% M(:,1)=time, M(:,2)=x, M(:,3)=z, M(:,4)=y

clear all;
m1=dlmread('file1.a01','',11,0);
error=mean(m1(:,5))+std(m1(:,5));
m1(m1(:,5)>error,:)=[];
%%%%Save as m1-m2.mat

m2=dlmread('file2.a01','',11,0);
error=mean(m2(:,5))+std(m2(:,5));
m2(m2(:,5)>error,:)=[];

m3=dlmread('file3.a01_02','',11,0);
error=mean(m3(:,5))+std(m3(:,5));
m3(m3(:,5)>error,:)=[];

m4=dlmread('file4.a01','',11,0);
error=mean(m4(:,5))+std(m4(:,5));
m4(m4(:,5)>error,:)=[];

m5=dlmread('file5.a01_02','',11,0);
error=mean(m5(:,5))+std(m5(:,5));
m5(m5(:,5)>error,:)=[];
m2(:,1)=m2(:,1)+m1(length(m1),1);
m3(:,1)=m3(:,1)+m2(length(m2),1);
m4(:,1)=m4(:,1)+m3(length(m3),1);
m5(:,1)=m5(:,1)+m4(length(m4),1);

M=vertcat(m1,m2,m3,m4,m5);

%% REMOVE THE ROW WITH LARGE ERROR
error=mean(M(:,5))+std(M(:,5));
M(M(:,5)>error,:)=[];

%% Finding Index
dif(:,1)=abs(diff(M(:,3)));
indx(:,1)=find(dif(:,1)>=400);
%M(indx(k+1,:)=[];
%% Finding the two rotation angles
[M]=rotaz(M,indx);

%% Centrizing the data element by element
 x0=min(M(:,2))+r;  %%%centre
 y0=min(M(:,4))+r;  %%%centre
 M(:,2)=M(:,2)-x0;
 M(:,4)=M(:,4)-y0;

%% Finding The position of each element
clear h;
for k=1:length(indx)-1
   h(k,1)=(find(M(indx(k)+1:indx(k+1),3)>=115,1,'first'))+indx(k); %first
index of each cross section
   h(k,2)=(find(M(indx(k)+1:indx(k+1),3)>=191,1,'first'))+indx(k);
   h(k,3)=(find(M(indx(k)+1:indx(k+1),3)>=267,1,'first'))+indx(k);
   h(k,4)=(find(M(indx(k)+1:indx(k+1),3)>=344,1,'first'))+indx(k);
   h(k,5)=(find(M(indx(k)+1:indx(k+1),3)>=419,1,'first'))+indx(k);
   h(k,6)=(find(M(indx(k)+1:indx(k+1),3)<=496,1,'last'))+indx(k);
   h(k,7)=(find(M(indx(k)+1:indx(k+1),3)<=550,1,'last'))+indx(k);
end
```

rotaz.m

```
function [M_r]=rotaz(M,indx)

for k=1:length(indx)-1
bottom_X(k,:) = M(indx(k)+1:indx(k)+5,2);         %x
bottom_Z(k,:) = M(indx(k)+1:indx(k)+5,3);         %z
bottom_Y(k,:) = M(indx(k)+1:indx(k)+5,4);         %y
end

for k=1:length(indx)-1
top_X(k,:) = M(indx(k+1)-4:indx(k+1),2);         %x
top_Z(k,:) = M(indx(k+1)-4:indx(k+1),3);         %z
top_Y(k,:) = M(indx(k+1)-4:indx(k+1),4);         %y
end

% %average position bottom and top
bottom_mean_X = mean(mean(bottom_X,1));
bottom_mean_Z = mean(mean(bottom_Z,1));
bottom_mean_Y = mean(mean(bottom_Y,1));
top_mean_X = mean(mean(top_X,1));
top_mean_Z = mean(mean(top_Z,1));
top_mean_Y = mean(mean(top_Y,1));

%slope angle along x from bottom to top. (if perfectly straight top_mean_X
%= bottom_mean_X)

theta = atan2((top_mean_Y - bottom_mean_Y),(top_mean_Z - bottom_mean_Z));
phi = atan2((top_mean_X - bottom_mean_X),(top_mean_Z - bottom_mean_Z));

theta_mean = mean(theta);
phi_mean = mean(phi);


%% ROTATING THE DATA
clear theta phi

theta = theta_mean;
M_r(:,3) = M(:,3)*cos(theta)+(M(:,4)*sin(theta));
M_r(:,4) = M(:,4)*cos(theta)-(M(:,3)*sin(theta));

phi= phi_mean;
M_r(:,2) = M(:,2)*cos(phi)-(M(:,3)*sin(phi));
M_r(:,3) = M(:,3)*cos(phi)+(M(:,2)*sin(phi));
end
```

Filtering_man.m

```
k = 1; k_inital = 1; k_final  = 7000; close all;
clear indx indx_cut
while k_final < 10000+length(M)

    close all

    if k ~= 1
        plot(M(indx_cut(k-1,2):indx_cut(k-1,2)+5000,1),M(indx_cut(k-
1,2):indx_cut(k-1,2)+5000,3),'-bd');hold
    else
        plot(M(k_inital:k_final,1),M(k_inital:k_final,3),'-bd');hold
    end

    fig=figure(1);
    dcm_obj = datacursormode(fig);
    set(dcm_obj,'DisplayStyle','datatip',...
```

```
        'SnapToDataVertex','on','Enable','on')

    hold on

    figure(1)
    title('Click on the start point');

    pause
    cursor_info_start = getCursorInfo(dcm_obj);

    dcm_obj = datacursormode(fig);
    set(dcm_obj,'DisplayStyle','datatip',...
        'SnapToDataVertex','on','Enable','on');

    figure(1)
    title('Click on the end point');


    pause
    cursor_info_end = getCursorInfo(dcm_obj);

    if k ~= 1
    indx_cut(k,1) = indx_cut(k-1,2)  + cursor_info_start(1).DataIndex;
    indx_cut(k,2) = indx_cut(k-1,2)  + cursor_info_end(1).DataIndex;
    else
    indx_cut(k,1) = cursor_info_start(1).DataIndex;
    indx_cut(k,2) = cursor_info_end(1).DataIndex;
    end

    k_inital = indx_cut(k,2);
    k_final  = indx_cut(k,2)+1000;
    k=k+1;

 end
```

kenics.m

```
%% Calculation of the cylindrical velocity

% make sure all the coordinates start at zero, including Z
% Data Handling
t=M(:,1);
x=M(:,2);
z=M(:,3);
y=M(:,4);
 if min(z)~=0
 z=z-min(z);
 end
  if min(x)~=0
 x=x-min(x);
  end
  if min(y)~=0
 y=y-min(y);
  end
[theta,r,z]=cart2pol(M(:,2),M(:,4),M(:,3));    % distance in millimiters
A_Pol=[t,theta,z,r];
theta_tmp = Rectify(theta);


  %%%%%% %% CALCULATION OF CYLENDRICAL VELOCITIES%%%%%%%%%%%%%%%%%%%

   n=5;            % Number of points over which interpolate
    [Vth ]       =InterpPEPT(t,theta_tmp,5);
    [Vr ]       =InterpPEPT(t,r,5);
    [Vz ]      =InterpPEPT(t,z,5);
  %%%%%%%%%%%%%%%%Eulerian Plot%%%%%%%%%%%%%%%%%%%%%%%%%%
```

```
MaxZ=550;
MaxR=max(r);
r_bins=33;
th_bins=6;
z_bins=137;


[E] = Eulerian_C([A_Cart],Vr,Vz,V_tan,MaxZ,MaxY,MaxX,y_bins,x_bins,z_bins);
[E] = Eulerian_C([A_Cart],Vx,Vz,Vy,MaxZ,MaxY,MaxX,y_bins,x_bins,z_bins);
%%%%% E(:,:,:,4): Vth,    E(:,:,:,6): Vr

%% Calculation of the Cartezian Velocities

t=M(:,1);                                          % time in milli seconds
x=M(:,2);
z=M(:,3);
y=M(:,4);


% make sure all the coordinates start at zero, including Z
 if min(z)~=0
 z=z-min(z);
 end
  if min(x)~=0
 x=x-min(x);
  end
  if min(y)~=0
 y=y-min(y);
  end
 A_Cart=[t,x,y,z];
  %%%%%% %% CALCULATION OF CARTEZIAN VELOCITIES%%%%%%%%%%%%%%%%%%%

   n=5;           % Number of points over which interpolate

    [Vy ]       =InterpPEPT(t,y,5);
    [Vz ]       =InterpPEPT(t,z,5);
    [Vx ]      =InterpPEPT(t,x,5);
  %%%%%%%%%%%%%%%%Eulerian Plot%%%%%%%%%%%%%%%%%%%%%%%%%%
MaxZ=520;
MaxY=max(y);
MaxX=max(x);
x_bins=33;
y_bins=33;
z_bins=74%70;


[E] = Eulerian_C([A_Cart],Vx,Vz,Vy,MaxZ,MaxY,MaxX,y_bins,x_bins,z_bins);
```

InterPEPT.m

```
function A=InterpPEPT(X,Y,n)
%% Interpolation Linear and give velocities
clear tmp
warning('off')

n=2.*round((n+1)/2)-1;

A=zeros(size(X,1),1);
k=1;
for i=n+1:size(X,1)-n
    x=X(i-n:i+n,1);
    y=Y(i-n:i+n,1);

Xx=[ones(length(x),1), x(:,1)];
```

```
    B=pinv(Xx)*y;

A(k,1)=B(2); k=k+1;
end
```

Eulerian_C.m

```
function [EulerianC] =
Eulerian_C( A_Cart,Vx,Vz,Vy,MaxZ,MaxY,MaxX,y_bins,x_bins,z_bins)

x_nodes=[(0:1:x_bins)/x_bins]*MaxX;
x_centers=(x_nodes(1:length(x_nodes)-1)+x_nodes(2:length(x_nodes)))/2;

y_nodes=[(0:1:y_bins)/y_bins]*MaxY;
y_centers=(y_nodes(1:length(y_nodes)-1)+y_nodes(2:length(y_nodes)))/2;


z_nodes=linspace(0,1,z_bins+1)*MaxZ;
z_centers=(z_nodes(1:length(z_nodes)-1)+z_nodes(2:length(z_nodes)))/2;

EulerianC=zeros(y_bins,x_bins,z_bins,9);

[EulerianC(:,:,:,1),EulerianC(:,:,:,2),EulerianC(:,:,:,3)]=meshgrid(y_center
s,x_centers,z_centers);


 izo=1;
 ixo=1;
 iyo=1;

 for i_lag=1:length(Vz)-1

y_act=A_Cart(i_lag,3);
x_act=A_Cart(i_lag,2);
z_act=abs(A_Cart(i_lag,4));
dt=(A_Cart(i_lag+1,1)-A_Cart(i_lag,1));


iy=find(y_nodes<=y_act,1,'last');
ix=find(x_nodes<=x_act,1,'last');
iz=find(z_nodes<=z_act,1,'last');

if iz>z_bins
iz=z_bins;
end

if iy>y_bins
iy=y_bins;
end

 if ix>x_bins
 ix=x_bins;
 end

EulerianC(iy,ix,iz,4) = EulerianC(iy,ix,iz,4) + Vy(i_lag);  %Vy
EulerianC(iy,ix,iz,5) = EulerianC(iy,ix,iz,5) + Vz(i_lag);  %Vz
EulerianC(iy,ix,iz,6) = EulerianC(iy,ix,iz,6) + Vx(i_lag);  %Vx
EulerianC(iy,ix,iz,7) = EulerianC(iy,ix,iz,7) + 1;   %PASS count

EulerianC(iy,ix,iz,8) = (EulerianC(iy,ix,iz,8) + dt)/max([1; abs(iz-izo);
abs(ix-ixo); abs(iy-iyo)]);     %TIME IN EACH CELL

izo=iz;
ixo=ix;
iyo=iy;
```

```
end
%%%AVERAGE VELOCITY

EulerianC(:,:,:,4) = (EulerianC(:,:,:,4)./EulerianC(:,:,:,7));  %FINAL Vy
EulerianC(:,:,:,5) =(EulerianC(:,:,:,5)./EulerianC(:,:,:,7)); %FINAL Vz
EulerianC(:,:,:,6) =(EulerianC(:,:,:,6)./EulerianC(:,:,:,7));%Final Vx
EulerianC(:,:,:,9)=sqrt(EulerianC(:,:,:,4).^2+EulerianC(:,:,:,5).^2+Eulerian
C(:,:,:,6).^2);

end
```

Blue and red.m

```
start_el=115;   %%%% where the first element is located along z
z_range_init=zrange(M(:,3),start_el,indx(:,1));   %first index of all the
passes for different z planes
h(:,1)=z_range_init;
%% Finding Blue and Red Groups
clear tmp_j Gr Gb G1 G2
  tmp_j=zeros(length(indx),1);
for i=1:length(indx)-1
    if M(h(i,1),4) >0 %%X=0 is the equation of the the line corresponding to
the position of the blade in the cross section.
        tmp_j(i)=1;
    end
end

Gb=zeros(length(indx),1);
Gr=zeros(length(indx),1);
for i=1:length(indx)-1
   if tmp_j(i)==0
       Gb(i)=i; %%%%X>0
   else
       Gr(i)=i;  %%%%X<0
   end
end
Gb=nonzeros(Gb);
Gr=nonzeros(Gr);
G1=Gb;G2=Gr;
%% Making the Animation
z1=76;              %Where to Start the Animation. This should be the same
number as the one where h(:,1) is.
for i=1:218

for k=1:length(indx)-1
       h(k,i)=(find(M(indx(k)+1:indx(k+1),3)>=z1,1,'first'))+indx(k); %first
index of each cross section
end
z1=z1+2;
end

fig=figure;
writerObj =
VideoWriter('/Users/Marjan/Desktop/Carbopol/New/Carbopol0.1%.mp4');
writerObj.FrameRate = 4;
open(writerObj);
for k=1:length(h(1,:))
      for j=G1
  plot(M(h(j,k),2),M(h(j,k),4),'bd','MarkerFaceColor','b');hold all;
  T= linspace(0,2*pi,870);p=0;K=0;rr=28;XX = rr*cos(T)+p;YY =
rr*sin(T)+K;plot(XX,YY,'k'); hold all;axis equal;
xlim([-30 30]);ylim([-28 28]);xlabel('x mm  ','fontsize',14);ylabel('y mm
','fontsize',14);
set(gca,'YTick',-28:28:28); set(gca,'XTick',-30:30:30);
set(gca,'XTickLabel',{'-25 ';'0';'25'});set(gca,'YTickLabel',{'-25
```

```
';'0';'25'});
      end

    for i=G2
  plot(M(h(i,k),2),M(h(i,k),4),'rd','MarkerFaceColor','r');hold all;
  T= linspace(0,2*pi,870);p=0;K=0;rr=28;XX = rr*cos(T)+p;YY =
rr*sin(T)+K;plot(XX,YY,'k'); hold all;axis equal;
xlim([-30 30]);ylim([-28 28]);xlabel('x mm  ','fontsize',14);ylabel('y mm
','fontsize',14);
set(gca,'YTick',-28:28:28); set(gca,'XTick',-30:30:30);
set(gca,'XTickLabel',{'-25 ';'0';'25'});set(gca,'YTickLabel',{'-25
';'0';'25'});
    end
F=getframe(fig);
writeVideo(writerObj, F);
hold off;
end

close (fig);
close(writerObj);
VideoWriter('/Users/Marjan/Desktop/Carbopol/New/Carbopol0.1%.mp4')
```

Segregation_index.m

```
start_el=190;   %%%where the first element located along z
z_range_init=zrange(M(:,3),start_el,indx(:,1));   %first index of all
the passes for different z planes
h=z_range_init;


%% Finding Blue and Red Groups
clear tmp_j  G1 G2
  tmp_j=zeros(length(h),1);
for i=1:length(h)
    if M(h(i),2)>0%%X=0 is the equation of the the line corresponding
to the position of the blade in the cross section.
        tmp_j(i)=1;
    end
end
G1=find(tmp_j(:)==1);
G2=find(tmp_j(:)==0);
%%=========================
%%%%Testing blue and red on the graph:
 for k=G1
  plot(M(h(k,1),2),M(h(k,1),4),'bd','MarkerFaceColor','b');hold all
  end

for i=G2
  plot(M(h(i,1),2),M(h(i,1),4),'rd','MarkerFaceColor','r');hold all
end

%%=========================
B_point=G1;R_point=G2;



%%
Element_position_vector=(115:2:546);

for kk=1:length(Element_position_vector)
    clear A minBB minBBR minBR minBR2 minRBR minRR  DB DBR DR
```

```
    el=Element_position_vector(kk);
    z_range=zrange(M(:,3),el,indx(:,1));   %first index of all the
passes for different z planes

    for i=1:length(indx)

        A(i,:)=M(z_range(i,1),:);   %in order to make the code easier,
        %after finding the indexes for different z planes, I put all
the data in A
    end

    %%%The distance between Red passes from each other
    for j=1:length(R_point)
        for i=1:length(R_point)

            DR(i,j)=sqrt((A(R_point(j),2)-
A(R_point(i),2))^2+(A(R_point(j),4)-A(R_point(i,1),4))^2);

        end
    end

    %%%The distance between Blue passes from each other
    for j=1:length(B_point)
        for i=1:length(B_point)

            DB(i,j)=sqrt( (A(B_point(j),2)-
A(B_point(i),2))^2+(A(B_point(j),4)-A(B_point(i),4))^2 );

        end
    end

    %%%The distance between Blue and Red passes from each other
    for j=1:length(B_point)
        for i=1:length(R_point)

            DBR(j,i)=sqrt((A(B_point(j),2)-
A(R_point(i),2))^2+(A(B_point(j),4)-A(R_point(i),4))^2);

        end
    end


    %%%%Comparison between the distances to choose the minimum onefor
i=1:length(DB)
    for i=1:length(DB)
        minBB(i,1)=min(nonzeros(DB(i,:)));     % minimum distance for
each row of B-B matrix
    end

    for i=1:length(DR)
        minRR(i,1)=min(nonzeros(DR(i,:)));     % minimum distance for
each row of R-R matrix
    end

    for i=1:length(DBR(:,1))
        minBR(i,1)=min(nonzeros(DBR(i,:)));     % minimum distance
for each row of B-R matrix
    end
       for i=1:length(DBR(1,:))
        minRB(i,1)=min(nonzeros(DBR(:,i)));     % minimum distance
for each row of R-B matrix
```

```
     end

     %%%% Getting an average from the contact distances
     avg_minBB(kk)=mean(minBB(:,1));
     avg_minBR(kk)=mean(minBR(:,1));
     avg_minRR(kk)=mean(minRR(:,1));
     avg_minRB(kk)=mean(minRB(:,1));


    %%%%To make the calculations easier, put everything in one
matrix:
    minBBR(:,1)=minBB;
    minBBR(:,2)=minBR;
    minBBR(:,3)=0;

    for i=1:length(minBBR(:,1))
        if minBBR(i,1)<=minBBR(i,2)
            minBBR(i,3)=1;
        else
            minBBR(i,3)=0;
        end
    end


    minRBR(:,1)=minRR;
    minRBR(:,2)=minRB;
    minRBR(:,3)=0;

    for i=1:length(minRBR(:,1))
        if minRBR(i,1)<=minRBR(i,2)
            minRBR(i,3)=1;
        else
            minRBR(i,3)=0;
        end
    end

    CBB(kk)=sum(minBBR(:,3));
    CRB1(kk)=length(minBBR(:,1))-CBB(kk);
    CRR(kk)=sum(minRBR(:,3));
    CRB2(kk)=length(minRBR(:,1))-CRR(kk);
    CRB(kk)=CRB1(kk);
    CBR(kk)=CRB2(kk);

    S(kk)=(CBB(kk)/(CBB(kk)+CBR(kk)))+(CRR(kk)/(CRR(kk)+CRB(kk)));

end
```